Role of TopBP1 during breast tumorigenesis

A Thesis Submitted in partial fulfilment of the requirements

Of the degree of

Doctor of Philosophy

Rintu M Umesh

20163446



Indian Institute of Science Education and Research Pune

2021

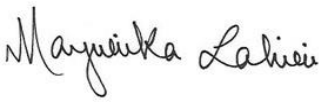
Dedication

I dedicate this thesis to my Appa and Amma

CERTIFICATE

Certified that the work incorporated in the thesis entitled "**Role of TopBP1 during breast tumorigenesis"** submitted by **Rintu M Umesh** was carried out by the candidate, under my supervision. The work presented here or any part of it has not been included in any other thesis submitted previously for the award of any degree or diploma from any other University or institution.

Date: 07 December 2021



Dr. Mayurika Lahiri

Associate Professor

Biology Division, IISER Pune

Declaration

I declare that this written submission represents my ideas in my own words and where others' ideas have been included, I have adequately cited and referenced the original sources. I also declare that I have adhered to all principles of academic honesty and integrity and have not misrepresented or fabricated or falsified any idea/data/fact/source in my submission. I understand that violation of the above will be cause for disciplinary action by the Institute and can also evoke penal action from the sources which have thus not been properly cited or from whom proper permission has not been taken when needed.

Date: 19-11-2021



Rintu M Umesh

20163348

Acknowledgements

At this stage of my PhD, I would like to thank everyone who guided me, helped me and supported me to reach this milestone.

I would like to express my sincere gratitude to **Dr. Mayurika Lahiri** for giving me the golden opportunity to be a part of her lab. I am grateful for her inspiring guidance and support throughout the period of my work. Working in her lab for the past 9 years laid the foundation for my research career. I am sure that the skills and training that I obtained from her will be of tremendous help in my future as a good researcher.

I would also like to thank my research advisory committee members, **Dr. Richa Rikhy** (IISER Pune) and **Dr. Sorab Dalal** (ACTREC Navi Mumbai), for there valuable suggestions and constructive criticism which have laid new paths to the project. I would also like to thank **Dr. Sourav Banerjee**, NBRC and **Dr. Manas Kumar Santra** from NCCS for their help with lentiviral preparation.

Next, I would like to thank my partner in crime, both in the lab and my life, **Dr. Virender Kumar Sharma**. He was my pillar of support in this journey. Being a great friend, he not just supported me when needed, but was honest to tell me my faults whenever I was wrong which helped me improve a lot in my personal as well as professional life. **Abhijith**, my batch mate and lab mate, have been a great friend. He was my all-time “go-to” person whenever I needed any help related to lab as well as life, like experiments, tour plan, technical issues, and the list goes on. I am grateful to my previous lab members **Satish** and **Libi** for their support and guidance in the initial times in the lab as an undergraduate which made me choose research as my carrier. I would like to thank **Rosu, Vandu**, **Fasi** and **Kezia** for being there for me whenever needed both inside and outside the lab. I would also like to thank all the past and present members of ML Lab, namely **Aishwarya, Benchamin, Nikki, Snehal, Madhu, Anisha, Apurva, Tathagata, Gautami, Suraj, , Abhinav, Payal, Vaishali, Ashiq, Meera, Marina, Nitheesh, Vishakha, Amruta, Pradnya, Rupa, Debiprasad, Janhvi, Sudiksha, Tanmaya, Sonali, Radhika, Sucharita, Shrunal, and Abhishek** who made the lab atmosphere so comfortable to work. I would also like to thank **Suman**, my only friend outside ML lab, for being a good listener and a great brother.

I would like to thank Bio-admin staff **Mrinalini, Kalpesh, Piyush, Shabnam, Sandeep, Mahesh, Hari, Sandip,** and **Rupali** for taking care of the infrastructure and help simplify the process of procuring reagents. I would also like to express my special thanks to **Vijay,** and IISER microscopy facility and **Saurabh** and IISER- BD FACS facility. I would like to thank **Dr. Sachin** for his help with initial mice training and National Facility for Gene Function in Health and Disease (IISER, Pune, India) for providing the animals and facilities. I am grateful to the Biology Department of Indian Institute of Science Education and Research (IISER) Pune for providing me with all the facilities and opportunities. I would like to extend my whole-hearted thanks to all the members of the IISER Pune Biology Research Lab especially **SFA labs** for making me a part of this enchanting endeavor.

I would like to thank my best friend **Devika** for listening to me during my difficult times without whom I might not have even completed my course at IISER. Thank you **Reethu** and **Sampath chetta** for the constant support. My loves and hugs to **Sachu** and **Isai baby** for bringing happiness in my life. I am so lucky to be part of my **UMR family** who was always there to cheer my up. I would also like to thank my **in-laws and Lalit** for being understanding and supportive in my work. In the end, I would like to express my appreciation to my Appa and Amma for believing in me and letting me follow my dreams.

Finally, I am thankful to the **Almighty**, for giving me the strength, both physically and mentally to complete this journey.

Synopsis

Role of TopBP1 during breast tumorigenesis

Name of the student: Rintu M Umesh
Student ID: 20163446
Name of the thesis supervisor: Dr Mayurika Lahiri
Date of registration: 1st August 2016
Indian Institute of Science Education and Research (IISER) Pune

Introduction

Breast cancer is the most common cancer among women worldwide. It is also the number one cause of cancer mortality in women. Understanding genes/ pathways which are altered in breast cancer will help in early prognosis, thus better survival of patients. DNA is prone to damage by various endogenous and exogenous agents. If the damage remains unchecked, it may lead to genomic instability leading to cancer. Fortunately, the cells have an elaborate checkpoint signalling mechanism to detect and repair the damage to ensure the faithful transmission of genetic material to the next generation. The canonical checkpoint pathway comprises sensors, mediators, transducers and effector proteins. The sensor proteins, ATM and ATR/ATRIP, sense double-strand or single-strand breaks respectively and activate Chk2 and Chk1 by phosphorylation through mediator proteins, like BRCA1, MDC1 (in Double-Strand Break), Claspin and TopBP1 (in Single-Strand Break pathway). Further, the signal is relayed to effector proteins like Cdc25C, Nbs1, p53, to name a few, which can induce cell cycle arrest to allow time for repair of damaged DNA or apoptosis depending upon the extent of the damage. Defects in checkpoint activation can lead to the accumulation of DNA damage, which may lead to genomic instability. Genomic instability is one of the hallmarks acquired by normal cells to become cancerous.

DNA topoisomerase IIβ-binding protein 1 (TopBP1) participates in the activation of the DNA damage checkpoint to maintain genome integrity (Xu and Leffak, 2010). TopBP1 has eight BRCA1 C-terminus (BRCT) repeat domains through which it interacts with other proteins (Yu et al., 2003) and an ATR activation domain (AAD)

which is necessary to stimulate the kinase activity of ATR (Kumagai et al., 2006) and thus checkpoint activation. Other than its essential role in DNA damage response, TopBP1 is also involved in transcriptional regulation of genes involved in cell proliferation and apoptosis, such as E2F1 and c-Myc (Liu et al., 2009; Liu et al., 2003). Akt phosphorylates TopBP1 at Ser-1159 that leads to its BRCT 7-8 domain oligomerisation and shifts its function from checkpoint activation to transcriptional regulation (Liu et al., 2006). Oligomerised TopBP1 binds to E2F1 and inhibit E2F1 mediated apoptosis (Liu et al., 2006). Its interaction with BLM (Bloom syndrome helicase) has been shown to inhibit sister chromatid exchange, thus maintaining genome stability (Wang et al., 2013). TopBP1 also plays a role during replication initiation by interacting with Treslin to facilitate Cdc45 loading onto replication origins (Kumagai et al., 2006). At the physiological level, TopBP1 is required for the G1 to S transition in the cell cycle. However, aberrant expression of TopBP1 has been observed in breast cancers.

Immunohistochemical studies performed on breast cancer biopsy samples showed that TopBP1 is upregulated in breast cancer tissues. TopBP1 overexpression was associated with higher-grade tumours and reduced patient survival (Forma et al., 2012; Going et al., 2007; Liu et al., 2009). Multiple studies suggest the oncogenic role of TopBP1. Depletion of TopBP1 makes various cancer cells susceptible to undergoing apoptosis; however, higher levels of TopBP1 promotes the survival of cancer cells. All mentioned studies focus and emphasise the tumour-promoting aspect of TopBP1. However, the role of TopBP1 in tumour initiation and the mechanism of tumorigenesis is not established.

Objectives

1. To analyse the TopBP1 expression in breast cancer

2. To characterise the MCF10A cancer progression series

3. To investigate the role of TopBP1 in the transformation of breast epithelial cells

Results

1. TopBP1 levels are high in breast cancer

TOPBP1 expression patterns in tumour and paired adjacent normal tissue were analysed. Using TCGA data analysis, it was observed that TOPBP1 transcript levels in the tumour were higher than the corresponding adjacent normal, confirming the previously reported studies that TopBP1 levels are high in breast cancer. It was also observed that TOPBP1 transcript levels were high across receptor status, molecular subtypes and stages. Higher TOPBP1 levels were associated with reduced patient survival using KM plot analysis . TopBP1 protein expression patterns in Indian breast cancer tissue samples were analysed using immunohistochemistry. It was observed that TopBP1 levels were high in tumour tissues compared to the adjacent normal. Preliminary studies investigating the TopBP1 expression pattern across receptor status revealed that TopBP1 levels were high in ER+ tissues compared to TNBC. Overall, these results suggest that TopBP1 levels are high in breast cancer tissues, suggesting its potential role as an oncogene.

2. Characterisation of MCF10A cancer progression series

To further investigate the role of TopBP1 in tumorigenesis, the MCF10A cancer progression series was used as a model system. The MCF10A series consists of MCF10A (non-transformed epithelial cells), MCF10AT1 (premalignant cells) and MCF10CA1a (malignant cells). As TopBP1 being a protein involved in DNA damage response, the levels of various DNA damage and DNA damage response markers in the MCF10A cancer progression series were analysed. TopBP1 levels were high in premalignant and malignant cells of the MCF10A cancer progression series compared to the non-tumorigenic MCF10A cells. The malignant cells also had endogenous DNA damage even in the absence of external DNA damage. Increased activation of single-strand break repair proteins was observed in MCF10CA1a cells, whereas activation of double-strand break repair pathways was reduced. The EMT and transformation phenotypes of the MCF10A cancer progression series was also characterised. MCF10CA1a cells had higher levels of epithelial markers and lower levels of mesenchymal markers. However, MCF10CA1a cells had higher collective cell migration compared to MCF10A and MCF10AT1. These cells also had colony-forming ability without cell-cell contact and anchorage-independent conditions.

3. TopBP1 overexpression causes mutation in TP53 and facilitates the transformation of non-tumorigenic epithelial cells

The role of TopBP1 in transformation and tumorigenesis was analysed using 3 dimensional (3D) cultures of TopBP1 overexpressing MCF10A and TopBP1 knockdown in MCF10CA1a, malignant cell line. Overexpression of TopBP1 in MCF10A 3D cultures induced hyperproliferation, disruption of polarity and cell-cell junctions. Moreover, TopBP1 overexpressing dissociated cells from acinar cultures exhibited EMT-like phenotype and cancer properties such as increased cell migration, invasion, colony formation capabilities and anchorage-independent growth, indicating acquisition of cellular transformation. Finally, we observed that TopBP1 overexpressing cells formed tumours in athymic mice, thereby confirming their tumorigenic potential. Knockdown of TopBP1 in MCF10CA1a reduced spheroidal size and proliferation in 3D cultures. TopBP1 knockdown also reduced the invasion and colony-forming ability of MCF10CA1a cells. However, the migration, EMT characteristics and tumour forming ability of MCF10CA1a cells were unaffected by TopBP1 knockdown. Mechanistically, TopBP1 OE leads to genomic instability and activation of the single-strand DNA damage response pathway. p53 activation/levels were also increased upon TopBP1 over-expression, where p21 levels were low. TopBP1 KD in MCF10CA1a could revert these activations. TopBP1 overexpression leads to a mutation in the TP53 gene similar to that was observed in MCF10CA1a, which can lead to the formation of mutp53 protein with M237I. To summarise, we observed that ectopic expression of TopBP1 transforms MCF10A breast epithelial cells into cancer cells. These transformed cells harbour phenotypic and genotypic characters of cancerous cells.

Summary

TOPBP1 transcript levels are high in breast cancer samples and higher levels are associated with reduced survival (Figure 1a-b). TopBP1 protein levels are high in Indian patient samples (Figure 1c). TopBP1 over expression induced genomic instability and facilitated transformation of non-tumorigenic breast epithelial cells when grown on 3D environment. These transformed cells had genotypic and phenotypic features of malignant cell line (Figure 1d).

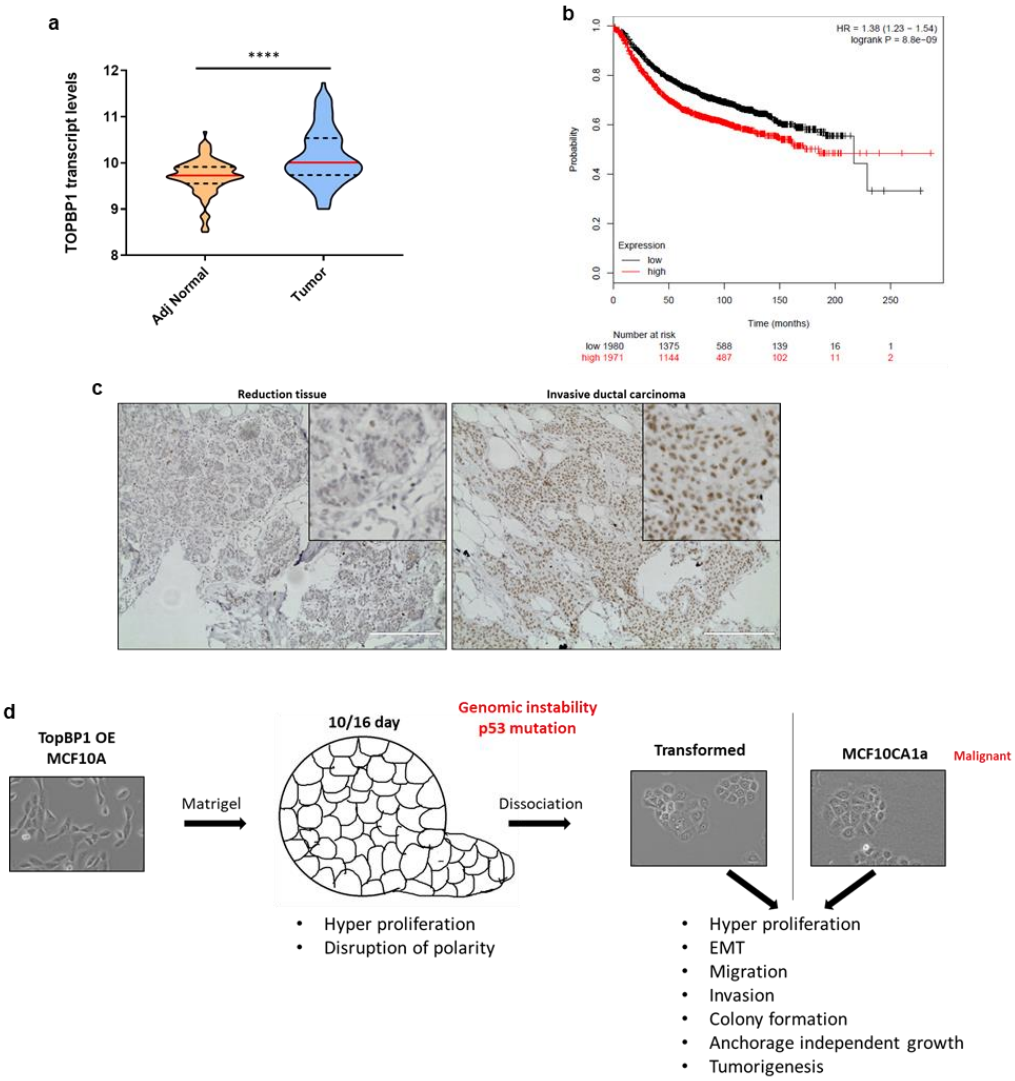


Figure 1: Role of TopBP1 during breast tumorigenesis. a) Scatter plot of TOPBP1 transcript levels in tumour and corresponding adjacent normal based on TCGA database. Statistical analysis was done using Mann Whitney test (**** p <0.0001). b) Survival curve of patient samples with varying TOPBP1 expression using KM plot analysis. c) Schematic representation of TopBP1 induced transformation of MCF10A cells grown on 3D cultures.

References

Cancer Genome Atlas, N. (2012). Comprehensive molecular portraits of human breast tumours. *Nature, 490*(7418), 61-70. doi:10.1038/nature11412

Chen, J., Miller, E. M., & Gallo, K. A. (2010). MLK3 is critical for breast cancer cell migration and promotes a malignant phenotype in mammary epithelial cells. *Oncogene, 29*(31), 4399-4411. doi:10.1038/onc.2010.198

Choi, S. H., Yang, H., Lee, S. H., Ki, J. H., Nam, D. H., & Yoo, H. Y. (2014). TopBP1 and Claspin contribute to the radioresistance of lung cancer brain metastases. *Mol Cancer, 13*, 211. doi:10.1186/1476-4598-13-211

Debnath, J., & Brugge, J. S. (2005). Modelling glandular epithelial cancers in three-dimensional cultures. *Nat Rev Cancer, 5*(9), 675-688. doi:10.1038/nrc1695

Debnath, J., Mills, K. R., Collins, N. L., Reginato, M. J., Muthuswamy, S. K., & Brugge, J. S. (2002). The role of apoptosis in creating and maintaining luminal space within normal and oncogene-expressing mammary acini. *Cell, 111*(1), 29-40.

Debnath, J., Muthuswamy, S. K., & Brugge, J. S. (2003). Morphogenesis and oncogenesis of MCF-10A mammary epithelial acini grown in three-dimensional basement membrane cultures. *Methods, 30*(3), 256-268.

Deisboeck, T. S., & Couzin, I. D. (2009). Collective behavior in cancer cell populations. *Bioessays, 31*(2), 190-197. doi:10.1002/bies.200800084

Forma, E., Krzeslak, A., Bernaciak, M., Romanowicz-Makowska, H., & Brys, M. (2012). Expression of TopBP1 in hereditary breast cancer. *Mol Biol Rep, 39*(7), 7795-7804. doi:10.1007/s11033-012-1622-z

Going, J. J., Nixon, C., Dornan, E. S., Boner, W., Donaldson, M. M., & Morgan, I. M. (2007). Aberrant expression of TopBP1 in breast cancer. *Histopathology, 50*(4), 418-424. doi:10.1111/j.1365-2559.2007.02622.x

Guo, H. B., Johnson, H., Randolph, M., Nagy, T., Blalock, R., & Pierce, M. (2010). Specific posttranslational modification regulates early events in mammary carcinoma formation. *Proc Natl Acad Sci U S A, 107*(49), 21116-21121. doi:10.1073/pnas.1013405107

Hebner, C., Weaver, V. M., & Debnath, J. (2008). Modeling morphogenesis and oncogenesis in three-dimensional breast epithelial cultures. *Annu Rev Pathol, 3*, 313-339. doi:10.1146/annurev.pathmechdis.3.121806.151526

Hedau, S., Jain, N., Husain, S. A., Mandal, A. K., Ray, G., Shahid, M., . . . Das, B. C. (2004). Novel germline mutations in breast cancer susceptibility genes BRCA1, BRCA2 and p53 gene in breast cancer patients from India. *Breast Cancer Res Treat, 88*(2), 177-186. doi:10.1007/s10549-004-0593-8

Hemminki, A., Markie, D., Tomlinson, I., Avizienyte, E., Roth, S., Loukola, A., . . . Aaltonen, L. A. (1998). A serine/threonine kinase gene defective in Peutz-Jeghers syndrome. *Nature, 391*(6663), 184-187. doi:10.1038/34432

Henry, L. A., Johnson, D. A., Sarrio, D., Lee, S., Quinlan, P. R., Crook, T., . . . Isacke, C. M. (2011). Endoglin expression in breast tumor cells suppresses invasion and metastasis and correlates with improved clinical outcome. *Oncogene, 30*(9), 1046-1058. doi:10.1038/onc.2010.488

Lim, S., Becker, A., Zimmer, A., Lu, J., Buettner, R., & Kirfel, J. (2013). SNAI1-mediated epithelial-mesenchymal transition confers chemoresistance and cellular plasticity by regulating genes involved in cell death and stem cell maintenance. *PLoS One, 8*(6), e66558. doi:10.1371/journal.pone.0066558

Liu, K., Bellam, N., Lin, H. Y., Wang, B., Stockard, C. R., Grizzle, W. E., & Lin, W. C. (2009). Regulation of p53 by TopBP1: a potential mechanism for p53 inactivation in cancer. *Mol Cell Biol, 29*(10), 2673-2693. doi:10.1128/MCB.01140-08

Liu, K., Lin, F. T., Ruppert, J. M., & Lin, W. C. (2003). Regulation of E2F1 by BRCT domain-containing protein TopBP1. *Mol Cell Biol, 23*(9), 3287-3304.

Liu, K., Ling, S., & Lin, W. C. (2011). TopBP1 mediates mutant p53 gain of function through NF-Y and p63/p73. *Mol Cell Biol, 31*(22), 4464-4481. doi:10.1128/MCB.05574-11

Malkin, D., Li, F. P., Strong, L. C., Fraumeni, J. F., Jr., Nelson, C. E., Kim, D. H., . . . et al. (1990). Germ line p53 mutations in a familial syndrome of breast cancer, sarcomas, and other neoplasms. *Science, 250*(4985), 1233-1238.

Meijers-Heijboer, H., van den Ouweland, A., Klijn, J., Wasielewski, M., de Snoo, A., Oldenburg, R., . . . Consortium, C. H.-B. C. (2002). Low-penetrance susceptibility to breast cancer due to CHEK2(*)1100delC in noncarriers of BRCA1 or BRCA2 mutations. *Nat Genet, 31*(1), 55-59. doi:10.1038/ng879

Moreno-Bueno, G., Portillo, F., & Cano, A. (2008). Transcriptional regulation of cell polarity in EMT and cancer. *Oncogene, 27*(55), 6958-6969. doi:onc2008346 [pii]

10.1038/onc.2008.346

Nelen, M. R., van Staveren, W. C., Peeters, E. A., Hassel, M. B., Gorlin, R. J., Hamm, H., . . . Kremer, H. (1997). Germline mutations in the PTEN/MMAC1 gene in patients with Cowden disease. *Hum Mol Genet, 6*(8), 1383-1387.

O'Brien, L. E., Tang, K., Kats, E. S., Schutz-Geschwender, A., Lipschutz, J. H., & Mostov, K. E. (2004). ERK and MMPs sequentially regulate distinct stages of epithelial tubule development. *Dev Cell, 7*(1), 21-32. doi:10.1016/j.devcel.2004.06.001

Reginato, M. J., Mills, K. R., Becker, E. B., Lynch, D. K., Bonni, A., Muthuswamy, S. K., & Brugge, J. S. (2005). Bim regulation of lumen formation in cultured mammary epithelial acini is targeted by oncogenes. *Mol Cell Biol, 25*(11), 4591-4601. doi:10.1128/MCB.25.11.4591-4601.2005

Szasz, A. M., Lanczky, A., Nagy, A., Forster, S., Hark, K., Green, J. E., . . . Gyorffy, B. (2016). Cross-validation of survival associated biomarkers in gastric cancer using transcriptomic data of 1,065 patients. *Oncotarget, 7*(31), 49322-49333. doi:10.18632/oncotarget.10337

Theveneau, E., & Mayor, R. (2011). Can mesenchymal cells undergo collective cell migration? The case of the neural crest. *Cell Adh Migr, 5*(6), 490-498. doi:10.4161/cam.5.6.18623

Woessner, J. F., Jr. (1991). Matrix metalloproteinases and their inhibitors in connective tissue remodeling. *FASEB J, 5*(8), 2145-2154.

Zhang, Y., Yan, W., & Chen, X. (2011). Mutant p53 disrupts MCF-10A cell polarity in three-dimensional culture via epithelial-to-mesenchymal transitions. *J Biol Chem, 286*(18), 16218-16228. doi:10.1074/jbc.M110.214585

Abstract

DNA topoisomerase IIβ -binding protein 1 (TopBP1) is a mediator protein that regulates cell cycle checkpoint signaling pathway. A plethora of studies suggest that TopBP1 protein levels are high and positively associated with various hallmark properties of cancers. Although TopBP1 transcript as well as protein expression levels are high in breast cancers, its role in breast tumorigenesis is yet to be explored. In our studies, we observed that TopBP1 levels are high in premalignant and malignant cells of the MCF10A cancer progression series compared to the non-tumorigenic MCF10A cells. In order to establish the role of TopBP1 in tumorigenesis and other hallmarks of cancers, TopBP1-MCF10A, and shTopBP1-MCF10CA1a cells were cultured in Matrigel. Overexpression of TopBP1 in MCF10A 3D cultures induced hyper proliferation, disruption of polarity and cell-cell junctions. Moreover, TopBP1 overexpressing dissociated cells from acinar cultures exhibited EMT-like phenotype and cancer properties such as increased cell migration, invasion, colony formation capabilities and anchorage-independent growth, indicating acquisition of cellular transformation. Finally, we observed that TopBP1 overexpressing cells formed tumours in athymic mice thereby confirming their tumorigenic potential. Mechanistically it was confirmed that overexpression of TopBP1 led to the mutations in TP53 and other genomic insults. To summarise, we observed that ectopic expression of TopBP1 transforms MCF10A breast epithelial cells into cancer cells. These transformed cells harbour phenotypic and genotypic characters of cancerous cells.

Key word- TopBP1, breast cancer, genomic instability, transformation, p53

Abbreviations

ATM	Ataxia telangiectasia mutated
ATR	ATM and Rad3 related
BRCA1	Breast cancer 1
Chk1	Checkpoint kinase 1
Chk2	Checkpoint kinase 2
CTCF	Corrected Total Cell Fluorescence
DMEM	Dulbecco's modified eagle's medium
DPBS	Dulbecco's phosphate buffered saline
DQ	Dye Quenched
DSB	Double strand break
EDTA	Ethylenediaminetetraacetic acid
EMT	Epithelial to mesenchymal transition
FACS	Fluorescence activated cell sorting
FBS	Fetal bovine serum
FFPE	Formalin Fixed Paraffin Embedded
G1	Growth 1 phase
G2	Growth 2 phase
GAPDH	Glyceraldehyde 3-phosphate dehydrogenase
GC	Growth Constituents
IF	Immunofluorescence
IHC	Immunohistochemistry
KD	Knock down
MMP	Matrix Metalloproteinases
OE	Over expression
PAGE	Polyacrylamide gel electrophoresis
PBS	Phosphate buffered saline
PFA	Paraformaldehyde
PI	Propidium iodide
RPA	Replication protein A
RT	Room Temperature
S	Synthesis phase
SDS	Sodium dodecyl sulfate
shRNA	Short hairpin RNA
SSB	Single strand break
TBST	Tris Buffered Saline- Tween 20
TBS-T	Tris buffered saline-Tween-20
TCGA	The Cancer Genome Atlas
TNBC	Triple Negative Breast Cancer
TopBP1	DNA topoisomerase IIβ -binding protein 1

Contents

Dedication……ii
Certificate……iii
Declaration……iv
Acknowledgements……v
Synopsis……vii
Abstract……xv
Abbreviations……xvi
Chapter 1 9
Introduction 9
1.1 Breast Cancer 10
1.2. DNA damage and checkpoint signalling pathway 11
1.3. DNA topoisomerase IIβ -binding protein 1 (TopBP1) 12
1.3.1 Functions of TopBP1 13
1.3.2. TopBP1 and breast cancer 15
Chapter 2 18
Materials and Methods 18
2.1 Chemicals and antibodies 19
2.2 *In-silico* analysis 22
2.3 Immunohistochemistry 22
2.4 Plasmids 23
2.5 Cloning 24
2.6 Cell lines 24
2.7 Cell culture 24
2.8 Lentiviral preparation and transduction using lipofectamine mediated transfection 25
2.9 3D "on-top" culture 25
2.10 3D dissociation 26
2.11 Immunofluorescence for 2D cultures 26
2.12 Immunofluorescence for 3D culture 27
2.13 Immunoblotting 28

2.14 Flow cytometry 28
2.15 Wound healing assay 28
2.16 Single-cell migration assay 29
2.17 Gelatin Zymography 29
2.18 Colony formation assay 30
2.19 Soft agar assay 30
2.20 Tumorigenesis in mice 30
2.21 Whole-exome sequencing 30
2.22 Statistical Analysis 31
2.23 Ethics statements 31
Chapter 3 32
TopBP1 expression in Breast cancers 32
3.1 Background 33
3.2 Results 33
3.2.1 In-silico analysis of TopBP1 expression in breast cancer 33
3.2.2. TopBP1 expression pattern in Indian breast cancer patient samples 39
3.3 Summary 42
Chapter 4 44
Characterisation of MCF10A cancer progression series 44
4.1 Background 45
4.2 Results 45
4.2.1 TopBP1 levels are high in MCF10CA1a compared to MCF10A 45
4.2.2 DNA damage response (DDR) proteins in MCF10A series 46
4.2.3 EMT characteristics of MCF10A series 50
4.3 Summary 55
Chapter 5 56
Role of TopBP1 in cellular transformation 56
5.1 Background 57
5.2 Results 60
5.2.1 Generation of stable cell line with TopBP1 over-expression in MCF10A and knockdown in MCF10AT1 and MCF10CA1 60
5.2.2. Investigation of phenotypic changes induced upon TopBP1 over-expression in MCF10A and TopBP1 knockdown in MCF10CA1a 64

5.2.2.1. TopBP1 over-expression leads to increase in acinar size 67
5.2.2.2. Overexpression of TopBP1 leads to increased proliferation 69
5.2.2.3. TopBP1 over-expression disrupts polarity 72
5.2.2.4. Expression of EMT markers in TopBP1 OE is similar to MCF10CA1a 76
5.2.2.5. TopBP1 OE leads to increased migration and invasion 81
5.2.2.6. TopBP1 OE induces anchorage-independent growth 85
5.2.2.7. TopBP1 over-expression leads to tumour formation 87
5.2.2.8. TopBP1 knockdown reduces spheroid size in MCF10CA1a 88
5.2.2.9. TopBP1 knockdown does not affect levels of EMT markers in MCF10CA1a 90
5.2.2.10. TopBP1 knockdown does not affect migration in MCF10CA1a 92
5.2.2.10. TopBP1 knockdown reduces invasive potential of MCF10CA1a cells 93
5.2.2.11. TopBP1 knockdown reduces the colony-forming ability of MCF10CA1a cells 94
5.2.2.12. TopBP1 knockdown does not affect tumour forming ability of MCF10CA1a cells 95
5.2.3. To elucidate the mechanism of TopBP1 induced transformation 96
5.2.3.1. TopBP1 OE induces DNA damage and activates DDR response 96
5.2.3.2. TopBP1 overexpression induces mutation in p53 at M237I 100
5.3 Summary 103
Chapter 6 105
Discussion and future perspectives 105
6.1 Discussion 106
6.2 Future perspectives 109
6.2.1. Role of TP53 mutation in transformation 109
6.2.2. Analysis of Whole-exome sequencing data to identify other novel mutations 109
Bibliography 111
Appendix 119
Appendix I- Vector maps 120
I.1 Vector map of a mCherry-CSII-EF-MCS vector with TopBP1 insertion sites 120

I.2 Vector map of packaging plasmid for generation of TopBP1 overexpression lentiviral particles. 121
I.3 Vector map of the envelop plasmid for generation of TopBP1 overexpression lentiviral particles. 122
I.4 Vector map of pLKO1.TRC vector with shTopBP1 insertion sites. 123
I.5 Vector map of the envelop plasmid for generation of TopBP1 knockdown lentiviral particles. 124
I.6 Vector map of packaging plasmid for generation of TopBP1 knockdown lentiviral particles. 125
Appendix II- shTopBP1 cloning 126
Appendix III- Buffer compositions 128
III.1. Western blotting buffer compositions 128
III.2. Immunofluorescence buffer compositions 129
Publications 130
List of Publications 131

List of Figures

Figure 1.1: Various Cancer cases and death 10
Figure 1.2: Region-wise estimate of breast cancer cases and death 11
Figure 1.3: The canonical checkpoint repair pathway 12
Figure 1.4: Domain structure of TopBP1 and its homologues 13
Figure 1.5: TopBP1 and its interacting partners 14
Figure 1.6: TopBP1 function in checkpoint activation 14
Figure 3.1: TOPBP1 transcript levels are high in breast cancer 34
Figure 3.2: Breast cancer classification 35
Figure 3.3: TOPBP1 transcript levels across various receptor statuses- 36
Figure 3.4: TOPBP1 transcript level across breast cancer subtypes 37
Figure 3.5: TOPBP1 transcript levels across various breast cancer stages 38
Figure 3.6: Higher TOPBP1 expression is associated with reduced survival- 39
Figure 3.7: TopBP1 levels in Indian breast tissue samples 40
Figure 3.8: TopBP1 levels in Indian breast tissue samples 41
Figure 3.9: TopBP1 levels in Indian breast tissue samples 42
Figure 4.1: TopBP1 levels in MCF10A series 46
Figure 4.2: RPA and γH2AX activation in MCF10A series 47
Figure 4.3: Single strand break repair proteins in MCF10A series 48
Figure 4.4: Double-strand break repair proteins in MCF10A series 49
Figure 4.5: p53 activation in MCF10A series 50
Figure 4.6: EMT markers in MCF10A series 51
Figure 4.7: Collective cell migration in MCF10A series 52
Figure 4.8: Single-cell migration in MCF10A series 53
Figure 4.9: Colony formation assay in MCF10A series 54
Figure 4.10: Anchorage-independent growth in MCF10A series 55
Figure 5.1: Anatomy of the mammary gland 58
Figure 5.2: Schematic showing morphogenesis of MCF10A and transformed cells when grown on Matrigel 59
Figure 5.3: Expression of TopBP1-mCherry in MCF10A cells 60
Figure 5.4: TopBP1 over-expression in MCF10A cells 61

Figure 5.5: Cloning of shTopBP1 into pLKO.1.TRC lentiviral vector 62
Figure 5.6: Cloning of shTopBP1 into pLKO.1.TRC lentiviral vector 63
Figure 5.7: TopBP1 knockdown in MCF10CA1a 64
Figure 5.8: 3D culture of MCF10A series cells and TopBP1 OE MCF10A 65
Figure 5.9: 3D culture of MCF10A series cells and TopBP1 OE MCF10A 66
Figure 5.10: TopBP1 OE MCF10A dissociated cells resemble MCF10CA1a 67
Figure 5.11-TopBP1 overexpression leads to increased acinar size in MCF10A 3D cultures 68
Figure 5.12: Ki67 positive cells in TopBP1 OE and MCF10CA1a 3D cultures 70
Figure 5.13-TopBP1 overexpression increase proliferation 71
Figure 5.14-TopBP1 overexpression leads to an increase in S phase markers 71
Figure 5.15: TopBP1 OE leads to disruption of α6-integrin 73
Figure 5.16: TopBP1 OE leads to disruption of laminin V- 73
Figure 5.17: TopBP1 OE leads to Golgi dispersal in MCF10A 3D cultures- 74
Figure 5.18: Golgi dispersal in TopBP1 OE dissociated cells and MCF10CA1a cells ... 75
Figure 5.19: TopBP1 OE leads to the dispersal of β catenin in MCF10A 3D cultures ... 76
Figure 5.20: Vimentin levels in TopBP1 OE MCF10A 3D cultures- 77
Figure 5.21: Vimentin levels in TopBP1 OE dissociated cells and MCF10CA1a cells .. 78
Figure 5.22: E-cadherin and N-cadherin levels in TopBP1 OE MCF10A 79
Figure 5.23: EMT markers in TopBP1 OE MCF10A and MCF10A series 80
Figure 5.24: Keratin levels in TopBP1 OE MCF10A 81
Figure 5.25: TopBP1 over-expression induces enhanced collective cell migration in MCF10A cells 82
Figure 5.26: TopBP1 over-expression induces enhanced single-cell migration in MCF10A cells 83
Figure 5.27: TopBP1 over-expression induces MMP2, and 9 activations in MCF10A 3D acini 84
Figure 5.28: TopBP1 overexpression leads to reduced MMP1 in MCF10A 85
Figure 5.29: TopBP1 over-expression leads to colony formation in MCF10A dissociated cells 86
Figure 5.30: TopBP1 over-expression leads to anchorage-independent growth in MCF10A dissociated cells 86
Figure 5.31: TopBP1 over-expression leads to tumour formation in athymic nude mice 87

Figure 5.32-TopBP1 knockdown reduces spheroid size in MCF10CA1a 3D cultures ... 89
Figure 5.33- E-cadherin and N-cadherin levels in TopBP1 KD MCF10CA1a cells 90
Figure 5.34- Keratin levels in TopBP1 KD MCF10CA1a cells 91
Figure 5.35: TopBP1 knockdown does not affect single-cell migration in MCF10CA1a cells 92
Figure 5.36: TopBP1 knockdown reduces MMP2 and 9 activation in MCF10CA1a 3D acini 93
Figure 5.37: TopBP1 knockdown leads to reduced MMP1 in MCF10CA1a 94
Figure 5.38: TopBP1 knockdown reduces colony formation in MCF10CA1a 95
Figure 5.39: TopBP1 knockdown does not affect tumour formation in athymic nude mice 96
Figure 5.40: TopBP1 OE induces activation of RPA and γH2AX 97
Figure 5.41: TopBP1 OE induces activation of ATR and Chk1 99
Figure 5.42: TopBP1 OE induces activation of p53 and reduces p21- 101
Figure 5.43: Genomic DNA isolation for whole-exome sequencing 102
Figure 5.44: Schematic representation depicting the role of TopBP1 tumorigenesis .. 104
..... 1

List of Tables

Table 2.1 MCF10A media components……..20

Table 2.2 Antibodies used for immunofluorescence and immunoblotting…….20

Table 2.3 Scoring criteria for stained tissue slides……...23

Table 5.1 TP53 mutation status…….103

Chapter 1

Introduction

1.1 Breast Cancer

Breast cancer is the most common cancer among women worldwide (Figure 1.1a). It is also the number one cause of cancer mortality in women (Figure 1.1b).

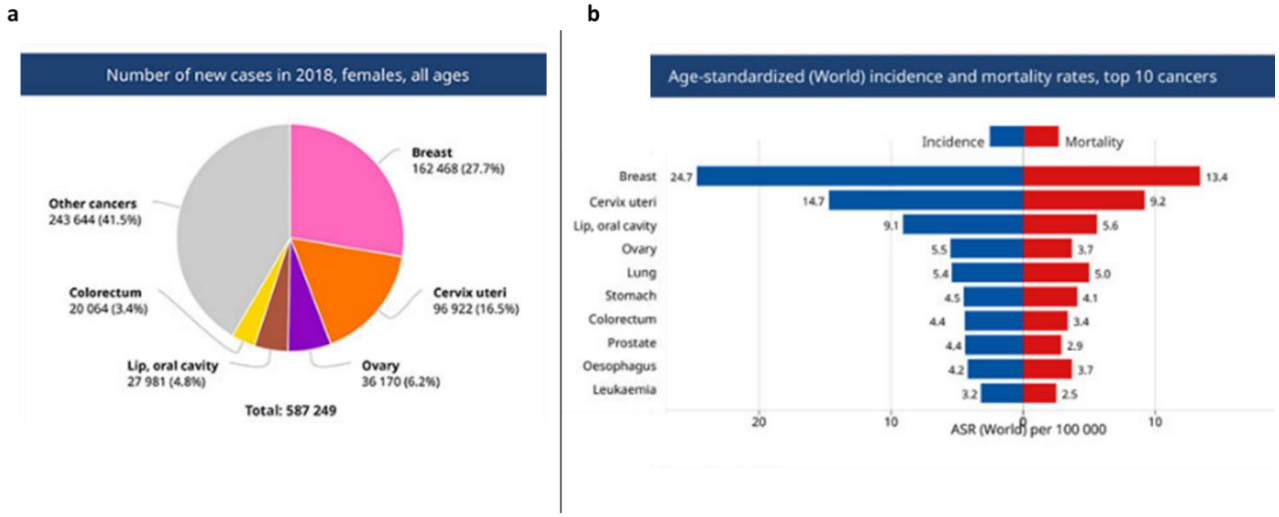


Figure 1.1: Various Cancer cases and death- a) Pie chart representing the number of new cases of various types of cancer in women and b) bar diagram representing age standardized incidences and mortality rates of top 10 cancers in the word (Reproduced from Globocan 2018).

A study in 2012, which estimated the region-wise breast cancer incidence and death in the world, showed that the estimated number of cases of breast cancer in India is 8.6% of the total world population. In contrast, the estimated death is 13.5% (Figure 1.2) (Cancer Atlas 2012, Cancer organisation). One reason for the high mortality rate in India is the lack of early detection of breast cancer. Identification of genes associated with breast cancer susceptibility will be helpful for the early diagnosis of the disease. Various studies have found the inactivation of genes, like BRCA1, BRCA2, TP53, PTEN, STK1 (Hemminki et al., 1998; Malkin et al., 1990; Meijers-Heijboer et al., 2002; Nelen et al., 1997), giving rise to increased susceptibility to breast cancer. More elaborate studies to find genes/ or pathways deregulated in various stages of breast cancer is required for early diagnosis and for developing efficient drug targeting strategies. Recent studies have shown that TopBP1, which is a mediator protein in DNA damage response (DDR), is associated with susceptibility to hereditary breast and ovarian cancer

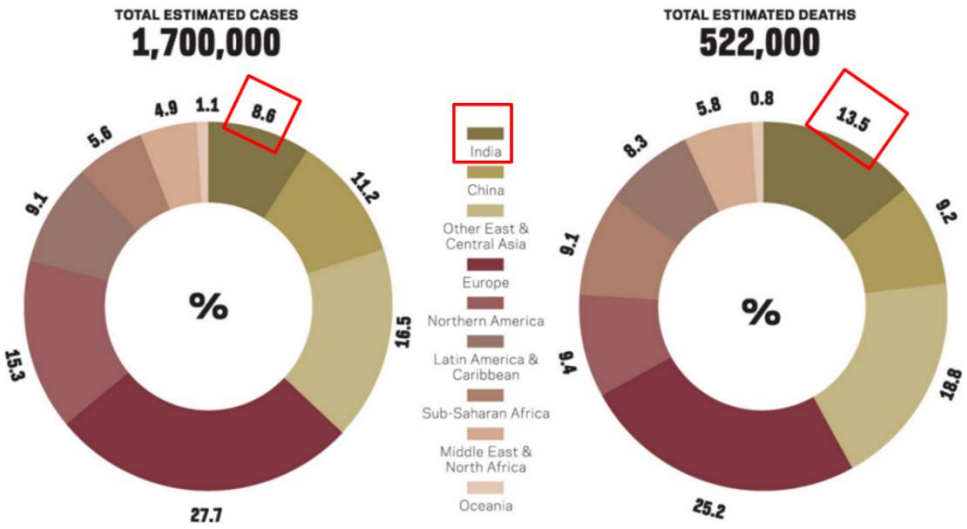


Figure 1.2: Region-wise estimate of breast cancer cases and death (Reproduced from Cancer Atlas 2012).

1.2. DNA damage and checkpoint signalling pathway

DNA is prone to damage by various endogenous and exogenous agents. If the damage remains unchecked, it may lead to genomic instability leading to cancer (Abraham, 2001). Fortunately, the cells have an elaborate checkpoint signalling mechanism to detect and repair the damage to ensure the faithful transmission of genetic material to the next generation. The canonical checkpoint pathway comprises sensors, mediators, transducers and effector proteins (Figure 1.3). The sensor proteins, ataxia-telangiectasia mutated (ATM) and ATM and Rad3 related (ATR) / ATR Interacting Protein (ATRIP), sense double-strand or single-strand breaks respectively and activate Chk2 and Chk1 by phosphorylation through mediator proteins, like BRCA1, MDC1 (in Double-Strand Break) (Cortez et al., 1999), Claspin and TopBP1 (in Single-Strand Break pathway) (Harper and Elledge, 2007). Further, the signal is relayed to effector proteins like Cdc25C, Nbs1, p53, to name a few (Banin et al., 1998; Brown et al., 1999; Petrini, 1999), which can induce cell cycle arrest to allow time for repair of damaged DNA or apoptosis depending upon the extent of the damage. TopBP1 is a major mediator protein involved in the single-strand break repair pathway (Wang and Elledge, 2002).

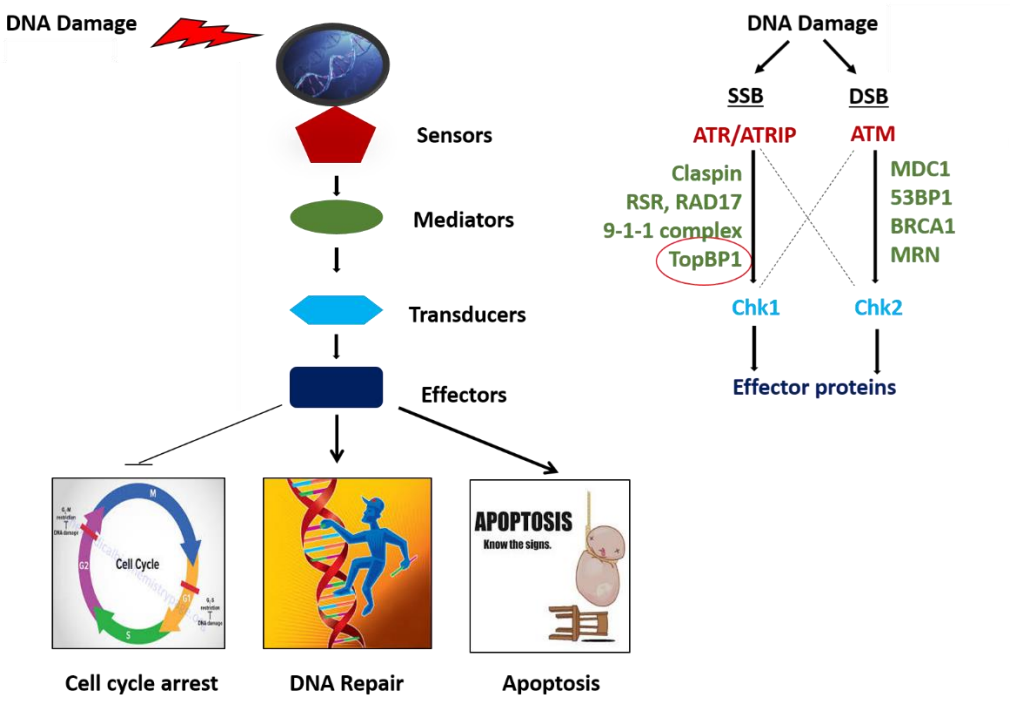


Figure 1.3: The canonical checkpoint repair pathway- Schematic representation of DNA damage response through various sensors, mediators, transducers and effectors leading to cell cycle arrest, DNA repair and apoptosis. Protein involved in single strand and double strand checkpoint activation is listed in the line diagram. Adapted from (Abraham, 2001)

1.3. DNA topoisomerase IIβ -binding protein 1 (TopBP1)

DNA topoisomerase IIβ -binding protein 1 (TopBP1) is involved in the activation of DNA damage checkpoint to maintain genome integrity (Xu and Leffak, 2010). TopBP1 gene is located at chromosome 3q22.1, and it is conserved across species (Wardlaw et al., 2014). It was first identified through two independent screens in *Schizosaccharomyces pombe* as rad4 (Schupbach, 1971) and cut5 (Hirano et al., 1986). Further human TopBP1 was identified as an interactor of Topoisomerase IIβ in a yeast two-hybrid screen (Wang and Elledge, 2002). The other known homologues of TopBP1 are Dpb11 (*S. cerevisiae*) (Araki et al., 1995), Mus101 (*D. melanogaster*) (Yamamoto et al., 2000), Mei1 (*A. thaliana*) and Xmus101 (*X. laevis*) (Figure 1.4).

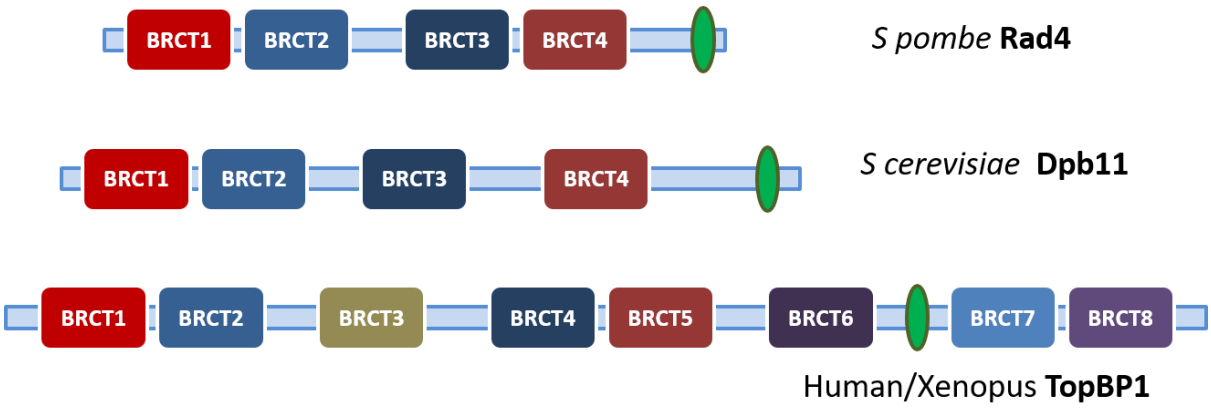


Figure 1.4: Domain structure of TopBP1 and its homologues: Highlighting BRCT domains and an AAD (green) of TopBP1. Image adapted from (Wardlaw et al., 2014)

TopBP1 has structural and functional similarities to BRCA1 (a tumour suppressor gene) (Karppinen et al., 2006; Yamane et al., 2003). It has eight BRCA1 C-terminus (BRCT) domains through which it interacts with other proteins (Yu et al., 2003) and an ATR activation domain (AAD) which is necessary to stimulate the kinase activity of ATR (Kumagai et al., 2006) and thus checkpoint activation (Figure 1.4). It is a nuclear protein co-localised with BRCA1 at the stalled replication forks (Yamane et al., 2002).

1.3.1 Functions of TopBP1

Major functions of TopBP1 are checkpoint activation, initiation of replication, transcriptional regulation and DNA repair. To facilitate these functions, it interacts with various protein through its BRCT domains (Figure 1.5).

For checkpoint activation, it interacts with Rad 9 through its BRCT 1-2 domain, MDC1 and 53BP1 through BRCT 4-5 and ATR through BRCT 7-8 (Makiniemi et al., 2001). The processed single stranded DNA formed by DNA damage is coated by RPA and ATR/ATRIP is recruited to the damage site with the help of 9-1-1 complex (Sokka et al., 2010). ATR is activated by the ATR activation domain of TopBP1 which further leads to activation of Chk1 (Kumagai et al., 2006). Activated Chk1 leads to activation of various effector proteins to induce cell cycle arrest and DNA repair (Liu et al., 2006) (Figure 1.6).

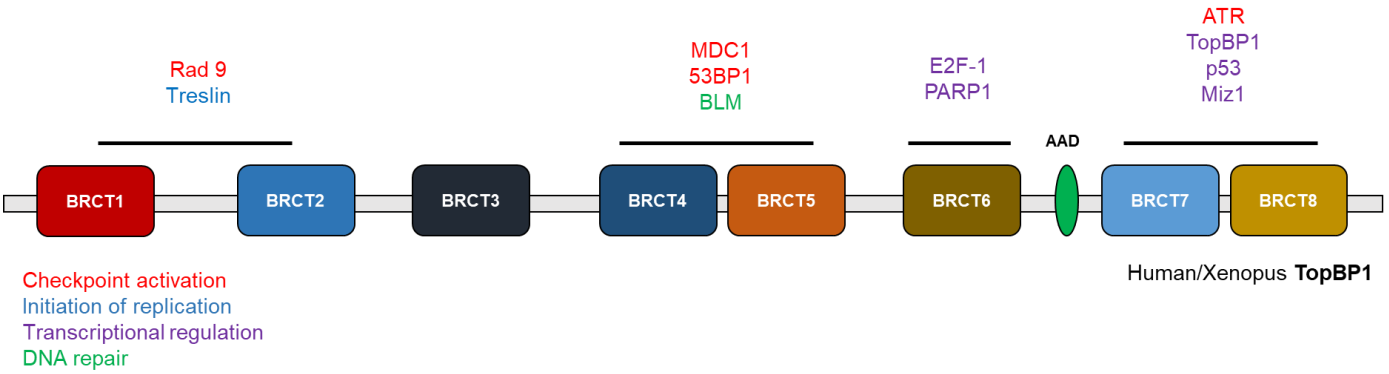


Figure 1.5: TopBP1 and its interacting partners: Proteins interacting with TopBP1 highlighting BRCT domains involved in the interaction to facilitate various functions. Image adapted from (Wardlaw et al., 2014)

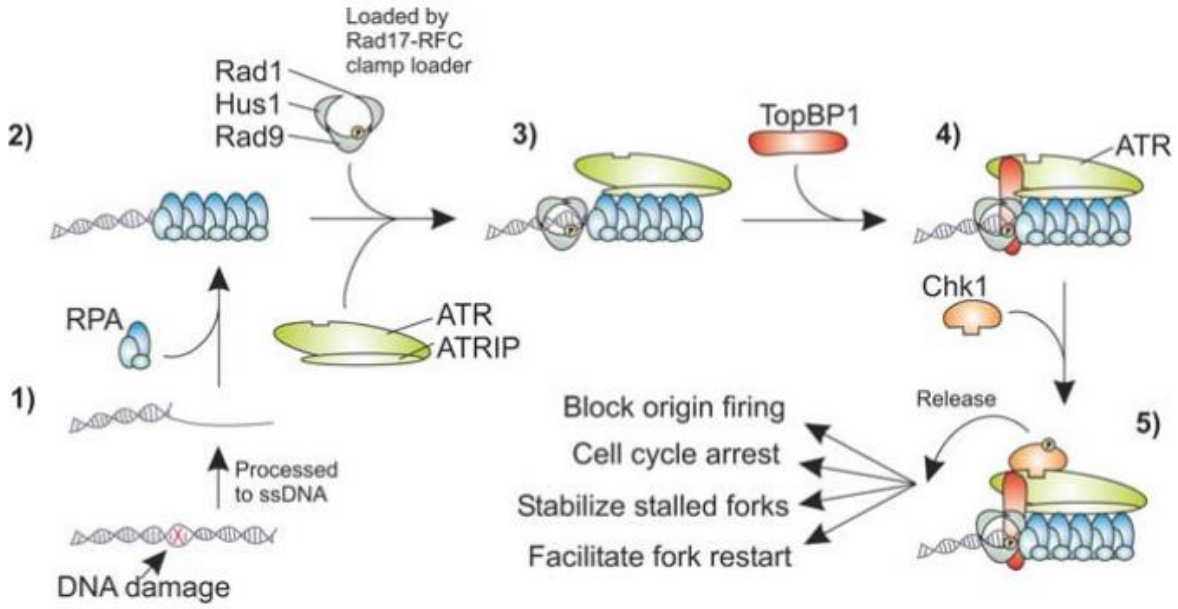


Figure 1.6: TopBP1 function in checkpoint activation- Schematic representation of ATR activation by TopBP1 and thus checkpoint activation (Reproduced from M. Sokka *et al.,* 2010)

Besides its essential role in DNA damage response, it is also involved in transcriptional regulation of genes involved in cell proliferation and apoptosis, such as E2F1 and c-Myc (Liu et al., 2009; Liu et al., 2003). Akt phosphorylates TopBP1 at Ser-1159 which leads to its oligomerization through TopBP1 BRCT 7-8 domains and shifts its function from checkpoint activation to transcriptional regulation (Liu et al., 2006). Oligomerised TopBP1 binds to E2F1 and inhibit E2F1 mediated apoptosis (Liu et al., 2006).

TopBP1 interacts with interaction with BLM (Bloom syndrome helicase) through its BRCT 4-5 domains. This interaction has been shown to inhibit sister chromatid exchange thus maintaining genome stability (Wang et al., 2013). TopBP1 also plays a role during replication initiation by interacting with Treslin to facilitate Cdc45 loading onto replication origins (Kumagai et al., 2006). At physiological levels, TopBP1 is required for the G1-S transition in the cell cycle. However, aberrant expression of TopBP1 has been observed in breast cancer.

1.3.2. TopBP1 and breast cancer

Immunohistochemical studies performed on breast cancer biopsy samples showed that TopBP1 is upregulated in breast cancer tissues. TopBP1 over expression was associated with higher grade tumours and reduced patient survival (Forma et al., 2012; Going et al., 2007; Liu et al., 2009). p53 is a well-studied tumour suppressor and in majority of cancers p53 is mutated leading to various gain of functions of the protein.TopBP1 interacts with the DNA binding domain of p53 through its BRCT 7-8 domains and inhibits the promotor binding of p53 (Liu et al., 2009). In their study, Liu and colleagues showed that TopBP1 overexpression reduced the p53 transcriptional activity upon DNA damage. However, total p53 and activation at the serine residue 15 remained unaffected (Liu et al., 2009). TopBP1 interacts with p53 hot spot mutants and increase proliferation and decrease apoptosis by affecting p53 transcriptional activity (Liu et al., 2011). Other studies have shown TopBP1 to induce chemoresistance by upregulating p53 levels (Lv et al., 2016). PI(3)K/Akt, p53 and E2F1 are some of the common pathways that are deregulated in cancers (Cancer Genome Atlas, 2012). A recent study found that TopBP1 paradoxically hinders ATR/Chk1 activation in cancers (Liu et al., 2021). As mentioned previously, TopBP1 regulates the function of various

cancer regulatory proteins such as PI(3)K/Akt, p53 and E2F1 and affects the viability of cancer cells making it a novel therapeutic target (Chowdhury et al., 2014).

As mentioned earlier, there are multiple studies that suggest the oncogenic role of TopBP1. Depletion of TopBP1 make various cancer cells susceptible to undergo apoptosis, however higher levels of TopBP1 promotes the survival of cancer cells. All mentioned studies suggest a strong positive correlation of TopBP1 with breast cancer. However, the role of TopBP1 in tumour initiation and progression is not well studied. After getting insights from the literature about TopBP1 and its functions we aimed to understand the **Role of TopBP1 during breast tumorigenesis**. This aim was further divided into three objectives as follows:

1. To analyse the TopBP1 expression in breast cancer

There are contradicting reports suggesting the role of TopBP1 as an oncogene and tumour suppressor. TopBP1 expression pattern in breast cancer patient samples will provide some insights into the problem. TOPBP1 transcript levels in breast cancer will be analysed *in-silico* using the TCGA data. Also, there are no reports suggesting the expression pattern of TopBP1 in Indian patient samples. Immunohistochemistry using TopBP1 antibody will be performed on formalin- fixed paraffin-embedded breast tissue samples to check TopBP1 levels. This will be compared to the reduction tissue and adjacent normal tissue from the same patient to quantify the TopBP1 protein levels in cancer tissues.

2. To characterise the MCF10A cancer progression series

MCF10A cancer progression series (MCF10A, MCF10AT1 and MCF10CA1a) cells will be utilised to understand the role of TopBP1 in transformation of breast epithelial cells. TopBP1 expression pattern in the MCF10A series will be analysed along with various DNA damage response proteins. EMT and transformation phenotypes of MCF10A series will also be analysed.

3. To investigate the role of TopBP1 in transformation of breast epithelial cells

TopBP1 expression in MCF10A series will be checked and based on the expression pattern, cell lines with TopBP1 over-expression or knock down will be generated using lentiviral or retroviral mediated transduction. These cells will be further grown on Matrigel® to form acini and the phenotypic changes of the acini will be characterised to investigate transformation. Mice model will be utilised to determine the tumorigenic potential of the transformed cell line

Chapter 2

Materials and Methods

2.1 Chemicals and antibodies

MCF10A media components were purchased from Sigma Aldrich, Invitrogen or Corning (Table 2.1). Matrigel® and Dispase (354235) were purchased from Corning, Sigma-Aldrich. DQ Collagen (D12060), Phalloidin 633 (A12380) and Lipofectamine-2000 (11668) were purchased from Invitrogen, Thermo Fisher Scientific. Puromycin dihydrochloride from Streptomyces alboniger (P8833), Polybrene (H9268), dimethyl sulfoxide (DMSO, D8418), Triton X-100 (T8787), Mitomycin C (M4287), Tris Base (B9754), EDTA (E6758), and Na_3VO (S6508) were purchased from Sigma-Aldrich. Pre-stained protein ladder (MBT092), NaF (RM1081), Na_2HPO_4 (GRM1417), and KH_2PO_4 (MB050) were purchased from HiMedia. NaCl (15918), Xylene (Q35417), Isopropanol (Q26897), and 30% H_2O_2 (Q15465) were purchased from Qualigens. 16% paraformaldehyde (AA433689M) was purchased from Alfa Aesar. Antibody Diluent (80981) and Dako Real Envision Kit (K5007) were purchased from Dako. Hoechst 33258 (H3569) and Hoechst 33342 (H3570) were purchased from Molecular Probes, Thermo Fisher Scientific, USA. Antibodies used were from Bethyl, Abcam, Millipore, cell signalling (CST), Santacruz or sigma (Table 2.2)

Table 2.1: MCF10A medium components- prepared in high glucose Dulbecco's Modified Eagle Medium (DMEM-11965126 Thermo) without sodium pyruvate

Components	Growth Medium (concentration)	Assay Medium (concentration)	Resuspension Medium
Horse serum (16050122-Invitrogen)	5%	2%	20%
Insulin (I1882-Sigma-Aldrich)	10 µg/ml	10 µg/ml	-
Hydrocortisone (H0888- Sigma-Aldrich)	0.5µg/ml	0.5µg/ml	-
Choleratoxin (C8052-Sigma-Aldrich)	100ng/ml	100ng/ml	-
Epidermal growth factor (EGF- E9644-Sigma-Aldrich)	20 ng/ml	5 ng/ml	-
Matrigel® (356231-Corning)	-	5%	-
Pencillin-Streptamycin (17-602E- Lonza)	100 units/ml	100 units/ml	100 units/ml

Table 2.2: Antibodies used for Immunofluorescence (Griffiths and Simons) and Immunoblotting

Primary Antibody	Catalogue no	IF	Immunoblotting
RPA 32/2 Phospho T21 (Abcam)	AB 61065		1:1000
RPA (CST)	2208		1:1000
Laminin V, anti-Mouse (Millipore)	MAB19562		
TopBP1, anti-Rabbit (Bethyl)	A300-111A	1:200	1:1000
Rat X Hu CD49fα6 integrin, anti –Rat (Millipore)	MAB1378	1:100	-

GM130, anti-Mouse (Millipore)	610822	1:100	
E-cadherin, anti-Mouse (BD)	610182		1:7500
N-cadherin, anti-Rabbit (Abcam)	AB18203		1:1000
Vimentin, anti-Mouse (Abcam)	AB 8069	1:200	1:10000
β-catenin, anti- Rabbit (Abcam)	ab32572	1:100	
PCNA- PC10 (CST)	2586		1:2500
Cytokeratin 14, anti-Mouse (Abcam)	ab7800		1:1000
Cytokeratin 19, anti-Rabbit (Abcam)	ab52625		1:1000
GAPDH, anti-Rabbit (Sigma)	G9545		1:40000
Slug- C19G7 (CST)	9585		1:1000
Twist (Abcam)	ab50581		1:1000
γH2AX Ser 139 (Santacruz)	sc517348		1:1000
pATR Ser 428 (CST)	2853		1:1000
ATR (Abcam)	AB 2905-100		1:1000
pChk1 (CST)	2348L		1:1000
Chk1(Santacruz)	SC 8408		1:1000
p-p53 S15 (CST)	9284S		1:1000
p53 (Bethyl)	A300-247A		1:5000
p21 (Abcam)	ab109520		1:1000
Bax (CST)	2772		1:1000
Bim (Abcam)	ab32158		1:1000
Cyclin A (Santacruz)	sc-271682		1:1000

2.2 *In-silico* analysis

IlluminalHiSeq dataset and clinical data from TCGA (The cancer genome atlas) was downloaded from the UCSC Xena browser. R package was used to merge the expression data based on sample ID. The adjacent normal and tumour data were sorted based on the sample ID. The data was plotted in Graph Pad Prism (GraphPad Software, La Jolla, CA, USA). KM plot online tool was used to perform Kaplan Meier analysis. TOPBP1 was selected as a gene symbol under breast cancer, and 202633_at was selected. The survival plot was generated using median cutoff.

2.3 Immunohistochemistry

Paraffin-embedded breast tissue samples were obtained from Prashanti Cancer Care Mission, Pune. The Institutional human ethics committee approved the agreement to use these tissue samples, and the confidentiality of patient information was maintained. The paraffin-embedded tissue sections (3 microns) were trimmed using a microtome (Leica ecosystems) and mounted on the dry Poly-L-lysine coated glass slides. The slides were pre-coated with L-lysine for better adhesion of the tissue. The slides were then heated to 62°C for a minimum duration of 4 hours in an oven for deparaffinisation. Any paraffin left in the interstices of the tissue was removed from the sections by two changes of xylene for 15 minutes each and rehydrated through graded alcohol concentrations from absolute to 96% for 5 minutes each, followed by distilled water treatment for five minutes. Endogenous peroxidase was quenched by a 3% H_2O_2 solution in methanol to reduce background noise on HRP (Horse Radish Peroxidase) treatment.

Antigen was retrieved using the heat-induced epitope retrieval method, where tissues were placed in 0.001M EDTA buffer inside a microwave oven for sequential heating and cooling cycles. Antigen retrieval breaks the cross-links between surrounding proteins or peptides and antigen, leading to the epitope's unmasking. The tissues area was demarcated using hydrophobic ink to reduce unnecessary wastage of chemicals. Nonspecific binding of antibody was blocked with 3% BSA on the sections for 30 minutes at RT. After 30 minutes of blocking, BSA was removed, and the primary antibody (TopBP1, ab2402, 1:500 dilution ABCAM) was added and incubated for 20 hrs

at 4°C in humidified conditions. Tissue slides were washed with TBST (Tris buffer saline and Tween 20) twice for five minutes to remove excess unbound primary antibodies on the tissues. After washes, secondary antibody HRP (DAKO REAL EnVision, Denmark) was added to the tissue for 30 minutes at RT and washed twice with TBST.

Sections were developed using 0.03M DAB in its substrate buffer for exact 4 minutes and counterstained with haematoxylin. Excess stains were removed and dehydrated by dipping them in increasing concentrations of isopropanol consecutively. Tissues were mounted with DPX mountant and then imaged using laser dissection microscope and scored using brightfield microscope (Mantra) facilitated at IISER Pune.

The histoscore (**H-score)** is a method of assessing the extent of immunoreactivity that can be co-related to specific protein expression in the patient tissues. H score is the product of the percentage of stained nuclei cells and the staining intensity in the nuclei or cytoplasm, giving a range of 0 to 9. The percentage of stained cells and the intensity of staining vary within a range of 0 to 3. Higher is the H score; higher is the level of protein expression.

Table 2.3. Scoring criteria of the stained tissue slides

Percentage positivity	Score	Intensity of the staining	Score
0%	0	No staining	0
<20%	1	Faint	1
20-60%	2	Moderate	2
>60%	3	High	3

2.4 Plasmids

CSII-EF-MCS plasmid was a gift from Dr Sourav Banerjee, NBRC, Manesar India. pCAG-HIVgp and pCMV-VSV-G-RSV-Rev plasmids were purchased from RIKEN BioResource Centre. pLKO.1 eGFP was a kind gift from Dr Sorab Dalal, ACTREC, India. psPAX2 and pMD2.G generous gift from Dr Manas K Santra, NCCS, India.

2.5 Cloning

TopBP1 overexpressing lentiviral plasmid with mCherry tag was prepared before (5th year Thesis project).

shTopBP1 lentiviral plasmids were generated as per Addgene protocol. Briefly, pLKO1. TRC vector was digested with EcoRI and AgeI restriction enzymes (NEB, USA) (Appendix II.1), and the 7 kb fragment was excised and gel extracted using QIAquick Gel Extraction Kit (28706). The shTopBP1 oligos (forwad: CCGGAAGTGGTTGTAACAGCGCATCTTCTCGAGAAGATGCGCTGTTACAACCACTT TTTTTG and reverse: AATTCAAAAAAAGTGGTTGTAACAGCGCATCTTCTCGAGAAGATGCGCTGTTACAA CCACTT) were annealed (Appendix II.2-3), and ligated into the digested vector (Appendix II.4). The clones obtained were screened using XhoI (NEB, USA) digestion.

2.6 Cell lines

HEK293T and MCF10A are generous gifts from Dr Jomon Joseph (NCCS, Pune) and Prof. Raymond C. Stevens (The Scripps Research Institute, California), respectively. MCF10AT1 and MCF10CA1a cells were purchased from ATCC.

2.7 Cell culture

HEK293T cells were grown on 100mm 2D tissue culture-treated dishes (Eppendorf or Corning) with high glucose-containing Dulbecco's Modified Eagle Medium (DMEM; Lonza) supplemented with 10% heat-inactivated fetal bovine serum (FBS- Invitrogen) and 100 units/ml of penicillin-streptomycin. MCF10A, MCF10AT1 and MCF10CA1a cells were grown as a monolayer in a Growth medium as previously mentioned (Anandi et al., 2017; Debnath et al., 2003)(Table 2.1. Cells were incubated at 37ºC humidified 5% CO_2 incubators (Eppendorf or Thermo Scientific). MCF10A cells were re-suspended in Resuspension Medium (Table 2.1), DMEM without sodium pyruvate with 20% horse serum, while sub-culturing.

2.8 Lentiviral preparation and transduction using lipofectamine mediated transfection

Lentiviral particles to generate TopBP1 overexpressing MCF10A cells were prepared as previously mentioned (Sharma and Lahiri, 2021). 7.5 X 10^5 HEK293T cells were seeded on a 35 well dish for viral production. Cells were incubated at 37ºC for 16 hours before transfection. 10 µl of Lipofectamine 2000 (Invitrogen, 11668) was added to 240 µl of OPTIMEM (Invitrogen) and incubated at room temperature for 5 minutes. Meanwhile, 1 µg of mCherry-CSII-EF-MCS or mCherry-CSII-EF-MCS-TopBP1 plasmid along with 1 µg of pCAG-HIVgp and 0.5 µg pCMV-VSV-G-RSV-Rev packaging plasmids were mixed and OPTIMEM was added to make up the volume to 250 µl. 250 µl of the lipofectamine-OPTIMEM mixture was added to the DNA-OPTIMEM mixture and incubated for 20 minutes at RT. In the meantime, DMEM was removed, and cells were preconditioned with 1 ml of OPTIMEM for 20 minutes. 500 µl of OPTIMEM was added to the reaction mixture and added to the cells. 1ml growth media containing 30% horse serum was added to the cells 24 hours post-transfection. 5 X 10^5 MCF10A cells were seeded on a 35 mm dish for transduction. The viral supernatant was collected 48 hours post-transfection and filtered through a 0.45 µm filter to remove the cell debris. Filtered viral supernatant containing media along with 1 ml fresh media was added to the MCF10A cells. 8 µg polybrene was added to the cells to increase the transduction efficiency. Cells were replenished with fresh medium 48 hours post-transduction. Transduced MCF10A cells were sorted using the BD Aria Fusion sorter.

For the generation of MCF10AT1 or MCF10CA1a cells with TopBP1 knockdown, lentiviral particles were generated as described before. HEK293T cells were transfected with 1 µg of pLKO1.TRC or shTopBP1-TRC plasmid along with 1 µg of psPAX2 and 0.5 µg pMD2 packaging plasmids using Lipofectamine 2000 to generate lentiviral particles. These lentiviral particles were used to transduce MCF10CA1a cells, and cells with TopBP1 knockdown were selected using 1 µg/ml puromycin.

2.9 3D "on-top" culture

3D cultures of MCF10A was grown as mentioned before (Anandi et al., 2017; Debnath et al., 2003). For immunofluorescence experiments, 0.6 X 10^4 mCherry MCF10A/or

TopBP1 OE MCF10A cells or 0.15 X 10^4 pLKO1 MCF10CA1a or shTopBP1 MCF10CA1a cells were suspended in Assay Medium (Table 2.1) and seeded on 8 well chamber coverglass (Nunc Lab Tek, Thermo Scientific) pre-coated with 50 µl of Matrigel®. Cells were maintained at 37ºC humidified 5% CO_2 incubators for 10 days and replenished with fresh Assay Medium with 5% Matrigel® and 5 ng/ml of EGF every 4 days.

2.10 3D dissociation

For generating 3D dissociated cells, 7.5 X 10^4 mCherry MCF10A/or TopBP1 OE MCF10A cells were suspended in Assay Medium (Table 2.1) and seeded on 12 well dishes pre-coated with 250 µl of Matrigel®. Cells were maintained at 37ºC humidified 5% CO_2 incubators for 16 days and replenished with fresh Assay Medium with 5% Matrigel® and 5 ng/ml of EGF every 4 days till day 8 and every 2 days afterwards. After 16 days, the cultures were treated with 250 µl of Dispase and incubated at 37ºC for 30 minutes. The dissociated cells along with Matrigel® were transferred to a 15 ml falcon and incubated at 37ºC for 10 minutes. The cells were centrifuged at 900 rpm for 10 minutes, and the supernatant was transferred to a 12 well dish containing 500 µl fresh growth media. The aqueous layer in the falcon was re-suspended in 500 µl growth media and centrifuged again at 900 rpm for 10 minutes. The supernatant and the cell pellet were plated on separate wells of 12 well dishes. The attached cells were passaged and expanded once 70% confluency was reached, similar to MCF10A passaging.

2.11 Immunofluorescence for 2D cultures

For immunofluorescence, 5 X 10^4 cells were seeded on a coverslip and incubated overnight. After one PBS wash, cells were fixed with 4 % paraformaldehyde (Fisher Scientific) for 20 minutes in the dark at room temperature (RT). Cells were washed thrice with 1X PBS for 10 minutes each before permeabilisation with ice-cold 0.5% Triton X-100 (USB Corporation) in 1X PBS at 4ºC for 10 minutes. Further, wells were washed thrice with PBS-Glycine (100mM glycine in 1X PBS) and blocked with 10% FBS in IF buffer (1X PBS, 0.05% [w/v] sodium azide, 0.1% [w/v] BSA, 0.2% [v/v] Triton-X-100 and 0.05% Tween 20) for 1 hour. Primary antibodies of required dilution (Table

2.2) prepared in 10% FBS in IF buffer was added onto the cells and incubated for 16 hours at 4ºC. Cells were washed thrice with IF buffer for 20 minutes and incubated with Alexa Flour® secondary antibodies prepared in 10% FBS in IF for 1 hour at RT. After incubation, cells were washed once with 1X IF buffer and twice with 1X PBS for 10 minutes. 0.5 μg/ml of Hoechst 33258 (Invitrogen) in PBS was added to cells and incubated for not more than 5 minutes and immediately washed with 1X PBS for 10 minutes. Excess PBS was removed, and Slow Fade® Gold antifade reagent (Molecular Probes) was added to mount the cells. Later cells were imaged under 63X oil immersion objective of SP8 confocal microscope (Leica, Germany).

2.12 Immunofluorescence for 3D culture

3D cultures were washed with 1X PBS and fixed with 4% paraformaldehyde (VWR International) in PBS for 20 minutes at RT. Cells were washed thrice with 1X PBS for 10 minutes each before permeabilisation with ice-cold 0.5% TritonX-100 in 1X PBS at 4ºC for 15 minutes (extreme care should be given while pipetting out the solution after permeabilisation). Further, wells were washed thrice with 100mM glycine in 1X PBS-T (0.5% TritonX-100) and blocked with primary blocking solution containing 10% goat serum (Abcam) in IF-T buffer for 1 hour followed by secondary blocking (primary blocking with 1% F(ab')2 fragment goat anti-mouse IgG (Jackson Immuno Research) for 1 hour. Primary antibodies of required dilution (Table 2) prepared in primary blocking solution was added onto the cultures and incubated for 36 hours at 4ºC. Cultures were kept at RT for 15-20 minutes before washes with IF-T buffer (3 times, 20 minutes each). Respective Alexa Flour® secondary antibodies prepared in primary blocking solution was added to the cultures and incubated for 2 hours. After incubation, cells were washed once with 1X IF-T buffer for 20 minutes and twice with 1X PBS-T for 10 minutes each. 0.5 μg/ml of Hoechst 33258 in PBS-T was added to cells, incubated for 10 minutes, and immediately washed twice with 1X PBS-T for 10 minutes. Excess PBS was removed, and Slow Fade® Gold antifade reagent was added to mount the cells. Later cells were imaged under a 40X oil immersion objective of SP8 confocal microscope (Leica, Germany). A minimum of 50 acini was analysed for phenotypic characterisation.

2.13 Immunoblotting

Immunoblotting analysis using specific antibodies were performed as mentioned previously (Bodakuntla et al., 2014). Briefly, cell lysates were prepared in 2X sample buffer (Tris with SDS, bromophenol blue, dithiothreitol, and glycerol, pH 6.8) and were separated on SDS-PAGE gels at 120V in a SE 260 mini-vertical gel electrophoresis unit (GE Healthcare)**.** Resolved proteins were transferred onto Immobilon-P polyvinyl difluoride (PVDF) membranes (Millipore) in TE22 mighty small transphor unit (GE Healthcare) at 250mA for 3 hours or 150mA for 16 hours. The blots were blocked in 5% (w/v) skimmed milk (SACO Foods, US) prepared in TBS-Tween (25mMTris -pH 7.6, 150 mM NaCl and 2 mM KCl and 0.1% Tween 20) for 1 hour at room temperature (RT) and probed with the respective primary antibody for 1 hour (GAPDH) at RT or overnight at 4ºC. Blots were washed thrice with TBS-T and probed with HRP-conjugated suitable secondary antibody for 1hour at RT. After 3-4 washes with TBS-T, blots were developed with Immobilon reagent (Millipore). Images were acquired on the ImageQuant LAS4000 gel documentation system (GE Healthcare).

2.14 Flow cytometry

The cell cycle profile was analyzed as mentioned previously (Sharma and Lahiri, 2021). Cells were trypsinised using 1X trypsin and collected in media. After pelleting, the cells were washed with cold PBS twice to remove excess media and fixed in 70% ethanol overnight at 4˚C. The fixed cells were stained with 1 mg/ml propidium iodide (PI, Sigma, P4170) in the presence of RNase A (20 mg/ml) at 37˚C for 1 hr. The cell cycle profile was analysed on the BD Accuri™ C6 flow cytometer (BD Biosciences).

2.15 Wound healing assay

Wound healing analysis was performed as mentioned previously (Anandi et al., 2016). Ibidi Culture Inserts, which have a defined cell-free space manufactured from biocompatible silicon, were placed in a 12 well dish. 5 X 10^5 cells suspended in Growth Medium were added on both sides of the insert. 16 hours post-seeding, cells were treated with 10 μg/ml mitomycin C (Sigma) for 2 hours. The medium was aspirated, and cells were washed with PBS before replenishing it with fresh medium. The insert was removed, and the wound was visualised at 0 and 12 hrs under the 10X objective of the

ECLIPSE TS100 (Nikon) microscope. After calculating the wound area using ImageJ software, percentage wound closure was calculated at 12 hrs using the formula

$$\%\ WoundClosure = \frac{Initial\ wound\ area - Final\ wound\ area}{Initial\ wound\ area}\ X\ 100$$

2.16 Single-cell migration assay

Cells were seeded in 24 well dishes at a density of 2 X 10^5 per well and incubated at 37˚C for 10 hrs. Cells were stained with Hoechst 33342 for 15 minutes and replenished with fresh L15 media containing growth constituents. Cells were tracked for 3 hrs at 37˚C, and images were taken every 2 minutes in Evos at 20X magnification. The cells were tracked using Fast track software, and the distance, displacement and velocity obtained were plotted in Graph pad prism.

2.17 Gelatin Zymography

Assay medium of 3D cultures was collected 10 days post-seeding and stored at -80º C. 10 µl of 87 µl 3D medium + 13 µl GZ sample buffer (denaturing buffer) mixture was resolved on an 8% SDS-PAGE containing 0.06% gelatin [w/v] as substrate at 125V at 4ºC (SDS buffer should be changed if the current reduces below 10mA). The gel was washed with distilled water before incubation with 1X Renaturing buffer (2.5 % v/v of Triton X-100 in water) at RT for 30 minutes with constant shaking. After washing with 300 ml of distilled water, the gel was incubated in 100 ml 1X Developing buffer (0.5 M Tris-HCL pH-7.8, 2M NaCl, 0.05M CaCl2 and 0.2% Brij35) for 30 minutes with constant shaking. The gel was incubated at 37ºC for 48 hours with fresh Developing buffer. Meanwhile, the same media (10 µl of 87 µl 3D medium + 13 µl of 6X sample buffer) was resolved on an 8% SDS-PAGE to find the total protein content in the media. Later, the gels were stained overnight with the staining solution (0.1% w/v Coomassie blue (Sigma-Aldrich), 50% v/v Methanol (Fisher Scientific) and 10% v/v acetic acid (Fisher Scientific) and destained with destaining solution (40% v/v methanol and 10% v/v acetic acid) for 1 hour. The gel images were acquired on the ImageQuant LAS4000 gel documentation system (GE Healthcare).

2.18 Colony formation assay

Cells were seeded on 6 well plates at a density of 300 cells per well. Cells were replenished with fresh media after 4 days of seeding. After 7 days of seeding, cells were washed with 1X PBS twice and fixed with 100% chilled methanol at 4^0 C for 15 minutes. Cells were stained with 0.5% of crystal violet stain for 15 minutes with shaking at room temperature. After removing the stain, cells were washed with distilled water and images were taken after drying the plates. The number of colonies was manually counted.

2.19 Soft agar assay

Soft agar assay was performed as mentioned previously (Anandi et al., 2017). 6 well plate was layered with 0.6% agar and incubated at 37^0 C for 20 minutes for solidification. 1.25 X 10^5 3D dissociated cells/ or MCF10CA1a 2D cells mixed in 0.3% agar was layered above the solid agar layer. After 4 hrs, cells were replenished with 750 µl of growth media. Cells were supplemented with fresh media on Day 4 and stained using 200 µl of 1mg/ml MTT on Day 7. Images were taken under the 10X objective of the ECLIPSE TS100 (Nikon) microscope, and the number of colonies was counted manually.

2.20 Tumorigenesis in mice

For mice injections, 6 X 10^6 cells were re-suspended in 100 µl of 1:1 mixture of PBS: Matrigel and injected into the flanks of athymic nude mice (Foxnl ^{nu} / Foxnl ^{nu}, 6-8 weeks old) (Approved by Institute Animal Ethics Committee, IAEC/2018_02/010). The mice were examined every week. The mice were sacrificed in the 7^{th} week, and the tumour was dissected. The tumour size and volume were calculated by measuring the tumour dimensions using the Vernier calliper.

2.21 Whole-exome sequencing

Genomic DNA was extracted from mCherry-MCF10A, TopBP1 OE 3D dissociated and MCF10CA1a cells using the DNeasy blood and Tissue kit (Qiagen, 69506) as per manufactures protocol. All three cell lines were targeted for whole exome sequencing (Makiniemi et al.) using Agilent V6r2 (Agilent Technologies, Santa Clara, CA 95051,

USA) and this targeted library was sequenced using HiSeq. The resultant raw data were then mapped to the human genome (Hg19/GRCh37) using BWA algorithm (Abuin et al., 2015; Li and Durbin, 2009, 2010) and duplicates were removed using Picard toolkit (Github, Board institute). For all 3 cell lines mapping were in the cut-off limit (i.e mapping= >95% and Read Duplicates <20%). Further target enrichment was done using samtools and subsequent variant calling was done on BAM file using GATK pipeline to produce VCF formatted output file (BSD, MIT). All variants in the VCF file were then annotated using in-house pipeline with all required databases including OMIM, ClinVar HGBS coordinates, different population databases, etc (Ulintz et al., 2019). Sequencing data was analyzed manually to identify TP53 gene mutations in the cell lines.

2.22 Statistical Analysis

At least 3 biological independent replicates were performed for all the experiments. Hygens software (SVI, Hilversum, Netherlands) was used to calculate the surface area, volume and sphericity of the 3D acini or spheroids. Results were analyzed and plotted using GraphPad Prism (GraphPad Software, La Jolla, CA, USA). Mann Whitney U test was used to test the significance of difference of various parameters in the morphometric analysis and immunofluorescence. Paired Student's t-test or One-way ANOVA was performed to analyze the significance of difference of protein expression in immunoblotting.

2.23 Ethics statements

Institutional Biosafety Committee (IBSC) clearance was obtained from the institute for preparing TopBP1 OE MCF10A cells and TopBP1 KD MCF10CA1a cells. All mouse studies were approved by the Institutional Animal Ethics Committee (IAEC) (IAEC/2018_02/010 and IISER_Pune/IAEC/2021_01/06). We only used athymic mice (Foxnl^{nu} / Foxnl^{nu}, 6-8 weeks old) for the *in vivo* tumorigenicity studies

Chapter 3

TopBP1 expression in Breast cancers

3.1 Background

TopBP1 is a major mediator protein involved in the single-strand break repair pathway. It has structural and functional similarities to BRCA1, a mediator protein involved in the double-strand break repair pathway and a well-studied tumour suppressor. Unlike BRCA1, TopBP1 levels were upregulated in breast cancer tissue samples. Immunohistochemical studies performed in breast cancer biopsy samples showed that TopBP1 is upregulated in breast cancer tissues. TopBP1 over-expression was associated with higher-grade tumours and lower patient survival (Forma et al., 2012; Going et al., 2007; Liu et al., 2009). However, there are studies where no TopBP1 expression was observed in invasive breast cancer samples (Forma et al., 2012; Going et al., 2007). Also, decreased levels of *TopBP1* mRNA were observed in high-grade breast tumour samples, which contradict its role as an oncogene (Going et al., 2007). However, the expression pattern of TopBP1 across various subtypes of breast cancer were not reported. Also, no reports are suggesting the expression pattern of TopBP1 in Indian breast cancer patient samples. These reports, along with the known functions of TopBP1 and its similarity to BRCA1 and the availability of limited reports stating the possible role of TopBP1 in breast cancer, prompted us to investigate the expression pattern of TopBP1 in breast cancer.

3.2 Results

3.2.1 In-silico analysis of TopBP1 expression in breast cancer

To find whether TopBP1 expression is associated with breast cancer, *in-silico* analysis was performed using The Cancer Genome Atlas (TCGA) data. TCGA data is a collaboration between the National Cancer Institute (NCI) and the National Human Genome Research Institute (NHGRI). It contains the transcript level information of genes in 33 types of cancer.

TOPBP1 transcript levels in the tumour and the corresponding adjacent normal tissues were analysed. It was observed that TOPBP1 transcript levels in the tumour were higher than the corresponding adjacent normal (Figure 3.1), confirming the previously reported studies that TopBP1 levels are high in breast cancer

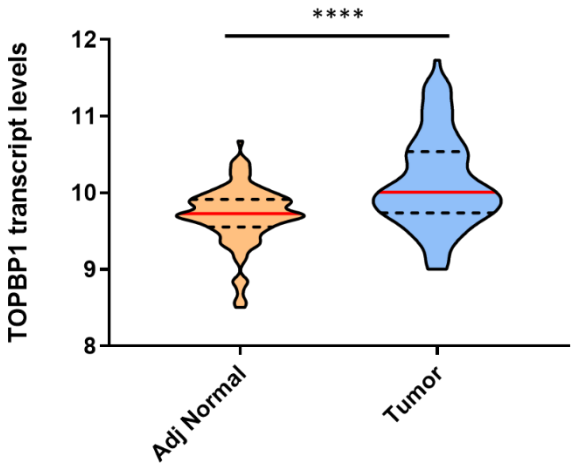


Figure 3.1: TOPBP1 transcript levels are high in breast cancer

Scatter plot of TOPBP1 transcript levels in tumour and corresponding adjacent normal based on TCGA database. Statistical analysis was done using Mann Whitney test (**** $p < 0.0001$)

We were interested in investigating the TOPBP1 expression pattern in various types of breast cancer. Breast cancer can be broadly classified based on the receptor status, molecular subtypes and stages (Figure 3.2). Estrogen (ER) and progesterone (PR) are the primary hormone receptors on breast tissue that regulate their growth in response to levels of hormones estrogen and progesterone, respectively. Human epidermal growth factor receptor 2 (HER2) is a member of the human epidermal growth factor receptor family, and the amplification of this oncogene is associated with various aggressive forms of breast cancer. The receptor status of the tumour has a significant role in therapeutic aspects.

TOPBP1 transcript levels expression in patients with various receptor statuses were analysed using the TCGA database. TCGA analysis revealed that TOPBP1 transcript levels are high in $ER^+PR^+HER2^+$ and Triple-negative breast cancer (TNBC; $ER^-PR^-HER2^-$) compared to adjacent normal (Figure 3.3).

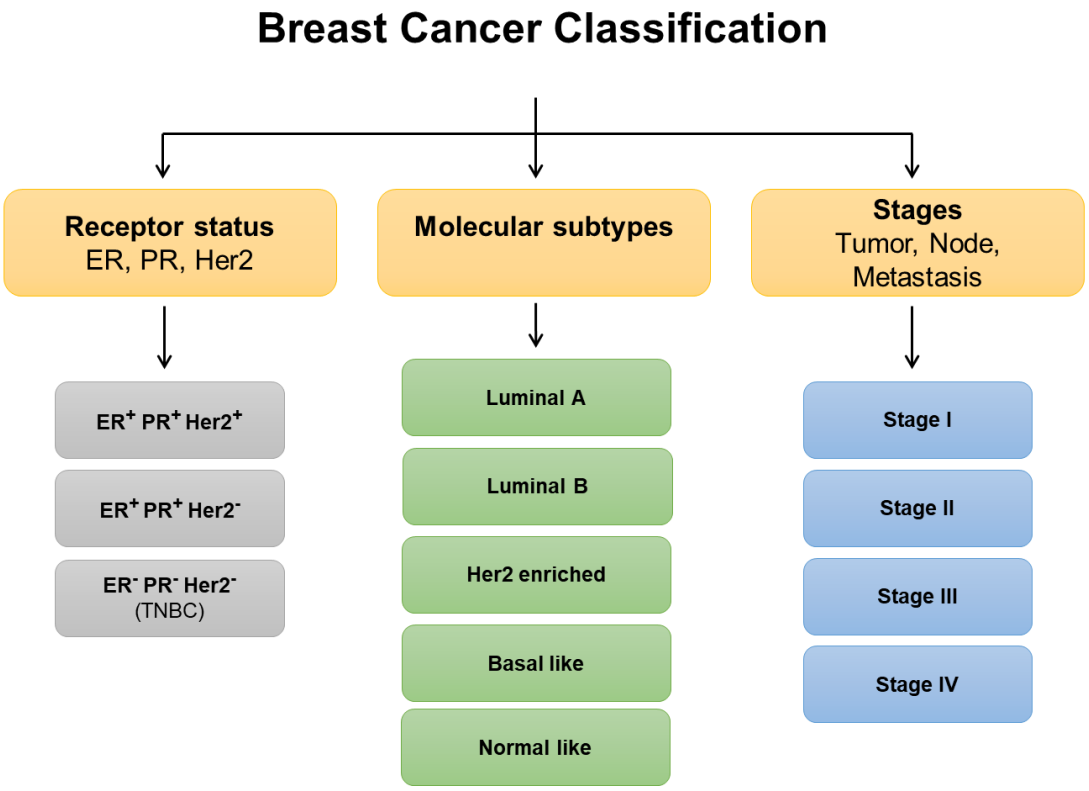


Figure 3.2: Breast cancer classification- Schematic representation of breast cancer classification based on receptor status, molecular subtypes and stages

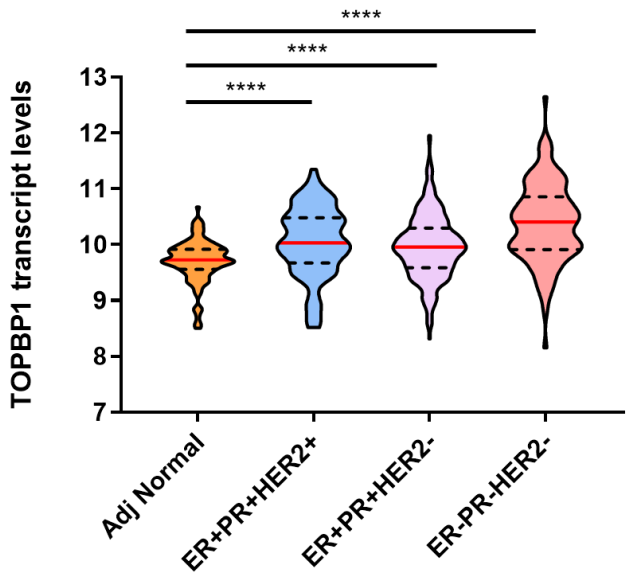


Figure 3.3: TOPBP1 transcript levels across various receptor statuses- Scatter plot of TOPBP1 transcript levels across various receptor statuses and adjacent normal based on TCGA database. Statistical analysis was done using the Kruskal-Wallis test, and Dunn's multiple comparisons test (**** p <0.0001)

The various subtypes of breast cancer based on PAM50 classification are Luminal A (ER/PR positive or HER2 negative), Luminal B (ER/PR positive, while HER2 positive or negative, high proliferation index rate expressed by Ki-67), HER2-enriched (ER/PR negative, HER2 positive), Basal-like (ER/PR negative, and HER2 negative, high expression of Ki-67) and normal-like (ER/PR positive, HER2 negative, low levels of Ki-67). TOPBP1 transcript level was found to be high in all subtypes (except normal-like) compared to the adjacent normal (Figure 3.4), suggesting that higher TopBP1 expression is associated with breast cancer.

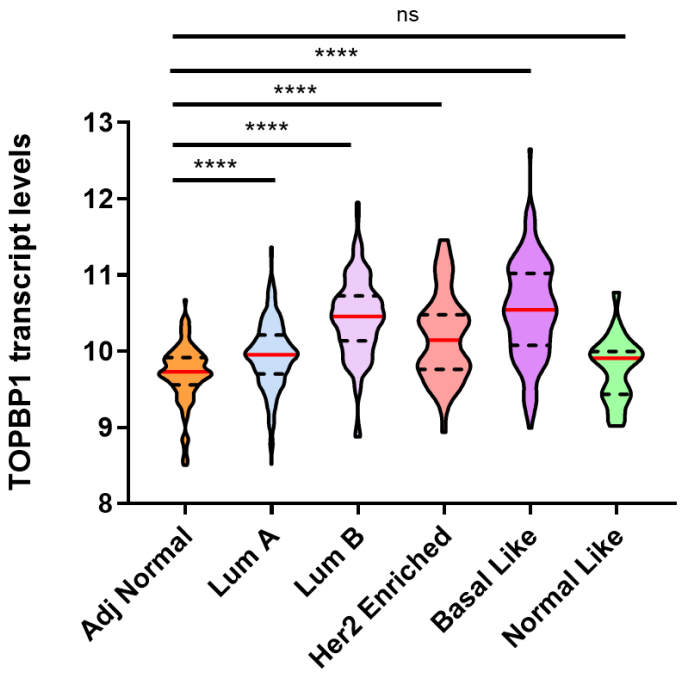


Figure 3.4: TOPBP1 transcript level across breast cancer subtypes: Scatter plot of TOPBP1 transcript levels across various subtypes and adjacent normal based on TCGA database. Statistical analysis was done using the Kruskal-Wallis test, and Dunn's multiple comparisons test (**** p <0.0001)

Breast cancer is classified into stages I, II, III and IV based on tumour size, lymph node metastasis and metastasis to other organs. Transcript levels analysis of TopBP1 from the TCGA database showed that TOPBP1 transcript level expression increases significantly across the stages, except stage IV (Figure 3.5)

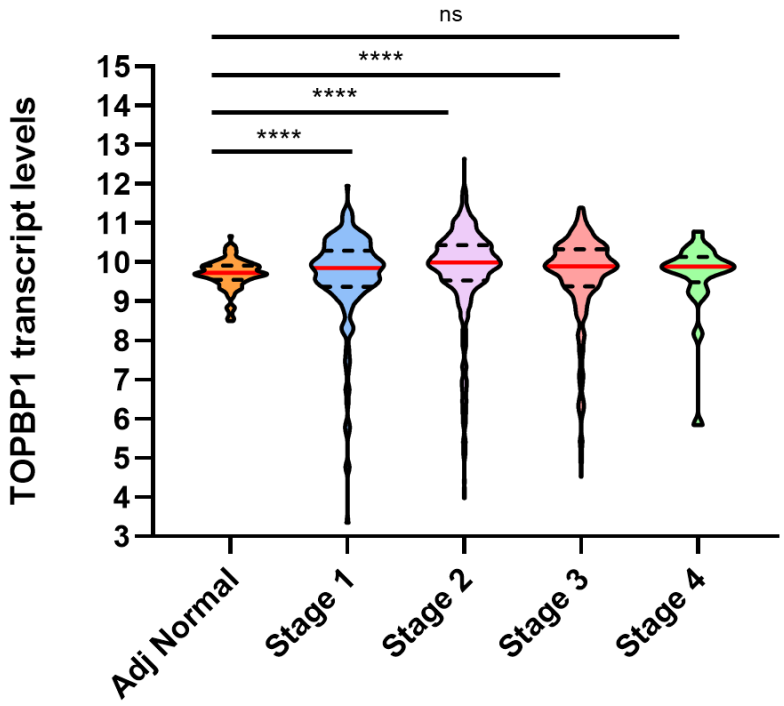


Figure 3.5: TOPBP1 transcript levels across various breast cancer stages: Scatter plot of TOPBP1 transcript levels across various stages and adjacent normal based on TCGA database. Statistical analysis was done using the Kruskal-Wallis test, and Dunn's multiple comparisons test (**** $p < 0.0001$, ns $p > 0.05$)

Previous studies have shown that TopBP1 over-expression leads to reduced survival in the patient sample. To validate this result, we used Kaplan Meier (KM) plotter (Szasz et al., 2016). KM plotter is a meta-analysis tool that uses the microarray data of over 50000 genes on survival using 10000 cancer samples. The analysis revealed that high TopBP1 expression is associated with a low probability of survival (Figure 3.6). These results show that higher TopBP1 expression is associated with breast cancer.

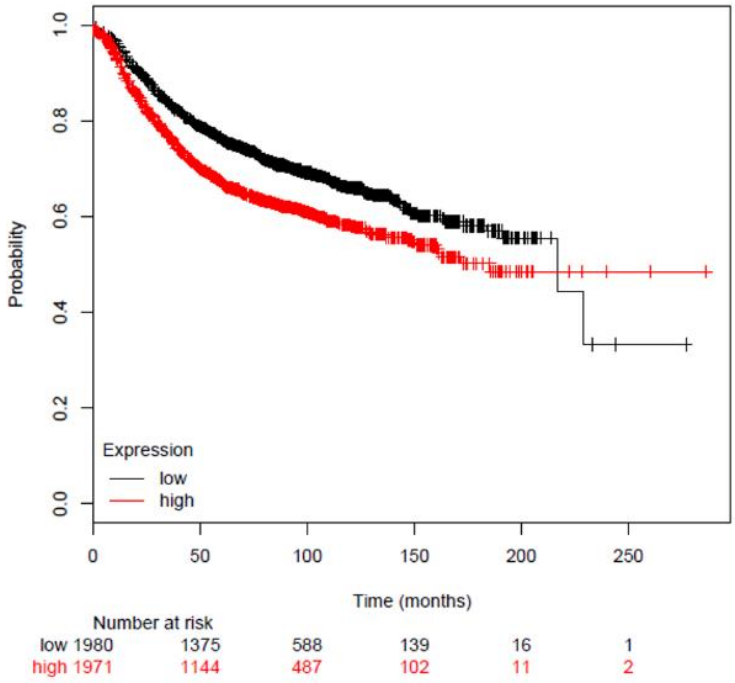


Figure 3.6: Higher TOPBP1 expression is associated with reduced survival- KM plot analysis showing survival of patients with varying expression of TOPBP1**.**

3.2.2. TopBP1 expression pattern in Indian breast cancer patient samples

TCGA analysis revealed that TOPBP1 transcript levels were high in tumour tissues compared to the adjacent normal, and the levels were high in different breast cancer subtypes. These data were from the western population. We were interested in investigating the levels of TopBP1 in Indian breast cancer patient samples.

Tissue samples collected during breast cancer biopsy or surgery and breast reduction surgeries (control) were fixed using formalin and were embedded in paraffin. These paraffin-embedded tissues were provided to us by Prashanti Cancer care mission Pune, and they were sliced using a microtome and coated on poly L-Lysine coated slides. These were stained using eosin and haematoxylin to understand the morphological variation. TopBP1 immunohistochemistry (IHC) was performed to understand the expression pattern and TopBP1 levels in Indian patient samples.

Preliminary IHC data suggests that TopBP1 expression is higher in tumour tissue compared to the reduction tissue from the same patient (Figure 3.7). This result was further validated using multiple paired tissue, and histoscore (H score) was calculated (Figure 3.8). It was observed that TopBP1 levels in normal tissue had an H score of 2, whereas the that of tumour tissue was above 6 (N=15 samples)

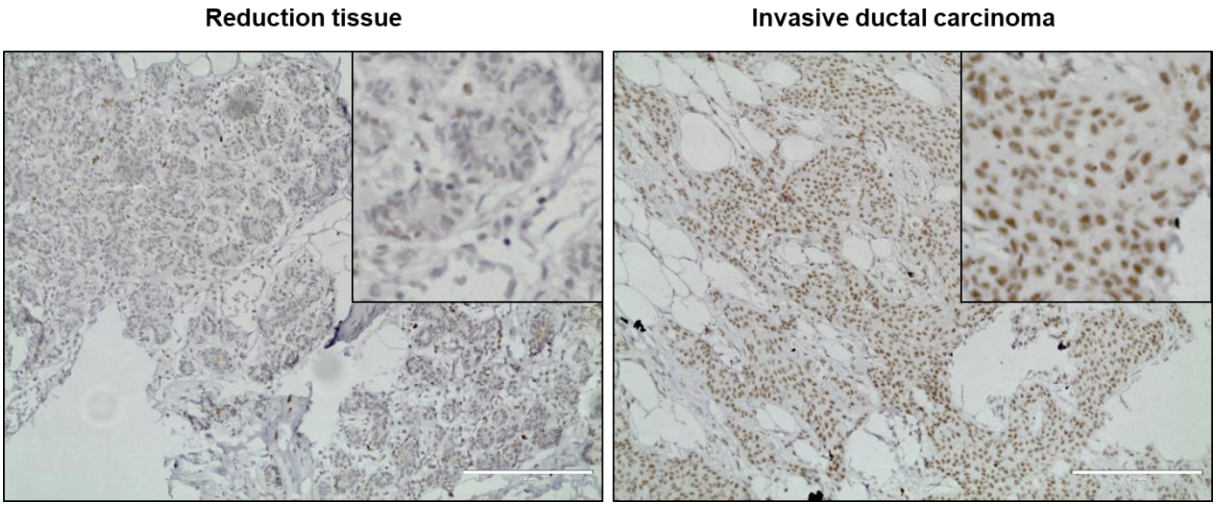


Figure 3.7: TopBP1 levels in Indian breast tissue samples- IHC analysis of FFPE tissue blocks using TopBP1 specific antibody. The image was acquired in EVOS at 20X magnification

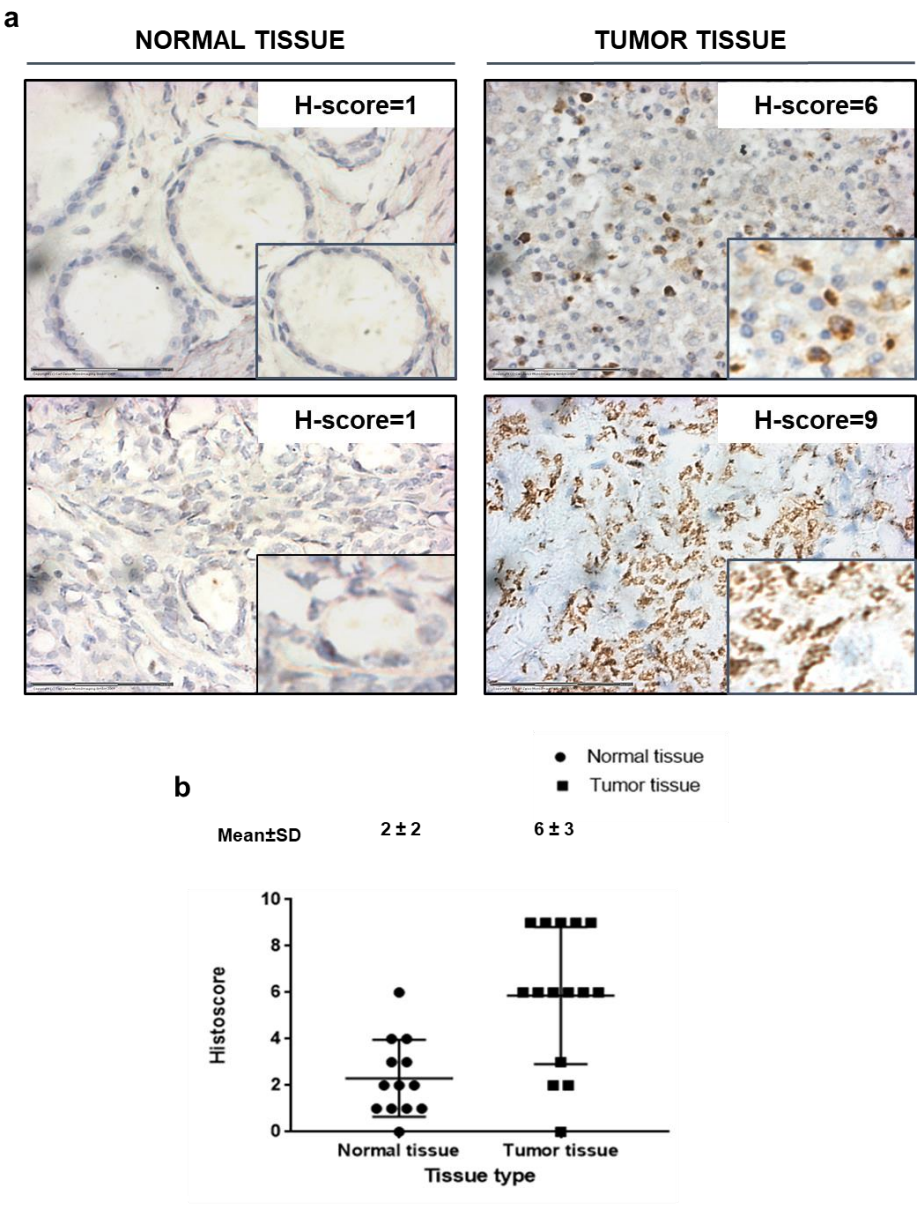


Figure 3.8: TopBP1 levels in Indian breast tissue samples- a) IHC analysis of Normal tissue and Tumour FFPE tissue blocks using TopBP1 specific antibody. The image was acquired at 40X magnification. b) Mean H scores plotted. N=15.

TopBP1 expression in TNBC and ER +ve tissues was also investigated using IHC to understand the TopBP1 expression across various receptor statuses. It was observed that ER +ve tumour tissues had higher TopBP1 levels compared to TNBC (Figure 3.9). The mean histoscore for TNBC was 3, and ER+ was 6

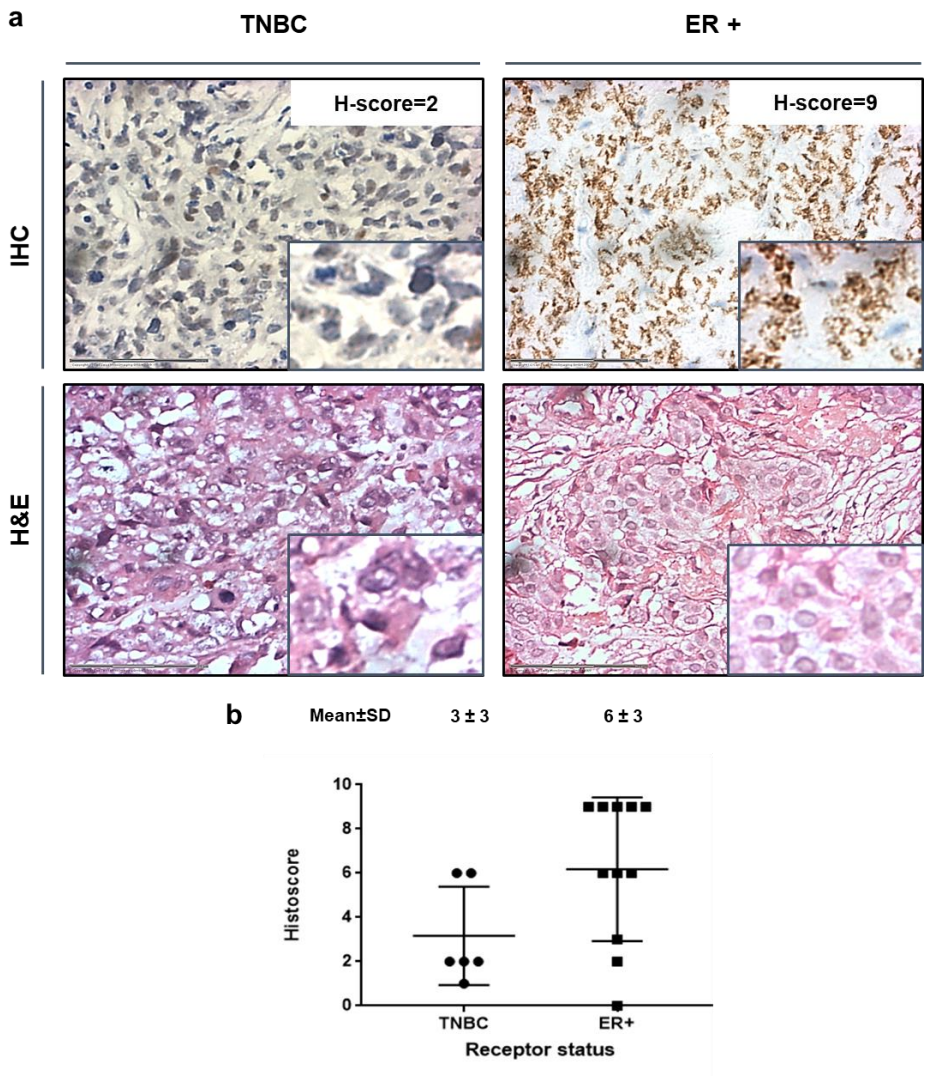


Figure 3.9: TopBP1 levels in Indian breast tissue samples- a) IHC analysis of TNBC, ER+ FFPE tissue blocks using TopBP1 specific antibody Hematoxylin and eosin staining images of TNBC and ER+ respectively. The image was acquired at 40X magnification. b) Mean H scores plotted (TNBC N=6 and ER+ve N=11).

3.3 Summary

TopBP1 is a mediator protein that activates ATR during single strand breaks, leading to checkpoint activation and cell cycle arrest. TopBP1 has a structural similarity to BRCA1. Also, TopBP1 protein is associated with hereditary breast and ovarian cancer in the western population. In this chapter, using TCGA analysis, we found that TOPBP1

transcript levels are high in tumour tissues compared to the paired adjacent normal tissues. Also, the TOPBP1 levels are high in various breast cancer patients with various receptor statuses, molecular subtypes and stages. We also confirmed the previously reported data on TopBP1 levels and patient survival. We found that higher TOPBP1 levels were associated with reduced patient survival using KM plotter analysis. No reports were investigating the TopBP1 expression pattern in Indian breast cancer patient samples. In this chapter, we also found that TopBP1 protein levels are high in Indian breast cancer patient samples compared to the normal tissues. We also found that TopBP1 levels are high in ER+ tissues compared to TNBC. Overall, these results suggest that TopBP1 levels are high in breast cancer tissues, suggesting its potential role as an oncogene.

Chapter 4

Characterisation of MCF10A cancer progression series

4.1 Background

According to literature and results from chapter 3, higher TopBP1 expression is associated with higher grades and stages of breast cancer. To further investigate the role of TopBP1 in tumorigenesis, the MCF10A cancer progression series was used as a model system. The MCF10A series consists of MCF10A (non-transformed epithelial cells), MCF10AT1 (premalignant cells) and MCF10CA1a (malignant cells). MCF10A was derived from the parental MCF10 cells from a woman with fibrocystic mammary tissue. The adherent MCF10A cells were transformed with constitutive H-RAS to generate MCF10AT1. MCF10CA1a was derived by continuous passaging of MCF10AT1 in mice for 100 generations.

The role of an oncogene in transformation can be investigated using two methods: either by overexpressing the gene in a non-transformed cell line or knocking down the gene in a transformed cell line. To study the role of TopBP1 in transformation, TopBP1 will be over-expressed in the cell line with lower TopBP1 levels in the MCF10A series. Meanwhile, TopBP1 will be knocked down in the one with higher levels to check for reversal of transformed phenotype. To understand the role of TopBP1 in transformation, various phenotypes, like epithelial to mesenchymal transition (EMT), migration, invasion and anchorage-independent growth, will be characterised in these cell lines. Also, TopBP1 being a protein involved in DNA damage response, the activation of various DNA damage response (DDR) proteins needs to be investigated in the MCF10A cancer progression series. However, no reports describe these properties of MCF10A series cell lines. Characterisation of the MCF10A series is required to understand their DDR, EMT status, migration and invasion properties.

4.2 Results

4.2.1 TopBP1 levels are high in MCF10CA1a compared to MCF10A

TopBP1 levels were high in breast cancer patients. To determine whether a similar pattern is observed in cell lines, the TopBP1 expression pattern in MCF10A cancer progression series cells was determined. TopBP1 expression in the MCF10A series was determined using western blotting and immunofluorescence assay. It was observed that there was an increase in TopBP1 expression across the series (Figure 4.1). Higher

TopBP1 expression was observed in premalignant MCF10AT1 and malignant cell line MCF10CA1a compared to non-tumorigenic MCF10A.

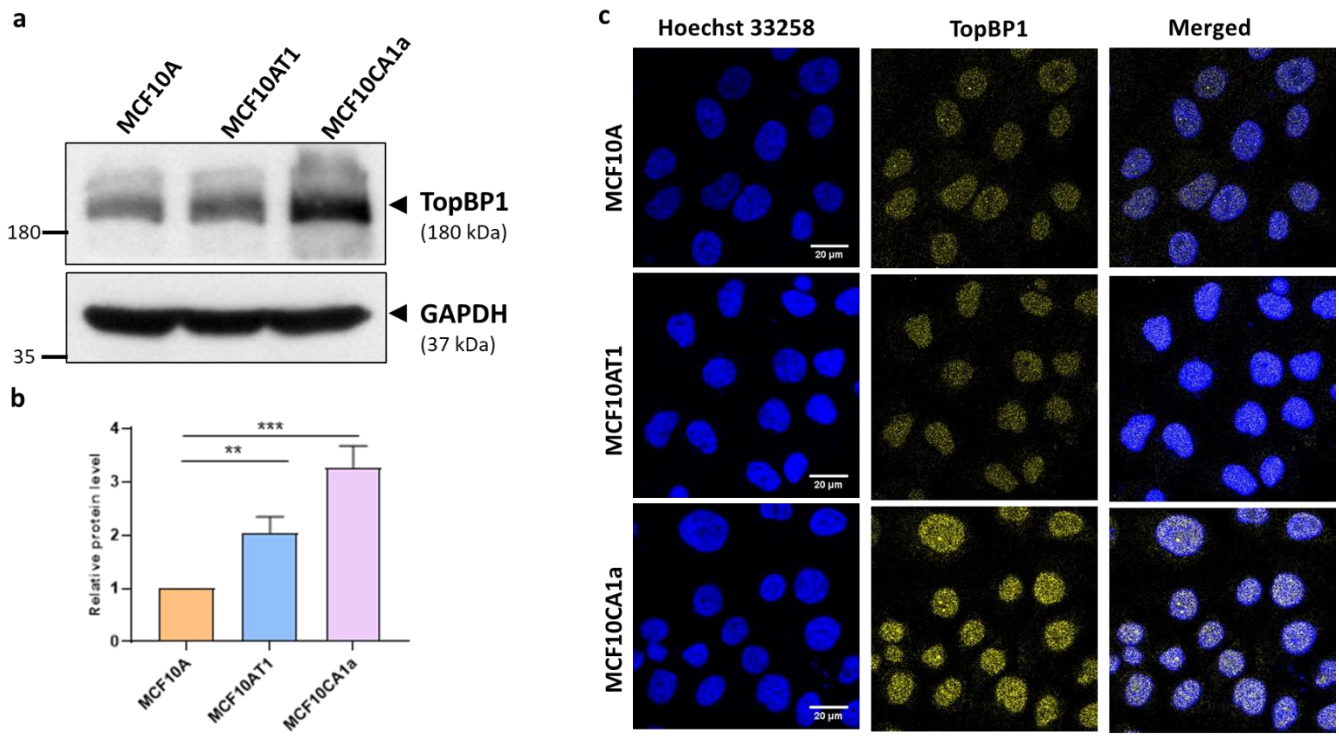


Figure 4.1: TopBP1 levels in MCF10A series-a) Western blot analysis and c) immunofluorescence assay showing varying levels of TopBP1 in MCF10A, MCF10AT1 and MCF10CA1a cells. b) The fold change of TopBP1 after normalising with GAPDH. Statistical analysis was done using One-way ANOVA (*** p <0.001, **p <0.01).

4.2.2 DNA damage response (DDR) proteins in MCF10A series

To identify whether increased TopBP1 levels in malignant cells compared to non-tumorigenic epithelial cells was in response to increased DNA damage or defects in DNA damage response, the levels of various proteins in the DDR pathway in the MCF10A series were investigated.

RPA and H2AX are two proteins that get activated and recruited to single-strand and double-strand DNA, respectively, after DNA damage. MCF10CA1a cells had RPA activation even without any induction of external DNA damage (Figure 4.2a, b and d).

These cells also have increased levels of γH2AX compared to MCF10A and MCF10AT1 suggesting the presence of endogenous double-strand breaks (Figure 4.2a, c and e).

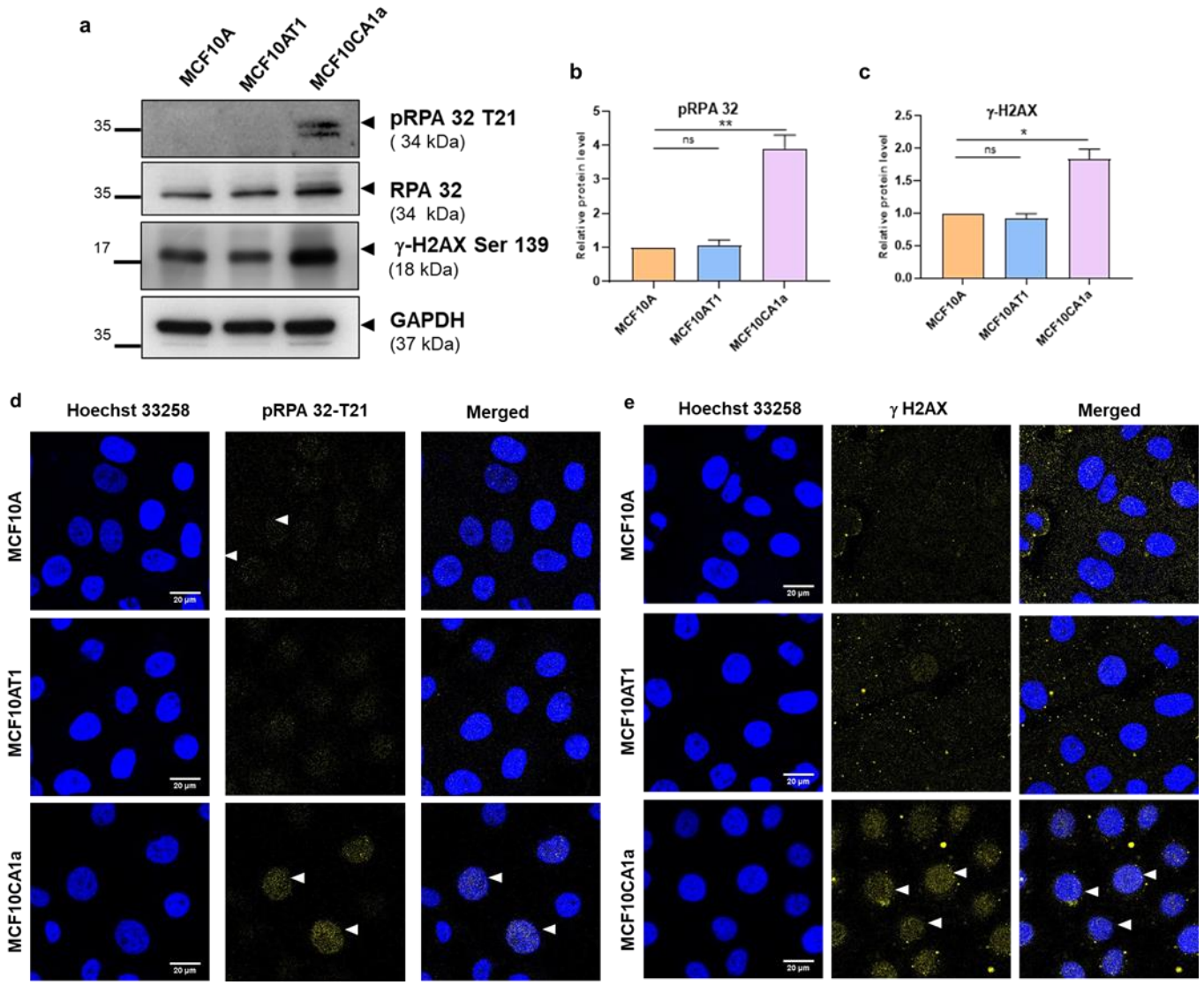


Figure 4.2: RPA and γH2AX activation in MCF10A series- Western blot analysis showing varying levels of **a-b)** pRPA T21 and **a-c)** γH2AX S139 in MCF10A, MCF10AT1 and MCF10CA1a cells and quantified after normalising to GAPDH. Statistical analysis was done using One-way ANOVA for MCF10A series (*** p <0.001, ** p <0.01, * p <0.05, ns p>0.05). IF staining of **d)** pRPA and **e)** γH2AX in MCF10A series.

The activation of various proteins in single and double-strand break repair pathways was observed in the MCF10A series using western blotting. ATR, Rad17 and Chk1, the sensor and transducer proteins involved in the single-strand break repair pathway, showed increased activation in MCF10CA1a compared to MCF10AT1 and MCF10A (Figure 4.3). However, the activation of ATM and Chk2, the sensor and transducer protein in the double-strand break repair pathway, was reduced in MCF10CA1a compared to MCF10AT1 and MCF10A (Figure 4.4)

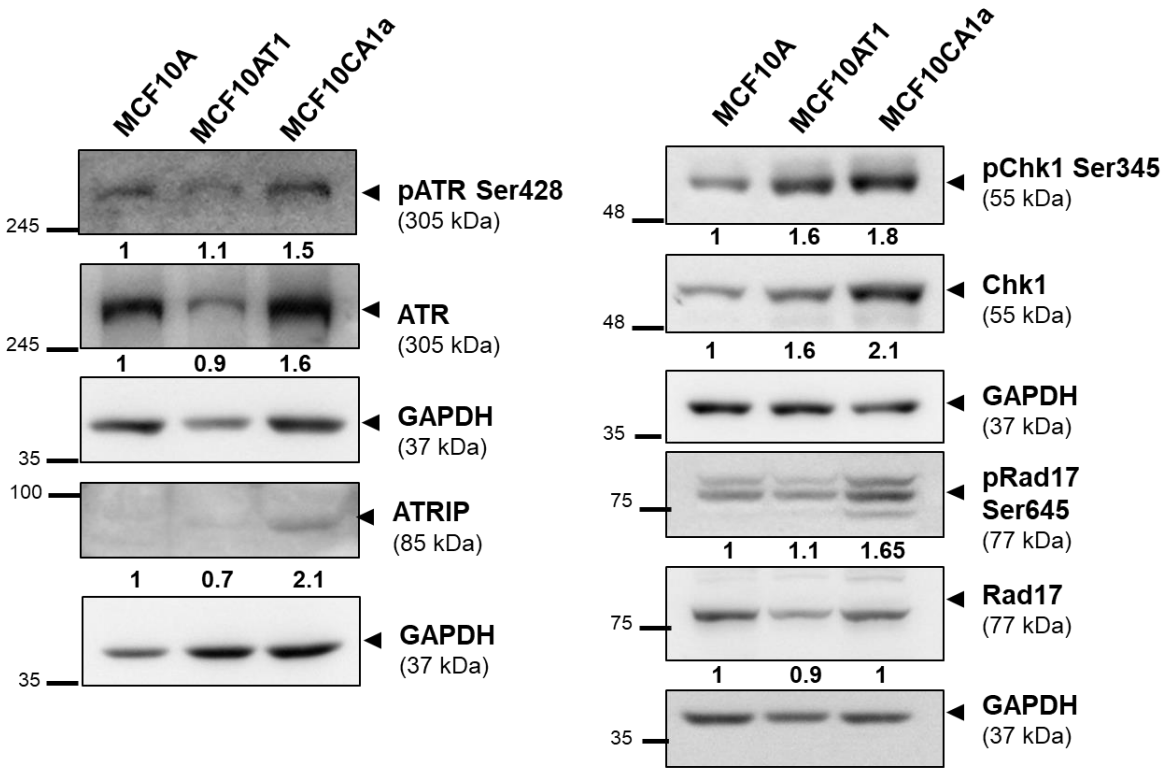


Figure 4.3: Single strand break repair proteins in MCF10A series- Western blot analysis showing activation/ levels of various proteins involved in single-strand break repair in MCF10A, MCF10AT1 and MCF10CA1a cells. GAPDH was used as a loading control.

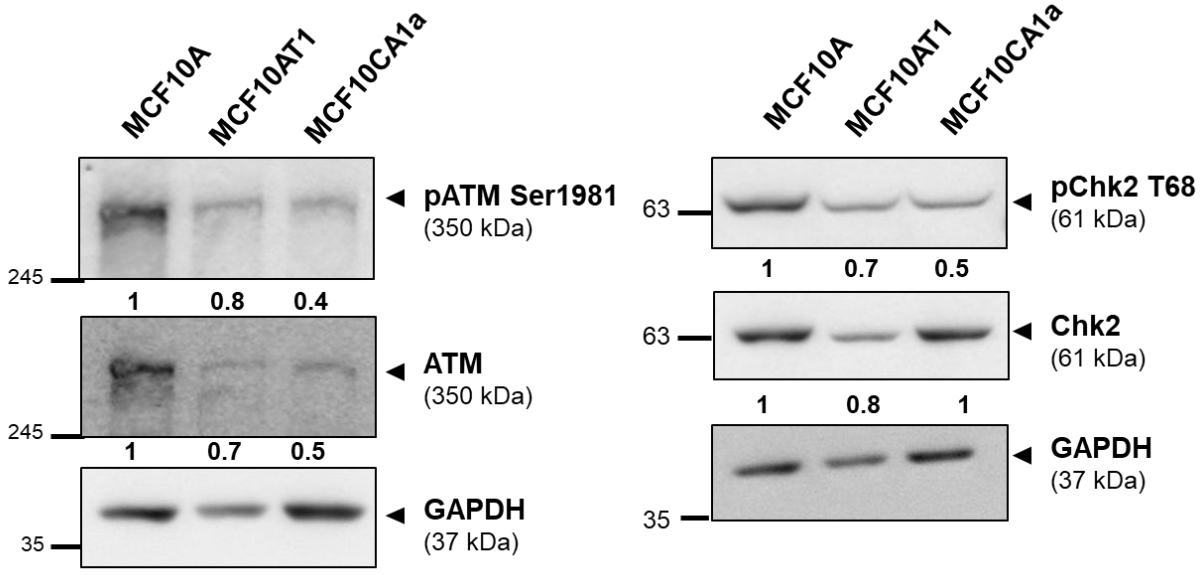


Figure 4.4: Double-strand break repair proteins in MCF10A series- Western blot analysis showing activation/ levels of various proteins involved in double-strand break repair in MCF10A, MCF10AT1 and MCF10CA1a cells. GAPDH was used as a loading control.

p53, a major effector protein activated by active Chk1 and Chk2 upon DNA damage, leads to cell cycle arrest and apoptosis based on the extent of the damage. MCF10CA1a had an increased level of p53 compared to MCF10A and MCF10AT1. MCF10CA1a also had increased phosphorylation of serine 15 and 37 sites of p53 which corresponds to increased DNA damage response (Figure 4.5a and b). However, the phosphorylation of p53 at Serine 46, which regulates various apoptotic proteins, was low in MCF10CA1a compared to MCF10A and MCF10CA1a (Figure 4.5c).

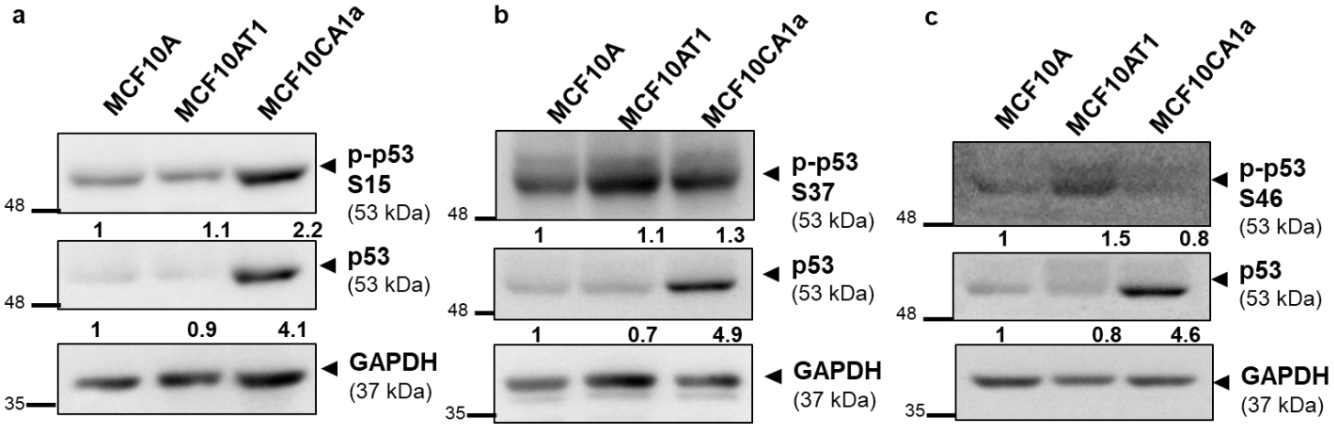


Figure 4.5: p53 activation in MCF10A series- Western blot analysis showing activation of p53 at a) serine 15, b) Serine 37 and c) Serine 46 sites in MCF10A, MCF10AT1 and MCF10CA1a cells. GAPDH was used as a loading control.

4.2.3 EMT characteristics of MCF10A series

Cell lysates of MCF10A series cells were analysed using immunoblotting to investigate the levels of various EMT markers (Figure 4.6). Vimentin, a mesenchymal marker, was absent in MCF10AT1 and MCF10CA1a. E-cadherin, an epithelial marker, was upregulated in MCF10AT1 and MCF10CA1a compared to MCF10A but MCF10CA1a had lesser levels than MCF10AT1. However, N-cadherin, a mesenchymal marker, levels were reduced in MCF10AT1 and MCF10CA1a. Slug levels were low in MCF10CA1a compared to MCF10A and MCF10AT1, whereas Twist levels were slightly upregulated in MCF10CA1a. Intermediate filaments like cytokeratin 14 levels were high in MCF10AT1 but low in MCF10CA1a. Cytokeratin 19 showed upregulation in MCF10AT1 and MCF10CA1a.

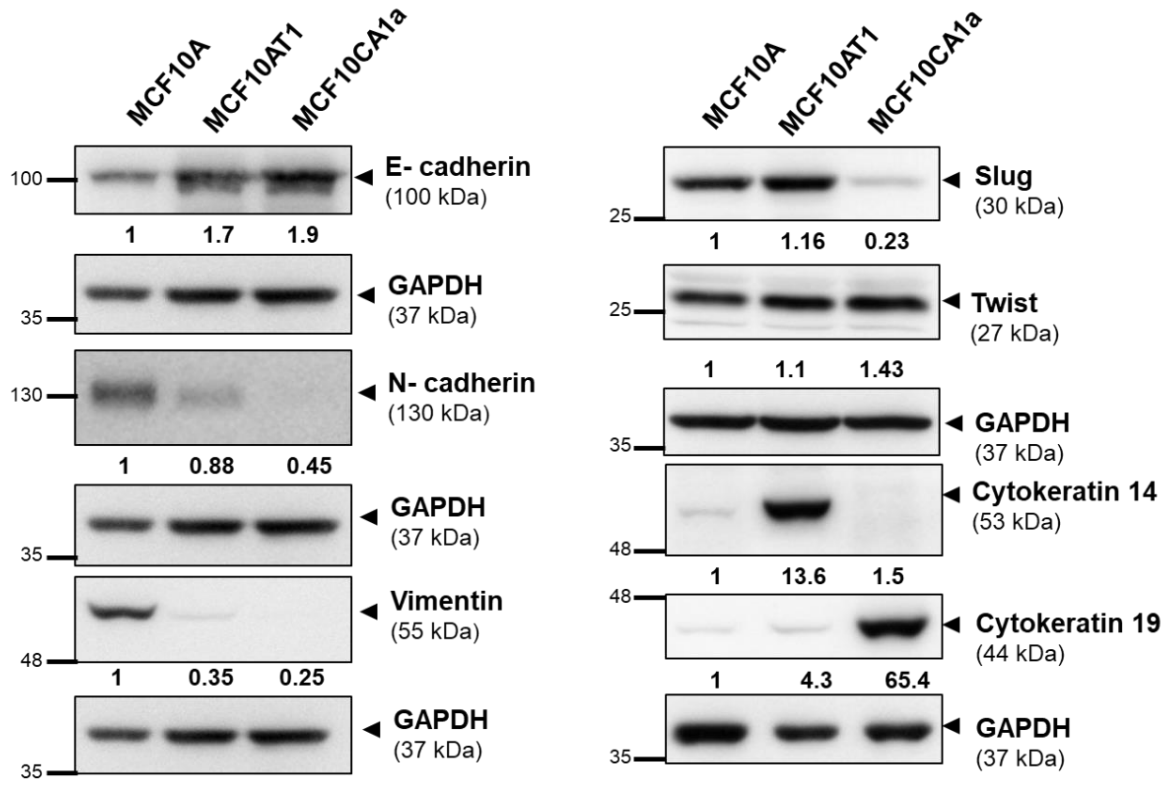


Figure 4.6: EMT markers in MCF10A series - Western blot analysis showing varying levels of various proteins in MCF10A, MCF10AT1 and MCF10CA1a cells. GAPDH was used as a loading control

A wound-healing assay was performed to find the collective migration of MCF10A series cell lines. MCF10A series cells were seeded on either side of the Ibidi silicon inserts, which have defined cell-free gaps. 16 hours post-seeding, cells were treated with mitomycin C for 2 hours. Inserts were removed, and the wound was visualised at 0, 6,12,18 and 24 hours. Increased wound closure was observed in MCF10CA1a cells compared to MCF10A and MCF10AT1 (Figure 4.7). However, no significant difference in single-cell migration was observed across these cell lines (Figure 4.8)

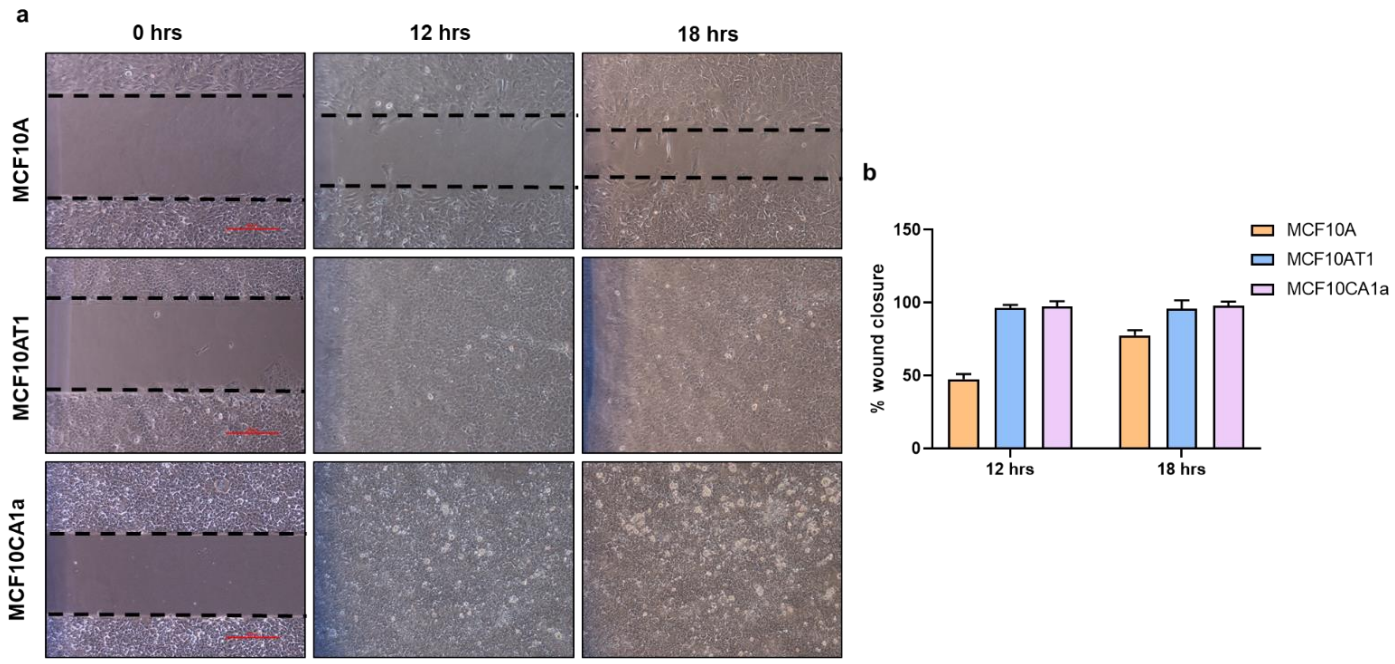


Figure 4.7: Collective cell migration in MCF10A series- a) Representative images of wound healing assay demonstrating collective cell migration of MCF10A, MCF10AT1 and MCF10CA1a cells at different time points. Images were acquired in ECLIPSE TS100 Nikon microscope at 10X magnification (scale bar-50 µm). **b)** Quantification of percentage (%) wound closure.

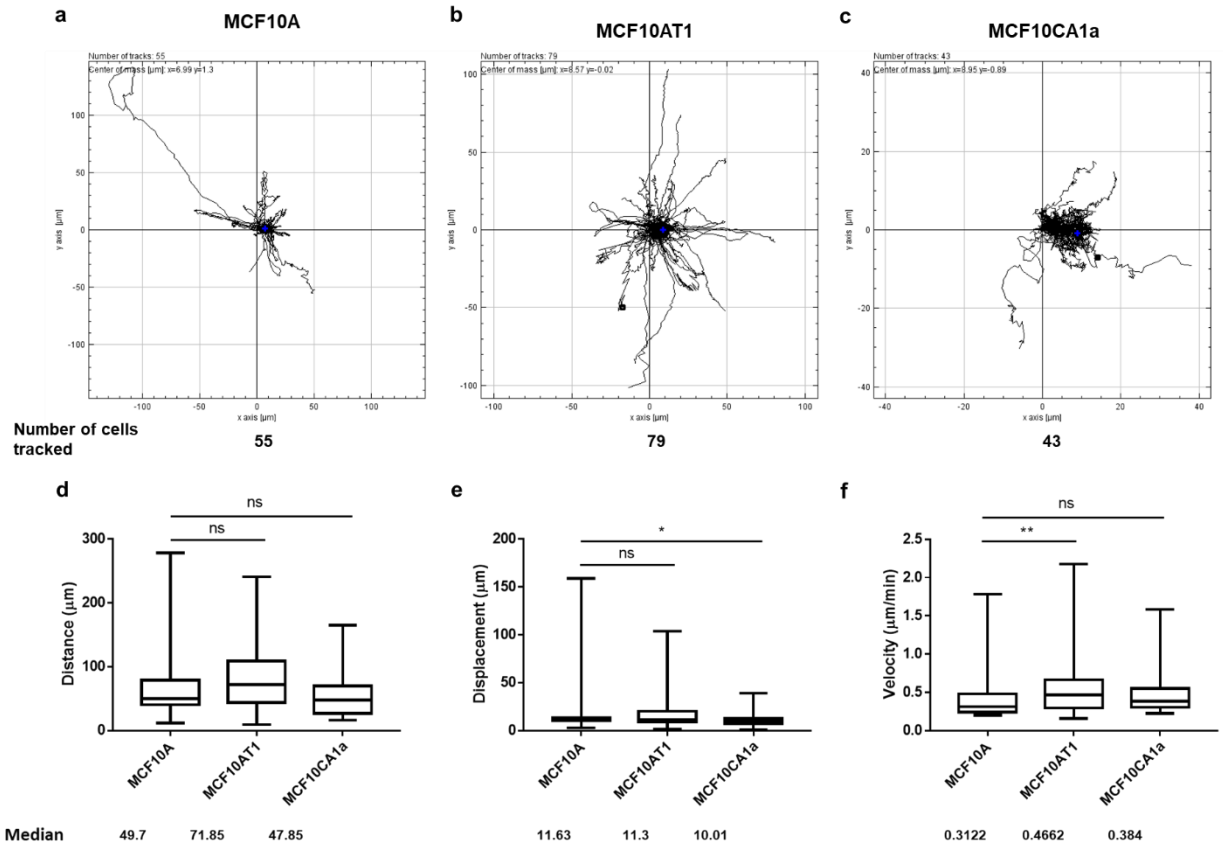


Figure 4.8: Single-cell migration in MCF10A series-Time-lapse images of MCF10A, MCF10AT1 and MCF10CA1a cells seeded as sparse populations was performed for a period of 3 hrs with an image taken at a 2-minute interval in Zeiss anisotropy confocal microscope. Trajectory plot showing the tracks of **a**) MCF10A, **b**) MCF10AT1 and **c**) MCF10CA1a. Cells were tracked using Fast track software, and the **d)** distance **e)** displacement and **f)** velocity are represented as violin plots

Epithelial cells require cell-cell contact and anchorage for their growth. However, transformed cells can grow without contact and anchorage. The colony formation and anchorage-independent growth of MCF10A series cells were analysed using colony formation and soft agar assays. MCF10AT1 cells formed few colonies when sparsely seeded in 14 days, whereas MCF10CA1a cells formed colonies in 7 days (Figure 4.9). However, MCF10A cells failed to form colonies even after 14 days.

Similarly, when seeded on the agar layer, MCF10AT1 cells formed colonies in 21 days, whereas MCF10CA1a cells formed colonies in 7 days (Figure 4.10). However, MCF10A cells failed to form colonies even after 21 days. These results confirmed the colony formation and anchorage-independent growth of MCF10CA1a cells.

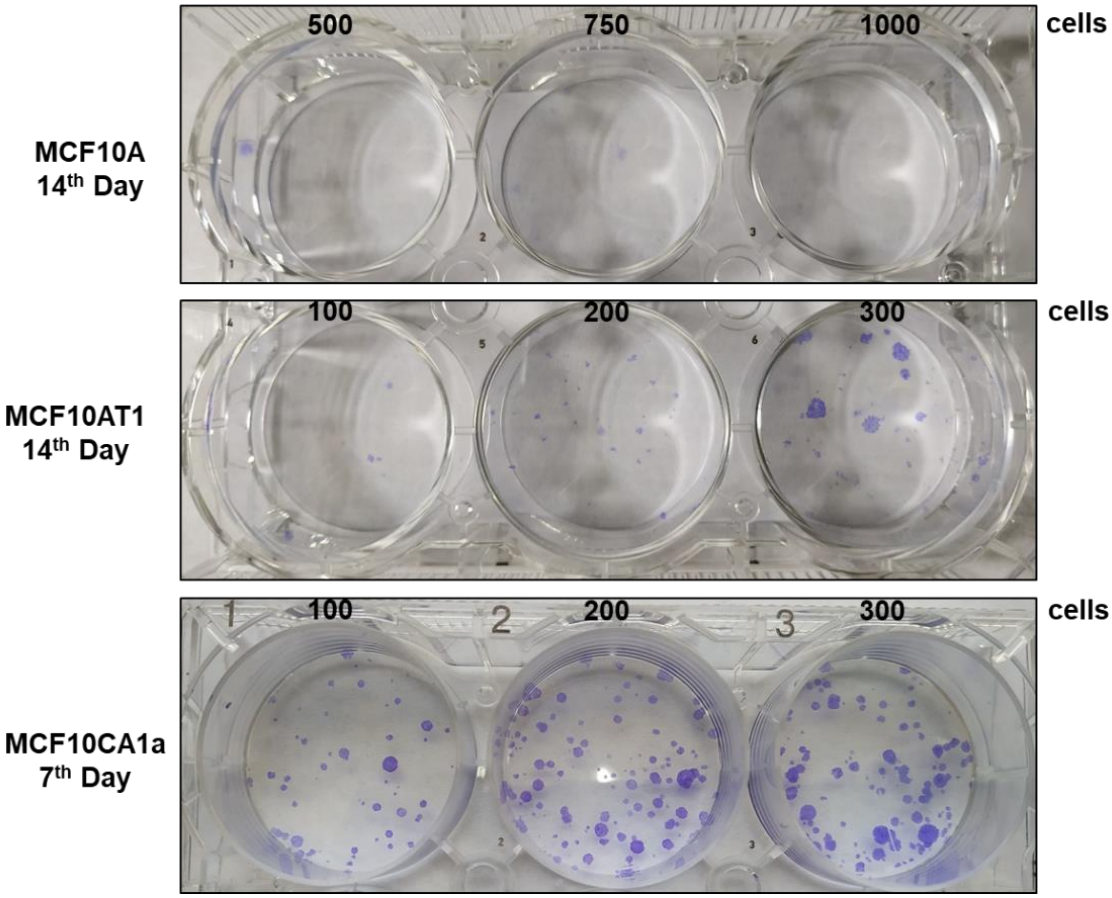


Figure 4.9: Colony formation assay in MCF10A series- Crystal violet stained colonies of MCF10A, MCF10AT1 and MCF10CA1a cells grown on cell culture treated 6 well plates for various days.

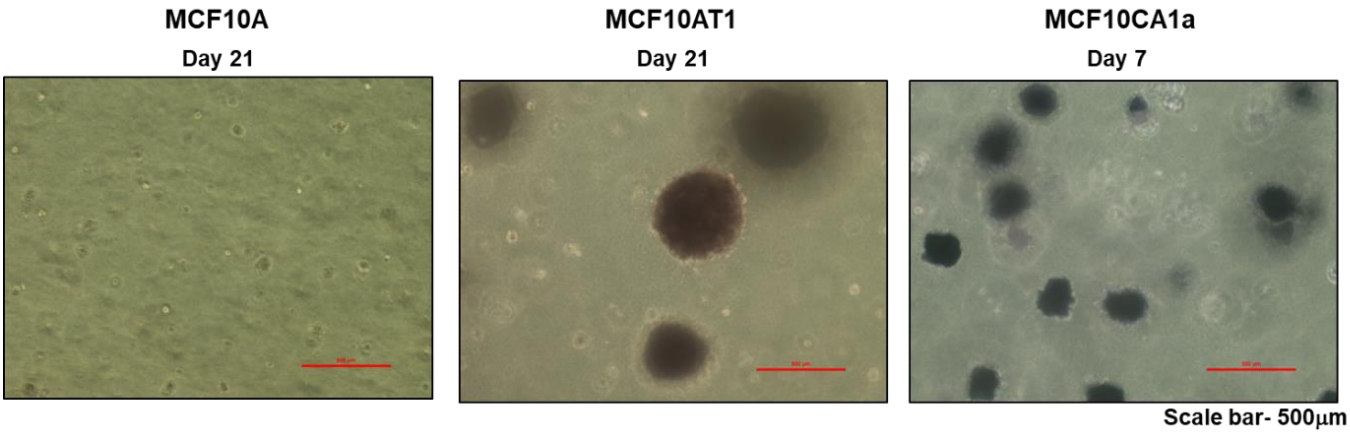


Figure 4.10: Anchorage-independent growth in MCF10A series- MTT stained colonies of MCF10A, MCF10AT1, and MCF10CA1a cells were grown on agar coated 35 mm dishes for various days. Images were acquired in ECLIPSE TS100 Nikon microscope at 10X magnification (scale bar-500 μm).

4.3 Summary

TopBP1 levels were high in premalignant and malignant cell lines of MCF10A cancer progression series compared to non-transformed MCF10A. These results are similar to what has been observed in breast cancer patient samples, where higher levels of TopBP1 is observed in tumour tissues compared to normal. We also observed that MCF10CA1a cells had endogenous DNA damage and altered DNA damage response activation compared to MCF10A cells. This altered activation may be because of higher TopBP1 levels as TopBP1 is a mediator protein involved in ATR activation and thus checkpoint response. Various EMT properties of MCF10A series cells were also investigated. We observed that MCF10CA1a cells had higher levels of epithelial markers and lower levels of mesenchymal markers. However, MCF10CA1a cells had higher collective cell migration compared to MCF10A and MCF10AT1. These cells also had colony-forming ability in anchorage-independent conditions.

Chapter 5

Role of TopBP1 in cellular transformation

5.1 Background

In chapter 3, we found that TopBP1 levels are in breast cancer patients, and higher levels are associated with reduced patient survival. In chapter 4, we found that TopBP1 levels are high in malignant and premalignant cell lines of MCF10A cancer progression series, and these cells have altered DNA damage response activation and EMT expression. These results suggest a robust positive correlation between TopBP1 expression and breast cancer. However, no studies are elucidating the role of TopBP1 in transformation and breast tumorigenesis. We decided to investigate the role of TopBP1 in transformation using 3 dimensional (3D) cultures as a model system.

Mouse models and primary tumour tissues are the most widely used models to study breast cancer. However, it is challenging to study the biochemical pathways involved in tumour formation using these models (Debnath and Brugge, 2005; Debnath et al., 2003). On the other hand, the monolayer cultures (2D) used to study the underlying mechanism in the oncogenic transformation does not recapitulate the three-dimensional (3D) breast glandular structure. In this scenario, 3D cultures of epithelial cells that reproduce the *in-vivo* glandular architecture serve as a physiologically relevant model to study breast tumorigenesis (Hebner et al., 2008).

The functional unit of a mammary gland, the acini, is composed of two cell layers: secretory cells with microvilli in the inner luminal layer, which secrete milk covered by a layer of contractile myoepithelial cells whose contraction helps in the ejection of milk to the ducts (Vidi et al., 2013). These acini have centrally located hollow lumen surrounded by a layer of polarised cells (Hebner et al., 2008). The 3D acini formed *in-vitro* when grown on externally provided extracellular matrix (ECM) recapitulates these structural features of acini in the mammary gland (Debnath et al., 2003) (Figure 5.1)

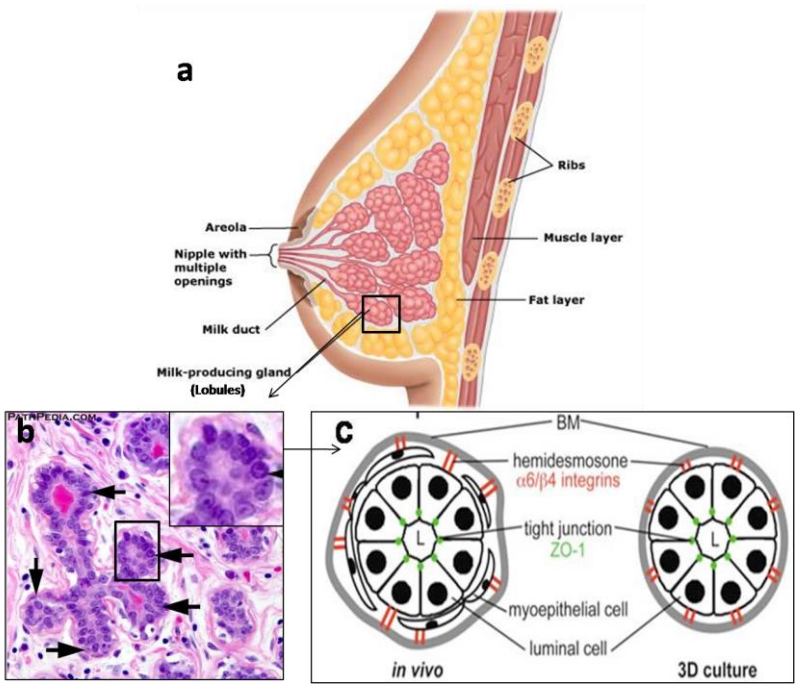


Figure 5.1: Anatomy of the mammary gland- a) Schematic diagram of the mammary gland with different lobules connecting to nipple **b)** Immunohistochemical staining of a section of the lobule. **c)** Comparison of acini in mammary gland and acini formed in 3D culture. (Adapted from Vidi et al., 2013)

MCF10A cells (mammary non-tumorigenic epithelial cell lines) have been primarily used to study the morphogenesis of breast epithelial cells. A single MCF10A cell seeded on an extracellular matrix (ECM; commercially available as Matrigel®) will proliferate and polarise to form a growth-arrested 3D acinus by day 16 (Figure 5.2). Reduced proliferation of MCF10A 3D acini after 16 days of morphogenesis, a distinguishing feature of *in-vivo* glandular epithelial, is of immense experimental value. It helps to investigate the role of oncogenes in morphogenesis MCF10A (Debnath et al., 2003). Previous studies have shown that polarised MCF10A acinar structure can be disrupted by mutations in a single or multiple gene (Chen et al., 2010; Guo et al., 2010; Henry et al., 2011). Various mutations can lead to different acinar morphologies like acini with filled lumen, multiple lumens, and protrusion like phenotype suggesting EMT (Figure 5.7). For example, mutations that induced overexpression of BCL2 (an apoptotic inhibitor) and reduction of BIM (a pro-apoptotic protein) resulted in the formation of acini with filled lumen phenotype (Debnath et al., 2002; Reginato et al., 2005). Multi acinar

structures with filled lumen are formed by ERBB2 (an oncoprotein) activation (Debnath et al., 2002). De-regulation of ERK and matrix metalloproteinase (MMP) activation promotes acini formation with protrusion-like phenotype indication EMT (O'Brien et al., 2004). These acini phenotypes resemble the architectural disorders of the mammary gland during various stages of breast cancer (Debnath & Brugge, 2005). These key features make the 3D culture system a good model for studying the role of a gene(s) in tumorigenesis.

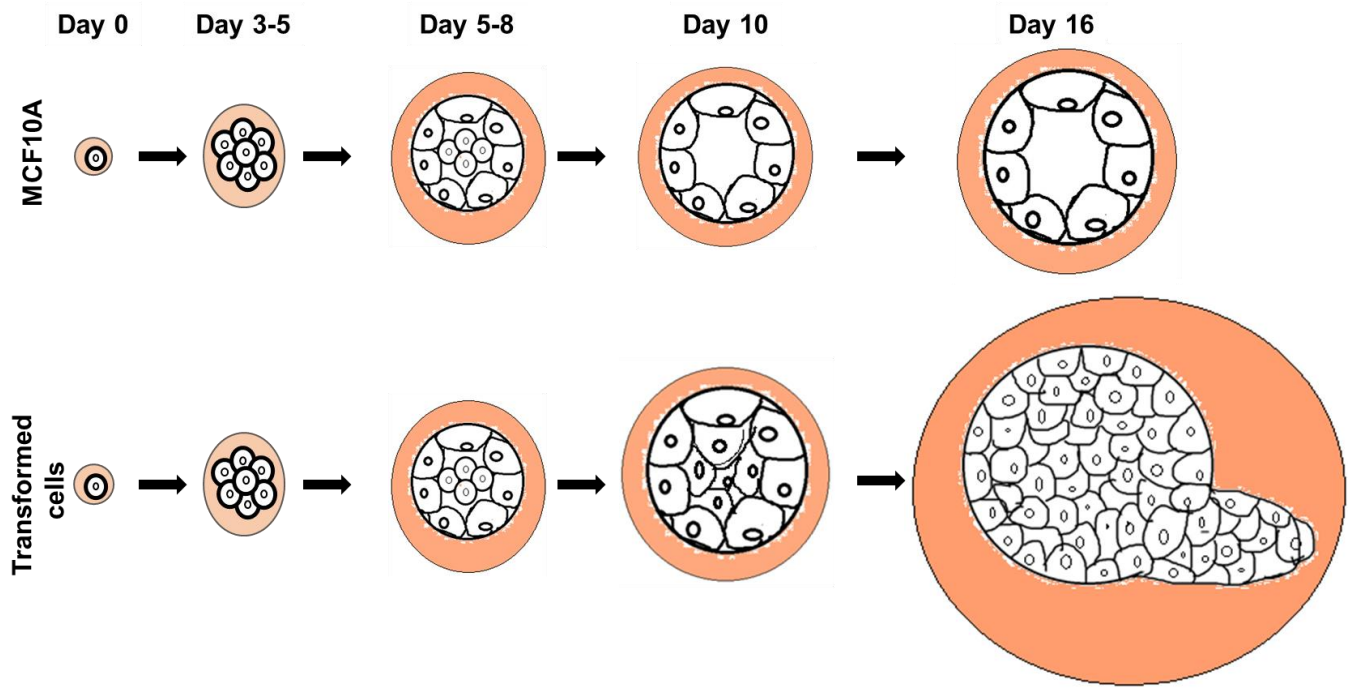


Figure 5.2: Schematic showing morphogenesis of MCF10A and transformed cells when grown on Matrigel- Image adapted from (Debnath & Brugge, 2005; Debnath et al., 2002; Debnath et al., 2003)

5.2 Results

5.2.1 Generation of stable cell line with TopBP1 over-expression in MCF10A and knockdown in MCF10AT1 and MCF10CA1

TOPBP1 gene along with mCherry fluorescent tag was cloned into CSII-EF-MCS lentiviral vector. HEK293T cells were transfected using mCherry-CSII-EF-MCS-TopBP1 clone along with the lentiviral packaging plasmids pCMV-VSV-G-RSV-Rev and pCAG-HIVgp by lipofectamine for lentiviral production. mCherry fluorescence was observed in HEK293T cells 24 hours post-transfection (Figure 5.3a). The viral supernatant obtained was used to transduce MC10A cells to generate stable MCF10A cell line expressing TopBP1-mCherry. Control MCF10A cells transduced with mCherry showed fluorescence after 48 hours of transduction, and the cells transduced with TopBP1-mCherry showed faint fluorescence in the nucleus (Figure 5.3b).

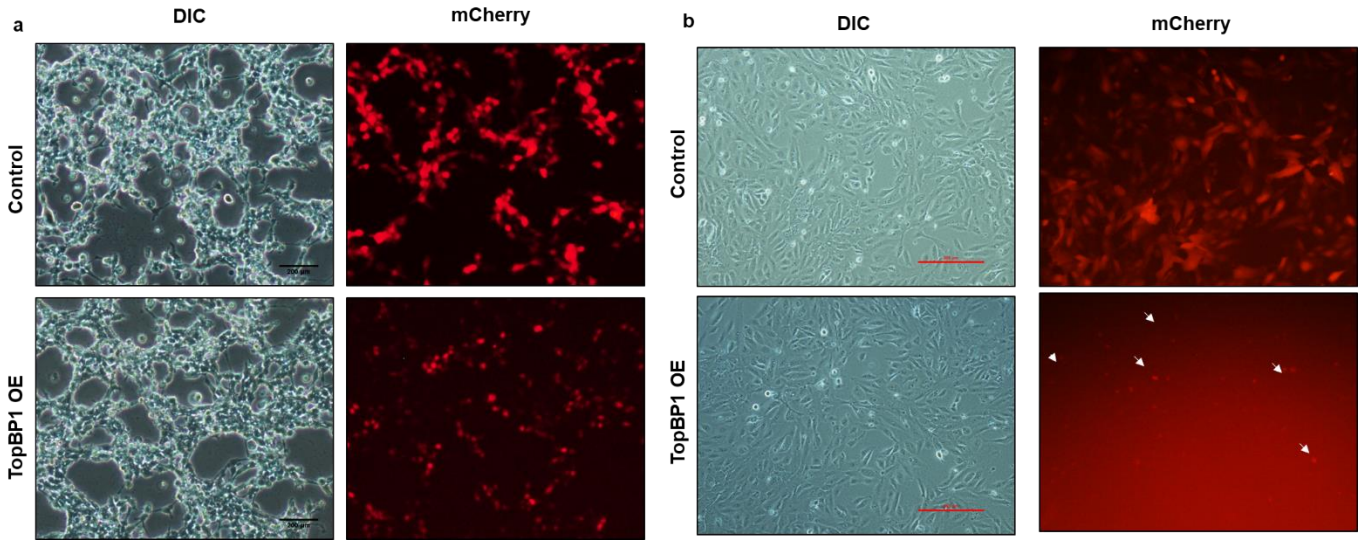


Figure 5.3: Expression of TopBP1-mCherry in MCF10A cells- a) Representative image of mCherry fluorescence in HEK293T cells transfected with mCherry or mCherry-TopBP1 for lentiviral generation. **b)** mCherry fluorescence in MCF10A cells transduced with the generated lentiviral particles. Images were acquired in ECLIPSE TS100 Nikon microscope at 10X magnification (scale bar-200 µm for a and 500 µm for b).

To obtain a pure population of MCF10A cells expressing TopBP1 mCherry, the cells with mCherry fluorescence were sorted using FACS, and these sorted cells were used

for further experiments. TopBP1 over-expression in the sorted cells was confirmed using immunoblotting and immunofluorescence assay (Figure 5.4)

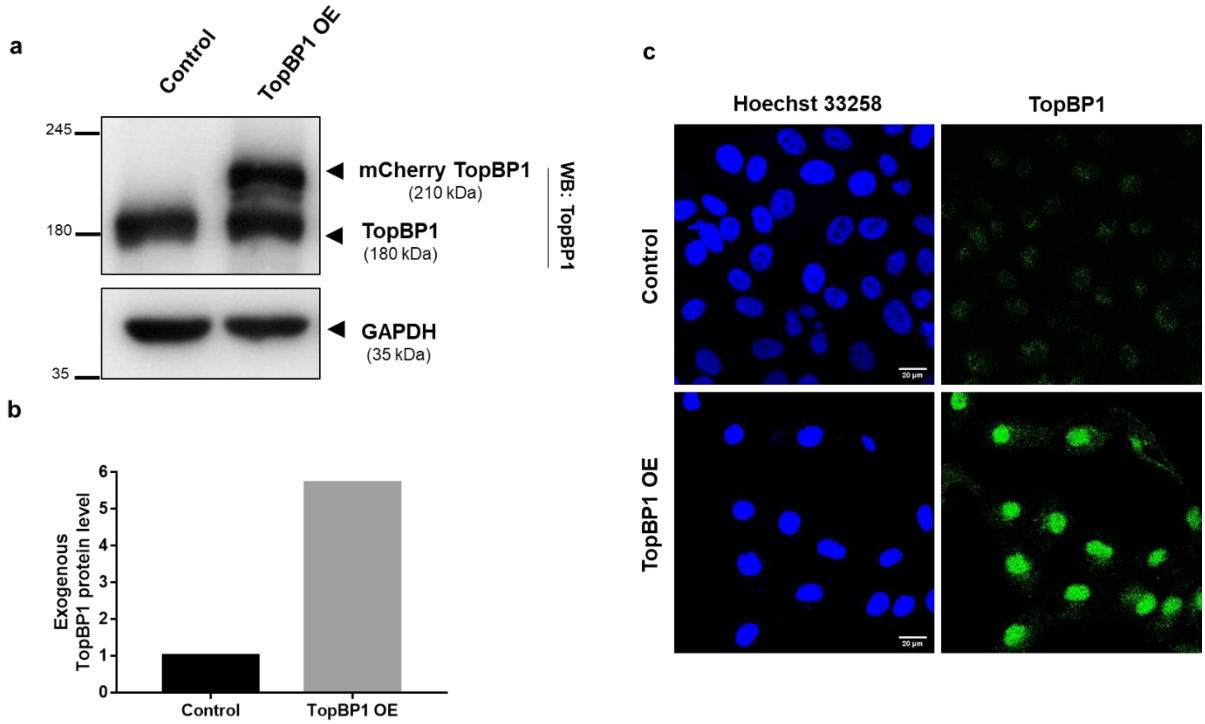


Figure 5.4: TopBP1 over-expression in MCF10A cells- MCF10A cells stably expressing mCherry and TopBP1 OE were A) lysed, and immunoblotting was performed using TopBP1 specific antibody. B) The fold change of exogenous TopBP1 was quantified after normalising with GAPDH. C) mCherry and TopBP1 OE MCF10A cells were immunostained using TopBP1 specific antibody to confirm the over-expression (scale bar-20 µm).

TopBP1 expression was found to be high in MCF10AT1 and MCF10CA1a cell lines which are premalignant and malignant, respectively (Figure 4.1). So, knockdown of TopBP1 in MCF10CA1a should revert (at least partially) the transformed phenotype if it has any role in transformation. For generating TopBP1 knockdown MCF10AT1/or MCF10CA1a cell line, shTopBP1 oligos were cloned into the lentiviral mediated knockdown vector, plko.1. puro. pLKO1.TRC vector was utilised for cloning (Figure 5.5a), and shTopBP1 oligos were designed according to pLKO1.TRC cloning strategy from Addgene (Figure 5.5b).

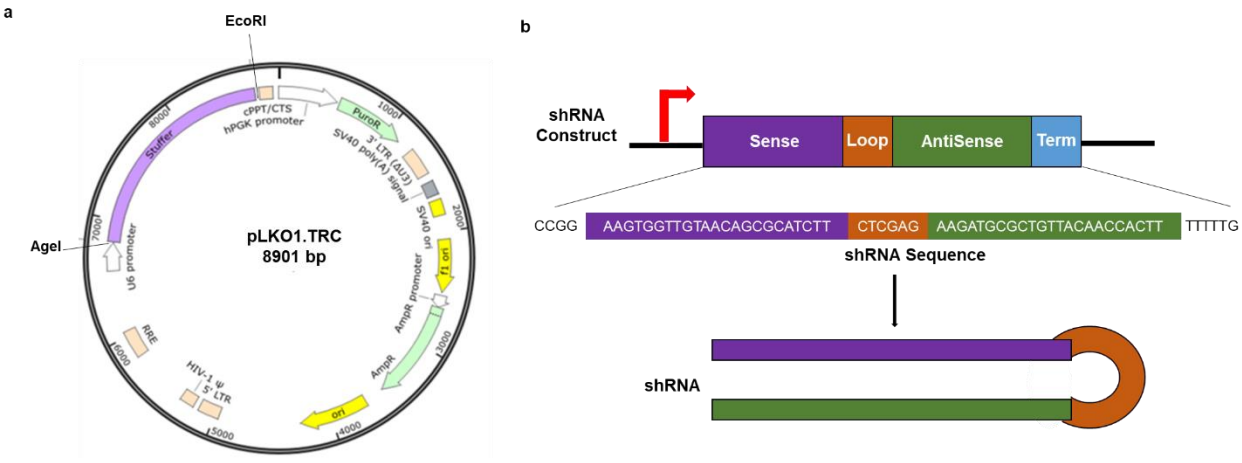


Figure 5.5: Cloning of shTopBP1 into pLKO.1.TRC lentiviral vector -a) pLKO.1.TRC vector map with restriction sites for cloning highlighted**. b)** Schematic demonstrating the designing of shTopBP1 oligos

pLKO1 TRC vector was digested with EcoRI and AgeI restriction enzymes (Figure 5.6a), and the 7 kb fragment was excised and gel extracted. The shTopBP1 oligos were annealed and ligated to the digested vector. The clones obtained were screened using XhoI digestion (Figure 5.6b). shTopBP1 clones #1 and #2 showed a release band of the expected size. To find whether the obtained clones have efficient TopBP1 knockdown, HEK293T cells were transfected with the shTopBP1 clone#1, and TopBP1 levels were checked using western blotting. Reduction in TopBP1 levels was observed in HEK293T cells transfected with shTopBP1 compared to cells transfected with pLKO1.TRC empty vector (Figure 5.6c). These clones were used for lentiviral production and stable cell line preparation. HEK293T cells were transfected using plko.1.TRC.shTopBP1 clone or empty vector along with its packaging plasmids pMd2 and pax2 by lipofectamine for lentiviral production. The viral supernatant obtained was used to transduce MCF10CA1a cells to generate stable cell lines. The cells with stable knockdown were selected using puromycin. TopBP1 knockdown in MCF10CA1a were confirmed using immunoblotting and immunofluorescence (Figure 5.7).

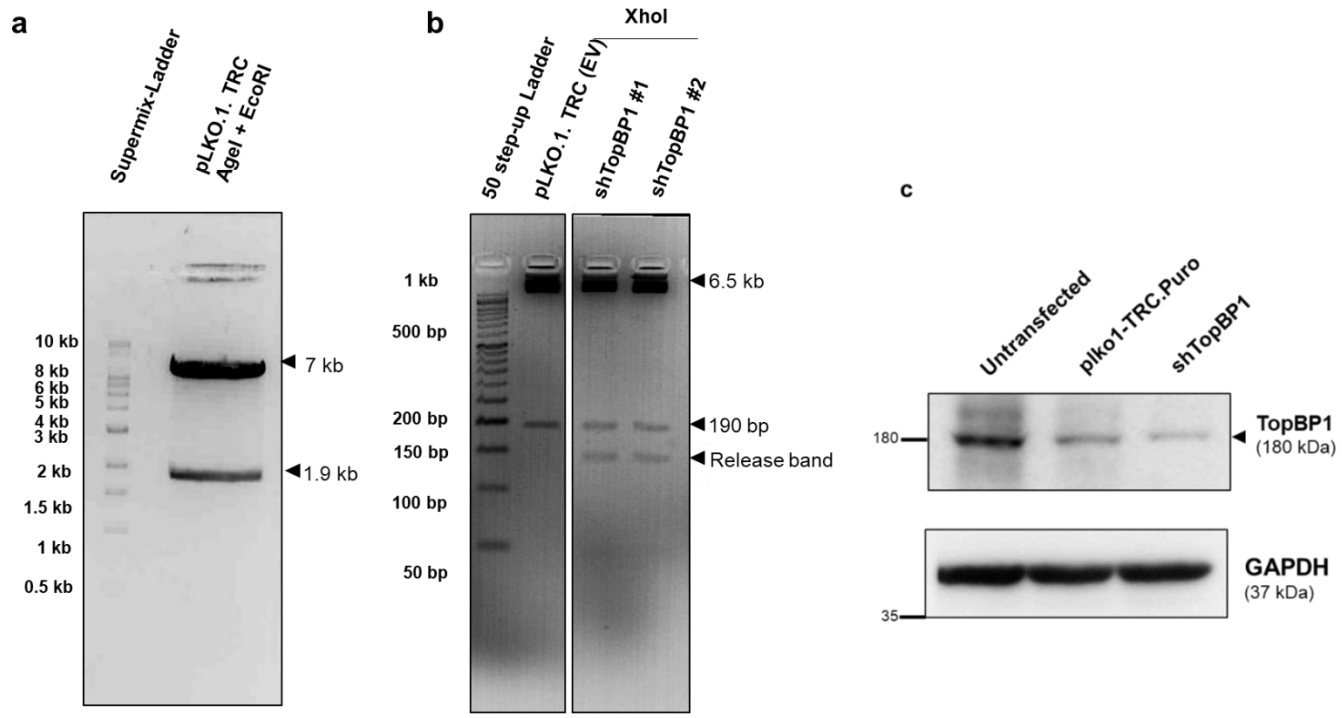


Figure 5.6: Cloning of shTopBP1 into pLKO.1.TRC lentiviral vector -a) Restriction digestion of pLKO.1.TRC using EcoRI and AgeI restriction enzymes. **b)** Screening of Clone#1 and Clone#2 by restriction digestion using XhoI (inverted images). **c)** Immunoblot analysis of shTopBP1 expression in HEK293T cells transfected with clone#1

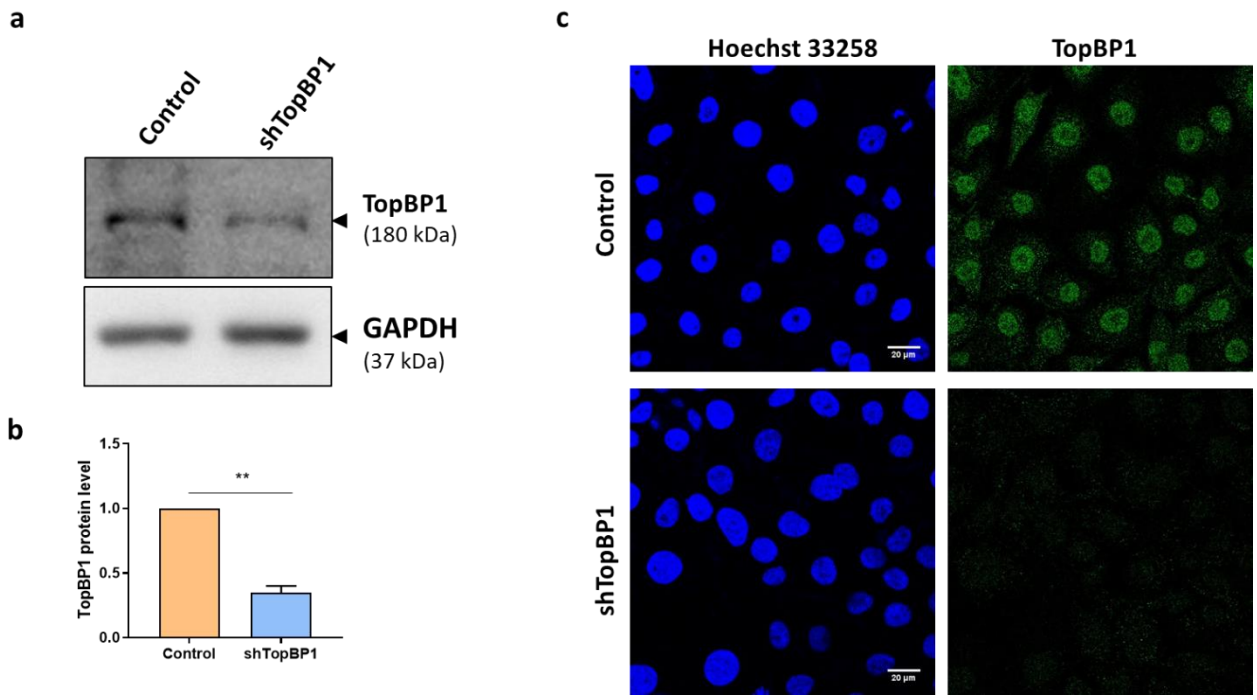


Figure 5.7: TopBP1 knockdown in MCF10CA1a- MCF10CA1a cells stably expressing pLKO1 and shTopBP1 were A) lysed, and immunoblotting was performed using TopBP1 specific antibody. B) The fold change of TopBP1 was quantified after normalising with GAPDH. Statistical analysis was done using t- test (** p <0.01). C) pLKO1 and shTopBP1 MCF10CA1a cells were immunostained using TopBP1 specific antibody to confirm the knockdown (scale bar-20 µm).

5.2.2. Investigation of phenotypic changes induced upon TopBP1 over-expression in MCF10A and TopBP1 knockdown in MCF10CA1a

MCF10A series cells were grown on Matrigel® for ten days to form 3D cultures. MCF10CA1a formed large spheres compared to MCF10A and MCF10AT1 (Figure 5.8a) on day 10. Interestingly, TopBP1 OE MCF10A cells, when grown on Matrigel®, formed large acini (Figure 5.8b). These 3D cultures were stained with Hoechst 33258. It was observed that TopBP1 OE MCF10A cells formed large spheroids with filled lumen similar to MCF10CA1a spheroids (Figure 5.9a- b). However, MCF10A and control mCherry- MCF10A had 3D cultures with clear lumen and monolayer of cells in the acini.

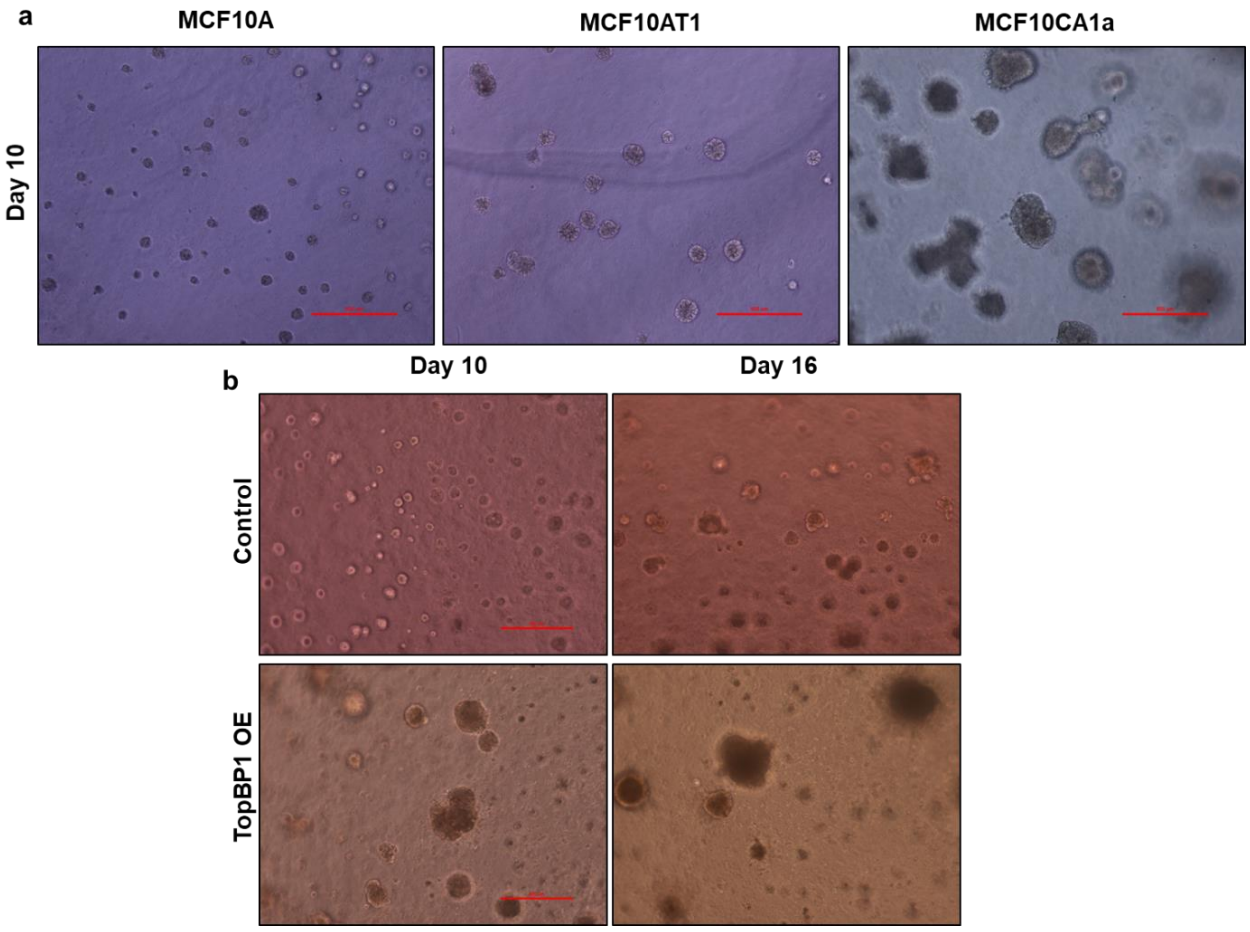


Figure 5.8: 3D culture of MCF10A series cells and TopBP1 OE MCF10A - Representative images of a) MCF10A, MCF10AT1 and MCF10CA1a and b) control and TopBP1 OE MCF10A cells grown on Matrigel® for 10/16 days. Images were acquired in ECLIPSE TS100 Nikon microscope at 10X magnification (scale bar-500 µm).

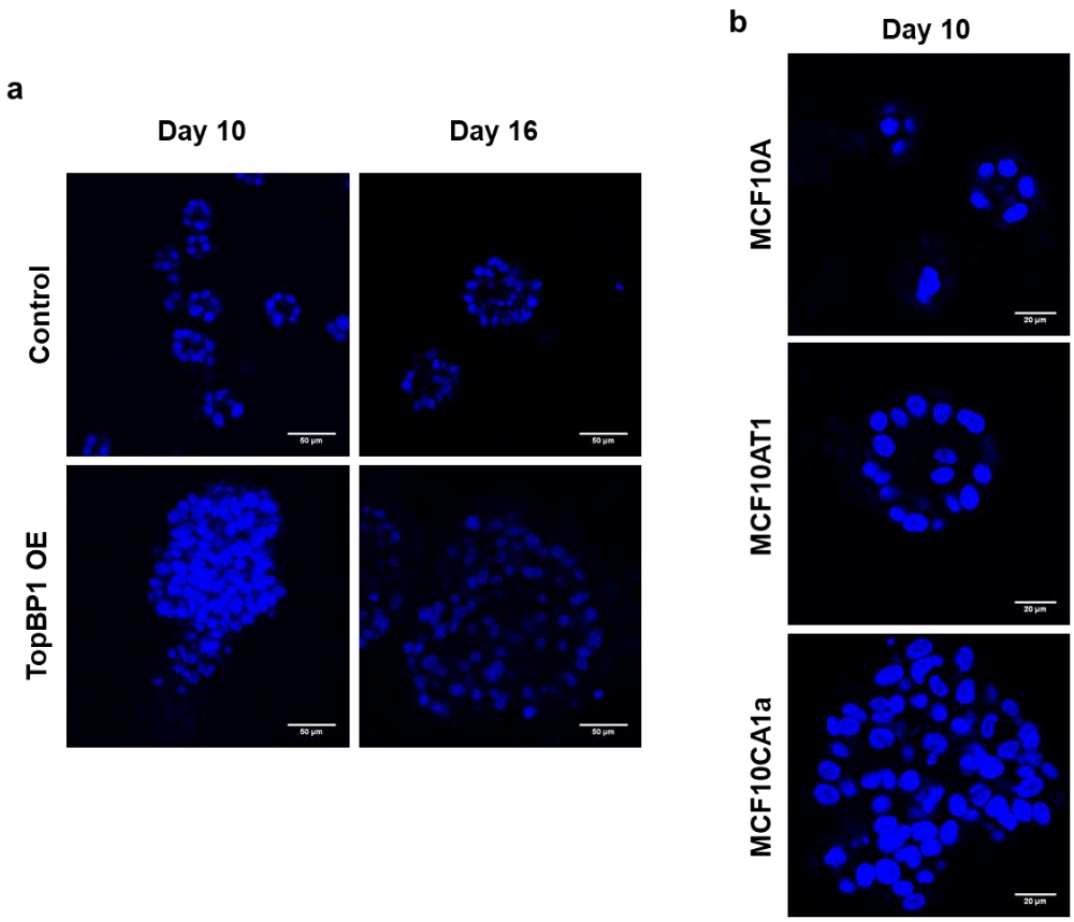


Figure 5.9: 3D culture of MCF10A series cells and TopBP1 OE MCF10A- Representative images of a) control and TopBP1 OE MCF10A and b) MCF10A, MCFAT1 and MCF10CA1a 3D acini stained with Hoechst 33258 nuclear staining dye. Images were acquired in a) Leica sp8 and b) Multiphoton Zeiss microscope at 40X magnification (scale bar-50 and 20 µm respectively).

TopBP1 OE MCF10A cells grown on Matrigel were dissociated using Dispase® and grown as monolayer cultures. Surprisingly, TopBP1 OE dissociated cells had morphology similar to MCF10CA1a (Figure 5.10)

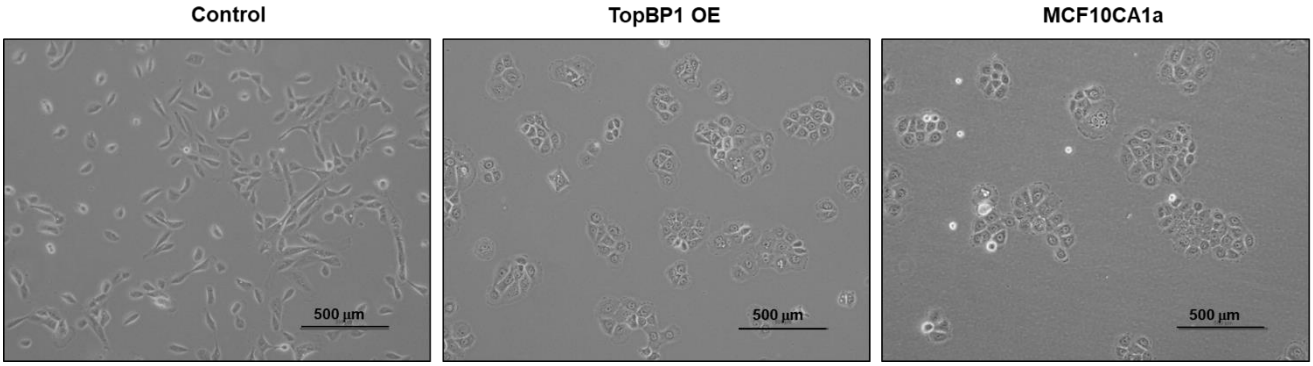


Figure 5.10: TopBP1 OE MCF10A dissociated cells resemble MCF10CA1a - Representative images of control and TopBP1 OE MCF10A dissociated cells and MCF10CA1a cells g. Images were acquired in ECLIPSE TS100 Nikon microscope at 10X magnification (scale bar-500 µm).

Investigation of phenotypic characteristics of 3D acini of MCF10A cells overexpressing TopBP1 and MCF10AT1/or MCFCA1a with TopBP1 knockdown will provide insights into the role of TopBP1 in the transformation of breast epithelial cells.

5.2.2.1. TopBP1 over-expression leads to increase in acinar size

Analysis of the cellular and nuclear pleomorphism and extent of the architectural disorder is the primary diagnostic and prognosis determination method for breast carcinoma (Debnath & Brugge, 2005). 3D cultures of breast epithelial cells and cancer cells recapitulate most of the features of cancer tissues *in-vivo*. Detailed analysis of these characteristic features can aid in ascertaining the role of perturbed genes. The TopBP1 OE MCF10A cells were grown on Matrigel® for 10 days, and the 3D acini formed were stained for Hoechst (nuclear marker) and Phalloidin and imaged in the confocal microscope. The TopBP1 OE acini, as mentioned before, had increased size and filled lumen compared to control (Figure 5.11a). The surface area, volume and sphericity of the acini were measured using Huygens (SVI). These acini's surface area and volume were significantly higher than the control acini (Figure 5.11b-c). MCF10A acini have a sphericity of 1 (Major diameter/minor diameter). The TopBP1 OE MCF10A 3D cultures had reduced sphericity compared to the control (Figure 5.11d).

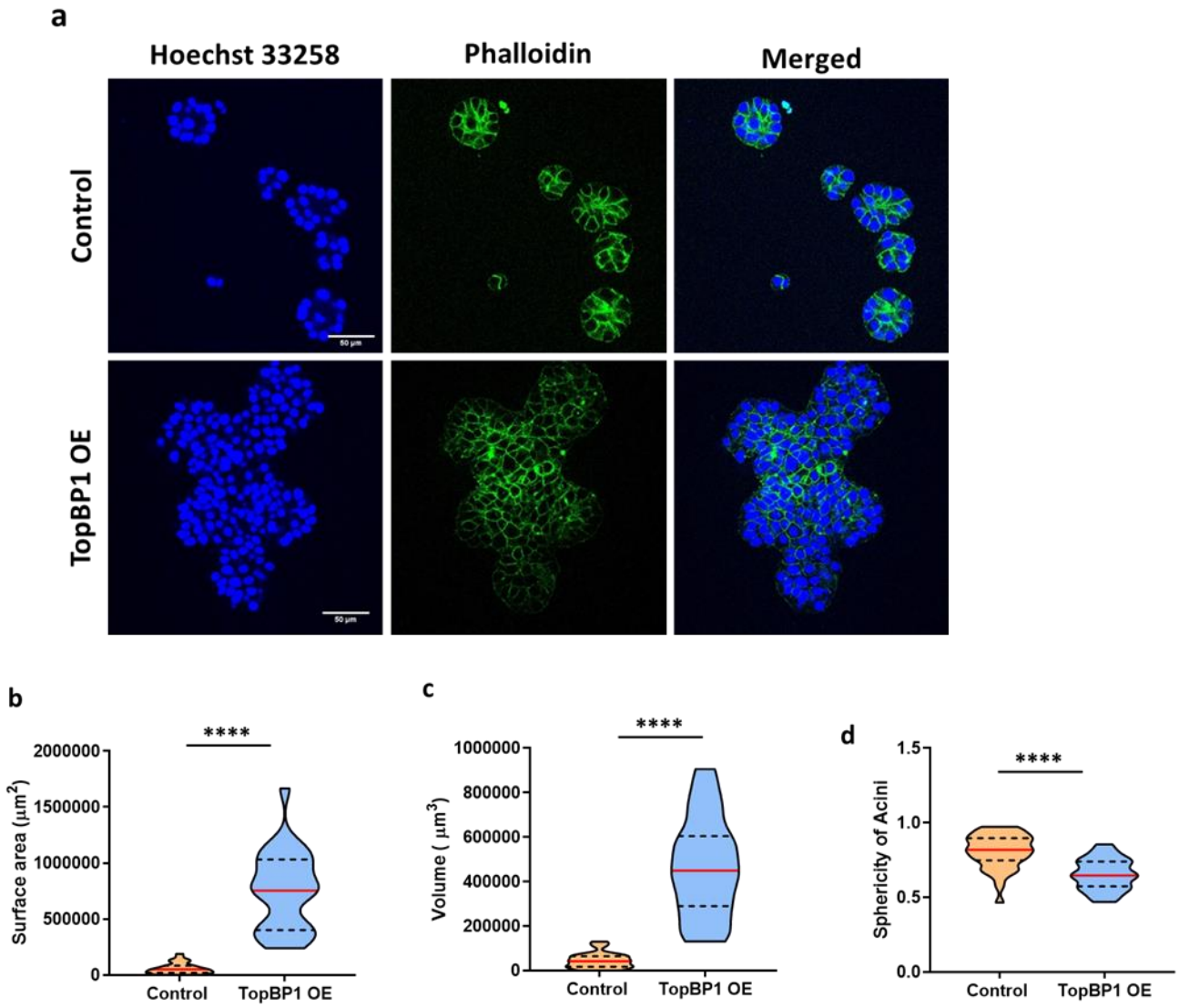


Figure 5.11-TopBP1 overexpression leads to increased acinar size in MCF10A 3D cultures- a) Representative images of mCherry or TopBP1 OE MCF10A cells grown as 3D “on-top” cultures for 10 days and fixed and stained for Phalloidin (green) and Hoechst 33258 (blue) (scale bar-50 µm). b) Surface area, c) volume, and d) sphericity of these acini were calculated using Hygans software and represented as box plots. >50 acini from 3 independent experiments were analysed. Statistical analysis was done using the Mann Whitney test (**** p <0.0001).

5.2.2.2. Overexpression of TopBP1 leads to increased proliferation

To find whether the increase in size upon TopBP1 OE in MCF10A was due to an increase in proliferation, the control and TopBP1 OE acini were stained using Ki67, a proliferation marker. It was observed that the percentage of acini with more than 33% Ki67 positive cells were high in TopBP1 OE compared to control (Figure 5.12a). Also, we found a similar increase in Ki67 in MCF10CA1a spheroids (Figure 5.12a). Increased levels of Ki67 was also observed in 3D cultures of TopBP1 OE and MCF10CA1a using immunoblotting compared to control lysates (Figure 5.12b-c). These results suggest that TopBP1 regulates the proliferation of cells in 3D cultures. TopBP1 OE dissociated cells also exhibited higher proliferation compared to control (Figure 5.13a). This increase in proliferation can be because of the increased number of cells in the S and G2-M phases of the cell cycle. To find the number of cells in each cell cycle phase, the cell cycle profile of MCF10CA1a, control and TopBP1 OE cells was analysed using propidium iodide (PI) staining. It was observed that TopBP1 OE and MCF10CA1a cells had more percentage of cells in S and G2-M phase compared to control (Figure 5.13b). We also analysed PCNA and Cyclin A levels, which are S phase markers, and found that the PCNA and Cyclin A levels were higher in TopBP1 OE cells than control, and a similar pattern was observed in MCF10CA1a (Figure 5.14). These results conclude that TopBP1 OE leads to increased proliferation.

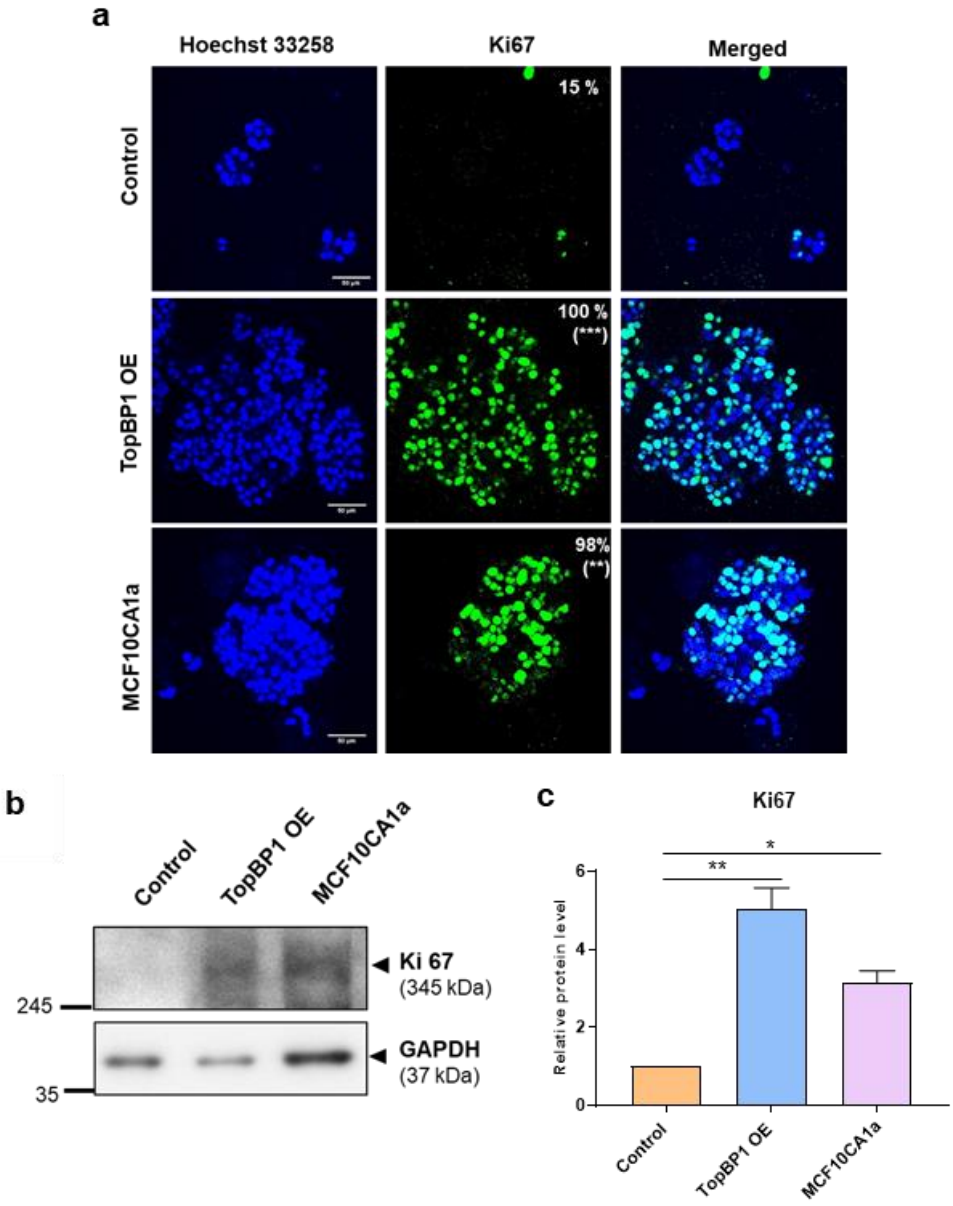


Figure 5.12: Ki67 positive cells in TopBP1 OE and MCF10CA1a 3D cultures- a) Representative images of mCherry, TopBP1 OE MCF10A and MCF10CA1a cells grown as 3D cultures for 10 days and fixed and immunostained for Ki67 (green) (scale bar-50 µm). Statistical analysis was done using Mann Whitney test (**** p <0.0001). b) 16-day 3D cultures of mCherry MCF10A and TopBP1 OE MCF10A and 10-day 3D cultures of MCF10CA1a were lysed, and immunoblotting was performed using Ki67 specific antibody. c) Quantification showing the fold change of Ki67 after normalising with GAPDH. Statistical analysis was done using One way ANOVA (* p <0.5, ** p <0.01)

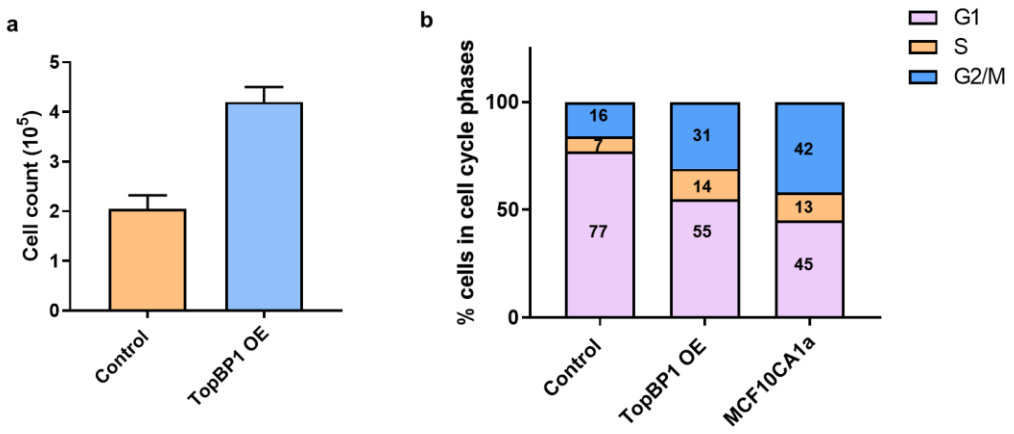


Figure 5.13-TopBP1 overexpression increase proliferation- a) mCherry MCF10A and TopBP1 OE MCF10A 3D dissociated cells and MCF10CA1a cell number was counted using Scepter 72 hrs post-seeding. b) mCherry MCF10A and TopBP1 OE MCF10A 3D dissociated cells, and MCF10CA1a cells were fixed in ethanol and stained using propidium iodide. Percentage of cells in the different cell cycle phases were analysed in a flow cytometer and plotted as box plots.

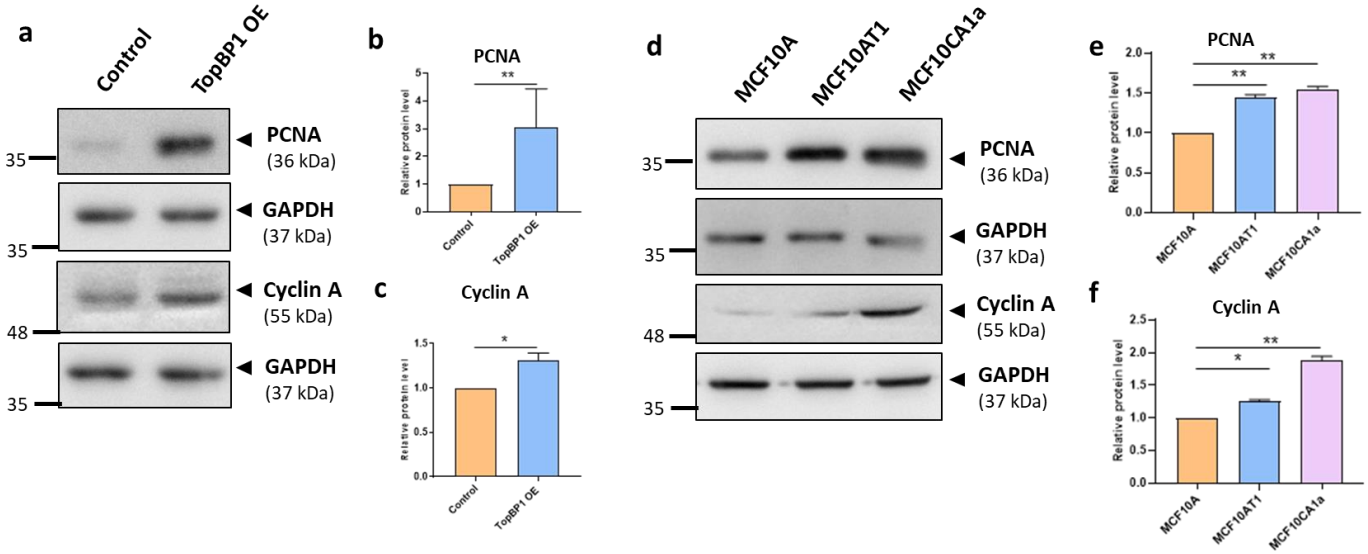


Figure 5.14-TopBP1 overexpression leads to an increase in S phase markers- mCherry MCF10A and TopBP1 OE MCF10A 3D dissociated cells, and MCF10A, MCF10AT1 and MCF10CA1a cells were lysed, and immunoblotting was performed to analyse the levels of a-b and d-e) PCNA and a-c and d-f) Cyclin A. Quantification

showing the fold change after normalising with GAPDH. Statistical analysis was done using t-test (* p <0.5, ** p <0.01)

5.2.2.3. TopBP1 over-expression disrupts polarity

De-regulation of apicobasal polarity is one of the characteristics of epithelial cancer (Debnath & Brugge, 2005). To investigate the effect of TopBP1 over-expression on basal polarity, TopBP1-OE cells grown on Matrigel® were stained using basal polarity markers like α6 integrin and Laminin V. Loss or discontinuous staining of α6 integrin (Figure 5.15), and Laminin V (Figure 5.16) at the basal region of acini and mislocalisation was observed in TopBP1 OE acini. These phenotypes were similar to that was observed in MCF10CA1a spheroids (Figure 5.15 and 5.16)

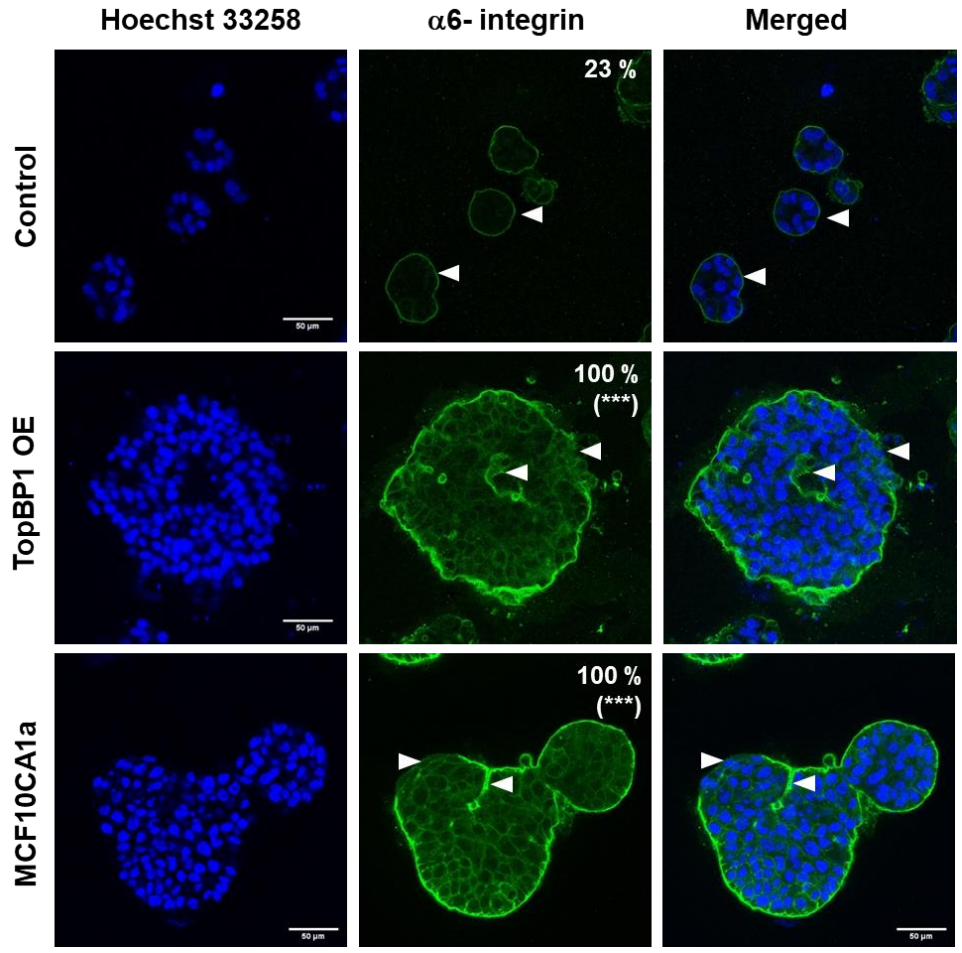


Figure 5.15: TopBP1 OE leads to disruption of α6-integrin - Representative images of mCherry, TopBP1 OE MCF10A and MCF10CA1a cells grown as 3D cultures for 10 days fixed and immunostained for α6-integrin. Images were acquired in Leica sp8 at 40X magnification (scale bar-50 µm). Statistical analysis was done using Mann Whitney test (**** p <0.0001)

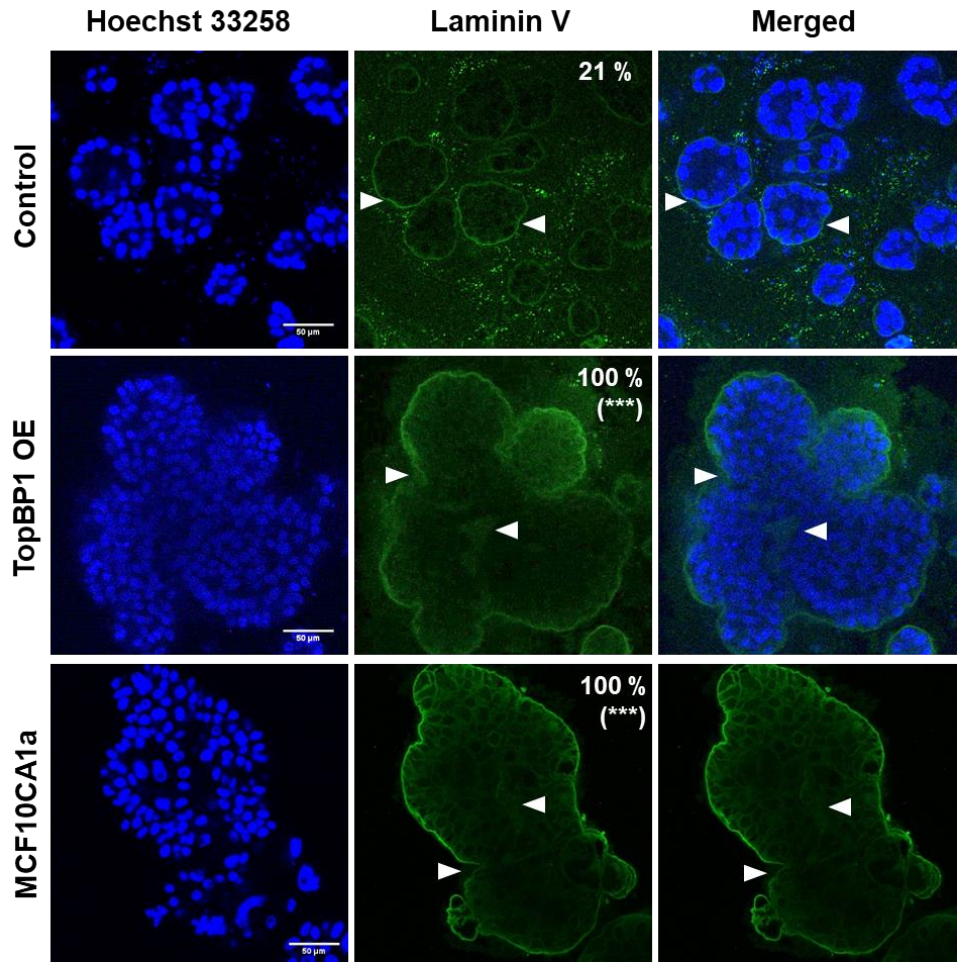


Figure 5.16: TopBP1 OE leads to disruption of laminin V- Representative images of mCherry, TopBP1 OE MCF10A, and MCF10CA1a cells grown as 3D cultures for 10 days fixed and immunostained for Laminin V. Images were acquired in Leica sp8 at 40X magnification (scale bar-50 µm). Statistical analysis was done using Mann Whitney test (**** p <0.0001)

Golgi is apically located in MCF10A 3D cultures and is thus known as an apical polarity marker. TopBP1 OE acini were stained with GM130, a cis-Golgi marker, to understand

the role of TopBP1 in apical polarity. It was observed that TopBP1 OE acini had dispersed Golgi architecture compared to the compact apically located Golgi in the control acini (Figure 5.17). Golgi dispersal was further confirmed by staining the 3D dissociated TopBP1 OE cells using GM130. The TopBP1 OE cells also had dispersed Golgi similar to the MCF10CA1a cells (Figure 5.18a), further quantified by measuring the Golgi area (Figure 5.18b).

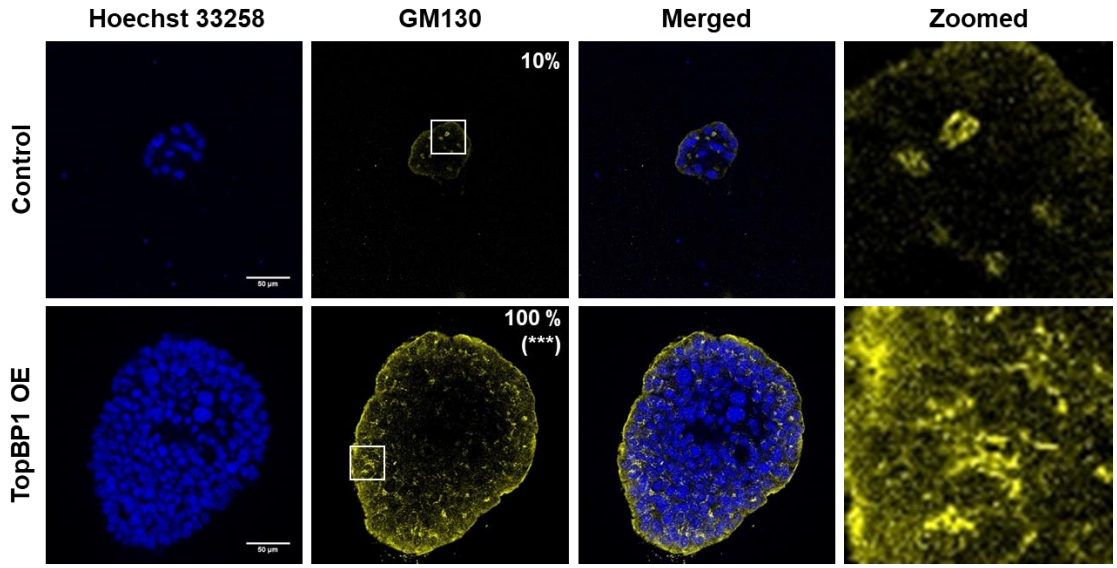


Figure 5.17: TopBP1 OE leads to Golgi dispersal in MCF10A 3D cultures- Representative images of mCherry and TopBP1 OE MCF10A cells grown as 3D cultures for 10 days fixed and immunostained for GM130. Images were acquired in Leica sp8 at 40X magnification (scale bar-50 µm). Statistical analysis was done using Mann Whitney test (**** p <0.0001)

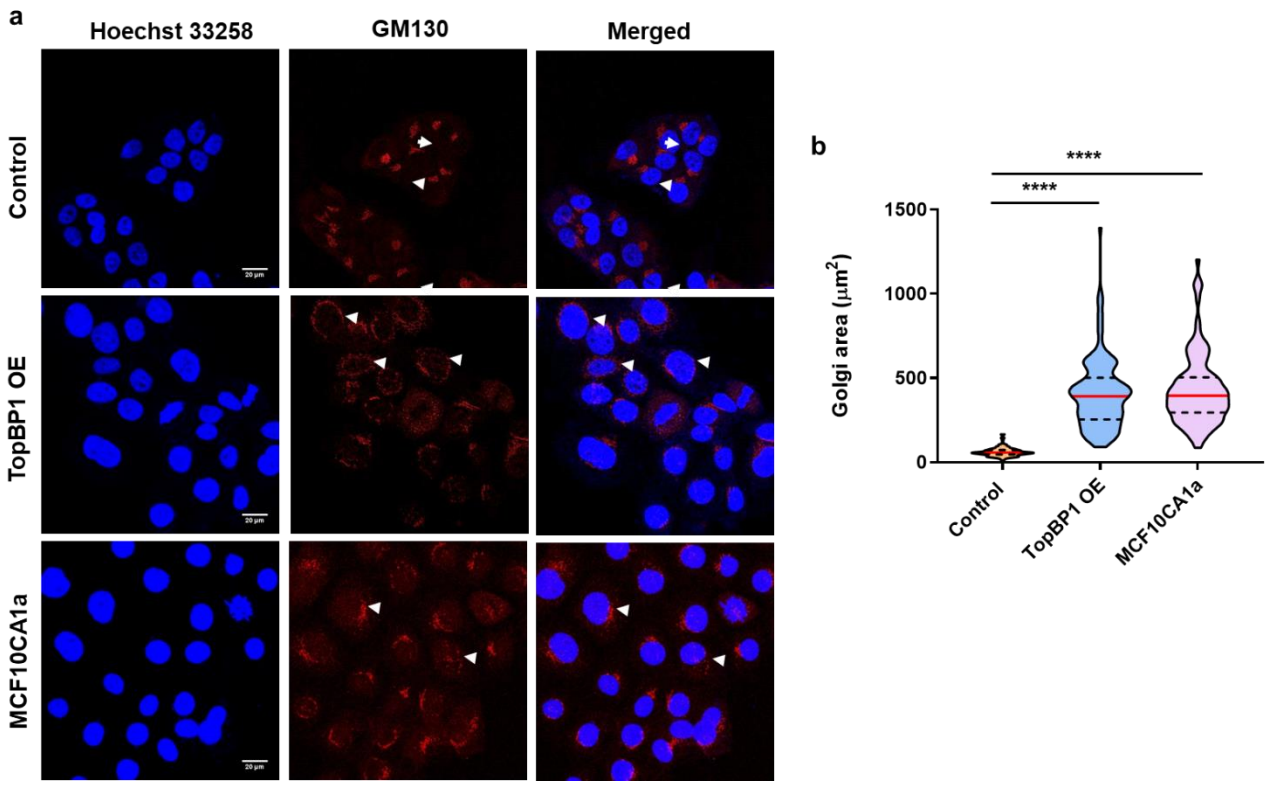


Figure 5.18: Golgi dispersal in TopBP1 OE dissociated cells and MCF10CA1a cells- a) mCherry MCF10A and TopBP1 OE MCF10A 3D dissociated cells and MCF10CA1a cells were immunostained using GM130, Golgi marker and b) Golgi dispersal was calculated by measuring Golgi area using ImageJ software. Images were acquired in Leica sp8 at 63X magnification (scale bar-20 μm). Statistical analysis was done using One-way Anova (**** $p < 0.0001$)

TopBP1 OE acini had dispersed/speckle-like staining of β catenin compared to control acini, similar to MCF10CA1a spheroids (Figure 5.19). These results suggest that TopBP1 OE disrupts the polarity of MCF10A acinar cultures.

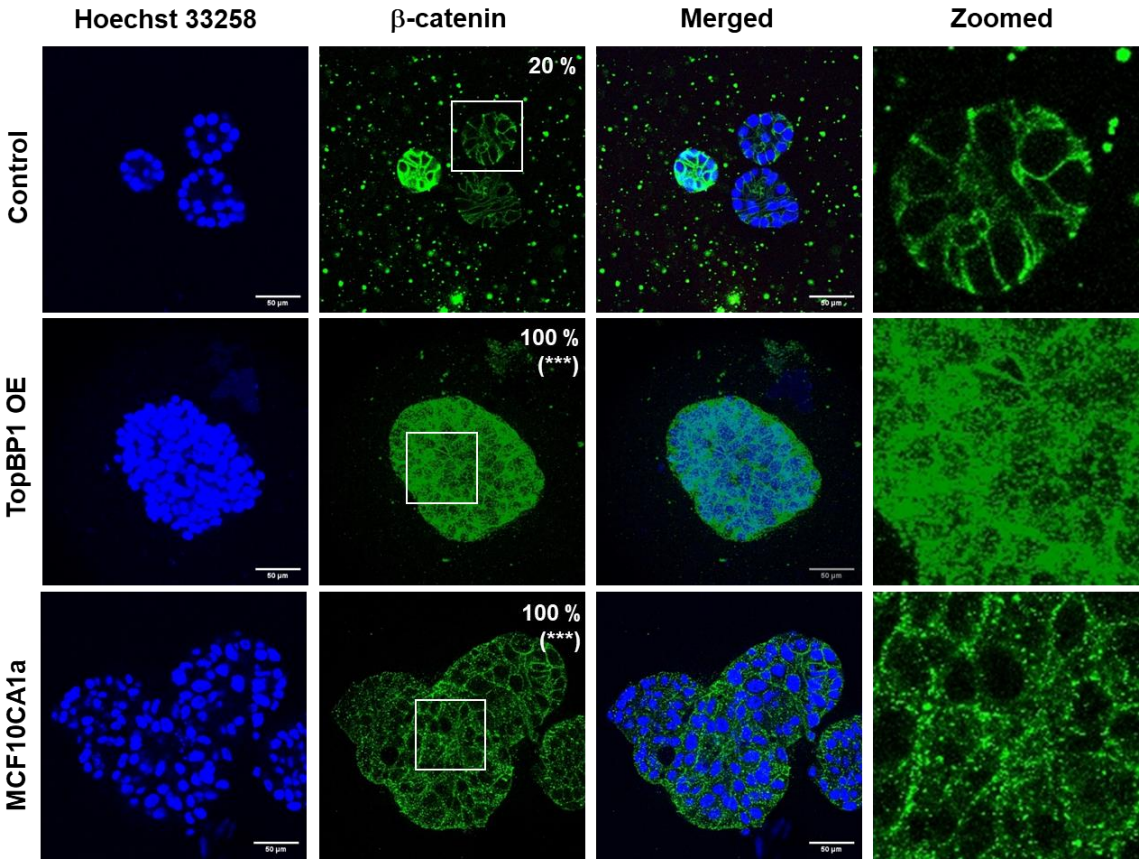


Figure 5.19: TopBP1 OE leads to the dispersal of β catenin in MCF10A 3D cultures- Representative images of mCherry and TopBP1 OE MCF10A cells grown as 3D cultures for 10 days and fixed and immunostained for β catenin. Images were acquired in Leica sp8 at 40X magnification (scale bar-50 µm). Statistical analysis was done using Mann Whitney test (**** p <0.0001)

5.2.2.4. Expression of EMT markers in TopBP1 OE is similar to MCF10CA1a

Epithelial to mesenchymal transition (EMT) is a process through which epithelial cells de-differentiate and acquire mesenchymal phenotype that can increase their motility and invasiveness. To investigate the role of TopBP1 overexpression in EMT, the expression of various EMT markers was analysed. Levels of Vimentin, a well-known mesenchymal marker, was investigated in TopBP1 OE acini. It was observed that there were acini with varying vimentin expressions. 89% of TopBP1 OE acini had low levels of vimentin, whereas 100% of mCherry MCF10A acini had vimentin expression (Figure 5.20). Interestingly, MCF10CA1a 3D acini also had a higher percentage of acini (86%)

having lower levels of vimentin (Figure 5.20). The TopBP1 OE dissociated cells also exhibited heterogeneity in vimentin expression similar to MCF10CA1a cells (Figure 5.21a). Only 14% of TopBP1 OE cells and 26% of MCF10CA1a cells were vimentin-positive, whereas 100% of control cells were vimentin-positive (Figure 5.21b). The immunoblotting assay also confirmed that vimentin levels are low in TopBP1 OE cells compared to control, and these reduced vimentin levels were similar to the levels in MCF10CA1a cells (Figure 5.21c-d).

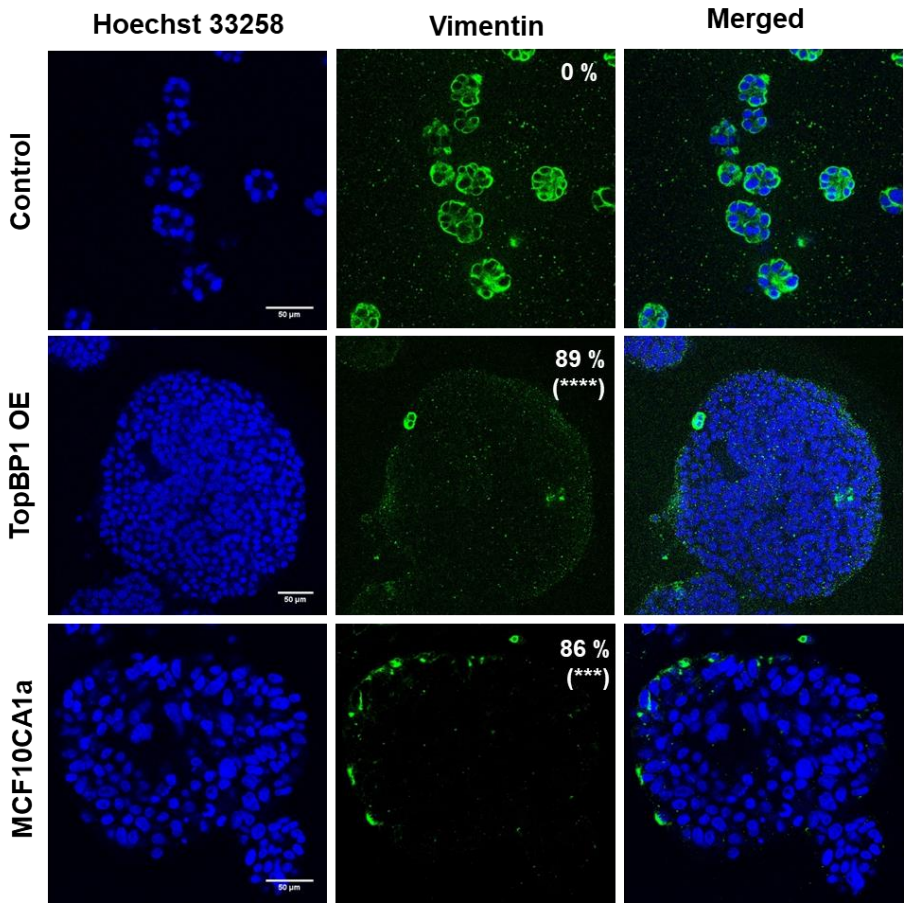


Figure 5.20: Vimentin levels in TopBP1 OE MCF10A 3D cultures- a) Representative images of control and TopBP1 OE MCF10A 3D acini showing vimentin staining counted and percentage of negative cells are written on the figure (scale bar-50 µm). Images were acquired in Leica sp8 at 40X magnification (scale bar-50 µm). Statistical analysis was done using Mann Whitney test (*** p <0.001, **** p <0.0001)

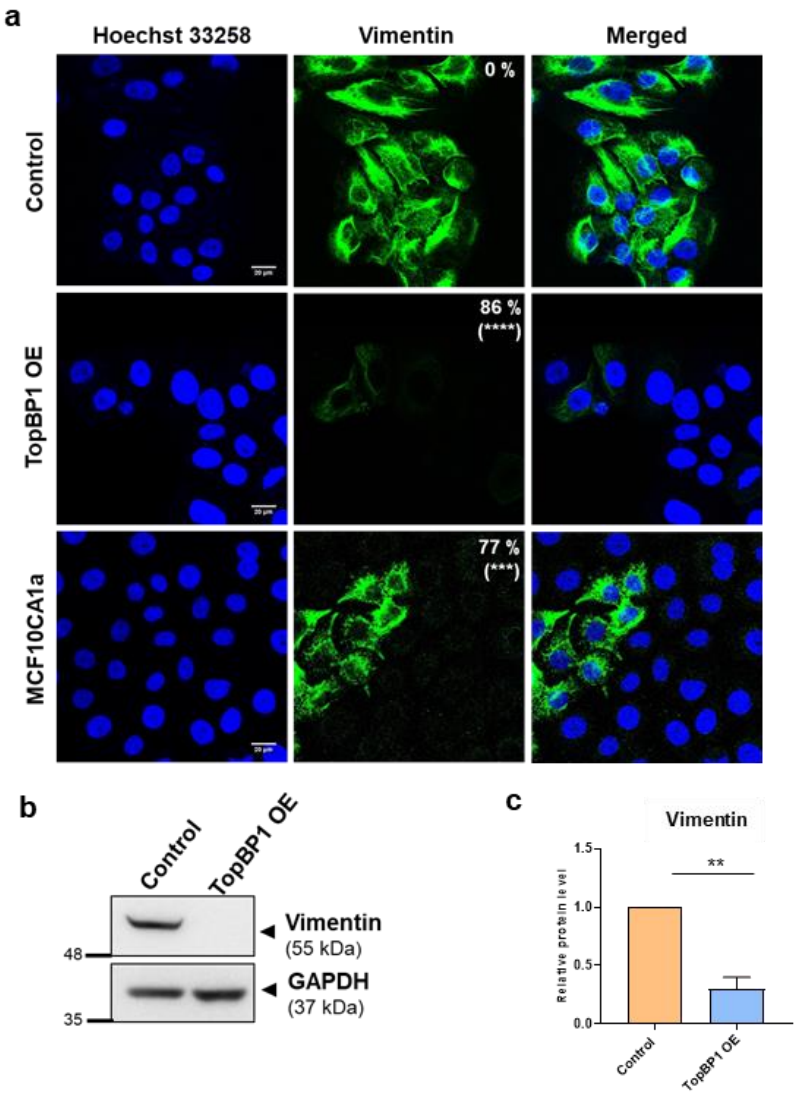


Figure 5.21: Vimentin levels in TopBP1 OE dissociated cells and MCF10CA1a cells- a) mCherry MCF10A and TopBP1 OE MCF10A 3D dissociated cells and MCF10CA1a cells were immunostained using vimentin and percentage of negative cells were written on the figure (scale bar-50 µm). Images were acquired in Leica sp8 at 40X magnification (scale bar-50 µm). Statistical analysis was done using Mann Whitney test (*** p <0.001, **** p <0.0001)**.** mCherry MCF10A and TopBP1 OE MCF10A 3D dissociated cells were lysed, and immunoblotting was performed to analyse the levels of c-d) vimentin. Quantification showing the fold change after normalising with GAPDH. Statistical analysis was done using t-test (** p <0.01)

The levels of E-cadherin and N-cadherin, epithelial and mesenchymal markers respectively, were analysed using the immunoblotting assay. TopBP1 OE cells had higher levels of E-cadherin and lower levels of N-cadherin compared to control (Figure 5.22). The higher levels of E-cadherin and lower levels of N-cadherin observed in TopBP1 OE was similar to MCF10CA1a (Figure 4.6).

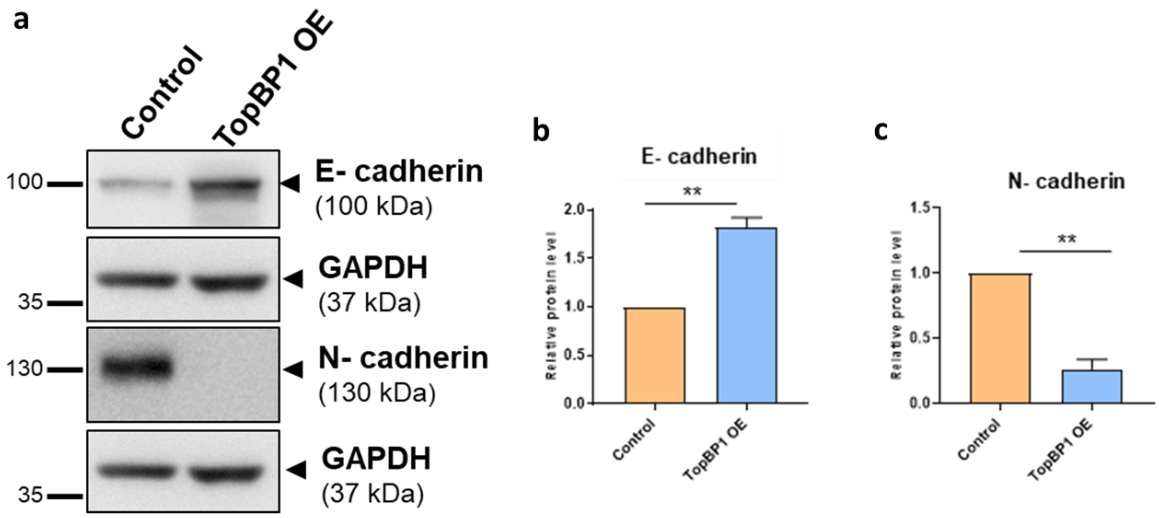


Figure 5.22: E-cadherin and N-cadherin levels in TopBP1 OE MCF10A- mCherry MCF10A and TopBP1 OE MCF10A 3D dissociated cells were lysed, and immunoblotting was performed to analyse the levels of a-b) E-cadherin and a-c) N-cadherin. Quantification showing the fold change after normalising with GAPDH. Statistical analysis was done using t-test (** $p < 0.01$)

Cell lysates of the TopBP1 OE cells were analysed to investigate the levels of various EMT markers like Slug and Twist. Slug levels were reduced in TopBP1 OE MCF10A 3D dissociated lysates compared to mCherry MCF10A, whereas Twist levels were increased (Figure 5.23). These protein expression patterns were similar to that of MCF10CA1a lysates (Figure 4.6).

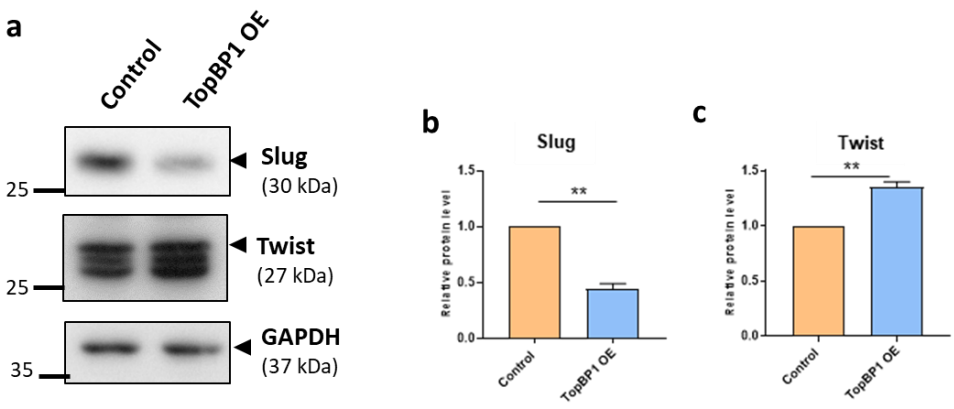


Figure 5.23: EMT markers in TopBP1 OE MCF10A and MCF10A series- mCherry MCF10A and TopBP1 OE MCF10A 3D dissociated cells were lysed, and immunoblotting was performed to analyse the levels of a-b) Slug, a-c) Twist. GAPDH was used as the loading control. Quantification showing the fold change after normalising with GAPDH. Statistical analysis was done using t-test (** p <0.01)

Keratins are intermediate filaments that are used as prognostic markers in breast cancer. Keratin 5 pairs with 14 and 8 pairs with 18. We found that upon TopBP1 over-expression, the levels of keratin 8 and its pair 18 increased, and Keratin 14 levels were reduced, whereas its pair keratin 5 levels remain unaltered (Figure 5.24). Keratin 19 levels were high in TopBP1 OE cells compared to control. The expression pattern of keratin 14 and 19 in TopBP1 OE is similar to that observed in MCF10CA1a (Figure 4.6). These results suggest that MCF10A cells with TopBP1 OE acquire EMT characteristics of MCF10CA1a after transformation in 3D cultures.

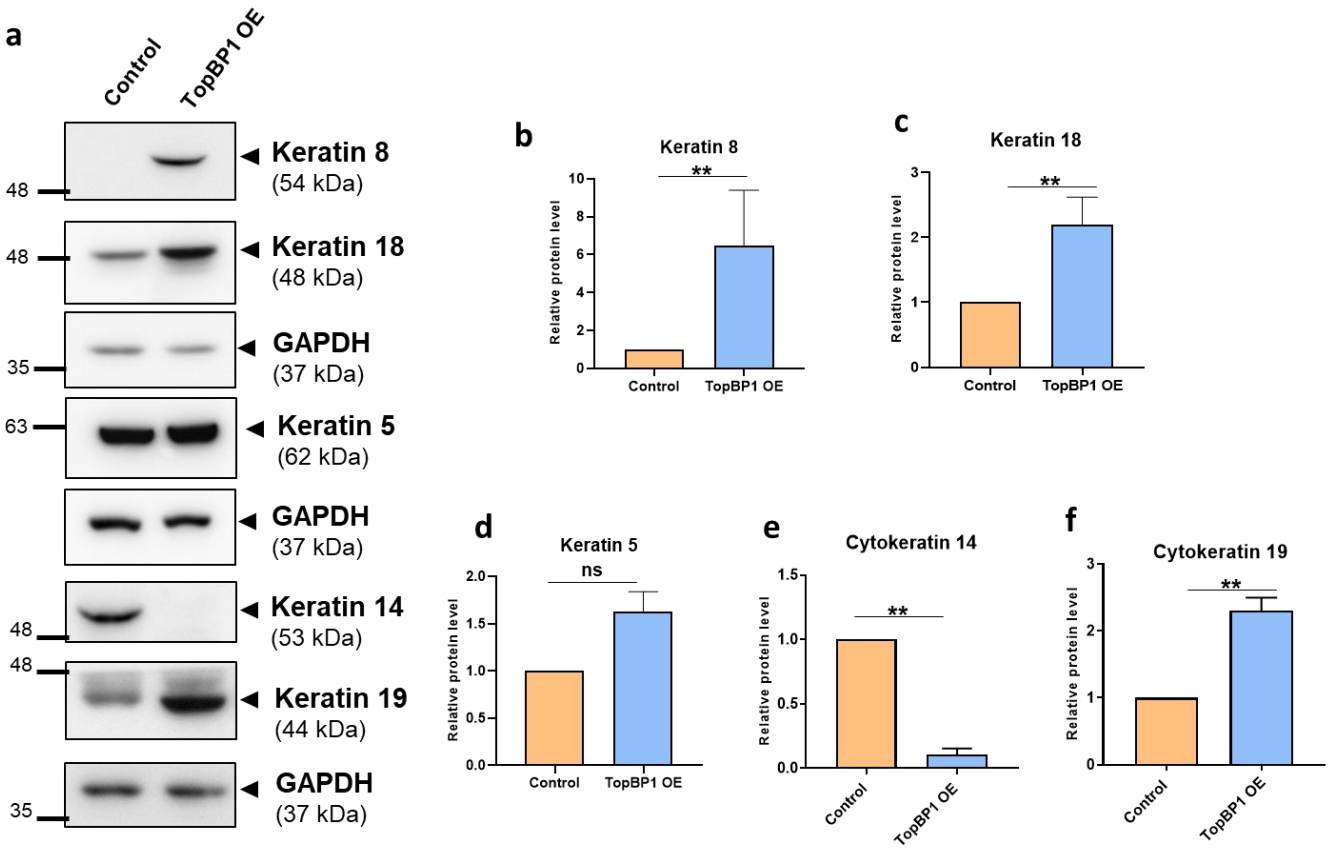


Figure 5.24: Keratin levels in TopBP1 OE MCF10A- mCherry MCF10A and TopBP1 OE MCF10A 3D dissociated cells were lysed, and immunoblotting was performed to analyse the levels of a-b) keratin 8, keratin 18, keratin 5, keratin 14 and keratin 19. b-f) The levels were normalised to GAPDH. Statistical analysis was done using t-test (** p <0.01)

5.2.2.5. TopBP1 OE leads to increased migration and invasion

During invasion and migration, cells move either as single entities (Theveneau and Mayor, 2011) or collectively as small groups (Deisboeck and Couzin, 2009). A wound healing assay was performed to investigate the collective cell migration of TopBP1 OE cells. 100% wound closure was observed in TopBP1 OE cells compared to 46% in control after 12 hrs of the assay (Figure 5.25a-b). Similar wound closure was observed in MCF10CA1a cells (Figure 5.25a-b). The cells' single-cell migration potential was investigated by tracking the movement of sparsely seeded cells for 3hrs. TopBP1 OE

cells had increased speed, distance and displacement compared to control cells and these properties were similar to that of MCF10CA1a cells (Figure 5.26).

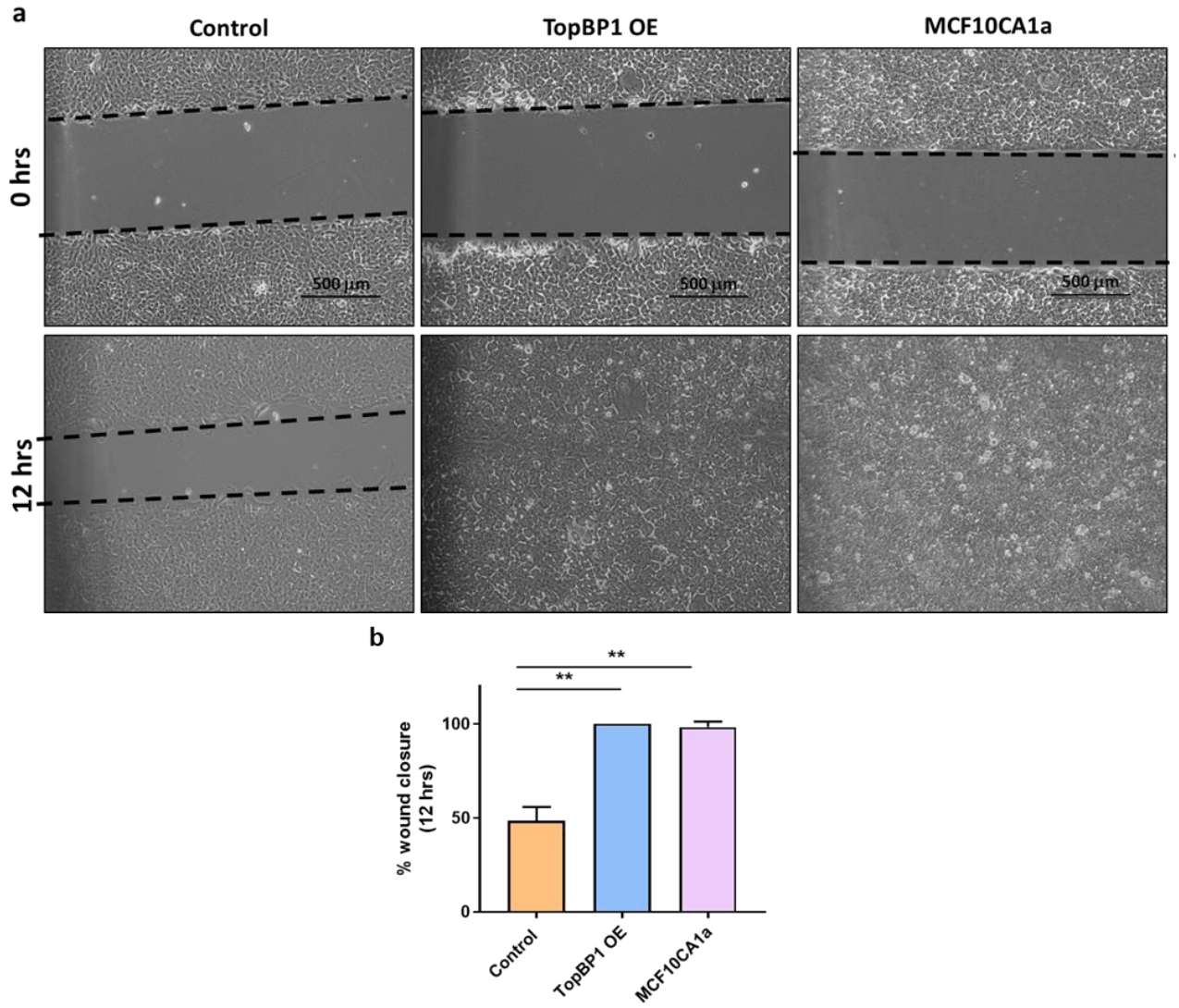


Figure 5.25: TopBP1 over-expression induces enhanced collective cell migration in MCF10A cells- A) Representative images of wound healing assay demonstrating collective cell migration of mCherry MCF10A and TopBP1 OE MCF10A 3D dissociated cells and MCF10CA1a at 0hrs and 12 hrs. Images were acquired in ECLIPSE TS100 Nikon microscope at 10X magnification (scale bar-500 µm). B) Wound area was manually measured using ImageJ, and percentage wound closure at 12 hrs was calculated and represented as a bar graph. Statistical analysis was done using One way Anova (** $p < 0.01$).

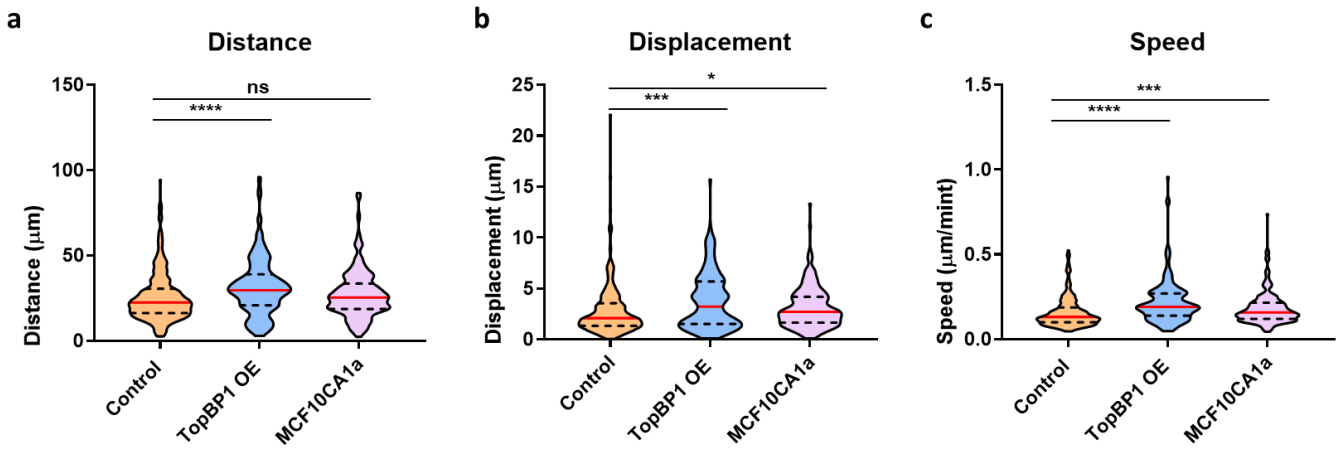


Figure 5.26: TopBP1 over-expression induces enhanced single-cell migration in MCF10A cells-Time-lapse images of mCherry MCF10A and TopBP1 OE MCF10A 3D dissociated cells and MCF10CA1a cells seeded as sparse populations were performed for a period of 3 hrs with an image taken at a 2-minute interval in Evos microscope. Cells were tracked using Fast track software, and the a) speed, b) distance and, c) displacement are represented as violin plots. Statistical analysis was done using One-way Anova (** p <0.01).

Invading cells secrete endopeptidases like matrix metalloproteinases (MMP) into its surrounding to degrade the extracellular matrix proteins (Woessner, 1991). MMP2 and MMP9 are two such proteinases that have gelatinase activity. Gelatin zymography assay was performed to investigate whether TopBP1 over-expression leads to MMP secretion. It was observed that TopBP1 OE 3D conditioned media has higher levels of MMP2 and MMP9 compared to the control 3D media after normalising with total protein content in the conditioned media. The MMP levels in TopBP1 OE were comparable to MCF10CA1a (Figure 5.27). The role of TopBP1 in invasion was further confirmed using DQ- Collagen assay. However, TopBP1 OE cells had reduced DQ-collagen fluorescence compared to control, suggesting reduced MMP1 activation (Figure 5.28).

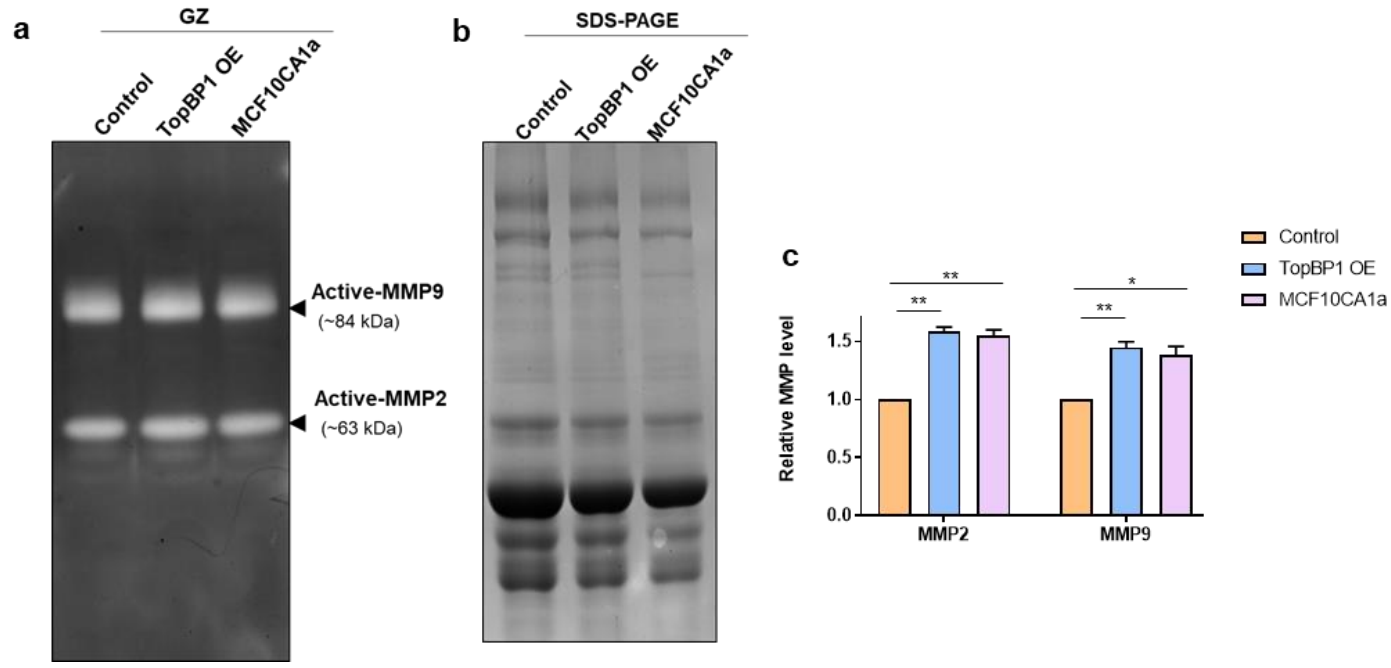


Figure 5.27: TopBP1 over-expression induces MMP2, and 9 activations in MCF10A 3D acini- Gelatin zymography was performed using conditioned media from 10-day 3D cultures of mCherry MCF10A and TopBP1 OE MCF10A and 10-day 3D cultures of MCF10CA1a. a) Gelatin zymography gel showing clearance of gelatin at the size of active MMP9 (~84 kDa) and MMP2 (~67 kDa) and b) the total protein in the media was quantified using SDS-PAGE. c) The MMP levels were quantified after normalising the total protein content of each sample. Statistical analysis was done using One-way Anova (** $p < 0.01$).

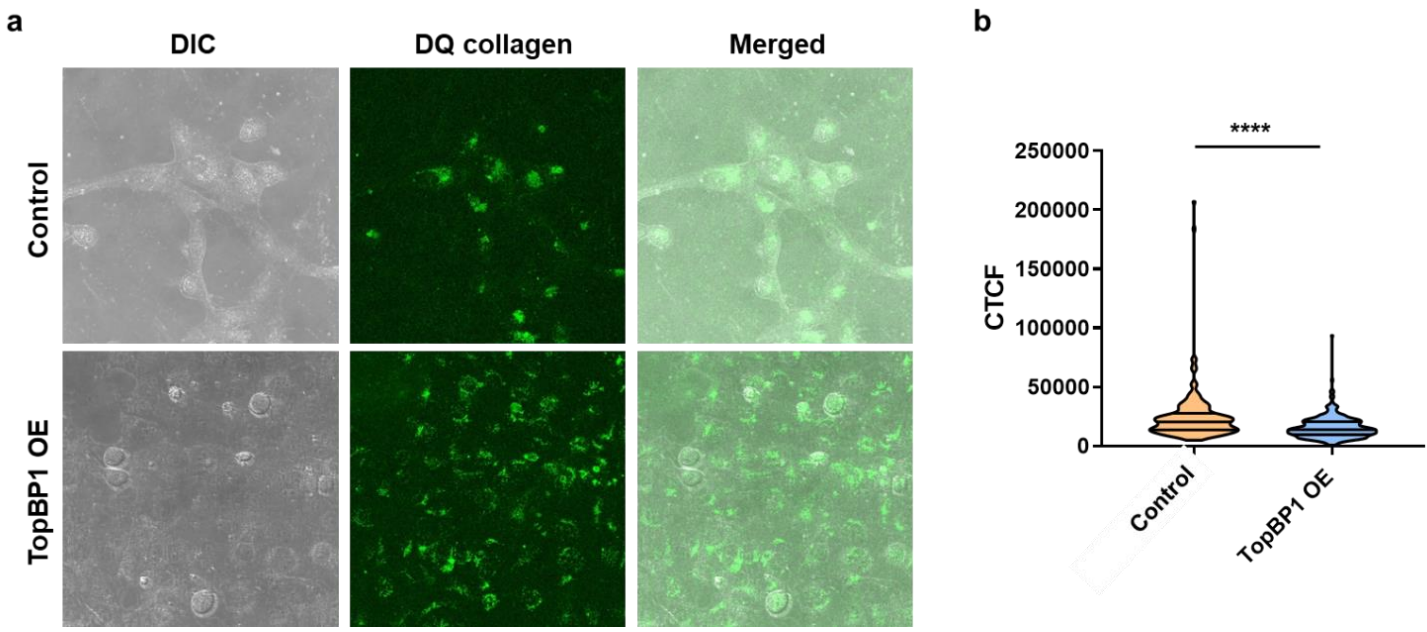


Figure 5.28: TopBP1 overexpression leads to reduced MMP1 in MCF10A- DQ Collagen assay was performed using mCherry MCF10A and TopBP1 OE MCF10A 3D dissociated cells, and fluorescence intensity was captured using SP8 confocal microscope (Leica, Germany). J) CTCF value of fluorescence intensity was represented as violin plots. Statistical analysis was done using t-test (** p <0.01).

5.2.2.6. TopBP1 OE induces anchorage-independent growth

Cancer cells have the ability to form colonies from single cells. The colony formation ability of TopBP1 OE cells was studied by growing the dissociated cells in 35 mm dishes sparsely (300 cells/well). These cells were stained using crystal violet to identify viable colonies after 7 days. It was observed that TopBP1 OE cells formed colonies similar to MCF10CA1a cells, where control cells failed to form any colonies (Figure 5.29). Anchorage-independent growth is one of the significant properties possessed by transformed cells. TopBP1 OE 3D dissociated cells were grown on a soft agar layer to find their ability to grow without any anchorage. It was observed that TopBP1 OE cells form large colonies in 7 days, whereas the control failed to form any colonies in the agar layer. These colonies were similar to MCF10CA1a colonies formed in 7 days (Figure 5.30).

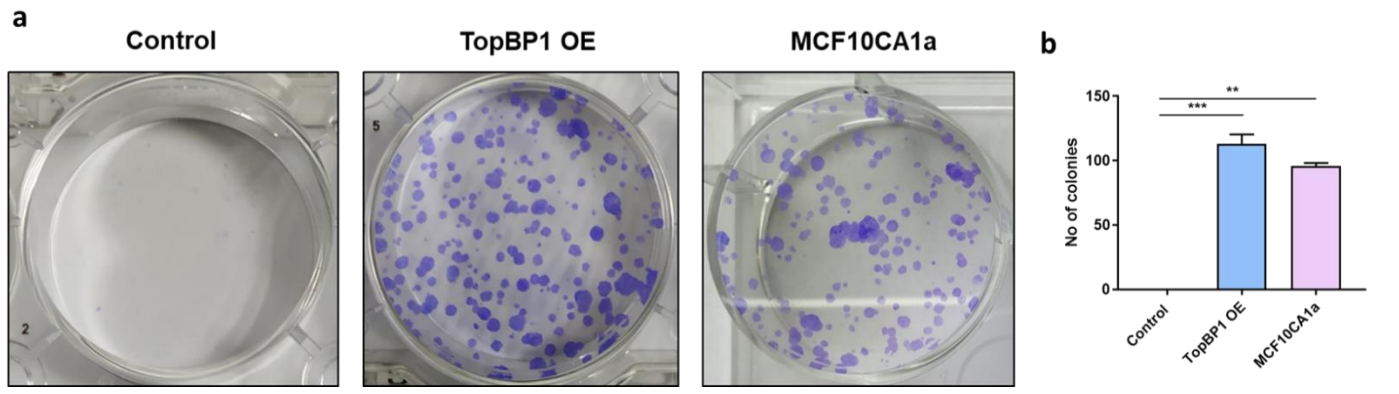


Figure 5.29: TopBP1 over-expression leads to colony formation in MCF10A dissociated cells- a) Crystal violet stained colonies of mCherry, TopBP1 OE MCF10A 3D dissociated and MCF10CA1a cells grown on cell culture treated 35 mm dishes for 7 days. b) Number of colonies were counted manually and represented as a bar graph. Statistical analysis was done using One-way Anova (** p <0.01, *** p <0.001).

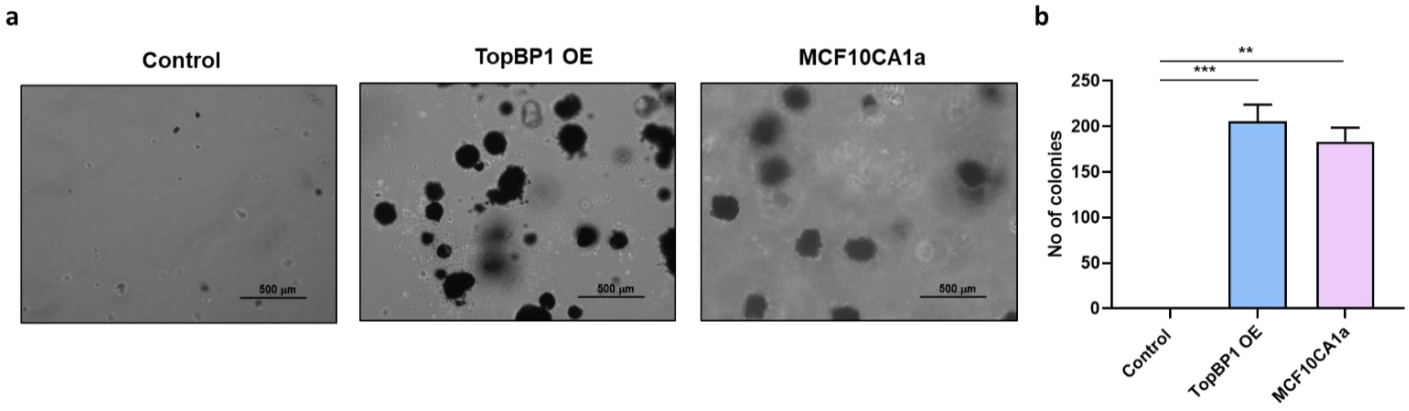


Figure 5.30: TopBP1 over-expression leads to anchorage-independent growth in MCF10A dissociated cells- a) MTT stained colonies of mCherry, TopBP1 OE 3D dissociated and MCF10CA1a cells grown on agar coated 35 mm dishes for 7 days. Images were acquired in ECLIPSE TS100 Nikon microscope at 10X magnification (scale bar-500 µm). b) Number of colonies were counted manually and represented as a bar graph. Statistical analysis was done using One-way Anova (** p <0.01, *** p <0.001).

5.2.2.7. TopBP1 over-expression leads to tumour formation

Mouse models were used to investigate the tumorigenic potential of TopBP1 over-expressing cells. 6 X 10^6 control and TopBP1 OE 3D dissociated cells along with 1:1 PBS: Matrigel® mix was injected subcutaneously into the left and right flank of athymic nude mice, respectively. Animals were monitored periodically for the presence of a tumour. Tumour was observed in TopBP1 OE injected right flank within 4 weeks, whereas control cells failed to form tumour even after 7 weeks. Mice were sacrificed after 7 weeks of injection and tumours were extracted, and tumour, size, volume and weight were measured (Figure 5.31). These results conclude that TopBP1 induces transformation of non-tumorigenic MCF10A cells.

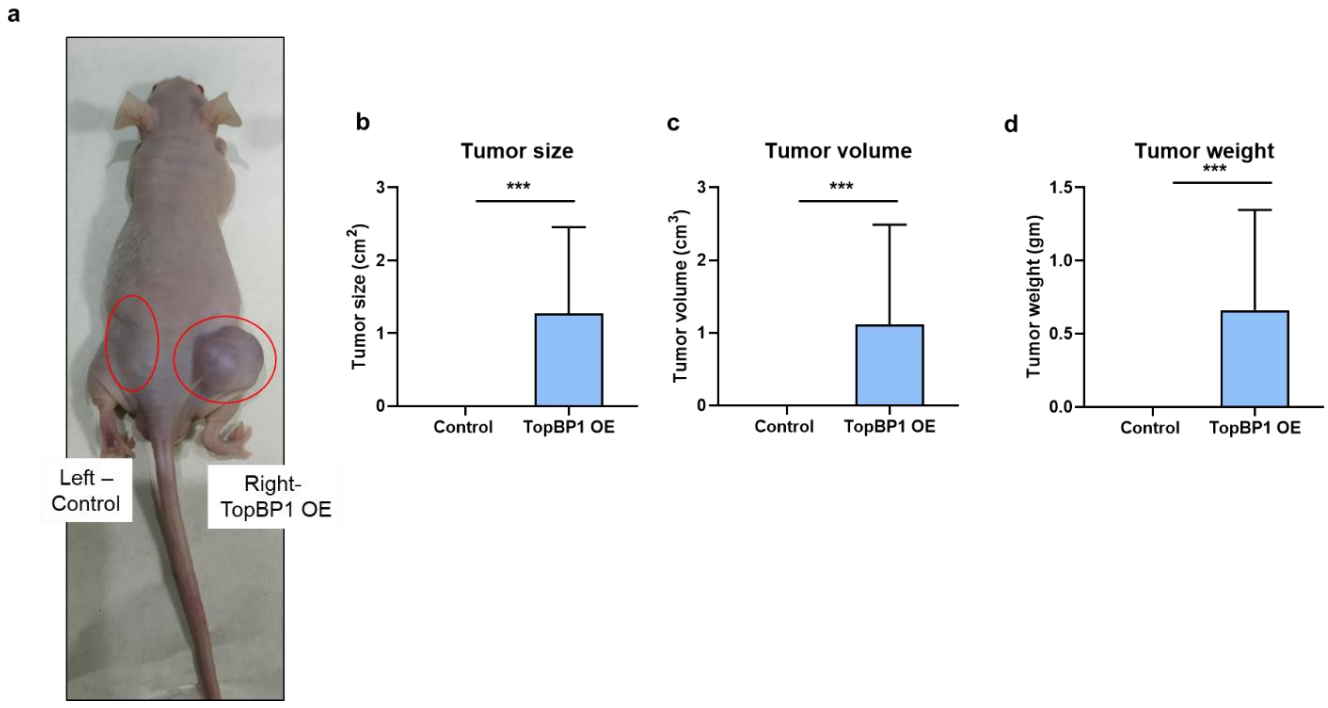


Figure 5.31: TopBP1 over-expression leads to tumour formation in athymic nude mice- a) Mice injected with control (left) and TopBP1 OE (right) dissociated cells subcutaneously on flanks were sacrificed after 7 weeks of injection. b) Tumour formed by TopBP1 OE cells excised from the right flank and tumour b) size, c) volume and d) weight were measured and represented as a bar graph. Statistical analysis was done using t-test (*** p <0.001).

5.2.2.8. TopBP1 knockdown reduces spheroid size in MCF10CA1a

Since MCF10CA1a had higher levels of TopBP1 and TopBP1 OE transformed MCF10A cells resembled MCF10CA1a cells, we knocked down TopBP1 in MCF10CA1a (shTopBP1) (Figure 5.5) and grown these cells on Matrigel to investigate the effect of TopBP1 knockdown in 3D cultures. Upon TopBP1 KD, MCF10CA1a formed spheroids with reduced size and cleared lumen (Figure 5.32a). The spheroid surface area and volume of TopBP1 KD in MCF10CA1a were reduced compared to control pLKO1 MCF10CA1a spheroids (Figure 5.32b-c). The sphericity of these spheroids increased upon TopBP1 KD (Figure 5.32d). Surprisingly, TopBP1 KD spheroids had a monolayer of cells and clear lumen compared to the filled lumen of control spheroids. These results suggest that TopBP1 KD in MCF10CA1a reduces spheroid size and morphologically resembles MCF10A acini.

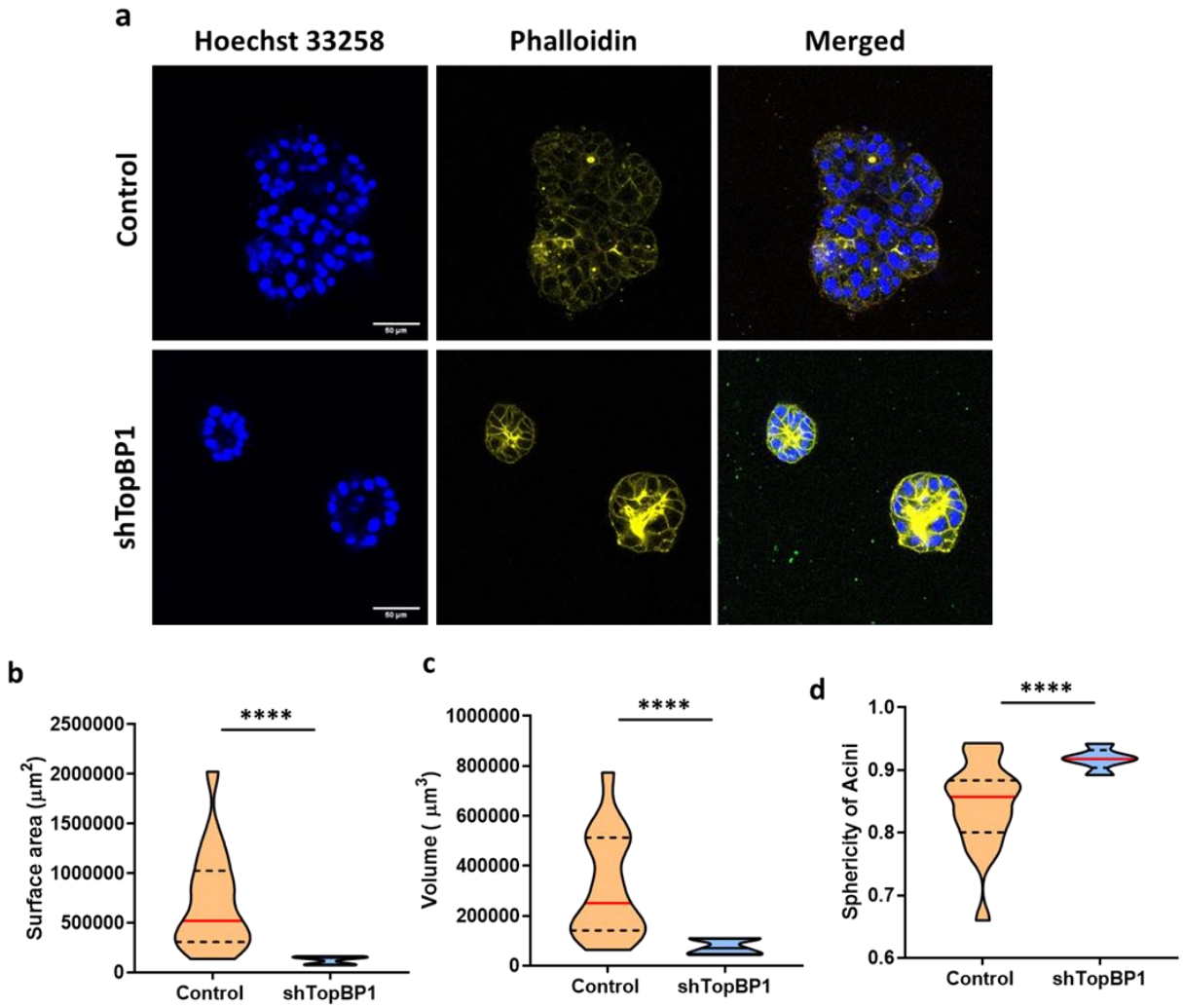


Figure 5.32-TopBP1 knockdown reduces spheroid size in MCF10CA1a 3D cultures- a) Representative images of pLKO1 and shTopBP1 MCF10CA1a cells grown as 3D cultures for 10 days and fixed and stained for Phalloidin (yellow) and Hoechst 33258 (blue) (scale bar-50 μm). b) Surface area, c) volume, and d) sphericity of these acini were calculated using Hygans software and represented as box plots. >50 acini from 3 independent experiments were analysed. Statistical analysis was done using Mann Whitney test (**** p <0.0001)

5.2.2.9. TopBP1 knockdown does not affect levels of EMT markers in MCF10CA1a

We were interested to understand the role of TopBP1 knockdown in altering the levels of EMT markers in MCF10CA1a. The levels of various EMT markers and keratins were analysed using an immunoblotting assay. We found that TopBP1 KD does not affect E-cadherin or keratin levels (Figure 5.33a-b and 5.34). However, vimentin levels were reduced in MCF10CA1a cells upon TopBP1 KD.

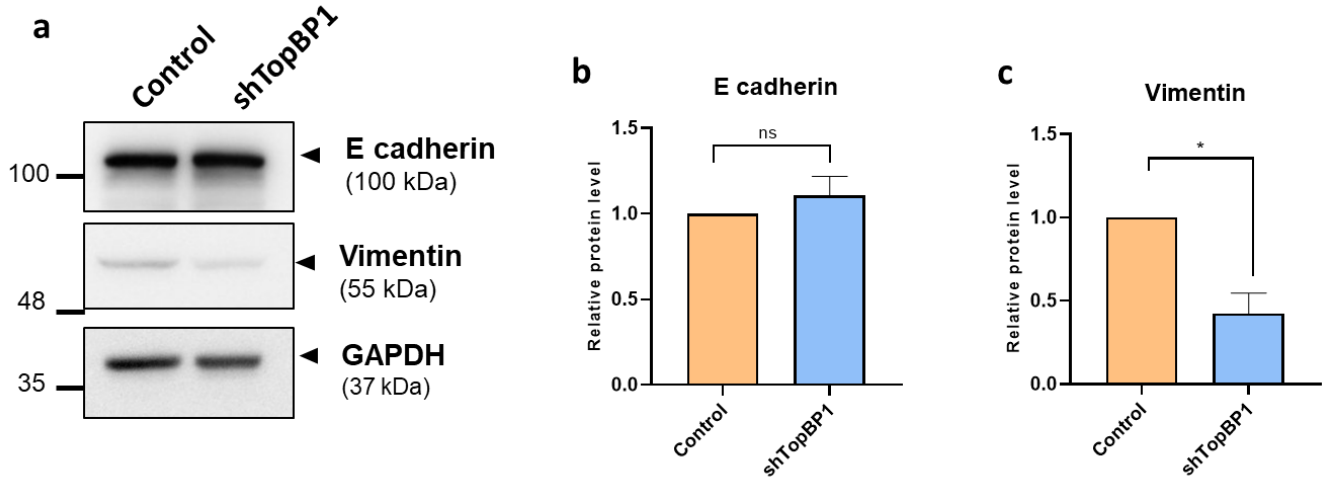


Figure 5.33- E-cadherin and vimentin levels in TopBP1 KD MCF10CA1a cells- Control (pLKO1 MCF10CA1a) and shTopBP1 MCF10CA1a cells were lysed, and immunoblotting was performed to analyse the levels of a-b) E-cadherin, a-c) Vimentin. GAPDH was used as the loading control. Statistical analysis was done using t-test (* $p < 0.5$, ns $p > 0.5$).

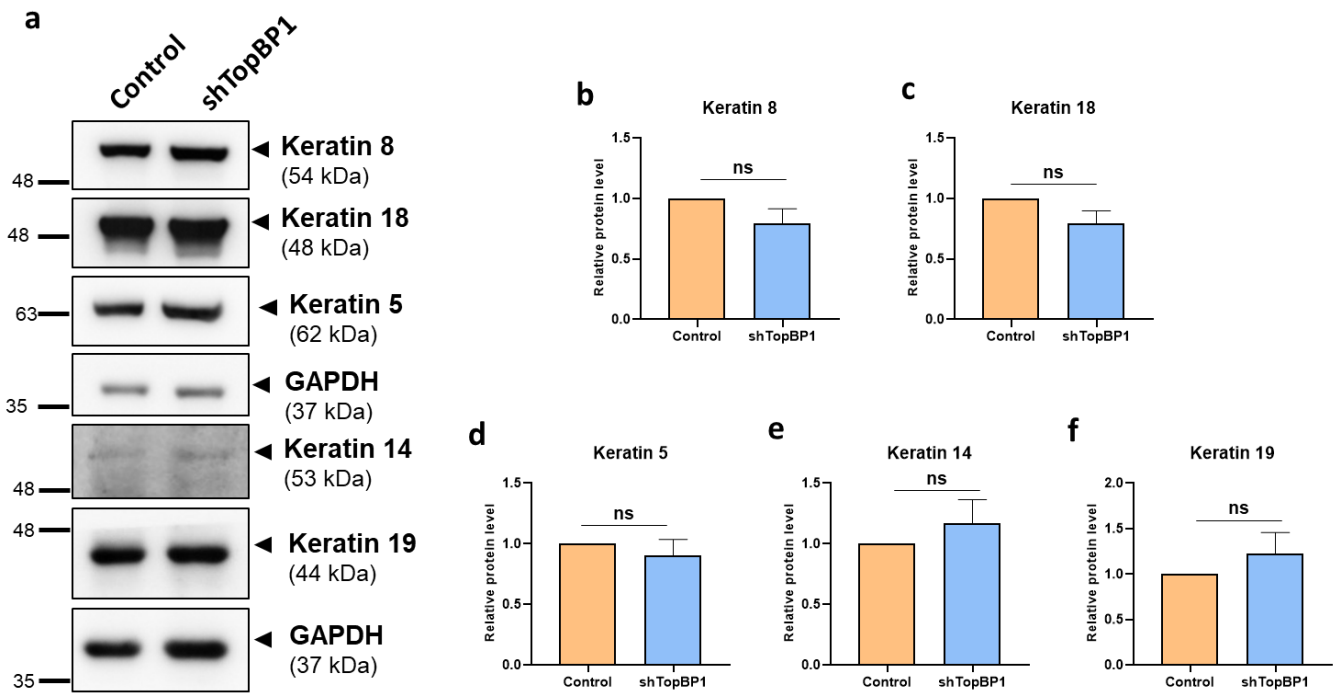


Figure 5.34- Keratin levels in TopBP1 KD MCF10CA1a cells- Control (pLKO1 MCF10CA1a) and shTopBP1 MCF10CA1a cells were lysed, and immunoblotting was performed to analyse the levels of a-b) keratin 8, keratin 18, keratin 5, keratin 14 and keratin 19. b-f) The levels were normalised to GAPDH. Statistical analysis was done using t-test (ns p>0.5).

5.2.2.10. TopBP1 knockdown does not affect migration in MCF10CA1a

To understand the role of TopBP1 in migration, the single-cell migration potential of TopBP1 KD cells were analysed. It was observed that TopBP1 KD does not affect the single-cell migratory potential of MCF10CA1a cells (Figure 5.35).

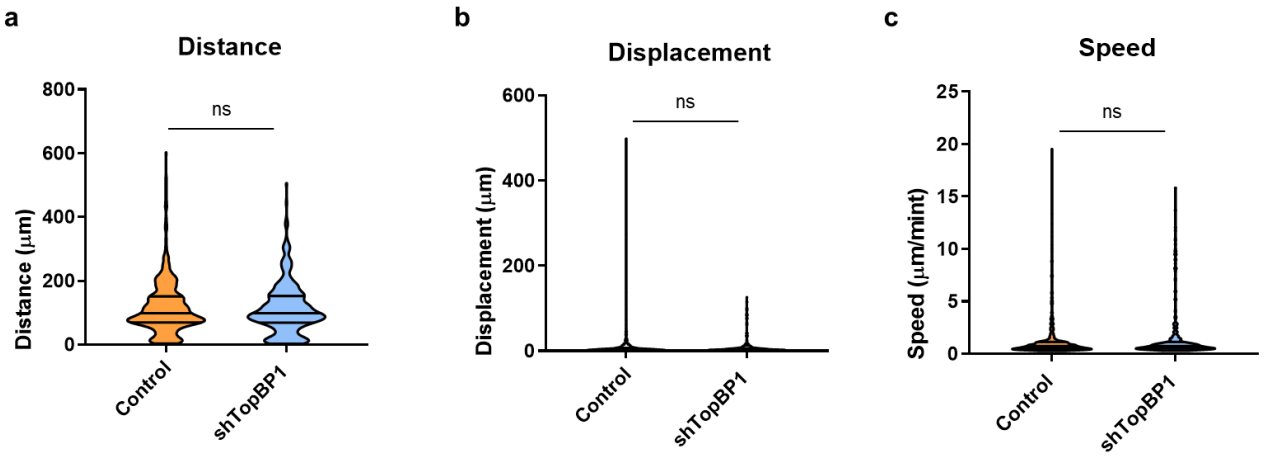


Figure 5.35: TopBP1 knockdown does not affect single-cell migration in MCF10CA1a cells-Time-lapse images of control (pLKO1 MCF10CA1a) and shTopBP1 MCF10CA1a cells seeded as sparse populations was performed for a period of 3 hrs with an image taken at a 2-minute interval in Leica sp8 microscope. Cells were tracked using Fast track software, and the a) speed, b) distance and, c) displacement are represented as violin plots. Statistical analysis was done using t-test (ns p>0.5).

5.2.2.10. TopBP1 knockdown reduces invasive potential of MCF10CA1a cells

The invasive potential of TopBP1 KD cells was investigated using gelatin zymography and DQ-collagen assay. It was observed that TopBP1 KD in MCF10CA1a reduced MMP2 and MMP9 activity (Figure 5.36). TopBP1 KD also reduced DQ-collagen activity (Figure 5.37), suggesting TopBP1 KD reduces the invasive potential of MCF10CA1a cells.

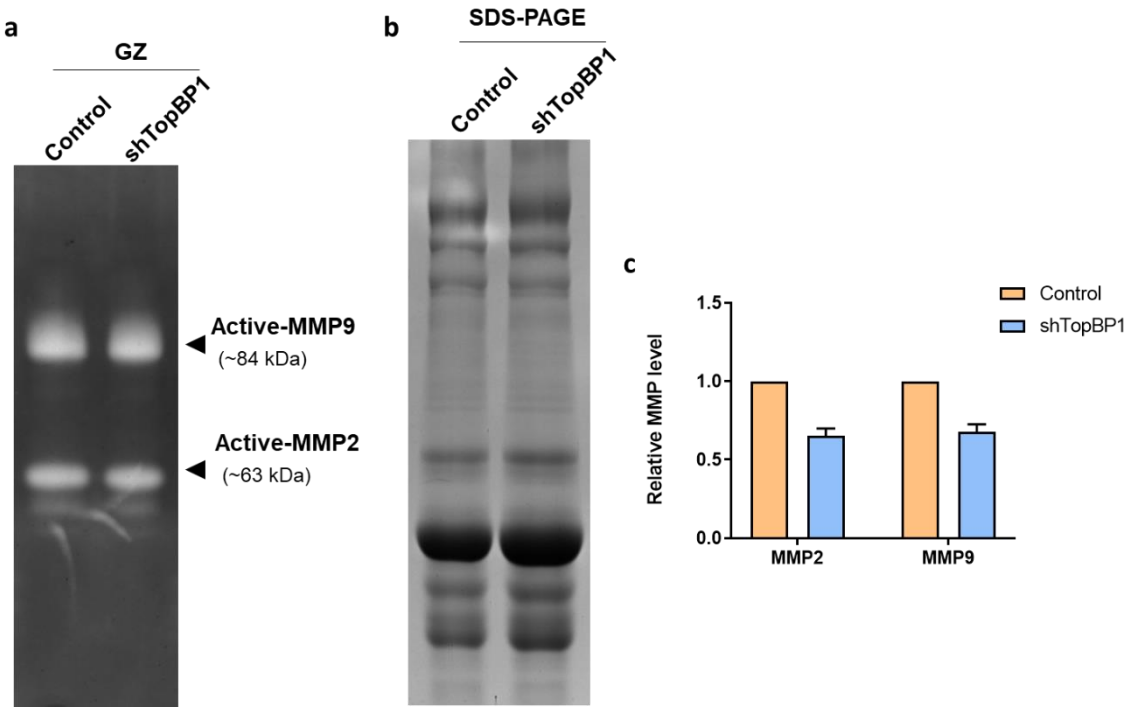


Figure 5.36: TopBP1 knockdown reduces MMP2 and 9 activation in MCF10CA1a 3D acini- Gelatin zymography was performed using conditioned media from 10 day 3D cultures of control (pLKO1 MCF10CA1a) and shTopBP1 MCF10CA1a. a) Gelatin zymography gel showing clearance of gelatin at the size of active MMP9 (~84 kDa) and MMP2 (~67 kDa) and b) the total protein in the media was quantified using SDS-PAGE. c) The MMP levels were quantified after normalising the total protein content of each sample.

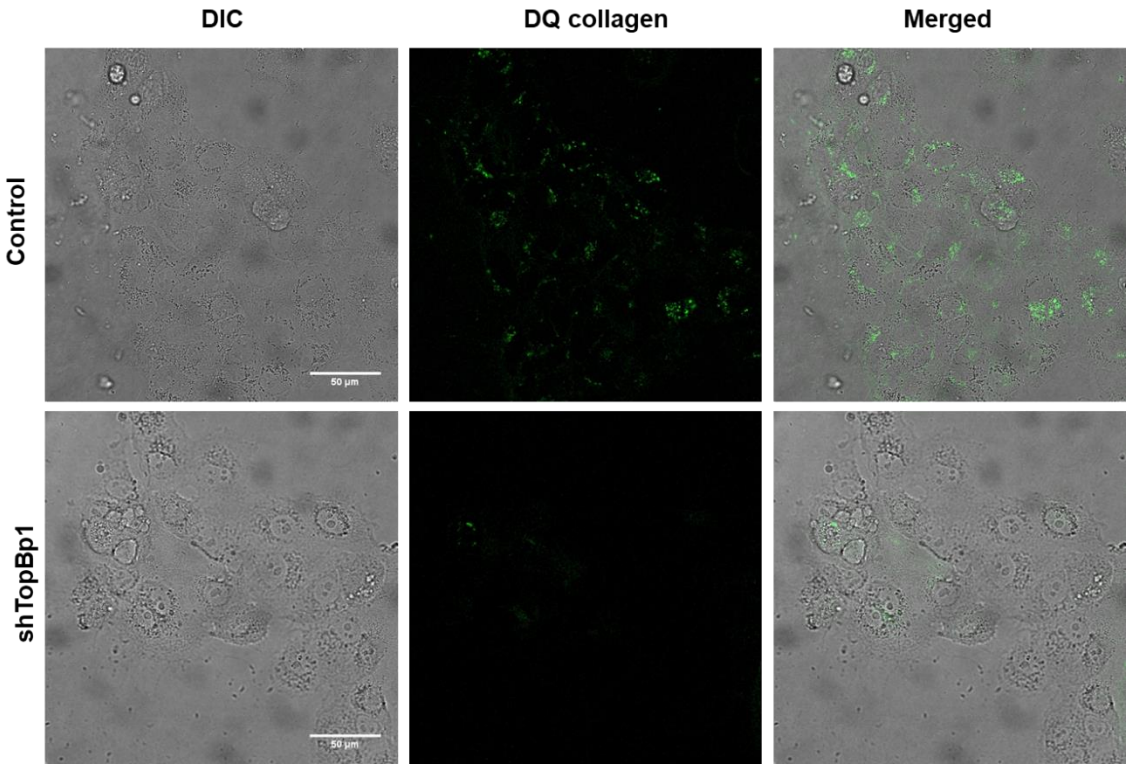


Figure 5.37: TopBP1 knockdown leads to reduced MMP1 in MCF10CA1a- DQ Collagen assay was performed using control (pLKO1 MCF10CA1a) and shTopBP1 MCF10CA1a, and fluorescence intensity was captured using SP8 confocal microscope (Leica, Germany).

5.2.2.11. TopBP1 knockdown reduces the colony-forming ability of MCF10CA1a cells

MCF10CA1a cells have shown colony-forming ability (Figure 4.9). We investigated whether TopBP1 KD affects the colony-forming ability of MCF10CA1a. We found that TopBP1 KD reduced the colony-forming ability of MCF10CA1a cells (Figure 5.38).

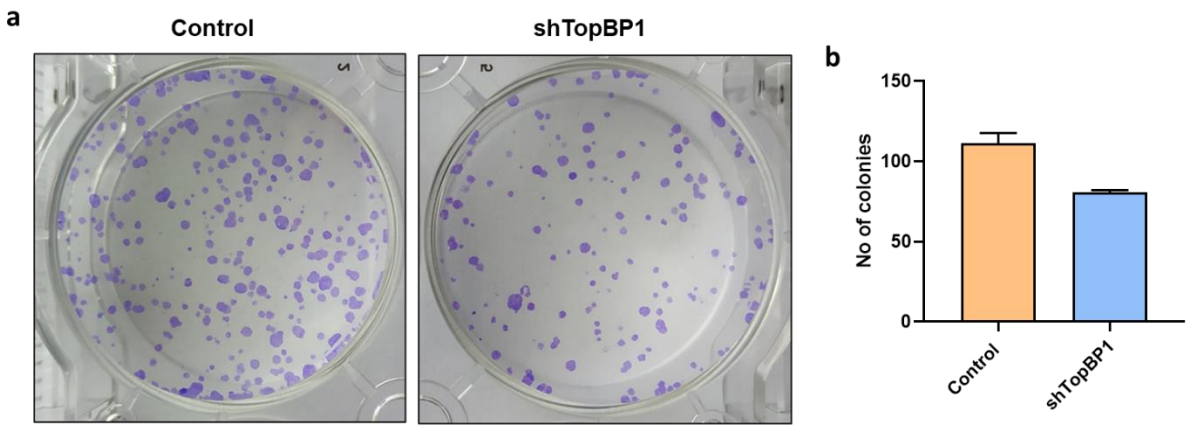


Figure 5.38: TopBP1 knockdown reduces colony formation in MCF10CA1a - a) Crystal violet stained colonies of control (pLKO1 MCF10CA1a) and shTopBP1 MCF10CA1a cells grown on cell culture treated 35 mm dishes for 7 days. b) Number of colonies were counted manually and represented as a bar graph

5.2.2.12. TopBP1 knockdown does not affect tumour forming ability of MCF10CA1a cells

MCF10CA1a are malignant cell lines that have tumour forming ability. The effect of TopBP1 KD in the tumour forming ability of MCF10CA1a was investigated using mice studies. Control (pLKO1 MCF10CA1a) and shTopBP1 MCF10CA1a cells were injected into the left, and right flank of athymic nude mice, respectively and tumour formation was monitored every week. The tumours were dissected 7 weeks after injection. The tumour forming ability of MCF10CA1a was not affected by TopBP1 KD (Figure 5.39).

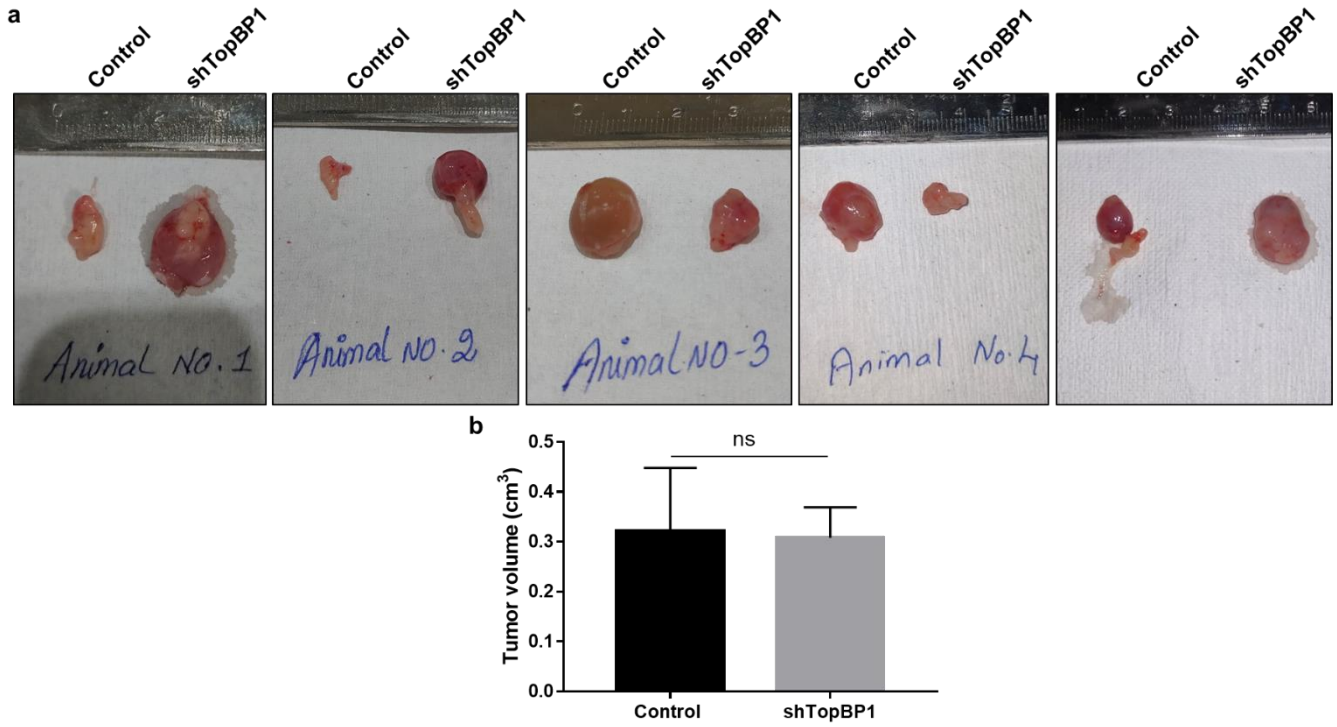


Figure 5.39: TopBP1 knockdown does not affect tumour formation in athymic nude mice- a) Mice injected with control (left) and TopBP1 KD (right) MCF10CA1a cells subcutaneously on flanks were sacrificed after 7 weeks of injection. b) Tumor formed were excised and b) tumour weight was measured and represented as a bar graph. Statistical analysis was done using t-test (ns p>0.5).

5.2.3. To elucidate the mechanism of TopBP1 induced transformation

5.2.3.1. TopBP1 OE induces DNA damage and activates DDR response

Genomic instability is one of the hallmarks of cancer, and defects in checkpoint activation can accumulate DNA damage, leading to genomic instability (Kastan & Bartek, 2004). TopBP1 being a mediator protein in DNA damage response, it was interesting to find whether TopBP1 OE induced transformation of non-tumorigenic MCF10A cells by altering the DNA damage response pathway. To identify whether TopBP1 OE induced DNA damage, we analysed the activation of RPA and γH2AX in TopBP1 OE 3D dissociated cells. Surprisingly we found that TopBP1 OE induces activation of RPA and γH2AX in the absence of any external DNA damaging agent (Figure 5.40 a-c). A similar trend was observed in malignant cell line MCF10CA1a

compared to MCF10A and MCF10AT1 cell lines, suggesting endogenous DNA damage in transformed cells (Figure 4.2). Also, knockdown of TopBP1 reduced RPA and γH2AX activation in MCF10CA1a (Figure 5.40 d-f).

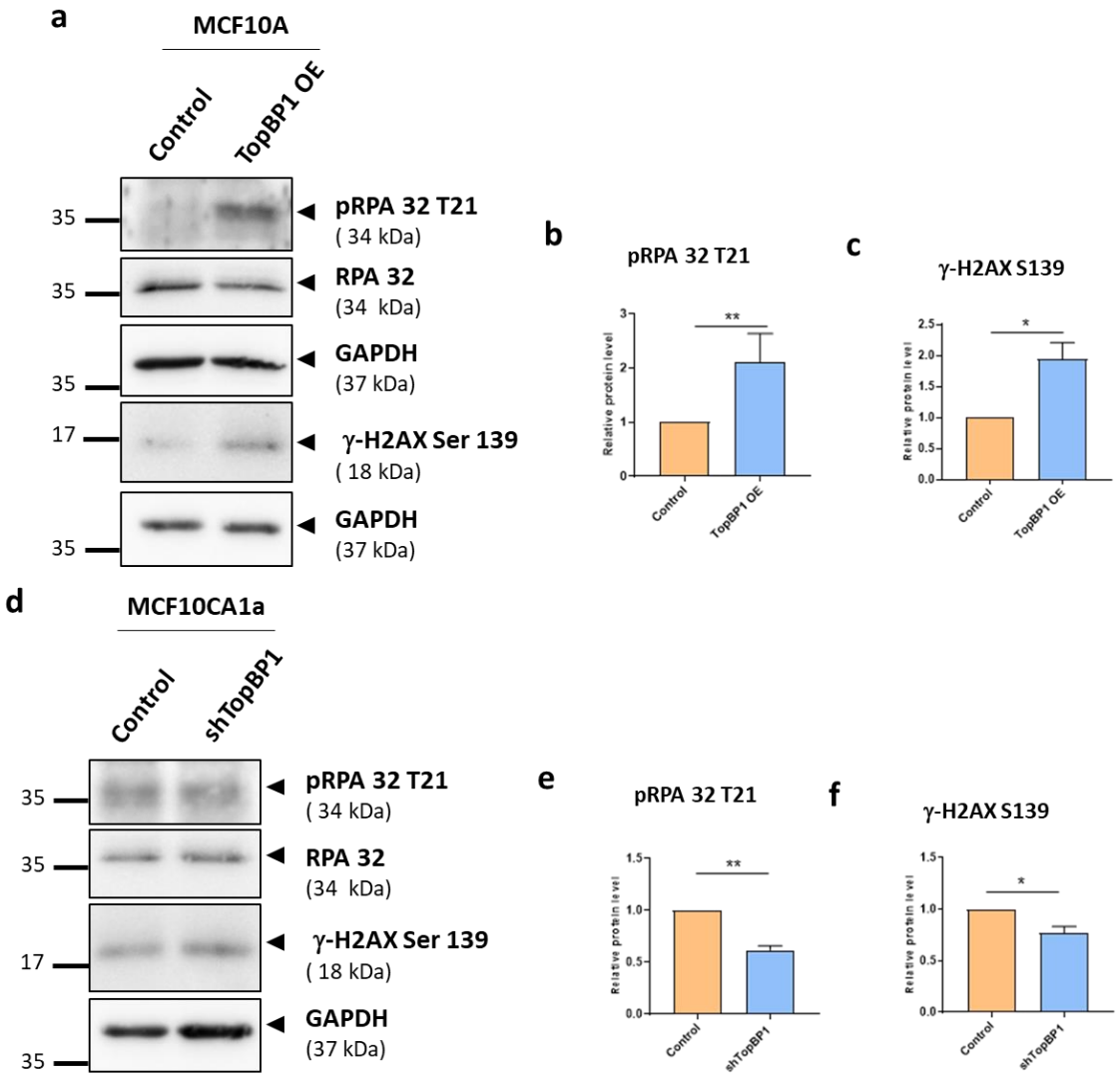


Figure 5.40: TopBP1 OE induces activation of RPA and γH2AX- a) mCherry MCF10A and TopBP1 OE MCF10A 3D dissociated cells and d) control (pLKO1 MCF10CA1a) and shTopBP1 MCF10CA1a cells were lysed, and immunoblotting was performed to analyse the levels/activation of RPA and γH2AX. GAPDH was used as the loading control. Statistical analysis was done using t-test (* p <0.5, ** p <0.01)

We next investigated whether the endogenous DNA damage induced by TopBP1 could activate DNA damage response. TopBP1 being a mediator protein in single-strand break repair pathway, we analysed the activation of ATR and Chk1 in TopBP1 OE 3D dissociated cells. ATR and Chk1 activation were observed in TopBP1 OE 3D dissociated cells compared to mCherry MCF10A (Figure 5.41a-c) in the absence of any external DNA damaging agent. A similar pattern of activation was observed in MCF10CA1a compared to MCF10A cells (Figure 4.3). Also, knockdown of TopBP1 reduced ATR and Chk1activation in MCF10CA1a (Figure 5.41d-f). These results suggest that TopBP1 induces endogenous DNA damage and altered DNA damage response during transformation without any external DNA damaging agent.

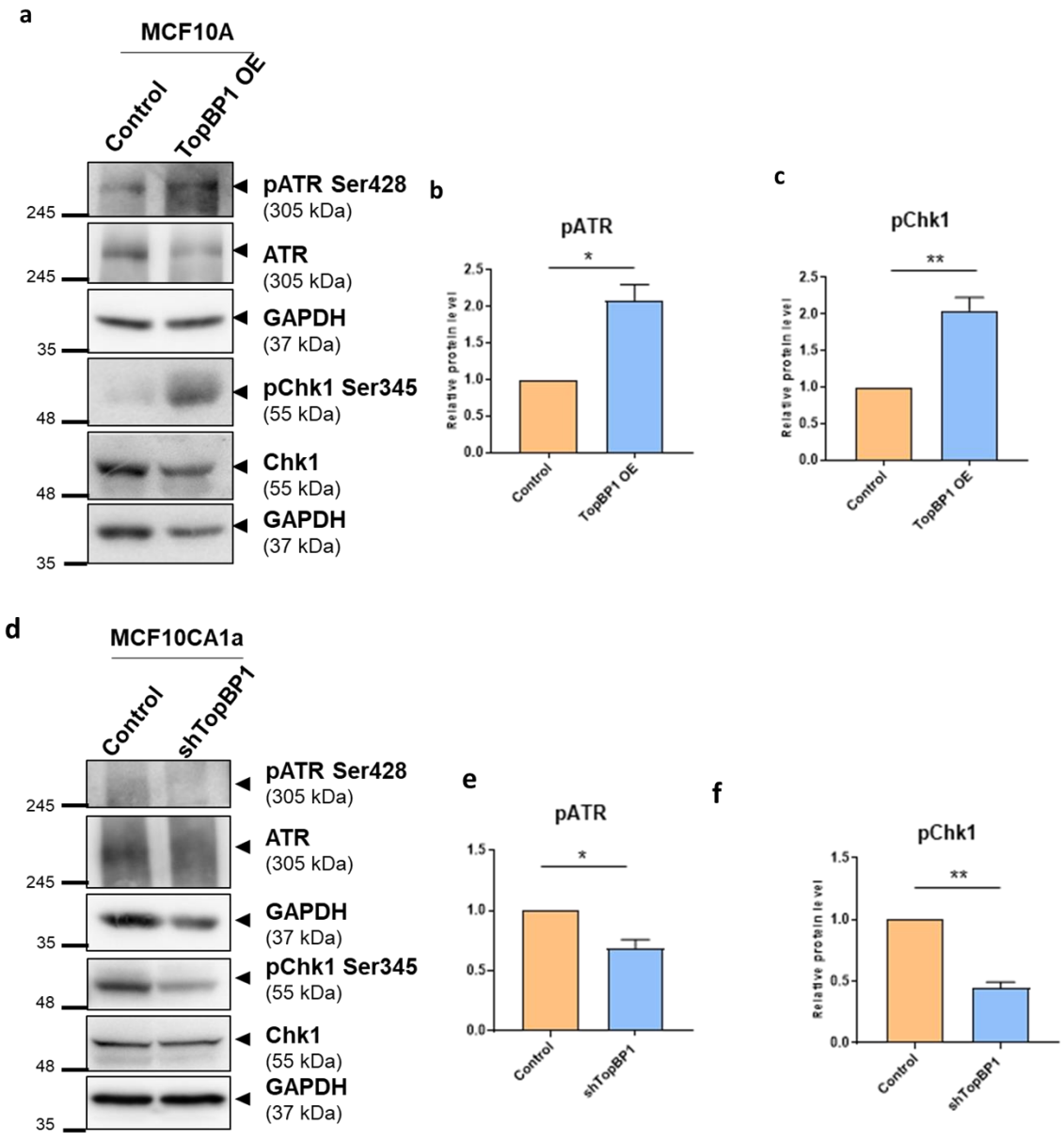


Figure 5.41: TopBP1 OE induces activation of ATR and Chk1- a) mCherry MCF10A and TopBP1 OE MCF10A 3D dissociated cells and d) control (pLKO1 MCF10CA1a) and shTopBP1 MCF10CA1a cells were lysed, and immunoblotting was performed to analyse the levels/activation of ATR and Chk1. GAPDH was used as the loading control. Statistical analysis was done using t-test (* p <0.5, ** p <0.01).

5.2.3.2. TopBP1 overexpression induces mutation in p53 at M237I

p53 is a tumour suppressor gene, which acts as an effector protein in checkpoint activation. Upon checkpoint activation, p53 gets activated and leads to cell cycle arrest, DNA repair or apoptosis based on the extent of the damage. To identify the activation of p53 effector protein to execute checkpoint response, total and activated p53 levels were analysed in TopBP1 OE cells. We observed an increase in total and activated p53 at S15 upon TopBP1 OE compared to control (Figure 5.42a-c). MCF10CA1a cells also had increased activation and total levels of p53 compared to MCF10A and MCF10AT1 (Figure 4.5a). The activation and total levels of p53 were reduced in MCF10CA1a cells upon TopBP1 knockdown (Figure 5.42e-g). However, the p21, which is activated by p53 to induce G1-S arrest, was reduced or absent in TopBP1 OE cells (Figure 5.42a and d), and p21 levels increased upon TopBP1 knockdown in MCF10CA1a (Figure 5.42e and h). TopBP1 over-expression can also increase proliferation and reduction in apoptosis by inducing mutant p53 (mut p53) gain of function (Liu et al., 2011). Previous reports have shown that polarity disruption in MCF10A cells can be induced by mutant p53 gain of function by inducing EMT (Zhang et al., 2011).

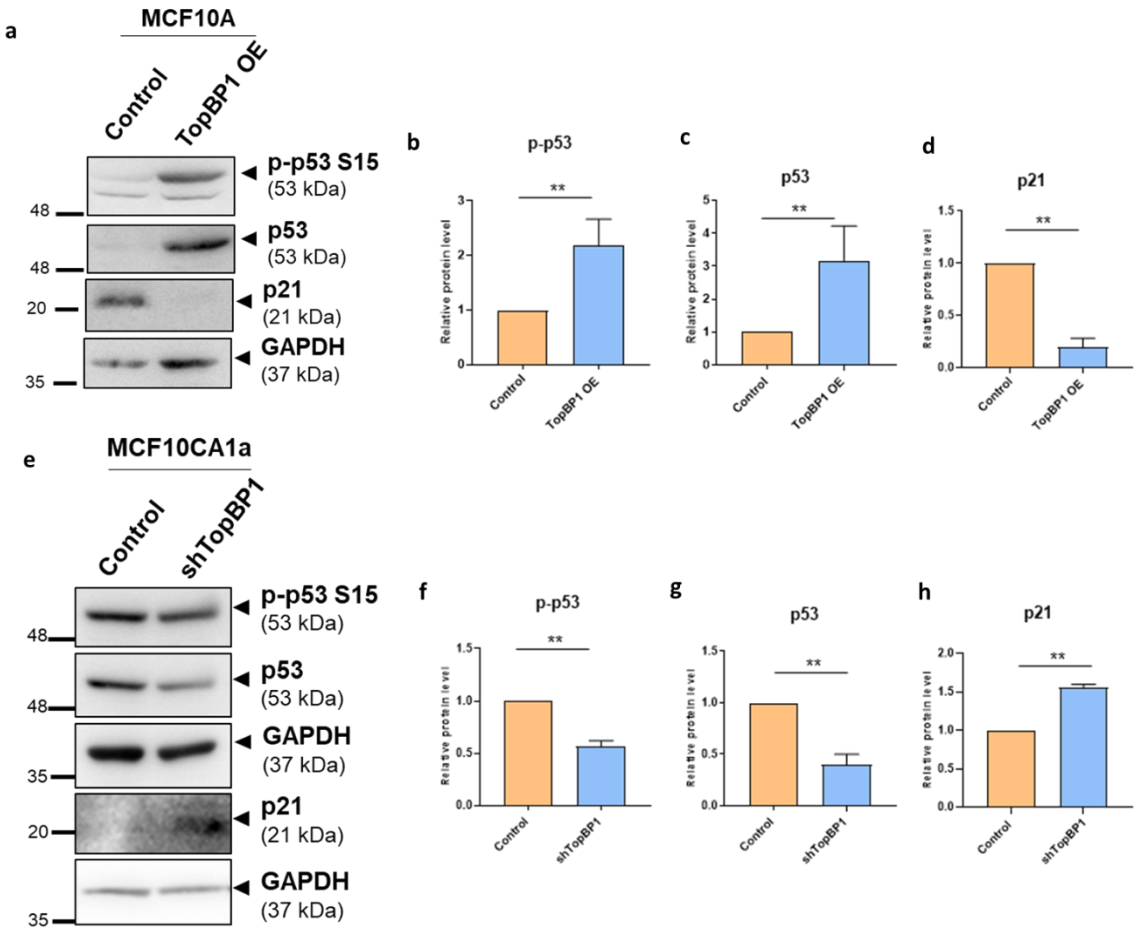


Figure 5.42: TopBP1 OE induces activation of p53 and reduces p21- a) mCherry MCF10A and TopBP1 OE MCF10A 3D dissociated cells and e) control (pLKO1 MCF10CA1a) and shTopBP1 MCF10CA1a cells were lysed, and immunoblotting was performed to analyse the levels/activation of p53 and p21. GAPDH was used as the loading control. Statistical analysis was done using t-test (** p <0.01)

The p53 mutation status was analysed in TopBP1 OE cells and control and MCF10CA1a cells using whole-exome sequencing. The genomic DNA (gDNA) was extracted, and the library preparation, sample quantitation was done using Agarose Gel Electrophoresis (Pages et al.) (Figure 5.43). All three samples met the QC requirements for library construction.

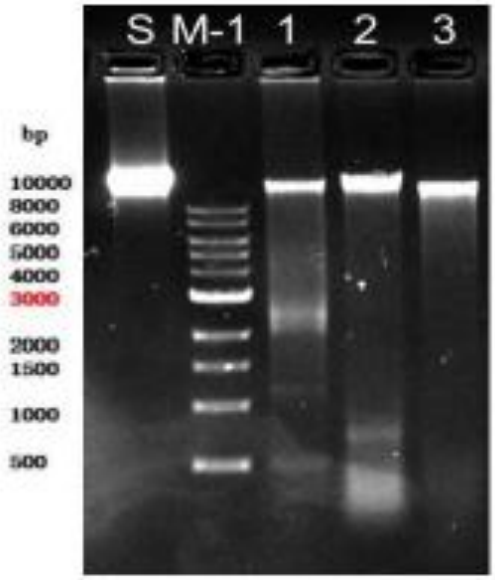


Figure 5.43: Genomic DNA isolation for whole-exome sequencing- Genomic DNA was extracted from frozen vials of 1-mCherry MCF10A, 2-TopBP1 OE MCF10A 3D dissociated cells, and 3-MCF10CA1a cells and preliminary quality for the extracted gDNA was carried out by Agarose Gel Electrophoresis (Pages et al.). S- standard sample (50ng) and M-1- NEB 1kb DNA ladder

All 3 cell lines were targeted in Whole exome sequencing (Makiniemi et al.) using Agilent V6r2 [Agilent Technologies, Santa Clara, CA 95051, United States], and this targeted library was sequenced using HiSeq. The resultant raw data were then mapped to the human genome (Hg19/GRCh37) using BWA algorithm 4,5,6, and duplicates were removed using the Picard toolkit. All 3 cell lines mapping were in the cutoff limit (i.e. mapping= >95% and Read Duplicates <20%). Further target enrichment was done using samtools and subsequent variant calling on BAM file using GATK pipeline to produce VCF formatted output file. All variants in the VCF file were then annotated using an in-house pipeline with all required databases, including OMIM, ClinVar HGBS coordinates, different population databases, etc.7. To identify the differential expression between 3 cell lines, these variants were inter-compared. We found that mCherry MCF10A had 3 mutations in the TP53 gene, out of which 2 were in the intronic region and one mutation was at cDNA position 417, leading to the formation of mutant p53 P72R (Table 5.1). These 3 mutations were also observed in TopBP1 OE dissociated

cells and MCF10CA1a. However, the 4th mutation in the TP53 gene was observed in TopBP1 OE cells and MCF10CA1a cells at 913 cDNA position, which was not present in control cells (Table 5.1). This single-nucleotide variation (svn) mutation leads to an exonic missense variant leading to the formation of a mutant p53 protein with isoleucine at 237 instead of methionine (M237). This M237I mutation observed was in the DNA binding region of p53, through which TopBP1 is known to interact with p53.

Table 5.1: TP53 mutation status

Gene	Variant	Chr	Coordinate	Type	Genotype	Exonic	Consequence	cDNA Position	Protein Position	Amino Acids	Codons	Exon
mCherry 10A												
TP53	G>C/C	17	7579472	snv	HOM	yes	missense_variant	417	72	P/R	cCc/cGc	4/11
TP53	CCCCCAGCCCTCCAGGT>C/C	17	7579643	deletion	HOM	no	intron_variant		0			
TP53	G>C/C	17	7579801	snv	HOM	yes	intron_variant		0			
TopBP1 OE 10A												
TP53	C>C/A	17	7577570	snv	het	yes	**missense_variant**	**913**	**237**	**M/I**	**atG/atT**	**7/11**
TP53	G>C/C	17	7579472	snv	hom	yes	missense_variant	417	72	P/R	cCc/cGc	4/11
TP53	CCCCCAGCCCTCCAGGT>C/C	17	7579643	deletion	hom	no	intron_variant		0			
TP53	G>C/C	17	7579801	snv	hom	yes	intron_variant		0			
MCF10CA1a												
TP53	C>C/A	17	7577570	snv	HET	yes	**missense_variant**	**913**	**237**	**M/I**	**atG/atT**	**7/11**
TP53	G>C/C	17	7579472	snv	HOM	yes	missense_variant	417	72	P/R	cCc/cGc	4/11
TP53	CCCCCAGCCCTCCAGGT>C/C	17	7579643	deletion	HOM	no	intron_variant		0			
TP53	G>C/C	17	7579801	snv	HOM	yes	intron_variant		0			

5.3 Summary

TopBP1 levels were high in breast cancer patient samples and malignant breast cancer cell lines. Upon over-expression of TopBP1 in non-tumorigenic breast epithelial cells MCF10A led to the transformation of the cells. TopBP1 overexpression leads to increased acinar size, proliferation, disruption of polarity, altered expression of EMT markers, increased migration and invasion. TopBP1 overexpression also induced tumour formation in athymic nude mice. The phenotypes observed in MCF10A upon TopBP1 OE were similar to MCF10CA1a, a malignant cell line. So we knocked down TopBP1 in MCF10CA1a, and phenotypic characters were analysed. TopBP1 KD reduced the spheroid size of MCF10CA1a and led to a reduced invasion. However, the migration, EMT and tumour formation was unaffected. While elucidating the mechanism of TopBP1 induced transformation, we found that TopBP1 OE leads to genomic instability and activation of the single-strand DNA damage response pathway. p53

activation/levels were also increased upon TopBP1 over-expression, where p21 levels were low. TopBP1 KD in MCF10CA1a could revert these activations. Interestingly, we also found that TopBP1 overexpression leads to a mutation in the TP53 gene similar to that was observed in MCF10CA1a, which can lead to the formation of mutp53 protein with M237I. Thus, taken together, we demonstrate that TopBP1 OE induces transformation of non-tumorigenic breast epithelial cells when grown on extracellular matrix, and these transformed cells have phenotypic and genotypic characteristics of MCF10CA1a malignant cell line with a mutation in TP53 gene (Figure 5.44).

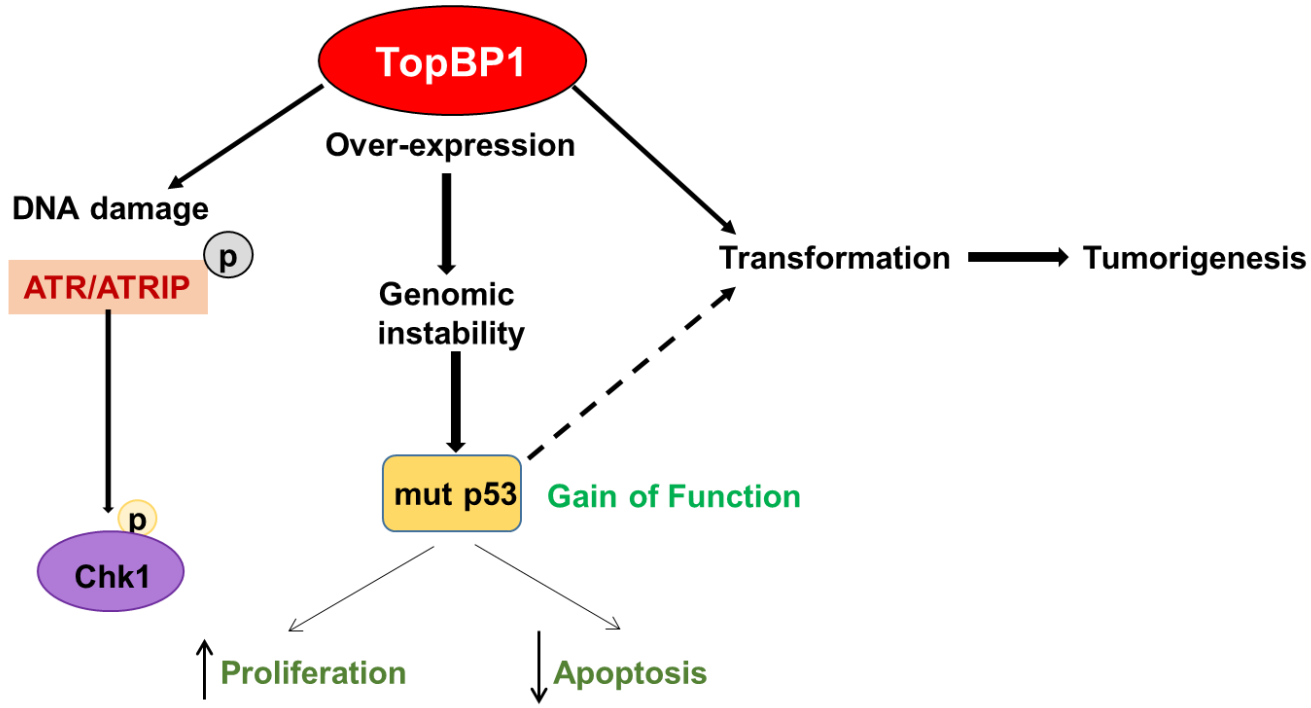


Figure 5.44: Schematic representation depicting the role of TopBP1 tumorigenesis.

Chapter 6

Discussion and future perspectives

6.1 Discussion

Cancer is caused by variation in a gene(s), which may give rise to an increase in cellular proliferation, decrease in apoptosis, increase in cell migration and invasion and/or EMT (Hanahan and Weinberg, 2011). These variations in the genes are caused by various DNA damaging agents, mutagens. The variations or mutations in the genes favours the cancerous properties of the cells.

TopBP1, DNA topoisomerase IIβ -binding protein 1, a mediator protein in the DNA damage checkpoint pathway, has been reported as a breast and ovarian cancer susceptibility gene by various groups (Forma et al., 2012; Karppinen et al., 2006). TopBP1 upregulation has been reported in high-grade breast cancer biopsy samples (Forma et al., 2012; Going et al., 2007; Liu et al., 2009).

In our study, we observed that, TopBP1 levels are high in malignant cell lines compared to non-tumorigenic breast epithelial cell lines. We demonstrate that TopBP1 overexpression can induce transformation of non-tumorigenic MCF10A 3D breast acini cultures to acquire properties similar to malignant cell lines by inducing genomic instability and mutation in the TP53 gene. Our finding also emphasises on the functional role of cellular microenvironment in the cancer initiation. TopBP1 expressing cells grown on the Matrigel underwent transformation while the same cells grown as monolayer culture could not initiate transformation in themselves.

We also found that TopBP1 induced TP53 mutation in MCF10A cells grown in 3D cultures. This suggest that TopBP1 also has potential to regulate genomic stability. This genomic stability regulatory function of TopBP1 is also dependent on the context as the TopBP1 expressing cells grown in 2D culture did not observe to cause TP53 mutation. This also emphasises the role of the 3D environment in transformation as we did not observe any difference in morphology or various protein expressions in MCF10A cells with TopBP1 OE (2D) before growing them on 3D.

Analysis of the cellular and nuclear pleomorphism and extent of the architectural disorder are the preliminary diagnostic and prognosis determination method for breast carcinoma (Debnath and Brugge, 2005). 3D cultures of breast epithelial cells and cancer cells recapitulate most of the features of these cells *in-vivo*. Detailed analysis of

these characteristic features can aid in ascertaining the role of perturbed genes. The morphometric analysis of TopBP1 OE MCF10A acini revealed that TopBP1 overexpression induced changes in the acinar morphology which resembles cancerous spheroids. TopBP1 overexpressing cells formed acini with a larger surface area and volume with filled lumen than the control acini. In support of this observation, TopBP1 is known to play a major role in maintaining genomic stability, ensuring proper DNA replication and G1-S transition in the cell cycle (Kim et al., 2005); perturbation in its level can distort the DNA synthesis and cell cycle which may alter the nuclear content. We also found that TopBP1 OE MCF10A 3D acini had increased proliferation, and these cells had more percentage of cells in S and G2-M phase than MCF10A control.

De-regulation of apicobasal polarity is one of the characteristics of epithelial cancer (Debnath and Brugge, 2005). In invasive cancer, the cells lose contact with neighbouring cells and break down the basement membrane to invade other tissues (Moreno-Bueno et al., 2008). Here, our results suggest that TopBP1 overexpression leads to disruption of basal polarity. The loss of basal polarity markers like α6 integrin and Laminin V indicates the reduced interaction of acini with ECM, which can indicate invasive phenotype. We also found that TopBP1 OE leads to Golgi dispersal, a known apical marker in MCF10A 3D cultures. Golgi dispersal is observed in various cancer cell lines, which may be the reason for altered polarity as Golgi plays a major role in maintaining polarised trafficking of proteins.

EMT is a process through which epithelial cells dedifferentiate and acquire mesenchymal phenotype that can increase their motility and invasiveness. However, recent studies suggest that partial EMT phenotypes help in migration and metastasis. TopBP1 OE cells had EMT protein levels similar to malignant cell lines. N-cadherin and vimentin (mesenchymal marker) were down-regulated, and E-cadherin (epithelial marker) was upregulated in TopBP1 OE dissociated cells similar to MCF10CA1a. A recent study also suggests the role of E-cadherin in promoting metastasis in invasive ductal carcinoma (Padmanabhan et al., 2019), which changes our perspective of EMT in tumorigenesis, which may be true in our scenario as well as TopBP1 OE induced increased migration and invasion. Also, there are breast cancer patient studies where

they found that majority of the breast cancer patients(78.8%) are vimentin negative (Kusinska et al., 2009). However, we could not find an explanation to the down regulation of N-cadherin in premalignant and malignant cells. MCF10A cells are non-tumorigenic breast epithelial cells that require cell-cell contact and anchorage for their growth and do not have tumour forming ability. We found that TopBP1 OE induced colony formation, anchorage-independent growth and tumor formation confirms the role of TopBP1 as potent tumor initiation and progression factor.

ATR is a major sensor kinase that gets activated by TopBP1 upon single-strand break and leads to activation of Chk1 to induce cell cycle arrest and DNA repair. Even though TopBP1 levels were already high in cancer cells, its role in inducing DNA damage was not proven. A recent study from Lin's group suggested an association between TopBP1 overexpression and genomic instability by TCGA analysis (Liu et al., 2021). We also found that malignant cells have endogenous damage compared to normal cells and altered activation of the protein involved in DNA damage response. Also, we prove that TopBP1 OE induces DNA damage and activation of DNA damage repair proteins in MCF10A 3D dissociated cells without induction of DNA damage. As TopBP1 knockdown could partially revert these phenotypes confirms the role of TopBP1 in inducing genomic instability.

p53 is a very well studied tumour suppressor gene that is generally mutated in cancer. TopBP1 was known to bind to the DNA binding domain of p53 and inhibit its transcription activity from inducing apoptosis and cell cycle arrest without affecting its total protein level and S15 activation (Liu et al, 2009). However, we found that total p53 and p53 S15 levels were high in TopBP1 OE dissociated cells. We observed that just TopBP1 OE in MCF10A 2D cells did not differ in p53 levels or activation (data not shown). These differences are due to the signalling from the 3D environment. Even though p53 levels were high, we observed that p21 levels were low, as well as the proportion of cells in S and G2-M phases were high in TopBP1 OE dissociated cells confirming the inability of p53 to induce cell cycle arrest. Lin's group have also demonstrated the role of TopBP1 in inducing mutant p53 gain of function to induce proliferation and reduce apoptosis (Liu et al., 2011). It was surprising that TopBP1 OE in

a non-tumorigenic MCF10A cell line grown for 16 days in 3D culture had a similar TP53 variation in a malignant cell line MCF10CA1a that was derived from MCF10A following H-Ras mutation and then passaging for 100 generations in mice. This mutation leads to the formation of the mut p53 protein with M237I. This mutation is reported in various cancers, where the somatic mutation is reported in 176 cancers, out of which 26 breast cancer and 1 germline family (Jordan et al., 2010). SUM149PT cells, a TNBC cell line, also have p53 mutation at M237I (ATCC website). M237I-p53 forms amyloid oligomers in glioblastoma cells expressing a chemoresistance gain-of-function phenotype (Pedrote et al., 2020).

Thus, taken together, TopBP1 OE induces transformation of non-tumorigenic breast epithelial cells when grown on an extracellular matrix. These transformed cells have phenotypic and genotypic characteristics of malignant cells with a mutation in the TP53 gene. Our study also opens multiple gates for understanding and tracking the initiation as well as early-stage changes in cancers. TopBP1 being such a novel regulator in the process of tumorigenesis, also exposes itself as a target for therapeutic as well as treatment. Cancers resulting from higher TopBP1 protein levels can be targeted by the therapeutic molecules that either can inhibit the function or reduce the half-life of TopBP1 inside the cells, that can finally regulate genomic instability and functions of p53.

6.2 Future perspectives

6.2.1. Role of TP53 mutation in transformation

We found that TopBP1 OE induces genomic instability and TP53 mutation. However, the cause and effect are not proven in this study. We can overexpress mut p53 M237I in MCF10A and investigate whether this mutant protein can induce genomic instability and transformation. TP53 status in MCF10CA1a with TopBP1 KD can also be analysed. TopBP1 KD cells can be dissociated after growing in 3D for 10 days, and the TP53 mutation status can be analysed.

6.2.2. Analysis of Whole-exome sequencing data to identify other novel mutations

The whole-exome sequencing of control, TopBP1 OE and MCF10CA1a have provided enormous information regarding 20000 genes and their alterations in these cell lines. It

is a great platform to understand the gene alterations in TopBP1 OE. Initial analysis has revealed a mutation in the TP53BP2 gene present in TopBP1 OE and MCF10CA1a cells not in control MCF10A.

This TP53BP2(NM_001031685.3):c.2900C>G(p.Thr967Arg), is a missense variant in the exon 18 of transcript ENSG00000143514.16 for gene TP53BP2 [GTEx v8]. This variant is not found in gnomAD exomes or genomes. It is predicted to be damaging by BayesDel_addAF, DANN, EIGEN, FATHMM-MKL, LIST-S2, M-CAP, MutationTaster, PrimateAI and SIFT, and predicted to be benign by MVP. This mutation is classified as a variant of unknown significance (VUS) per ACMG guidelines, whether germline or somatic- in the absence of further functional or biochemical studies.

Also, there is another mutation in the TP53INP1 gene is also observed in ToPBP1 OE and MCF10CA1a cells and not in MCF10A.
TP53INP1(NM_033285.4):c.473+168_473+171delGTCA is a deletion located at chr8:95951917 (Hg19). It has a gnomAD Genomes, Version: 2.1.1f = 0.628. Whether germline or somatic—in the absence of further functional or biochemical studies, we classify it as a variant of unknown significance (VUS) per ACMG guidelines.

Similar analysis of the whole-exome sequence data will provide new insights into genes that are altered upon TopBP1 OE in MCF10A and whether similar mutations are present in MCF10CA1a or not. The role of these genes can be further analysed in the TopBP1 OE MCF10A cells by analysing the protein expressions and downstream proteins which may be affected by mutant protein expression. Also, overexpressing the mutant proteins in TopBP1 overexpression and knockdown backgrounds can provide a mechanistic role of the mutations in TopBP1 induced transformation.

Bibliography

Abraham, R.T. (2001). Cell cycle checkpoint signaling through the ATM and ATR kinases. Genes & development *15*, 2177-2196.

Abuin, J.M., Pichel, J.C., Pena, T.F., and Amigo, J. (2015). BigBWA: approaching the Burrows-Wheeler aligner to Big Data technologies. Bioinformatics *31*, 4003-4005.

Anandi, L., Chakravarty, V., Ashiq, K.A., Bodakuntla, S., and Lahiri, M. (2017). DNA-dependent protein kinase plays a central role in transformation of breast epithelial cells following alkylation damage. J Cell Sci *130*, 3749-3763.

Anandi, V.L., Ashiq, K.A., Nitheesh, K., and Lahiri, M. (2016). Platelet-activating factor promotes motility in breast cancer cells and disrupts non-transformed breast acinar structures. Oncol Rep *35*, 179-188.

Araki, H., Leem, S.H., Phongdara, A., and Sugino, A. (1995). Dpb11, which interacts with DNA polymerase II(epsilon) in Saccharomyces cerevisiae, has a dual role in S-phase progression and at a cell cycle checkpoint. Proc Natl Acad Sci U S A *92*, 11791-11795.

Banin, S., Moyal, L., Shieh, S., Taya, Y., Anderson, C.W., Chessa, L., Smorodinsky, N.I., Prives, C., Reiss, Y., Shiloh, Y.*, et al.* (1998). Enhanced phosphorylation of p53 by ATM in response to DNA damage. Science *281*, 1674-1677.

Bodakuntla, S., Libi, A.V., Sural, S., Trivedi, P., and Lahiri, M. (2014). N-nitroso-N-ethylurea activates DNA damage surveillance pathways and induces transformation in mammalian cells. BMC Cancer *14*, 287.

Brown, A.L., Lee, C.H., Schwarz, J.K., Mitiku, N., Piwnica-Worms, H., and Chung, J.H. (1999). A human Cds1-related kinase that functions downstream of ATM protein in the cellular response to DNA damage. Proceedings of the National Academy of Sciences of the United States of America *96*, 3745-3750.

Cancer Genome Atlas, N. (2012). Comprehensive molecular portraits of human breast tumours. Nature *490*, 61-70.

Chen, J., Miller, E.M., and Gallo, K.A. (2010). MLK3 is critical for breast cancer cell migration and promotes a malignant phenotype in mammary epithelial cells. Oncogene *29*, 4399-4411.

Chowdhury, P., Lin, G.E., Liu, K., Song, Y., Lin, F.T., and Lin, W.C. (2014). Targeting TopBP1 at a convergent point of multiple oncogenic pathways for cancer therapy. Nat Commun *5*, 5476.

Cortez, D., Wang, Y., Qin, J., and Elledge, S.J. (1999). Requirement of ATM-dependent phosphorylation of brca1 in the DNA damage response to double-strand breaks. Science *286*, 1162-1166.

Debnath, J., and Brugge, J.S. (2005). Modelling glandular epithelial cancers in three-dimensional cultures. Nat Rev Cancer *5*, 675-688.

Debnath, J., Mills, K.R., Collins, N.L., Reginato, M.J., Muthuswamy, S.K., and Brugge, J.S. (2002). The role of apoptosis in creating and maintaining luminal space within normal and oncogene-expressing mammary acini. Cell *111*, 29-40.

Debnath, J., Muthuswamy, S.K., and Brugge, J.S. (2003). Morphogenesis and oncogenesis of MCF-10A mammary epithelial acini grown in three-dimensional basement membrane cultures. Methods *30*, 256-268.

Deisboeck, T.S., and Couzin, I.D. (2009). Collective behavior in cancer cell populations. Bioessays *31*, 190-197.

Forma, E., Krzeslak, A., Bernaciak, M., Romanowicz-Makowska, H., and Brys, M. (2012). Expression of TopBP1 in hereditary breast cancer. Mol Biol Rep *39*, 7795-7804.

Going, J.J., Nixon, C., Dornan, E.S., Boner, W., Donaldson, M.M., and Morgan, I.M. (2007). Aberrant expression of TopBP1 in breast cancer. Histopathology *50*, 418-424.

Griffiths, G., and Simons, K. (1986). The trans Golgi network: sorting at the exit site of the Golgi complex. Science *234*, 438-443.

Guo, H.B., Johnson, H., Randolph, M., Nagy, T., Blalock, R., and Pierce, M. (2010). Specific posttranslational modification regulates early events in mammary carcinoma formation. Proc Natl Acad Sci U S A *107*, 21116-21121.

Hanahan, D., and Weinberg, R.A. (2011). Hallmarks of cancer: the next generation. Cell *144*, 646-674.

Harper, J.W., and Elledge, S.J. (2007). The DNA damage response: ten years after. Molecular cell *28*, 739-745.

Hebner, C., Weaver, V.M., and Debnath, J. (2008). Modeling morphogenesis and oncogenesis in three-dimensional breast epithelial cultures. Annu Rev Pathol *3*, 313-339.

Hemminki, A., Markie, D., Tomlinson, I., Avizienyte, E., Roth, S., Loukola, A., Bignell, G., Warren, W., Aminoff, M., Hoglund, P.*, et al.* (1998). A serine/threonine kinase gene defective in Peutz-Jeghers syndrome. Nature *391*, 184-187.

Henry, L.A., Johnson, D.A., Sarrio, D., Lee, S., Quinlan, P.R., Crook, T., Thompson, A.M., Reis-Filho, J.S., and Isacke, C.M. (2011). Endoglin expression in breast tumor cells suppresses invasion and metastasis and correlates with improved clinical outcome. Oncogene *30*, 1046-1058.

Hirano, T., Funahashi, S., Uemura, T., and Yanagida, M. (1986). Isolation and characterization of Schizosaccharomyces pombe cutmutants that block nuclear division but not cytokinesis. EMBO J *5*, 2973-2979.

Jordan, J.J., Inga, A., Conway, K., Edmiston, S., Carey, L.A., Wu, L., and Resnick, M.A. (2010). Altered-function p53 missense mutations identified in breast cancers can have subtle effects on transactivation. Mol Cancer Res *8*, 701-716.

Karppinen, S.M., Erkko, H., Reini, K., Pospiech, H., Heikkinen, K., Rapakko, K., Syvaoja, J.E., and Winqvist, R. (2006). Identification of a common polymorphism in the TopBP1 gene associated with hereditary susceptibility to breast and ovarian cancer. Eur J Cancer *42*, 2647-2652.

Kim, J.E., McAvoy, S.A., Smith, D.I., and Chen, J. (2005). Human TopBP1 ensures genome integrity during normal S phase. Mol Cell Biol *25*, 10907-10915.

Kumagai, A., Lee, J., Yoo, H.Y., and Dunphy, W.G. (2006). TopBP1 activates the ATR-ATRIP complex. Cell *124*, 943-955.

Kusinska, R.U., Kordek, R., Pluciennik, E., Bednarek, A.K., Piekarski, J.H., and Potemski, P. (2009). Does vimentin help to delineate the so-called 'basal type breast cancer'? J Exp Clin Cancer Res *28*, 118.

Li, H., and Durbin, R. (2009). Fast and accurate short read alignment with Burrows-Wheeler transform. Bioinformatics *25*, 1754-1760.

Li, H., and Durbin, R. (2010). Fast and accurate long-read alignment with Burrows-Wheeler transform. Bioinformatics *26*, 589-595.

Liu, K., Bellam, N., Lin, H.Y., Wang, B., Stockard, C.R., Grizzle, W.E., and Lin, W.C. (2009). Regulation of p53 by TopBP1: a potential mechanism for p53 inactivation in cancer. Mol Cell Biol *29*, 2673-2693.

Liu, K., Graves, J.D., Lin, F.T., and Lin, W.C. (2021). Overexpression of TopBP1, a canonical ATR/Chk1 activator, paradoxically hinders ATR/Chk1 activation in cancer. J Biol Chem *296*, 100382.

Liu, K., Lin, F.T., Ruppert, J.M., and Lin, W.C. (2003). Regulation of E2F1 by BRCT domain-containing protein TopBP1. Mol Cell Biol *23*, 3287-3304.

Liu, K., Ling, S., and Lin, W.C. (2011). TopBP1 mediates mutant p53 gain of function through NF-Y and p63/p73. Mol Cell Biol *31*, 4464-4481.

Liu, K., Paik, J.C., Wang, B., Lin, F.T., and Lin, W.C. (2006). Regulation of TopBP1 oligomerization by Akt/PKB for cell survival. EMBO J *25*, 4795-4807.

Lv, Y., Huo, Y., Yu, X., Liu, R., Zhang, S., Zheng, X., and Zhang, X. (2016). TopBP1 contributes to the chemoresistance in non-small cell lung cancer through upregulation of p53. Drug Des Devel Ther *10*, 3053-3064.

Makiniemi, M., Hillukkala, T., Tuusa, J., Reini, K., Vaara, M., Huang, D., Pospiech, H., Majuri, I., Westerling, T., Makela, T.P.*, et al.* (2001). BRCT domain-containing protein TopBP1 functions in DNA replication and damage response. J Biol Chem *276*, 30399-30406.

Malkin, D., Li, F.P., Strong, L.C., Fraumeni, J.F., Jr., Nelson, C.E., Kim, D.H., Kassel, J., Gryka, M.A., Bischoff, F.Z., Tainsky, M.A.*, et al.* (1990). Germ line p53 mutations in a familial syndrome of breast cancer, sarcomas, and other neoplasms. Science *250*, 1233-1238.

Meijers-Heijboer, H., van den Ouweland, A., Klijn, J., Wasielewski, M., de Snoo, A., Oldenburg, R., Hollestelle, A., Houben, M., Crepin, E., van Veghel-Plandsoen, M.*, et al.* (2002). Low-penetrance susceptibility to breast cancer due to CHEK2(*)1100delC in noncarriers of BRCA1 or BRCA2 mutations. Nature genetics *31*, 55-59.

Moreno-Bueno, G., Portillo, F., and Cano, A. (2008). Transcriptional regulation of cell polarity in EMT and cancer. Oncogene *27*, 6958-6969.

Nelen, M.R., van Staveren, W.C., Peeters, E.A., Hassel, M.B., Gorlin, R.J., Hamm, H., Lindboe, C.F., Fryns, J.P., Sijmons, R.H., Woods, D.G.*, et al.* (1997). Germline mutations in the PTEN/MMAC1 gene in patients with Cowden disease. Human molecular genetics *6*, 1383-1387.

O'Brien, L.E., Tang, K., Kats, E.S., Schutz-Geschwender, A., Lipschutz, J.H., and Mostov, K.E. (2004). ERK and MMPs sequentially regulate distinct stages of epithelial tubule development. Dev Cell *7*, 21-32.

Pages, V., Bresson, A., Acharya, N., Prakash, S., Fuchs, R.P., and Prakash, L. (2008). Requirement of Rad5 for DNA polymerase zeta-dependent translesion synthesis in Saccharomyces cerevisiae. Genetics *180*, 73-82.

Pedrote, M.M., Motta, M.F., Ferretti, G.D.S., Norberto, D.R., Spohr, T., Lima, F.R.S., Gratton, E., Silva, J.L., and de Oliveira, G.A.P. (2020). Oncogenic Gain of Function in Glioblastoma Is Linked to Mutant p53 Amyloid Oligomers. iScience *23*, 100820.

Petrini, J.H. (1999). The mammalian Mre11-Rad50-nbs1 protein complex: integration of functions in the cellular DNA-damage response. American journal of human genetics *64*, 1264-1269.

Reginato, M.J., Mills, K.R., Becker, E.B., Lynch, D.K., Bonni, A., Muthuswamy, S.K., and Brugge, J.S. (2005). Bim regulation of lumen formation in cultured mammary epithelial acini is targeted by oncogenes. Mol Cell Biol *25*, 4591-4601.

Schupbach, M. (1971). The isolation and genetic classification of UV-sensitive mutants of Schizosaccharomyces pombe. Mutat Res *11*, 361-371.

Sharma, V.K., and Lahiri, M. (2021). Interplay between p300 and HDAC1 regulate acetylation and stability of Api5 to regulate cell proliferation. Sci Rep *11*, 16427.

Sokka, M., Parkkinen, S., Pospiech, H., and Syvaoja, J.E. (2010). Function of TopBP1 in genome stability. Subcell Biochem *50*, 119-141.

Theveneau, E., and Mayor, R. (2011). Can mesenchymal cells undergo collective cell migration? The case of the neural crest. Cell Adh Migr *5*, 490-498.

Ulintz, P.J., Wu, W., and Gates, C.M. (2019). Bioinformatics Analysis of Whole Exome Sequencing Data. Methods Mol Biol *1881*, 277-318.

Vidi, P.A., Bissell, M.J., and Lelievre, S.A. (2013). Three-dimensional culture of human breast epithelial cells: the how and the why. Methods Mol Biol *945*, 193-219.

Wang, H., and Elledge, S.J. (2002). Genetic and physical interactions between DPB11 and DDC1 in the yeast DNA damage response pathway. Genetics *160*, 1295-1304.

Wang, J., Chen, J., and Gong, Z. (2013). TopBP1 controls BLM protein level to maintain genome stability. Mol Cell *52*, 667-678.

Wardlaw, C.P., Carr, A.M., and Oliver, A.W. (2014). TopBP1: A BRCT-scaffold protein functioning in multiple cellular pathways. DNA Repair (Amst) *22*, 165-174.

Woessner, J.F., Jr. (1991). Matrix metalloproteinases and their inhibitors in connective tissue remodeling. FASEB J *5*, 2145-2154.

Xu, Y.J., and Leffak, M. (2010). ATRIP from TopBP1 to ATR--in vitro activation of a DNA damage checkpoint. Proc Natl Acad Sci U S A *107*, 13561-13562.

Yamamoto, R.R., Axton, J.M., Yamamoto, Y., Saunders, R.D., Glover, D.M., and Henderson, D.S. (2000). The Drosophila mus101 gene, which links DNA repair, replication and condensation of heterochromatin in mitosis, encodes a protein with seven BRCA1 C-terminus domains. Genetics *156*, 711-721.

Yamane, K., Chen, J., and Kinsella, T.J. (2003). Both DNA topoisomerase II-binding protein 1 and BRCA1 regulate the G2-M cell cycle checkpoint. Cancer research *63*, 3049-3053.

Yamane, K., Wu, X., and Chen, J. (2002). A DNA damage-regulated BRCT-containing protein, TopBP1, is required for cell survival. Mol Cell Biol *22*, 555-566.

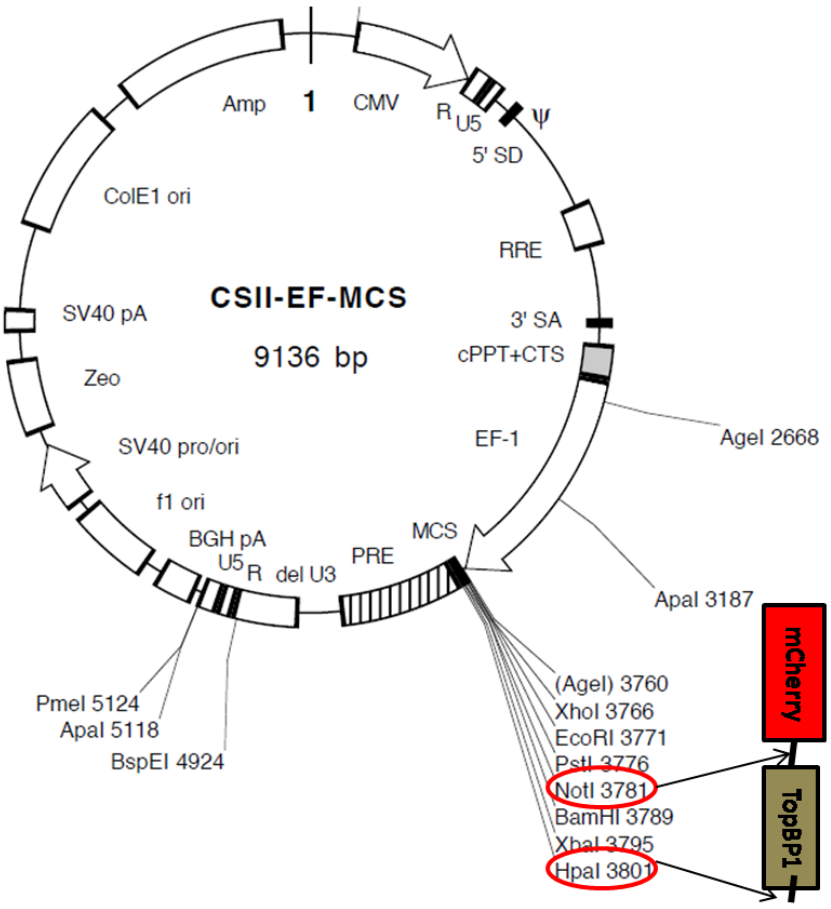
Yu, X., Chini, C.C., He, M., Mer, G., and Chen, J. (2003). The BRCT domain is a phospho-protein binding domain. Science *302*, 639-642.

Zhang, Y., Yan, W., and Chen, X. (2011). Mutant p53 disrupts MCF-10A cell polarity in three-dimensional culture via epithelial-to-mesenchymal transitions. J Biol Chem *286*, 16218-16228.

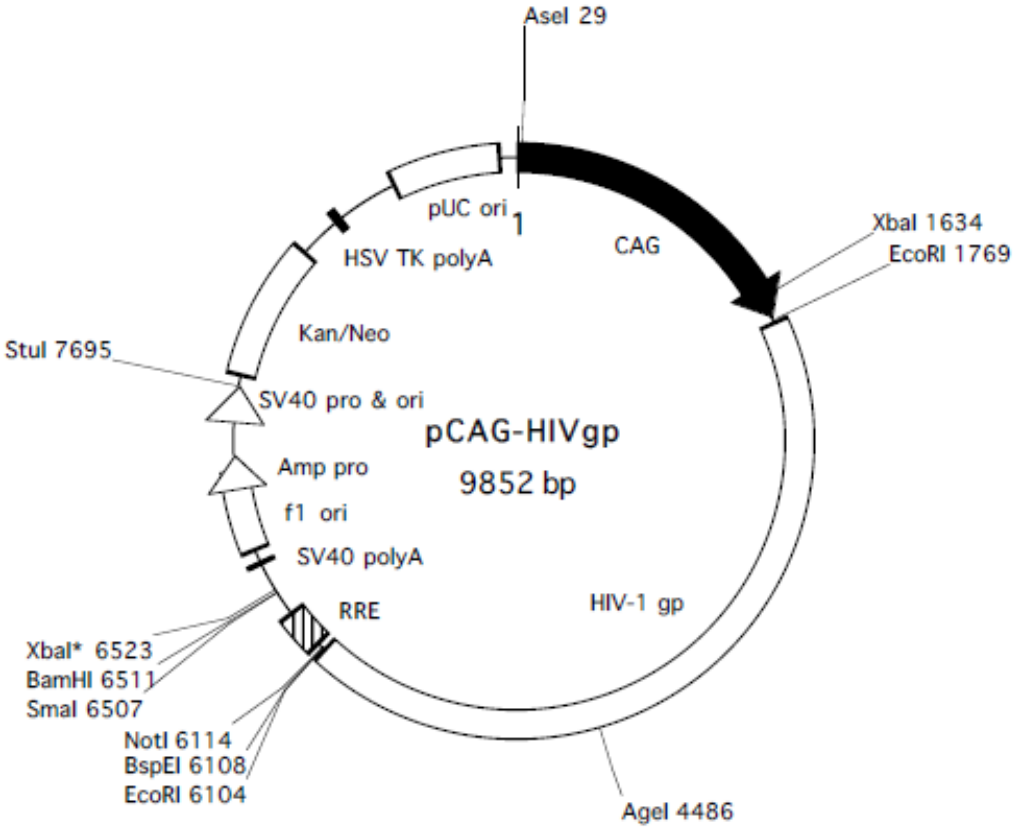
Appendix

Appendix I- Vector maps

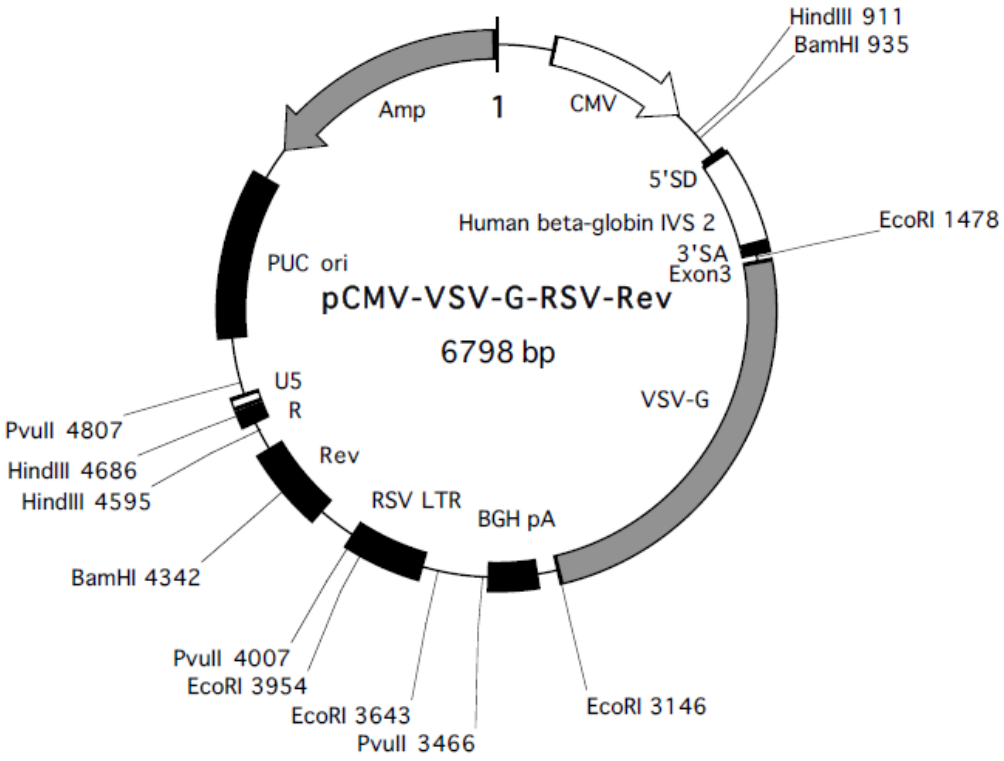
I.1 Vector map of a mCherry-CSII-EF-MCS vector with TopBP1 insertion sites.



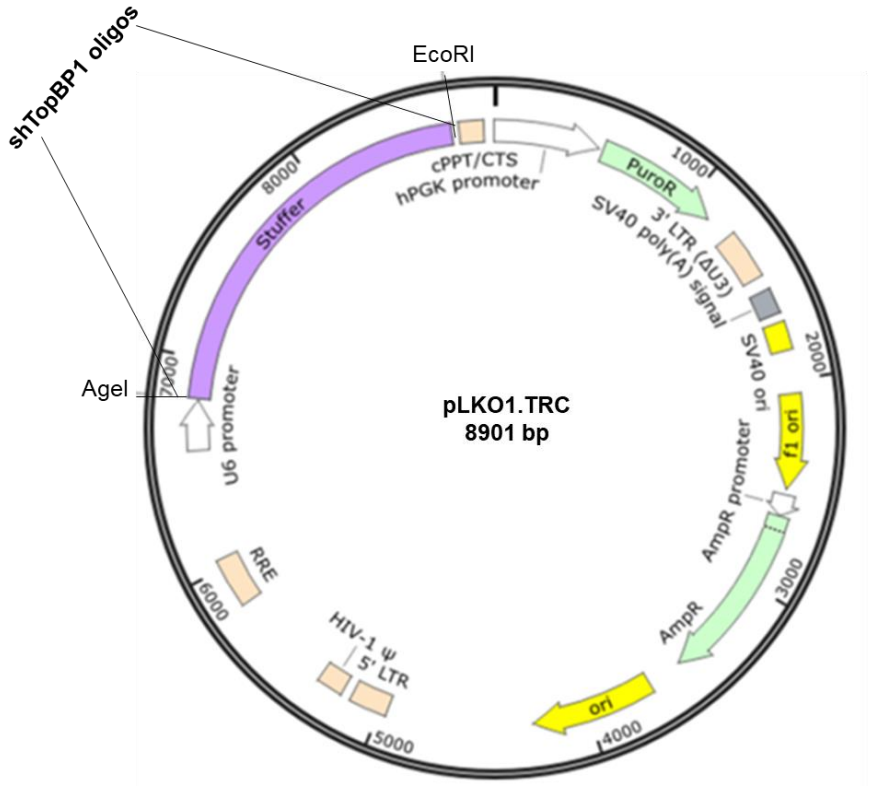
I.2 Vector map of packaging plasmid for generation of TopBP1 overexpression lentiviral particles.



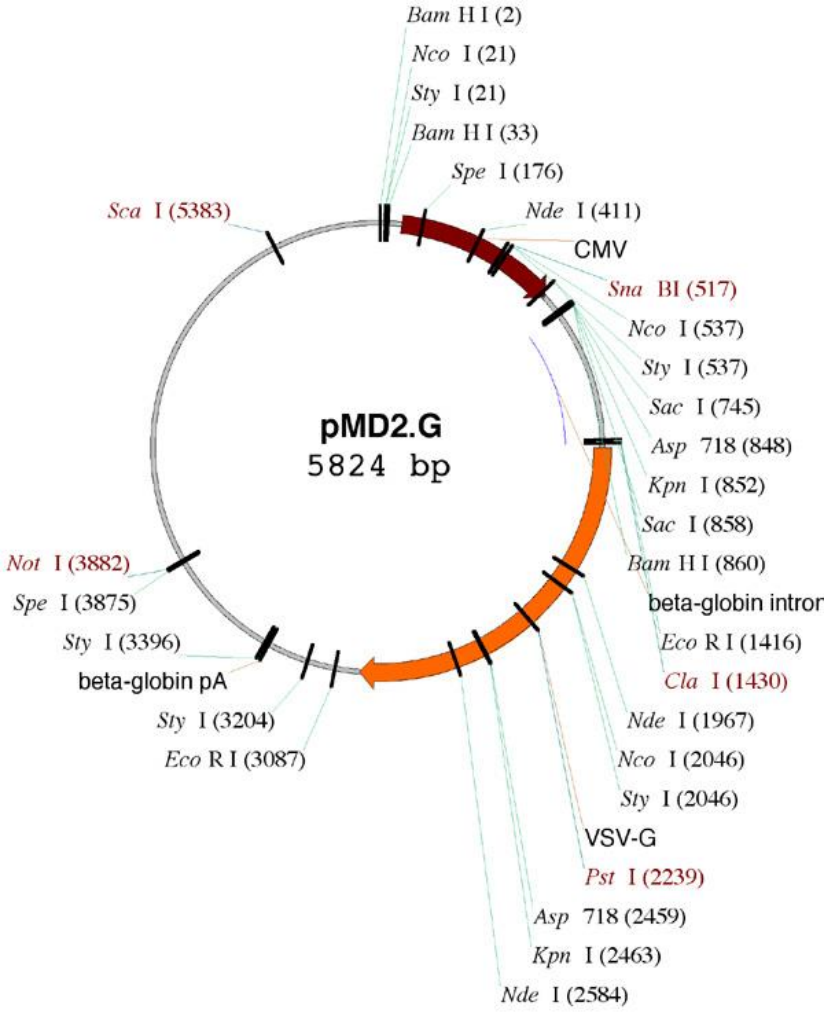
I.3 Vector map of the envelop plasmid for generation of TopBP1 overexpression lentiviral particles.



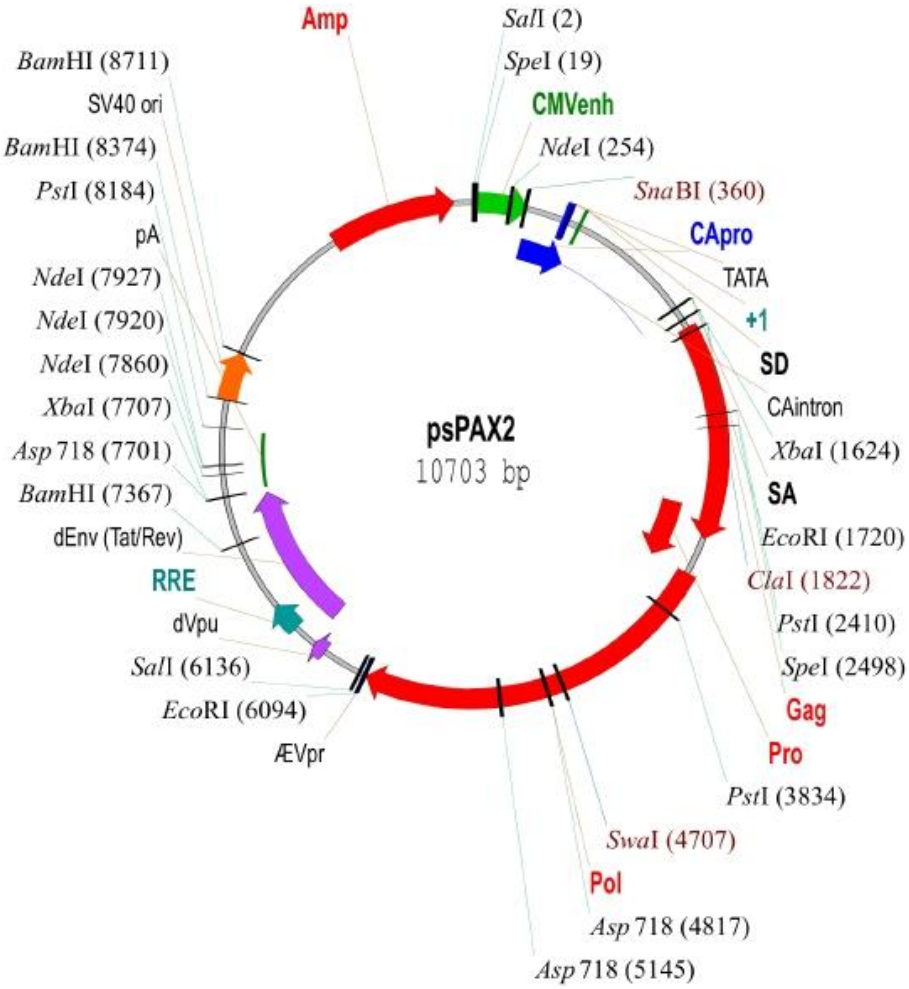
I.4 Vector map of pLKO1.TRC vector with shTopBP1 insertion sites.



I.5 Vector map of the envelop plasmid for generation of TopBP1 knockdown lentiviral particles.



I.6 Vector map of packaging plasmid for generation of TopBP1 knockdown lentiviral particles.



Appendix II- shTopBP1 cloning

II.1 Restriction digestion of pLKO1. TRC vector

Digestion Reagents	Volume (µl)
DNA	~3 µg
10x cut smart buffer (NEB)	5
AgeI Hf (NEB)	3
EcoRI Hf (NEB)	3
Nuclease free water	Make upto 50 µl

II.2: Anealing reaction of shTopBP1 oligos

Anealing Reagents	Volume (µl)
TopBP1 shRNA forward oligo	1.0
TopBP1 shRNA reverse oligo	1.0
10 x T4 DNA Ligase buffer (Takara)	1.0
T4 PNK	0.5
Nuclease free water	6.5

II.3. PCR program for annealing of shTopBP1 oligos

Temperature	37 °C	95 °C	90 °C	85 °C	80 °C	75 °C	70 °C	65 °C	60 °C	55 °C	50 °C	45 °C	40 °C	35 °C	30 °C	25 °C	4°C
Time	30’	5’	1’	1’	1’	1’	1’	1’	1’	1’	1’	1’	1’	1’	1’	1’	hold

II.4: Ligation reaction of annealed shTopBP1 oligos and digested pLKO1. TRC

Reagents	Volume (µl)
Digested pLKO.1-TRC	25ng
shTopBP1	125ng
T4 DNA Ligase (Takara)	1
10x T4DNA Ligase buffer(Takara)	1
Nuclease free water	Upto 10 µl

Appendix III- Buffer compositions

III.1. Western blotting buffer compositions

6X sample buffer (10 ml)

1M Tris pH6.8	3.5 ml
DTT	0.93 g
Glycerol	3.6 ml
SDS	1.1 g
1% bromo-phenol blue	0.6 ml

10X SDS Running Buffer (2L)

Tris base	60.6 g
Glycine	288 g
SDS	20 g

10X Transfer Buffer (2L)

Tris base	58g
Glycine	293g

20X TBS (2L)

Tris base	120 g
NaCl	320 g
KCl	8 g
pH 7.6 with HCl	

III.2. Immunofluorescence buffer compositions

10X PBS (500ml)

NaCl	38 g
$NaHPO_4$	9.38
NaH_2PO_4	2.07 g
pH 7.4 with NaOH	

10X IF buffer (200ml)

PBS (10X)	20 ml
NaN3 (10%)	1ml
BSA	0.2 g
Triton-X	0.4 ml
Tween- 20	0.1 ml

Mounting media (50ml)

Tris (pH 8, 1M)	1 ml
N-propyl gallate	0.25 g
Glycerol	2.07 g
Water	4 ml

Publications

List of Publications

1. **Rintu M Umesh** and Mayurika Lahiri, “Overexpression of TopBP1 leads of transformation with a TP53 mutation of non-tumorigenic breast epithelial cells” ***BioRxiv,*** DOI: https://doi.org/10.1101/2022.04.05.487132
2. Virender Kumar Sharma, Rose Roshan, **Rintu M Umesh,** Aishwarya Venkataravi, and Mayurika Lahiri, “Aurora Kinase B regulate ubiquitin-proteasomal degradation of de-acetylated Api5 in G2/M phase to regulate cell cycle” *(Manuscript under preparation)*
3. Vaishali Chakravarty, Libi Anandi, K. A. Ashiq, K. Abhijith, **Rintu Umesh** and Mayurika Lahiri (2021), “Prolonged Exposure to Platelet Activating Factor Transforms Breast Epithelial Cells”. ***Frontiers in Genetics,*** DOI: 10.339/fgene.2021.634938

Collaborative work

1. Abhijit Chatterjee, Joy Chatterjee, Subrahmanyam Sappati, Tariq Sheikh, **Rintu M Umesh,** Madan Ambhore, Mayurika Lahiri, and Partha Hazra (2021), “Emergence of Aggregation Induced Emission (AIE), Room Temperature Phosphorescence (RTP) and Multi-Stimuli Response from a Single Organic Luminogen by Directed Structural Modification”. ***Journal of Physical Chemistry B,*** DOI: 10.1021/acs.jpcb.1c08126
2. Javid A Malla., **Rintu M Umesh,** Salim Yousf., Shrunal Mane, Surabhi Sharma, Mayurika Lahiri and Pinaki Talukdar (2020) “A Glutathione Activatable Ion Channel Induces Apoptosis in Cancer Cells by Depleting Intracellular Glutathione Levels”. ***Angewandte Chemie***, DOI: 10.1002/anie.202000961.
3. Javid A Malla, **Rintu M Umesh**, Amal Vijay, Arnab Mukherjee, Mayurika Lahiri, and Pinaki Talukdar, (2020) “Apoptosis-inducing activity of a fluorescent barrelrosette M+/Cl channel”. ***Chemical Science*** DOI: 10.1039/c9sc06520b

bioRxiv preprint doi: https://doi.org/10.1101/2022.04.05.487132; this version posted April 6, 2022. The copyright holder for this preprint (which was not certified by peer review) is the author/funder, who has granted bioRxiv a license to display the preprint in perpetuity. It is made available under aCC-BY-NC-ND 4.0 International license.

Overexpression of TopBP1 leads to transformation with a TP53 mutation of non-tumorigenic breast epithelial cells

Rintu M Umesh and Mayurika Lahiri*

Department of Biology, Indian Institute of Science Education and Research, Dr. Homi Bhabha Road, Pune, Maharashtra 411008, India

*Author for correspondence (mayurika.lahiri@iiserpune.ac.in)

Orcid ID: RU., 0000-0003-2157-6028, **M.L.,** 0000-0001-9456-4920

Key word: TopBP1, breast cancer, genomic instability, transformation, p53

Abstract

DNA topoisomerase IIβ - binding protein 1 (TopBP1) is a mediator protein that regulates the cell cycle checkpoint signaling pathway. A plethora of studies suggests high TopBP1 levels are positively associated with various cancers. Although TopBP1 transcript, as well as protein expression levels, are high in breast cancers, its role in breast tumorigenesis is not yet explored. In our studies, we observed that TopBP1 levels are high in premalignant and malignant cells of the MCF10A cancer progression series compared to the non-tumorigenic MCF10A cells. In order to establish the role of TopBP1 in tumorigenesis, TopBP1 overexpression in non-tumorigenic MCF10A, and stable knock-down in malignant MCF10CA1a cells were performed and grown in Matrigel™ as breast spheroids. Overexpression of TopBP1 in MCF10A spheroids induced hyperproliferation, disruption of polarity and cell-cell junctions. Moreover, TopBP1 overexpressing 3D dissociated cells exhibited EMT-like phenotype and tumorigenic properties such as increased cell migration, invasion, colony formation capabilitiy and anchorage-independent growth, indicating acquisition of cellular transformation. Finally, we demonstrated TopBP1 overexpressing cells to form tumors in athymic mice thereby confirming their tumorigenic potential. We also confirmed that overexpression of TopBP1 led to a mutation in TP53 and other genomic insults. To summarise, we observed that ectopic expression of TopBP1 transforms MCF10A breast epithelial cells. These transformed cells harbour phenotypic and genotypic characteristics similar to that of malignant cells.

bioRxiv preprint doi: https://doi.org/10.1101/2022.04.05.487132; this version posted April 6, 2022. The copyright holder for this preprint (which was not certified by peer review) is the author/funder, who has granted bioRxiv a license to display the preprint in perpetuity. It is made available under aCC-BY-NC-ND 4.0 International license.

Introduction

DNA topoisomerase IIβ-binding protein 1 (TopBP1) participates in the activation of the DNA damage checkpoint to maintain genome integrity (Xu and Leffak, 2010). TopBP1 gene is located at chromosome 3q22.1, and is conserved across species (Wardlaw et al., 2014). It was first identified through two independent screens in *S. pombe* as rad4 (Schupbach, 1971), and cut5 (Hirano et al., 1986). Further human TopBP1 was identified as an interactor of Topoisomerase IIβ in a yeast two-hybrid screen (Wang and Elledge, 2002). The other known homologues of TopBP1 are Dpb11 (*S. cerevisiae*) (Araki et al., 1995), Mus101 (*D. melanogaster*) (Yamamoto et al., 2000), Mei1 (*A. thaliana*) and Xmus101 (*X. laevis*).

TopBP1 has eight BRCA1 C-terminus (BRCT) repeat domains through which it interacts with other proteins (Yu et al., 2003) and an ATR activation domain (AAD) which is necessary to stimulate the kinase activity of ATR (Kumagai et al., 2006) and thus checkpoint activation. Other than its essential role in DNA damage response, TopBP1 is also involved in transcriptional regulation of genes involved in cell proliferation and apoptosis such as E2F1 and c-Myc (Liu et al., 2003). Akt phosphorylates TopBP1 at serine residue 1159 which leads to its oligomerization through the BRCT domains 7 and 8 and thus shifts its function from checkpoint activation to transcriptional regulation (Liu et al., 2006). Oligomerized TopBP1 binds to E2F1 and inhibits E2F1-mediated apoptosis (Liu et al., 2006). TopBP1's interaction with BLM (Bloom syndrome helicase) has been reported to inhibit sister chromatid exchange thus maintaining genome stability (Wang et al., 2013). TopBP1 also plays a role during replication initiation by interacting with Treslin to facilitate Cdc45 loading onto the replication origins (Kumagai et al., 2006). At the physiological level, TopBP1 is required for the G1 to S transition in the cell cycle.

Aberrant expression of TopBP1 has been observed in breast cancers. Immunohistochemical studies performed on breast cancer biopsy samples showed TopBP1 to be upregulated in breast cancer tissues. TopBP1 overexpression was associated with higher-grade tumors and reduced patient survival (Forma et al., 2012; Going et al., 2007; Liu et al., 2009). p53 is a well-studied tumor suppressor and in the majority of cancers, p53 is mutated leading to gain of function mutations in the protein.TopBP1 interacts with the DNA binding domain of p53 through its BRCT domains 7 and 8 and thus inhibits the promotor binding activity of p53 (Liu et al., 2009). In their study, Liu and colleagues showed that TopBP1 overexpression reduced the p53 transcriptional

bioRxiv preprint doi: https://doi.org/10.1101/2022.04.05.487132; this version posted April 6, 2022. The copyright holder for this preprint (which was not certified by peer review) is the author/funder, who has granted bioRxiv a license to display the preprint in perpetuity. It is made available under aCC-BY-NC-ND 4.0 International license.

activity upon DNA damage. However, the levels of total p53 and its activation at the serine residue 15 remained unaffected (Liu et al., 2009). TopBP1 interacts with p53 hot spot mutants and increase proliferation and decrease apoptosis by affecting p53 transcriptional activity (Liu et al., 2011). Other studies have shown TopBP1 to induce chemoresistance by upregulating p53 levels (Lv et al., 2016). PI(3)K/Akt, p53 and E2F1 are some of the common pathways that are deregulated in cancers (Cancer Genome Atlas, 2012). A recent study found that TopBP1 paradoxically hinders ATR/Chk1 activation in cancers (Liu et al., 2021). As mentioned previously, TopBP1 regulates the function of various cancer regulatory proteins such as PI(3)K/Akt, p53 and E2F1 and affects the viability of cancer cells making it a novel therapeutic target (Chowdhury et al., 2014).

There are a number of studies that suggest an oncogenic role for TopBP1. Depletion of TopBP1 makes various cancer cells susceptible to undergo apoptosis, however, higher levels of TopBP1 promotes the survival of cancer cells. Most of the published studies focus and emphasize on the tumor-promoting property of TopBP1. To investigate the role of TopBP1 in breast tumorigenesis, the MCF10A cancer progression series was used as a model system. The MCF10A series consists of MCF10A (non-transformed epithelial cells), MCF10AT1 (premalignant cells) and MCF10CA1a (malignant cells). MCF10A was derived from the parental MCF10 cells from a woman with fibrocystic mammary tissue (Soule et al., 1990). The adherent MCF10A cells were transformed with constitutive H-RAS to generate MCF10AT1. MCF10CA1a was derived by continuous passaging of MCF10AT1 in mice for 100 generations (Santner et al., 2001). In our study, we report a novel tumor initiatory role of TopBP1. In this study, we demonstrate that ectopic expression of TopBP1 in non-tumorigenic cells promote the signaling cascade in favor of initiation of various tumorigenic properties. Breast epithelial cells with ectopic expression of TopBP1 when grown as 3D cultures formed spheroids with increased size, filled lumen, hyperproliferation, and altered polarity similar to spheroids formed by malignant cells. Also, the cells dissociated from the 3D cultures of TopBP1 overexpressing acini had morphology similar to the malignant MCF10CA1a cells. As expected, knockdown of TopBP1 in the malignant cells represses the spheroidal size and proliferation in the 3D cultures. TopBP1 overexpressing cells dissociated from 3D cultures exhibited increased migration, invasion, colony formation, anchorage-independent growth and tumorigenic potential similar to the malignant MCF10CA1a cells. TopBP1 overexpression in non-tumorigenic cells induced endogenous DNA damage and activation of DNA damage response (DDR) similar to the

bioRxiv preprint doi: https://doi.org/10.1101/2022.04.05.487132; this version posted April 6, 2022. The copyright holder for this preprint (which was not certified by peer review) is the author/funder, who has granted bioRxiv a license to display the preprint in perpetuity. It is made available under aCC-BY-NC-ND 4.0 International license.

malignant cells suggesting its role in maintaining genome stability. TopBP1 overexpressing cells also exhibited mutation in TP53 gene similar to the malignant MCF10CA1a cells. Taken together we report TopBP1 as a novel initiator as well as a regulator of breast tumorigenesis that is required to maintain genomic stability.

Results

Overexpression of TopBP1 leads to an increase in breast acinar size

To investigate the role of TopBP1 in the transformation of breast epithelial cells, TopBP1 protein expression levels were analyzed in the MCF10A cancer progression series. There was a significant increase in TopBP1 expression in pre-malignant MCF10AT1 with a further increase in the malignant MCF10CA1a cells when compared to the non-tumorigenic MCF10A cells (Figure 1A-C). These results suggest TopBP1 may play an important role during the process of tumorigenesis. To investigate further the role of TopBP1 in breast tumorigenesis, TopBP1 was overexpressed in MCF10A (TopBP1 OE) (Figure 1D-E), and the transformative potential of these cells was analyzed. TopBP1 OE cells formed large spheroids similar to multiacinar cultures with filled lumen as compared to the control cells (mCherry-MCF10A) (Figure 1F). There was a significant increase in the surface area and volume of the TopBP1 OE spheroids when compared to the control acini (Figure 1G-H). Interestingly, TopBP1 OE spheroids showed a reduction in sphericity when compared to the control acini suggesting the presence of protrusion-like phenotype that are the initial events of transformation (Figure 1I). TopBP1 OE spheroids were dissociated and grown as monolayer cultures. TopBP1 OE 3D dissociated cells exhibited morphology similar to the malignant MCF10CA1a cells (Figure 1J). However, when TopBP1 OE cells were grown as monolayer cultures, they showed phenotypes similar to the non-tumorigenic MCF10A cells (Figure 1K). These results suggest that overexpression of TopBP1 in non-tumorigenic MCF10A cells grown as three-dimensional breast acinar cultures leads to morphological changes that are similar to the malignant cells MCF10CA1a.

bioRxiv preprint doi: https://doi.org/10.1101/2022.04.05.487132; this version posted April 6, 2022. The copyright holder for this preprint (which was not certified by peer review) is the author/funder, who has granted bioRxiv a license to display the preprint in perpetuity. It is made available under aCC-BY-NC-ND 4.0 International license.

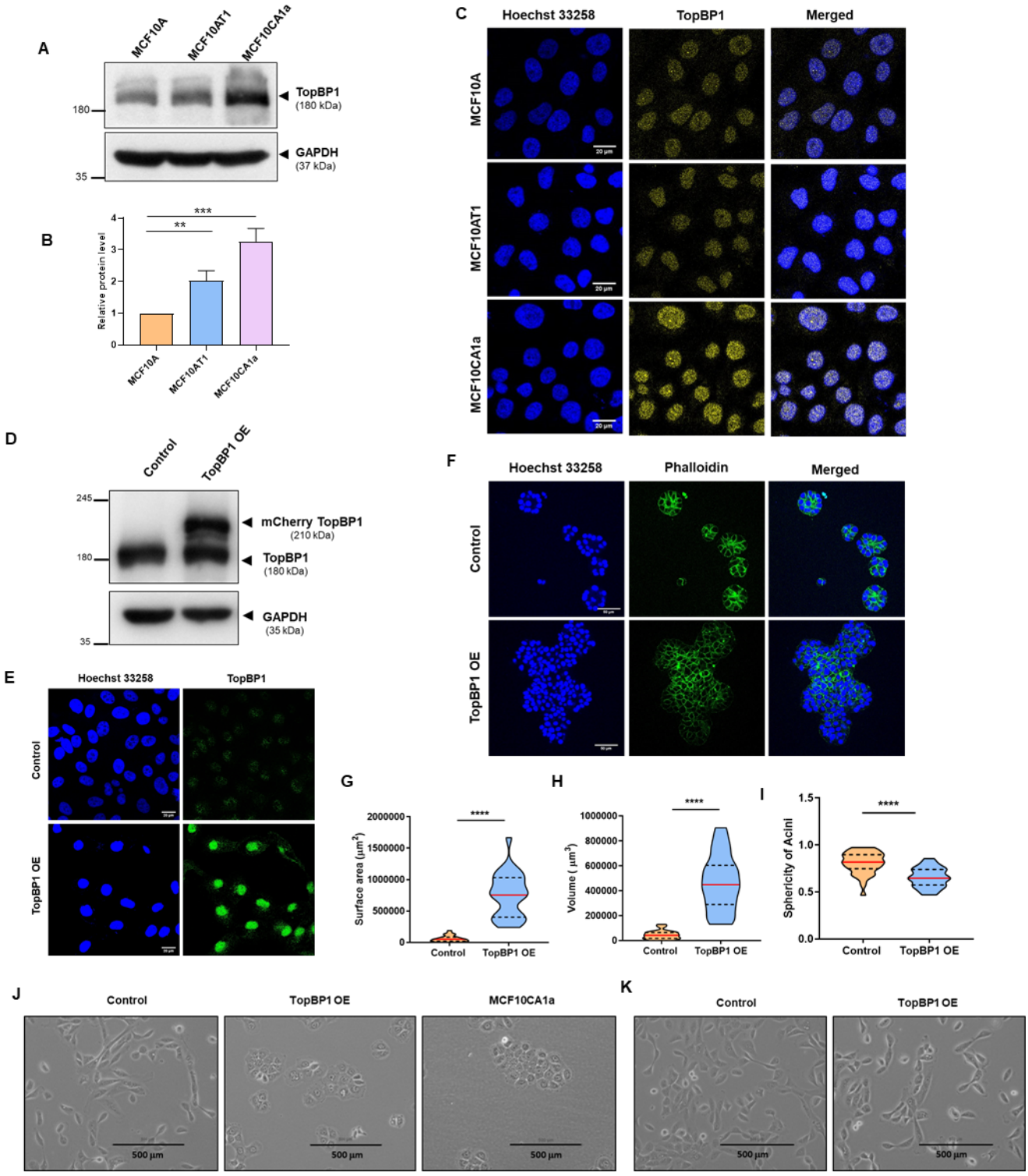


Figure 1: TopBP1 overexpression leads to increased acinar size in MCF10A 3D cultures

A) Western blot analysis and C) immunofluorescence assay showing varying levels of TopBP1 in MCF10A, MCF10AT1 and MCF10CA1a (2D) cells. GAPDH was used as loading control. B) Quantification showing the fold change of TopBP1 levels after normalizing with GAPDH. Statistical analysis was done using One-way ANOVA (*** p

bioRxiv preprint doi: https://doi.org/10.1101/2022.04.05.487132; this version posted April 6, 2022. The copyright holder for this preprint (which was not certified by peer review) is the author/funder, who has granted bioRxiv a license to display the preprint in perpetuity. It is made available under aCC-BY-NC-ND 4.0 International license.

<0.001, **p <0.01). D) MCF10A cells stably expressing mCherry (control) and TopBP1 OE (2D) were lyzed and immunoblotting was performed using TopBP1 specific antibody. E) mCherry MCF10A (control) and TopBP1 OE MCF10A (2D) cells were immunostained using TopBP1 specific antibody to confirm the overexpression (scale bar: 20 μm). F) Representative images of mCherry MCF10A (control) and TopBP1 OE MCF10A cells grown as 3D "on-top" cultures for 10 days and fixed and stained for phalloidin (green) and Hoechst 33258 (blue) (scale bar: 50 μm). G) Surface area, H) Volume, and I) Sphericity of TopBP1 OE MCF10A acini were calculated using Huygens software (SVI, Netherlands) and represented as violin plots. >50 acini from 3 independent experiments were analyzed. Statistical analysis was done using the Mann Whitney test (**** p <0.0001). J) Representative images of mCherry MCF10A (control) and TopBP1 OE MCF10A 3D dissociated and MCF10CA1a 2D cells. K) Representative images of mCherry and TopBP1 OE MCF10A 2D cells. Images were acquired on the ECLIPSE TS100 Nikon microscope (scale bar: 500 μm).

TopBP1 knockdown reduces spheroid size in malignant cells

As we have demonstrated MCF10CA1a to have higher levels of TopBP1 and TopBP1 OE cells morphologically resembled MCF10CA1a cells, we next investigated whether stable knockdown of TopBP1 in MCF10CA1a would lead to a reversal from the malignant to the non-tumorigenic phenotype when grown as 3D cultures (Figure 2A-C). Filled lumen and lower sphericity are properties associated with cancer cells. Upon TopBP1 knockdown, MCF10CA1a cells formed spheroids with a clear lumen (Figure 2D). The surface area and volume of the spheroids of shTopBP1- MCF10CA1a spheroids were significantly reduced when compared to the control pLKO.1 MCF10CA1a spheroids (Figure 2E-F). The sphericity of these spheroids increased upon TopBP1 KD (Figure 2G). These results suggest that TopBP1 KD in MCF10CA1a reduces spheroid size, thus leading to alteration in the morphology of the malignant cells.

bioRxiv preprint doi: https://doi.org/10.1101/2022.04.05.487132; this version posted April 6, 2022. The copyright holder for this preprint (which was not certified by peer review) is the author/funder, who has granted bioRxiv a license to display the preprint in perpetuity. It is made available under aCC-BY-NC-ND 4.0 International license.

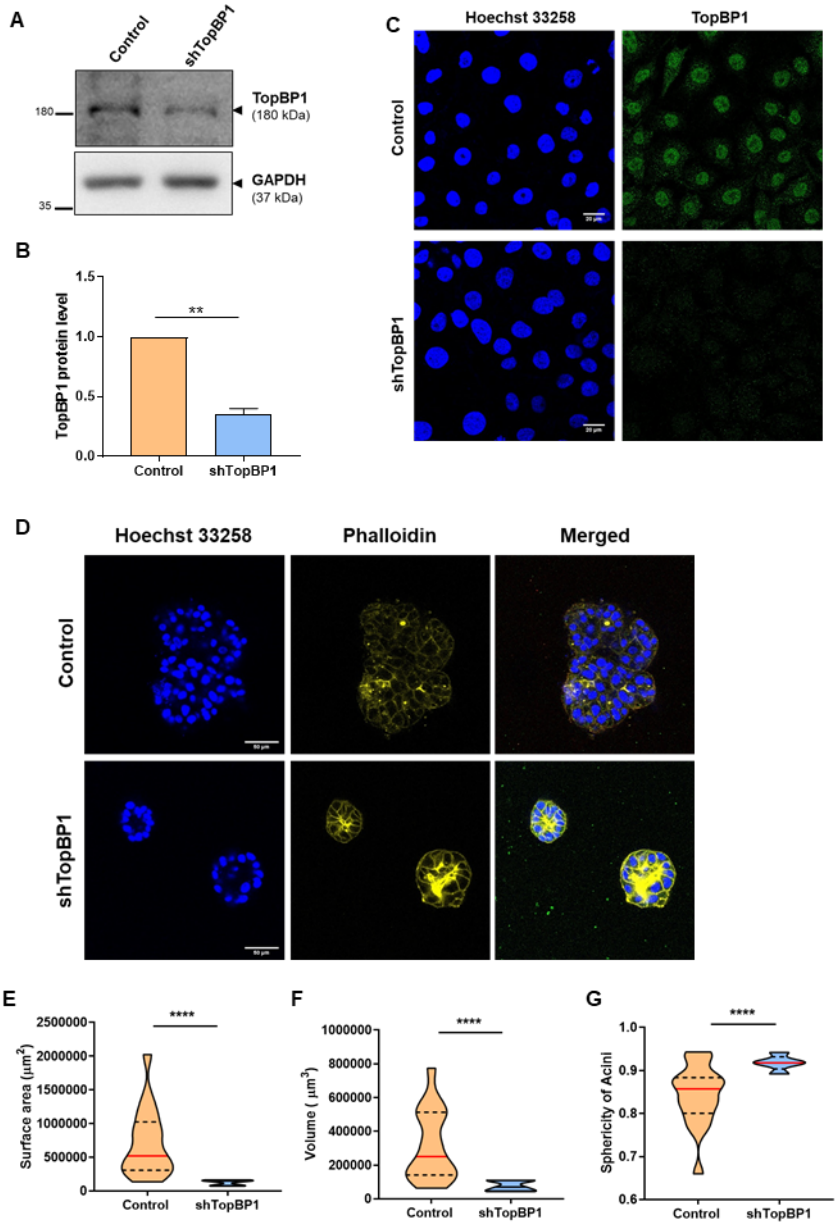


Figure 2: TopBP1 knockdown reduces spheroid size in MCF10CA1a 3D cultures

MCF10CA1a cells stably expressing pLKO1.TRC (control) and shTopBP1 (2D) were A) lyzed and immunoblotting was performed using TopBP1 specific antibody. B) The fold change of TopBP1 was quantified after normalizing with GAPDH. Statistical analysis was done using Student's t-test (** p <0.01). C) pLKO.1 MCF10CA1a (control) and shTopBP1 MCF10CA1a 2D cells were immunostained using TopBP1 specific antibody to confirm the knockdown (scale bar: 20 µm). D) Representative images of pLKO.1 MCF10CA1a (control) and shTopBP1 MCF10CA1a cells grown as 3D cultures for 10 days and fixed and stained for phalloidin (yellow) and Hoechst 33258 (blue) (scale bar: 50 µm). E) Surface area, F) Volume and G) Sphericity of these acini were calculated using Huygens software

bioRxiv preprint doi: https://doi.org/10.1101/2022.04.05.487132; this version posted April 6, 2022. The copyright holder for this preprint (which was not certified by peer review) is the author/funder, who has granted bioRxiv a license to display the preprint in perpetuity. It is made available under aCC-BY-NC-ND 4.0 International license.

(SVI, Netherlands) and represented as violin plots. >50 acini from 3 independent experiments were analyzed. Statistical analysis was done using Mann Whitney test (**** p <0.0001).

Overexpression of TopBP1 leads to cell hyperproliferation

Our results demonstrate that acinar size increases upon overexpression of TopBP1. To further corroborate this data, the number of cells that form the acini were calculated. MCF10A acini are normally comprised of 30-35 cells. Overexpression of TopBP1 led to a significant increase in the percentage of acini that were comprised of more than 50 cells when compared to the control (Figure 3A). Upon knockdown of TopBP1 in MCF10CA1a, there was a significant reduction in the percentage of acini that had more than 50 cells when compared to the control (Figure 3B). These results suggest TopBP1 expression levels affect proliferation. To investigate the proliferative potential of TopBP1, acini ectopically expressing TopBP1 were stained for Ki67, a proliferation marker. It was observed that 100% of TopBP1 OE acini had more than 33% Ki67 positive cells when compared to the control (Figure 3C) which was similar to the malignant MCF10CA1a spheroids (Figure 3C). Immunoblotting analysis demonstrated increased Ki67 protein expression in the lysates from TopBP1 OE and malignant MCF10CA1a spheroids when compared to the control (Figure 3D-E). TopBP1 knockdown led to a significant reduction in Ki67 expression levels in MCF10CA1a 3D lysates (Figure F-G). These results suggest TopBP1 to regulate proliferation of cells grown as 3D cultures. TopBP1 OE 3D dissociated cells also exhibited increased proliferation when compared to the control as was observed by an increase in cell numbers (Figure 3H). This increase in proliferation indicates a higher fraction of the cells in the S and G2-M phases of the cell cycle. To investigate the number of cells in each phase of the cell cycle, the cell cycle profile of control, TopBP1 OE and MCF10CA1a cells were analyzed. It was observed that TopBP1 OE had a higher percentage of cells in the S (14%) and G2-M (31%) phases, which was similar to the malignant MCF10CA1a cells (S: 13% and G2-M: 42%) when compared to the control (S: 7% and G2-M: 16%) (Figure 3I). Cells were also analyzed for the expression of two other S phase cell cycle markers, PCNA and Cyclin A. Both PCNA and Cyclin A expression levels were significantly higher in TopBP1 OE cells when compared to the control. This increase in expression was similar to the expression pattern of both PCNA and Cyclin A in MCF10CA1a cells (Figure 3J-O). These results conclude that overexpression of TopBP1 leads to cellular hyper-proliferation, which is one of the hallmarks of cancer cells.

bioRxiv preprint doi: https://doi.org/10.1101/2022.04.05.487132; this version posted April 6, 2022. The copyright holder for this preprint (which was not certified by peer review) is the author/funder, who has granted bioRxiv a license to display the preprint in perpetuity. It is made available under aCC-BY-NC-ND 4.0 International license.

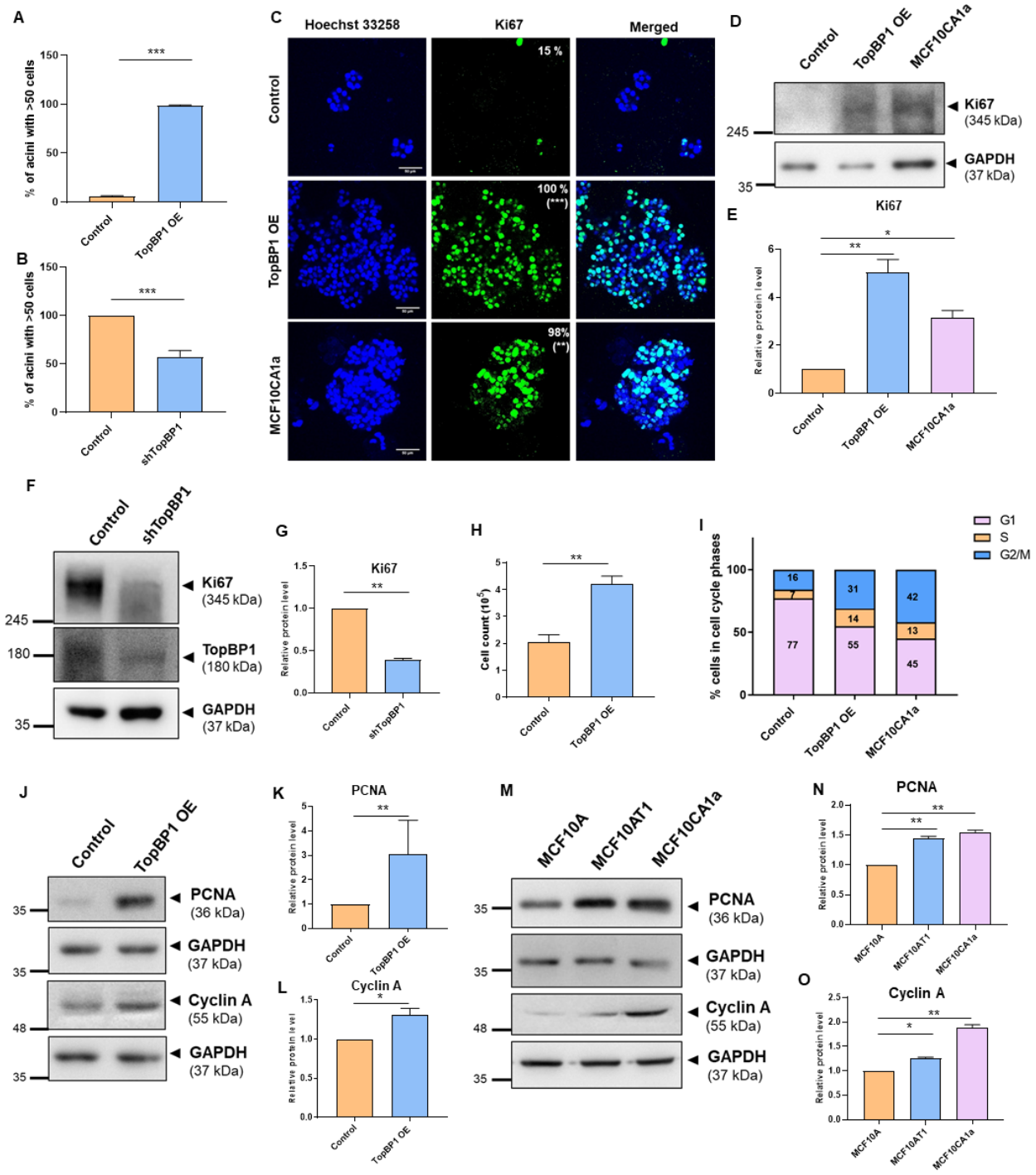


Figure 3:TopBP1 overexpression increases proliferation

The number of cells per acini of A) mCherry MCF10A (control), TopBP1 OE MCF10A, B) pLKO1-MCF10CA1a (control) and shTopBP1 MCF10CA1a were counted manually and the percentage of acini with more than 50 cells were plotted as a bar graph. C) Representative images of mCherry MCF10A (control), TopBP1 OE and MCF10CA1a cells grown as 3D cultures for 10 days and fixed and immunostained for Ki67 (green) (scale bar: 50 µm). Number of Ki67 positive cells were manually counted and divided by total number

bioRxiv preprint doi: https://doi.org/10.1101/2022.04.05.487132; this version posted April 6, 2022. The copyright holder for this preprint (which was not certified by peer review) is the author/funder, who has granted bioRxiv a license to display the preprint in perpetuity. It is made available under aCC-BY-NC-ND 4.0 International license.

of cells per acini. Percentage of acini with more than 33% of Ki67 positive cells (clinically relevent value) were mentioned on the upper right corner of the Ki67 image. >50 acini from 3 independent experiments were analyzed. Statistical analysis was done using Mann Whitney test (** p <0.01, *** p <0.001). D) 16-day 3D cultures of mCherry MCF10A (control), TopBP1 OE spheroids and 10-day cultures of MCF10CA1a spheroids were lyzed and immunoblotting was performed using Ki67 specific antibody. E) Quantification showing the fold change of Ki67 after normalizing with GAPDH. F) 10-day 3D cultures of pLKO1-MCF10CA1a (control) and shTopBP1 MCF10CA1a were lyzed and immunoblotting was performed using Ki67 specific antibody. G) Quantification showing the fold change of Ki67 after normalizing with GAPDH. H) mCherry MCF10A (control) and TopBP1 OE MCF10A 3D dissociated cell number was counted using Scepter™ 72 hrs post-seeding. Statistical analysis was done using a Paired Student's t-test (** p <0.01). I) mCherry MCF10A (control), TopBP1 OE MCF10A 3D dissociated cells and MCF10CA1a 2D cells were fixed in ethanol and stained using propidium iodide. Percentage of cells in the different cell cycle phases were analyzed on a BD Accuri flow cytometer and plotted as box plots. J) mCherry MCF10A (control) and TopBP1 OE MCF10A 3D dissociated cells and M) MCF10A, MCF10AT1 and MCF10CA1a 2D cells were lyzed and immunoblotting was performed to analyze the levels of PCNA and Cyclin A. Quantification showing the fold change of J, K, M and N) PCNA and J, L, M and O) Cyclin A after normalizing to GAPDH. Statistical analysis was done using Paired Student's t-test for TopBP1 OE and One-way ANOVA for MCF10A series (** p <0.01, * p <0.05).

TopBP1 overexpression leads to disruption of polarity

De-regulation of polarity is one of the characteristics of epithelial cancers (Debnath and Brugge, 2005). To investigate the effect of TopBP1 on polarity, TopBP1 OE acini were stained using basal polarity markers α6-integrin, and Laminin V. Loss or mislocalization of α6-integrin (Figure 4A) and Laminin V (Figure 4B) at the basal region were observed in TopBP1 OE speroids, similar to that of the malignant spheroids (Figure 4A-B). Golgi is apically located in MCF10A 3D cultures and is thus considered as an apical polarity marker (Debnath et al., 2003). To investigate whether TopBP1 plays a role in maintaining apical polarity, TopBP1 OE acini were stained with GM130, a cis-Golgi marker. It was observed that TopBP1 OE acini had dispersed Golgi architecture compared to the compact apically located Golgi in the control acini (Figure 4C). Golgi dispersal was further confirmed by staining the 3D dissociated TopBP1 OE cells using GM130. Similar

bioRxiv preprint doi: https://doi.org/10.1101/2022.04.05.487132; this version posted April 6, 2022. The copyright holder for this preprint (which was not certified by peer review) is the author/funder, who has granted bioRxiv a license to display the preprint in perpetuity. It is made available under aCC-BY-NC-ND 4.0 International license.

dispersed Golgi was also observed in the malignant cells (Figure 4D), which was quantified by measuring the Golgi area (Figure 4E). β-catenin, a cell-cell junction marker, showed dispersed or speckle-like staining in TopBP1 OE acini when compared to the control acini, which was similar to MCF10CA1a spheroids suggesting disruption of cell-cell contact (Figure 4F). These results suggest that overexpression of TopBP1 led to disruption of the apicobasal and lateral polarity of MCF10A acini which is comparable to the disruption observed in the malignant MCF10CA1a spheroids, thus indicating a transformative potential of TopBP1.

bioRxiv preprint doi: https://doi.org/10.1101/2022.04.05.487132; this version posted April 6, 2022. The copyright holder for this preprint (which was not certified by peer review) is the author/funder, who has granted bioRxiv a license to display the preprint in perpetuity. It is made available under aCC-BY-NC-ND 4.0 International license.

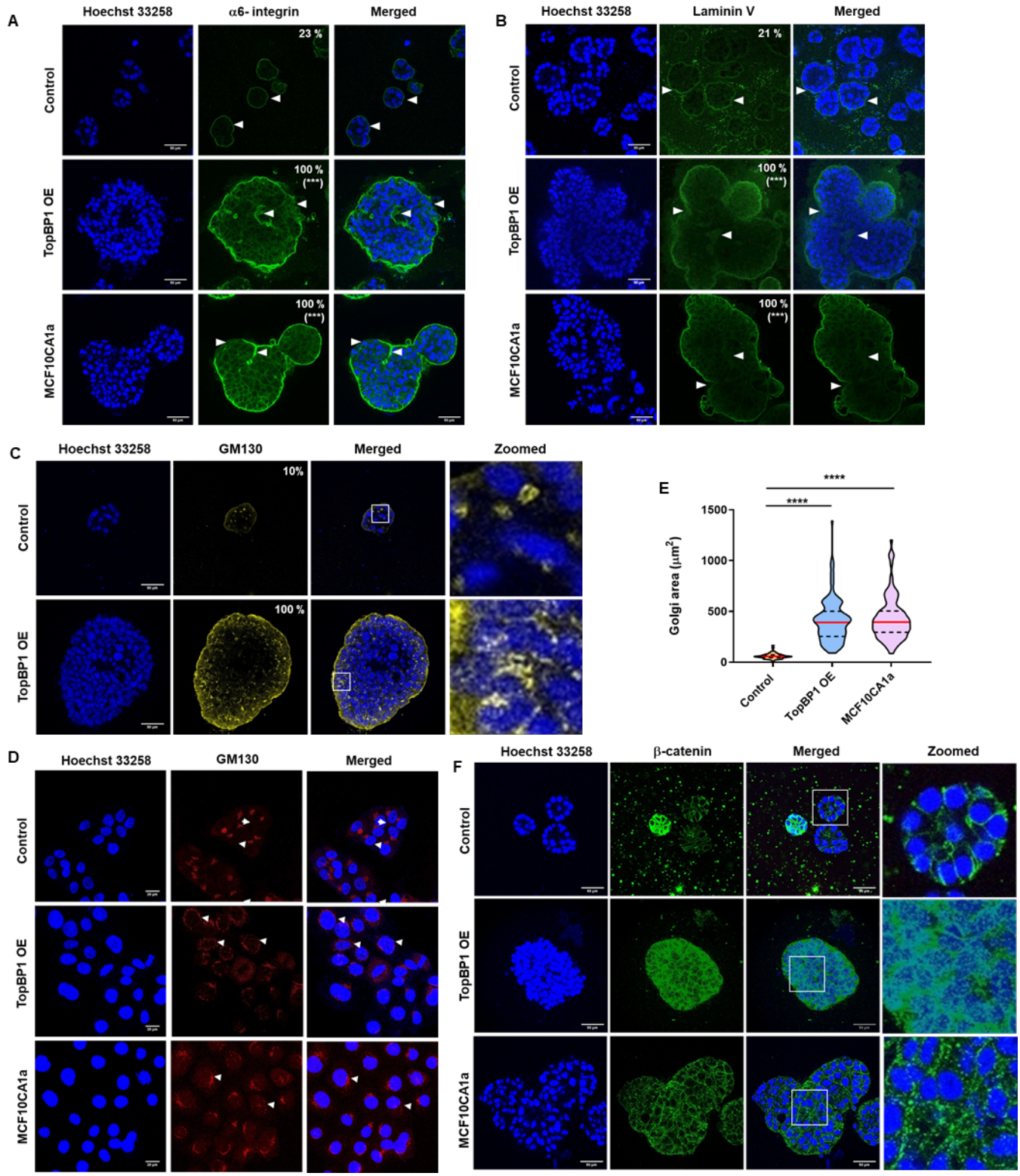


Figure 4: TopBP1 overexpression disrupts cell polarity

Representative images of mCherry MCF10A (control), TopBP1 OE MCF10A and MCF10CA1a cells grown as 3D cultures for 10 days, fixed and immunostained for A) α6-integrin B) Laminin V, C) GM130 and F) β-catenin (scale bar: 50 μm). D) mCherry

bioRxiv preprint doi: https://doi.org/10.1101/2022.04.05.487132; this version posted April 6, 2022. The copyright holder for this preprint (which was not certified by peer review) is the author/funder, who has granted bioRxiv a license to display the preprint in perpetuity. It is made available under aCC-BY-NC-ND 4.0 International license.

MCF10A (control), TopBP1 OE MCF10A 3D dissociated and MCF10CA1a 2D cells were immunostained using GM130, a Golgi marker and E) Golgi dispersal was calculated by measuring Golgi area using ImageJ software. >50 acini from 3 independent experiments were analyzed. Statistical analysis was done using Mann Whitney test (*** p <0.001).

Expression of EMT markers in TopBP1 overexpression is similar to malignant cells

Epithelial to mesenchymal transition (EMT) is a process acquired by cancer cells that favors their motility and invasiveness. To investigate the function of TopBP1 in the regulation of EMT, the expression of various EMT markers were analyzed. It was observed that there were acini with varying expressions of vimentin, a mesenchymal marker. 100% of mCherry-MCF10A acini (control) were vimentin-positive compared to only 11% of TopBP1 OE acini (Figure 5A). Similarly, only 14% of the MCF10CA1a 3D spheroids were vimentin-positive (Figure 5A). The TopBP1 OE dissociated cells also exhibited heterogeneity in vimentin expression similar to that of MCF10CA1a cells. Only 14% of TopBP1 OE and 23% of MCF10CA1a cells were vimentin-positive, whereas 100% of control cells were vimentin-positive (Figure 5B). Vimentin expression was further confirmed using immunoblotting where TopBP1 OE cells were observed to have negligible levels of vimentin when compared to the control, which was also similar to the low levels observed in MCF10CA1a cells (Figure 5C-D and S1A-B). The levels of the epithelial marker, E-cadherin and mesenchymal marker, N-cadherin, were also analyzed. TopBP1 OE cells had significantly higher levels of E-cadherin and reduced levels of N-cadherin when compared to the control (Figure 5E and S1C and E). The higher levels of E-cadherin and lower levels of N-cadherin observed in TopBP1 OE was similar to the observed levels in the malignant cells (Figure 5F and S1D and F). Other EMT markers like Slug, Twist, cytokeratin 14 and cytokeratin 19 were also analyzed in TopBP1 OE 3D dissociated cells and the pre-malignant and malignant cells. Slug and cytokeratin 14 levels were significantly reduced in TopBP1 OE, MCF10AT1 and MCF10CA1a lysates in comparison to the control, whereas Twist and cytokeratin 19 levels were observed to significantly upregulated (Figure 5G-H and S1G-N). These results demonstrate that overexpression of TopBP1 in the non-tumorigenic MCF10A cells steers the cells to acquire EMT-like characteristics similar to that of the malignant MCF10CA1a cells.

bioRxiv preprint doi: https://doi.org/10.1101/2022.04.05.487132; this version posted April 6, 2022. The copyright holder for this preprint (which was not certified by peer review) is the author/funder, who has granted bioRxiv a license to display the preprint in perpetuity. It is made available under aCC-BY-NC-ND 4.0 International license.

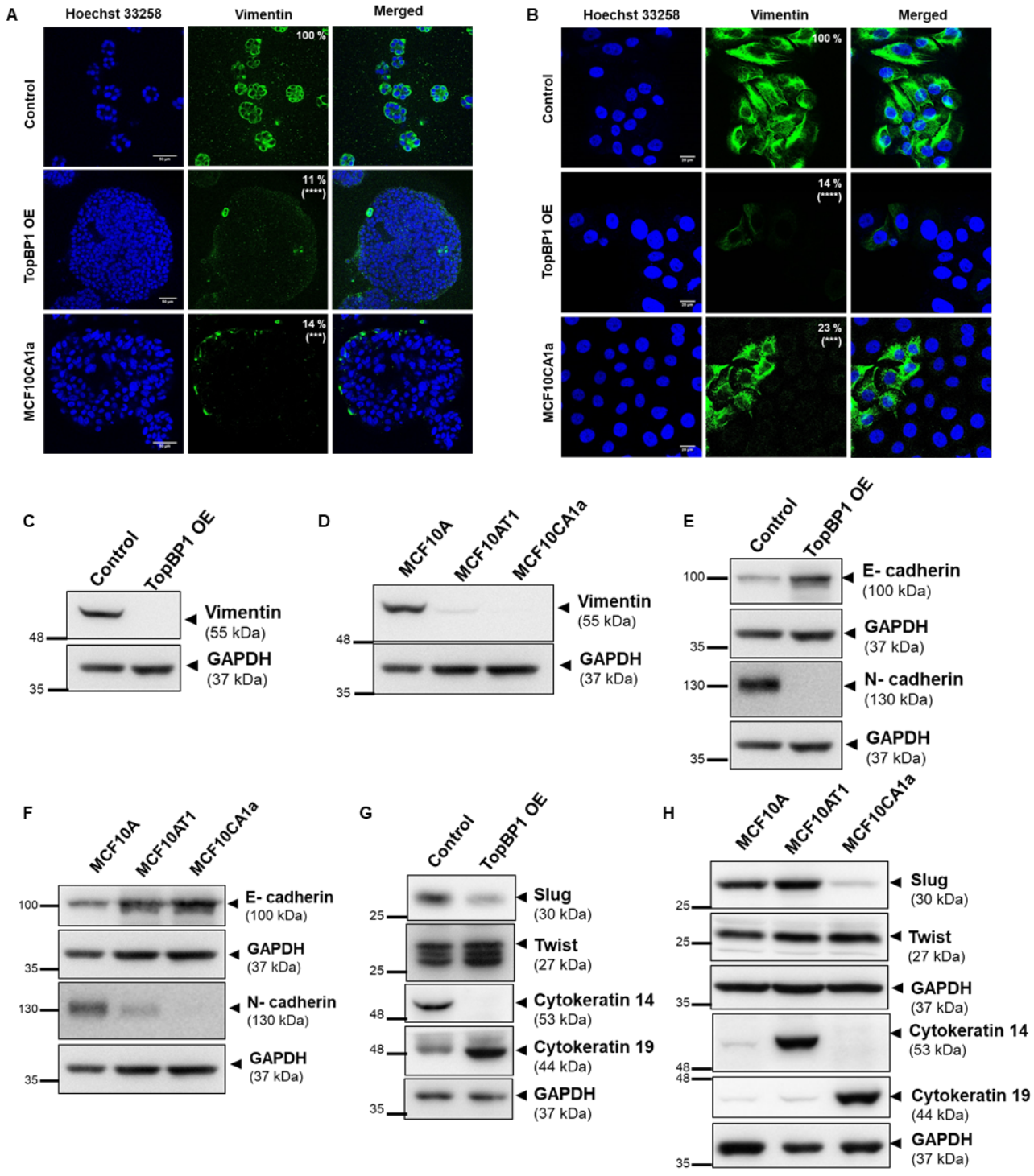


Figure 5: TopBP1 OE in MCF10A resembles MCF10CA1a EMT phenotypes

A) Representative images of mCherry MCF10A (control), TopBP1 OE MCF10A and MCF10CA1a cells grown as 3D cultures for 10 days, fixed and immunostained for vimentin. The number of vimentin-positive acini was manually counted and the percentage of positive acini was calculated and mentioned in the figures (scale bar: 50 μm). >50 acini from 3 independent experiments were analyzed. Statistical analysis was done using Mann

bioRxiv preprint doi: https://doi.org/10.1101/2022.04.05.487132; this version posted April 6, 2022. The copyright holder for this preprint (which was not certified by peer review) is the author/funder, who has granted bioRxiv a license to display the preprint in perpetuity. It is made available under aCC-BY-NC-ND 4.0 International license.

Whitney test (*** p <0.001, **** p <0.0001). B) mCherry MCF10A (control) and TopBP1 OE MCF10A 3D dissociated and MCF10CA1a (2D) cells were immunostained using vimentin and the number of vimentin-positive cells were manually counted and the percentage of positive cells are mentioned in the figures. >300 cells from 3 independent experiments were analyzed. Statistical analysis was done using Mann Whitney test (*** p <0.001, **** p <0.0001). mCherry MCF10A (control) and TopBP1 OE MCF10A 3D dissociated cells as well as MCF10A, MCF10AT1 and MCF10CA1a (2D) cells were lyzed and immunoblotting was performed to analyze the levels of C-D) vimentin, E-F) E-cadherin, N-cadherin, G-H) Slug, Twist, Cytokeratin 14 and cytokeratin 19.

TopBP1 overexpression leads to increased migration and invasion

In order for cancer cells to metastasize, the acquisition of both invasive and migratory potential is important. During invasion and migration, cells move either as single entities (Theveneau and Mayor, 2011) or collectively in small groups (Deisboeck and Couzin, 2009). Wound healing assays were performed to investigate collective cell migration of TopBP1 OE and MCF10CA1a cells. 100% wound closure was observed in TopBP1 OE and MCF10CA1a cells compared to 46% in the control cells after 12 hrs of creating the wounds thus confirming TopBP1 overexpression enabled the cells to undergo collective cell migration (Figure 6A-B). The single-cell migration potential of TopBP1 OE and MCF10CA1a cells were also investigated. TopBP1 OE cells showed increase in speed (Figure 6C), distance (Figure 6D) and displacement (Figure 6E) in comparison to the control cells. MCF10CA1a cells also showed increased speed and displacement compared to the control cells (Figure 6C-E). During the invasion process, invading cells secrete endopeptidases like matrix metalloproteinases (MMPs) into the surroundings to degrade the extracellular matrix proteins (Woessner, 1991). MMP2 and 9 are two such proteinases that have gelatinase activity. Gelatin zymography assay was performed to investigate whether TopBP1 overexpression leads to increased MMP secretion. It was observed that TopBP1 OE and MCF10CA1a 3D conditioned media had increased levels of MMP2 and MMP9 when compared to the control 3D media (Figure 6F-H). These results conclude that overexpression of TopBP1 in MCF10A cells leads to increased migration and invasion that is comparable to that observed in the malignant cells.

bioRxiv preprint doi: https://doi.org/10.1101/2022.04.05.487132; this version posted April 6, 2022. The copyright holder for this preprint (which was not certified by peer review) is the author/funder, who has granted bioRxiv a license to display the preprint in perpetuity. It is made available under aCC-BY-NC-ND 4.0 International license.

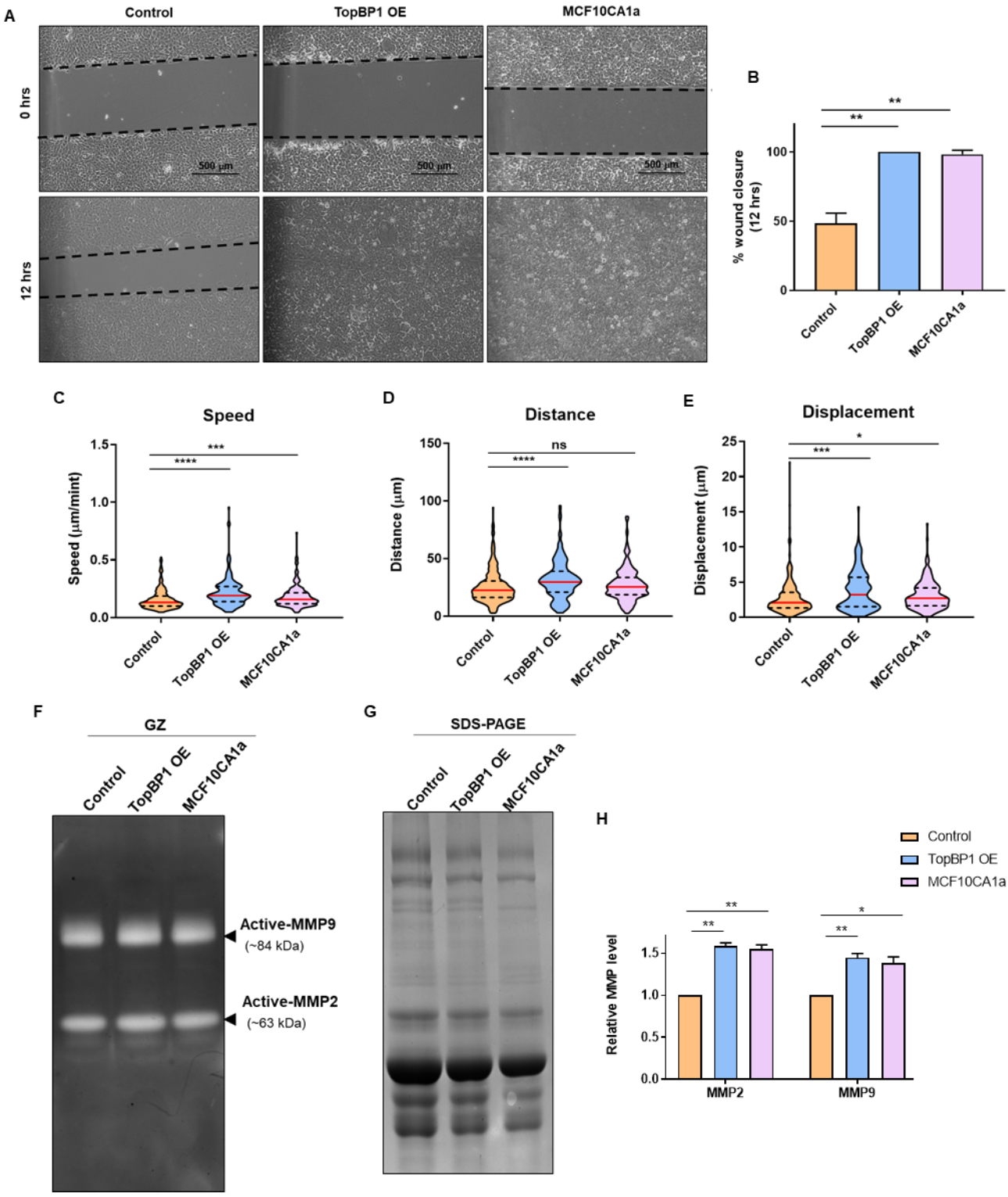


Figure 6: TopBP1 OE induces migration and invasion in MCF10A 3D dissociated cells

A) Representative images of wound healing assay demonstrating collective cell migration of mCherry MCF10A (control), TopBP1 OE MCF10A 3D dissociated cells and MCF10CA1a (2D) cells at 0 hrs and 12 hrs. Images were acquired on an ECLIPSE TS100

bioRxiv preprint doi: https://doi.org/10.1101/2022.04.05.487132; this version posted April 6, 2022. The copyright holder for this preprint (which was not certified by peer review) is the author/funder, who has granted bioRxiv a license to display the preprint in perpetuity. It is made available under aCC-BY-NC-ND 4.0 International license.

Nikon microscope at 10X magnification (scale bar: 500 μm). B) Wound area was manually measured using ImageJ and the percentage wound closure at 12 hrs was calculated and represented as a bar graph. Time-lapse imaging of mCherry MCF10A (control), TopBP1 OE MCF10A 3D dissociated cells and MCF10CA1a (2D) cells seeded as sparse populations were performed for a period of 3 hrs with images taken at 2-minute intervals on an Evos FL Auto microscope (Life Technologies). Cells were tracked using Fast track software and the C) speed, D) distance and, E) displacement were calculated and represented as violin plots. Gelatin zymography was performed using conditioned media from 10-day 3D cultures of mCherry MCF10A (control), TopBP1 OE MCF10A and MCF10CA1a. F) Gelatin zymography gel showing clearance of gelatin at the size of active MMP9 (~84 kDa) and MMP2 (~67 kDa) and G) the total protein in the media was quantified using SDS-PAGE. H) The MMP levels were quantified after normalizing to the total protein content of each sample. All data represented as Mean ± SEM from 3 independent biological experiments. Statistical analysis was done using One-way ANOVA (**** $p < 0.001$, *** $p < 0.001$, ** $p < 0.01$, * $p < 0.05$, ns $p > 0.05$).

TopBP1 overexpression induces transformation of MCF10A cells

In order to establish the role of TopBP1 in transformation, the colony formation ability of TopBP1 OE cells was studied. It was observed that TopBP1 OE cells formed colonies similar to that of the malignant cells while control cells failed to form colonies after 7 days (Figure 7A-B). Anchorage-independent growth is one of the properties of transformed cells. TopBP1 OE 3D dissociated cells were layered on soft agar to investigate their ability to grow in an anchorage-independent manner. TopBP1 OE and MCF10CA1a cells formed large colonies in 7 days, whereas the control cells failed to form colonies on soft agar (Figure 7C-D). To further establish the tumorigenic potential of TopBP1, TopBP1 OE and control cells were injected subcutaneously into the left and right flanks of athymic nude mice, respectively. Cells overexpressing TopBP1 formed tumors in the right flank within 4 weeks suggesting the tumor initiating role of TopBP1, whereas the control cells failed to form tumors even after 7 weeks. (Figure 7E-F). These results conclude that TopBP1 overexpression induces transformation of non-tumorigenic MCF10A cells that is capable of inducing tumorigenesis in mice.

bioRxiv preprint doi: https://doi.org/10.1101/2022.04.05.487132; this version posted April 6, 2022. The copyright holder for this preprint (which was not certified by peer review) is the author/funder, who has granted bioRxiv a license to display the preprint in perpetuity. It is made available under aCC-BY-NC-ND 4.0 International license.

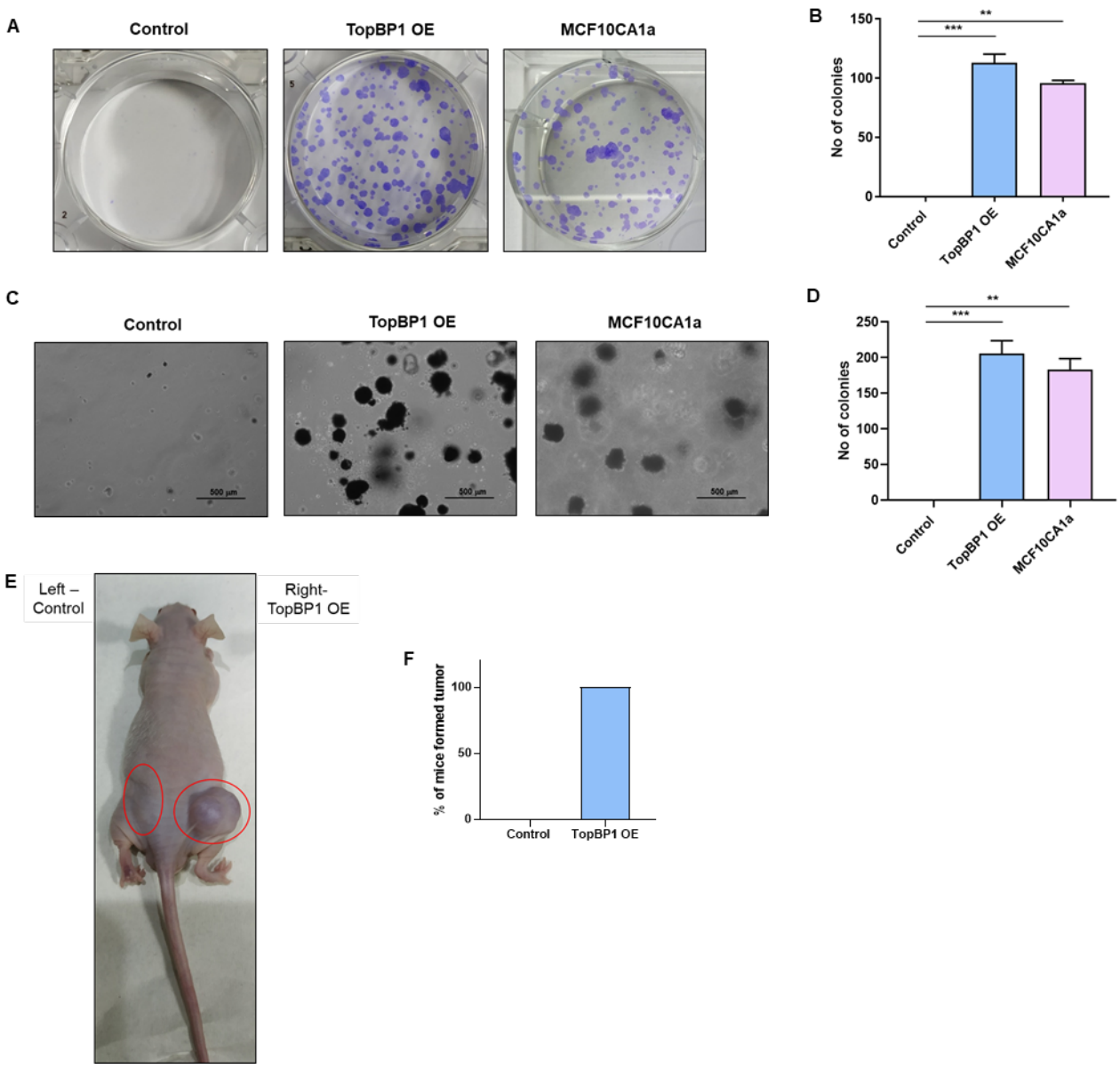


Figure 7: MCF10A cells acquire transformation potential upon TopBP1 OE in 3D cultures

A) Crystal violet stained colonies of mCherry MCF10a (control), TopBP1 OE MCF10A 3D dissociated and MCF10CA1a (2D) cells grown on cell culture-treated 35 mm culture plates for 7 days. B) The number of colonies were counted manually and represented as bar graphs. C) MTT-stained colonies of mCherry MCF10A (control), TopBP1 OE MCF10A 3D dissociated and MCF10CA1a (2D) cells grown on agar-coated 35 mm culture plates for 7 days. Images were acquired on an ECLIPSE TS100 Nikon microscope at 10X magnification (scale bar: 500 µm). D) Number of colonies were counted manually and represented as bar graphs. All data represented as Mean ± SEM from 3 independent biological experiments. Statistical analysis was done using One-way ANOVA (**** p

bioRxiv preprint doi: https://doi.org/10.1101/2022.04.05.487132; this version posted April 6, 2022. The copyright holder for this preprint (which was not certified by peer review) is the author/funder, who has granted bioRxiv a license to display the preprint in perpetuity. It is made available under aCC-BY-NC-ND 4.0 International license.

<0.001, *** p <0.001, ** p <0.01, * p <0.05, ns p>0.05). E) Mice injected with mCherry MCF10A (control, left) and TopBP1 OE (right) 3D dissociated cells subcutaneously in flanks were sacrificed after 7 weeks of injection. F) Percentage of mice that formed tumor were represented as bar graph. Data pooled from N=12 mice.

Overexpression of TopBP1 induces DNA damage that leads to activation of the DDR response

Genomic instability is one of the hallmarks of cancer (Hanahan and Weinberg, 2011). Defects in checkpoint activation can lead to the accumulation of DNA damage, leading to genomic instability (Kastan and Bartek, 2004). TopBP1 is a mediator protein in the DNA damage response (DDR) pathway and plays a pivotal role in the DDR and repair pathways. Our data confirms that overexpression of TopBP1 leads to the transformation of breast epithelial cells into a malignant phenotype. Thus it was intriguing to check whether overexpression of TopBP1 leads to an alteration in the cell's response to DNA damage. To investigate whether TopBP1 overexpression induces DNA damage, we analyzed the activation of RPA (marker for single-strand breaks) and γH2AX (marker for double-strand breaks) in TopBP1 OE 3D dissociated cells. Interestingly, activation of RPA and γH2AX were observed in TopBP1 OE cells even in the absence of any external DNA damage (Figure 8A and S2 A-B). A similar pattern of activated pRPA and γH2AX were observed in the malignant MCF10CA1a cells compared to MCF10A and MCF10AT1, suggesting the presence of endogenous DNA damage in these transformed cells (Figure 8B and S2 C-D). As expected, knockdown of TopBP1 in the malignant MCF10CA1a cells showed relatively low activation of RPA and γH2AX (Figure 8C and S2 E-F). These results indicate that TopBP1 help to regulate the endogenous DNA damage inside the cells. Overexpression of the protein leads to an imbalance where TopBP1 is no longer able to perform its required function. We next investigated whether the endogenous DNA damage induced due to overexpressionTopBP1 leads to activation of the DNA damage response. As TopBP1 is a mediator protein in the single-strand DNA break pathway we analyzed the activation of ATR and Chk1 in TopBP1 OE cells. Both ATR and Chk1 were observed to be activated in TopBP1 OE cells compared to control cells. (Figure 8E and S2 G-H). A similar activation pattern of ATR and Chk1 was also observed in MCF10CA1a cells in comparison to the non-tumorigenic MCF10A cells (Figure 8F and S2 I-J). The knockdown of TopBP1 in the malignant cells led to reduced ATR and Chk1 activation (Figure 8G and S2 K-L). These results suggest that overexpression of TopBP1 leads to increased endogenous DNA

bioRxiv preprint doi: https://doi.org/10.1101/2022.04.05.487132; this version posted April 6, 2022. The copyright holder for this preprint (which was not certified by peer review) is the author/funder, who has granted bioRxiv a license to display the preprint in perpetuity. It is made available under aCC-BY-NC-ND 4.0 International license.

damage and altered DNA damage response in MCF10A cells along with cellular transformation.

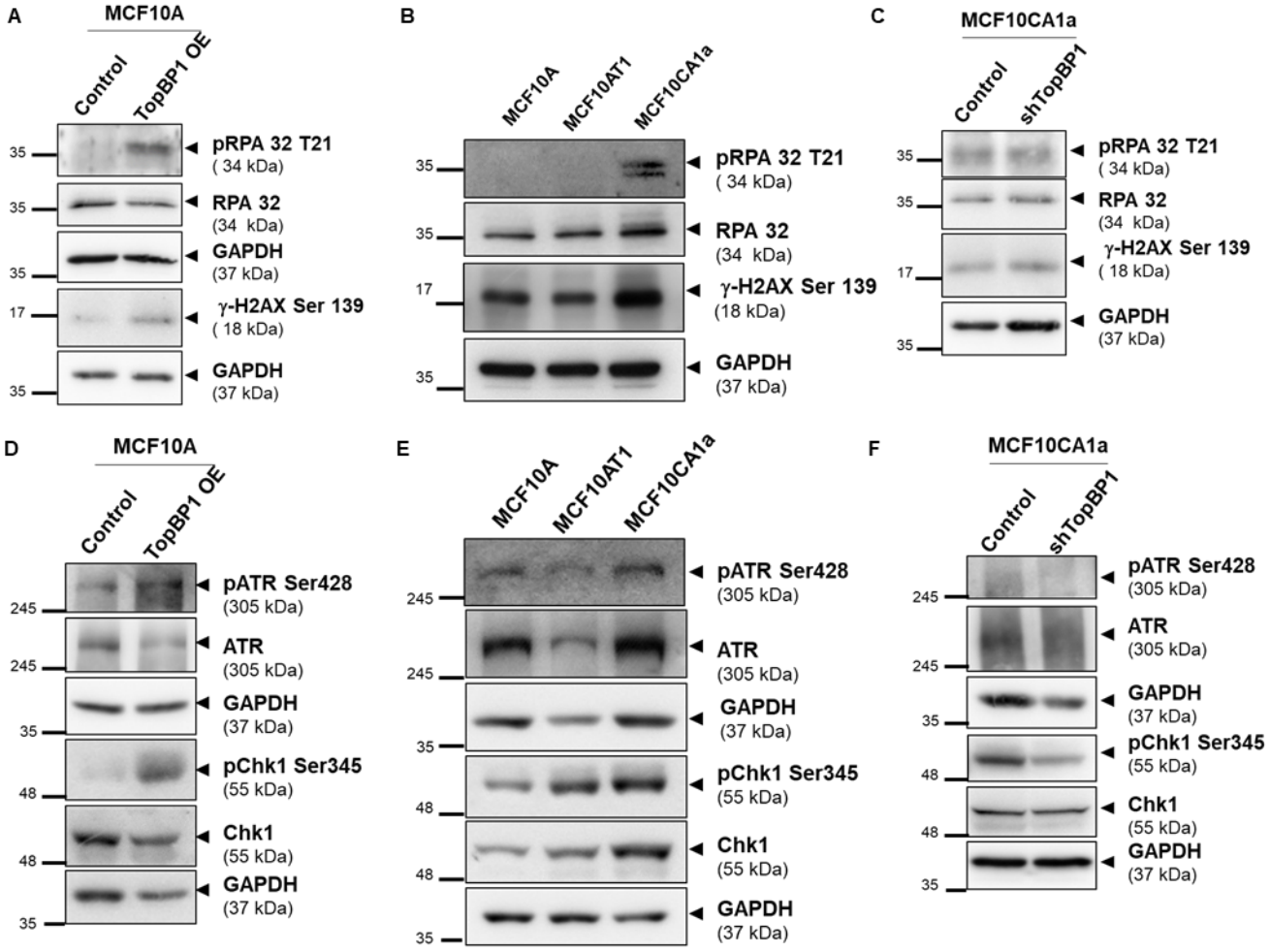


Figure 8: TopBP1 OE induces DNA damage and DDR activation

A and D) mCherry MCF10A (control) and TopBP1 OE MCF10A 3D dissociated cells, B and E) MCF10A, MCF10AT1, MCF10CA1a (2D) and C and F) control (pLKO1 MCF10CA1a) and shTopBP1 MCF10CA1a (2D) cells were lyzed and immunoblotting was performed to analyze the levels/activation of A-C) RPA, γH2AX D-F) ATR and Chk1. The phosphoproteins were quantified after normalizing to GAPDH.

TopBP1 overexpression leads to TP53 mutation

p53 is a well-known tumor suppressor gene, which is an effector protein in the DNA damage checkpoint signaling pathway. Upon checkpoint activation, p53 is activated leading to a temporary cell cycle arrest to allow for DNA repair to occur. If the damage is beyond repair apoptosis signaling cascade is activated. In order to investigate whether

bioRxiv preprint doi: https://doi.org/10.1101/2022.04.05.487132; this version posted April 6, 2022. The copyright holder for this preprint (which was not certified by peer review) is the author/funder, who has granted bioRxiv a license to display the preprint in perpetuity. It is made available under aCC-BY-NC-ND 4.0 International license.

TopBP1 overexpression leads to activation of p53 to execute a checkpoint response, total and activated p53 levels were analyzed in TopBP1 OE cells. Significant increases in total p53 and phosphorylated p53 at serine 15 were observed in TopBP1 OE cells when compared to the control cells (Figure 9A-C). Similar increases in total protein levels of p53 and phosphorylated p53 at serine 15 were also observed in MCF10CA1a cells in comparison to the pre-malignant MCF10AT1 and non-tumorigenic MCF10A cells (Figure 9E-G). However, p21, a p53 target protein that is active during G1-S arrest, was observed to be reduced or absent in TopBP1 OE (Figure 9A and D) and malignant cells (Figure 9B and H). Knockdown of TopBP1 in MCF10CA1a cells led to a significant decrease in the activation and total levels of p53 (Figure 9I-K) with a concomitant increase in p21 levels (Figure 9I and L). Studies have reported overexpression of TopBP1 to induce increased proliferation and reduced apoptosis through mutant p53 (mut p53) gain of function (Liu et al., 2011). Earlier reports have shown that polarity disruption in MCF10A cells can be induced by mutant p53 gain of function by inducing EMT (Zhang et al., 2011). Thus, TP53 mutation status was analyzed in mCherry MCF10A (control), TopBP1 OE MCF10A 3D dissociated cells and MCF10CA1a cells using whole-exome sequencing. Interestingly one mutation at 913 cDNA position in the TP53 gene was observed in TopBP1 OE cells, which was not present in the control cells (Table 1). This single-nucleotide variation (snv) mutation led to an exonic missense variant leading to the formation of a mutant p53 protein with isoleucine at 237 instead of methionine (M237I). This M237I mutation resides in the DNA binding region of p53 that is required for p53-TopBP1 interaction. This exact M237I mutation was also observed in the malignant cell line MCF10CA1a that has been demonstrated to have increased levels of TopBP1 suggesting that TopBP1 overexpression can also regulate the genomic stability inside the cells.

bioRxiv preprint doi: https://doi.org/10.1101/2022.04.05.487132; this version posted April 6, 2022. The copyright holder for this preprint (which was not certified by peer review) is the author/funder, who has granted bioRxiv a license to display the preprint in perpetuity. It is made available under aCC-BY-NC-ND 4.0 International license.

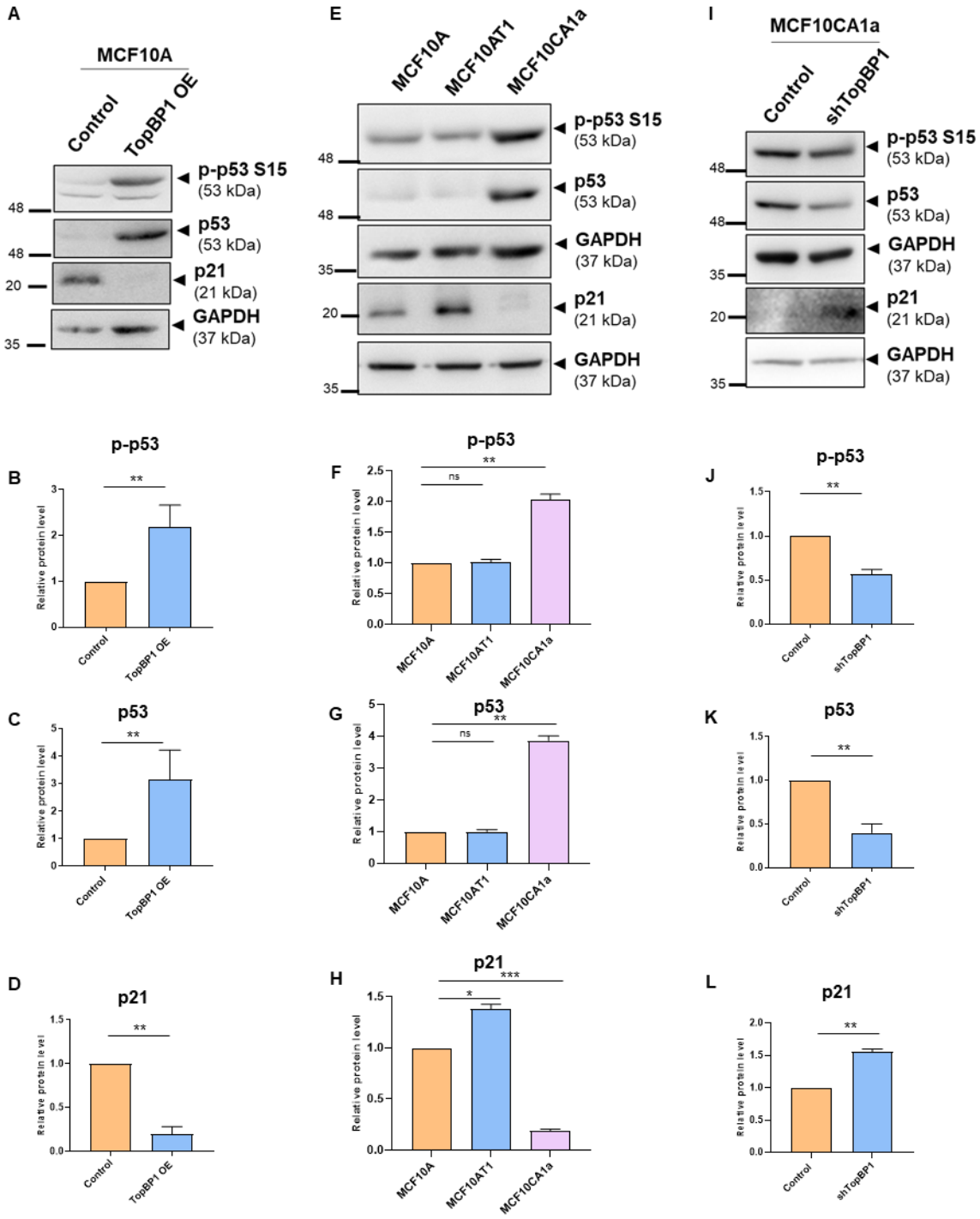


Figure 9: TopBP1 OE induces aberrant p53 activation

A) mCherry MCF10A (control) and TopBP1 OE MCF10A 3D dissociated cells, E) MCF10A, MCF10AT1, MCF10CA1a (2D) and I) pLKO1 MCF10CA1 (control) and shTopBP1 MCF10CA1a (2D) cells were lyzed and immunoblotting was performed to analyze the levels/activation of p53 and p21. Phosphoproteins were quantified after normalizing to GAPDH. Quantification showing the fold change of B, F, J) p-p53, C, G, K)

bioRxiv preprint doi: https://doi.org/10.1101/2022.04.05.487132; this version posted April 6, 2022. The copyright holder for this preprint (which was not certified by peer review) is the author/funder, who has granted bioRxiv a license to display the preprint in perpetuity. It is made available under aCC-BY-NC-ND 4.0 International license.

p53 and D, H, L) p21 after normalizing to GAPDH. Statistical analysis was done using paired Paired Student's t-test for TopBP1 OE and shTopBP1 lysates and One-way ANOVA for MCF10A series (*** p <0.001, ** p <0.01, * p <0.05, ns p>0.05).

Table 1: TP53 mutation in TopBP1 OE and MCF10CA1a cells

Gene	Codons	Chr	Type	Genotype	Exonic	Consequence	cDNA Position	Protein Position	Amino Acids
Control									
TP53									
TopBP1 OE									
TP53	**atG/atT**	17	snv	het	yes	**missense variant**	**913**	**237**	**M/I**
MCF10CA1a									
TP53	**atG/atT**	17	snv	het	yes	**missense variant**	**913**	**237**	**M/I**

Discussion

Cancer is caused by mutations in genes, which may give rise to increased cellular proliferation, decreased apoptosis, increased cell migration and invasion and/or EMT (Hanahan and Weinberg, 2011). These mutations in the genes are caused by various mutagens and carcinogens that work in favor of transforming the cells into a cancerous phenotype.

TopBP1 has been reported as a breast and ovarian cancer susceptibility gene by various groups (Forma et al., 2012; Karppinen et al., 2006). TopBP1 upregulation has been reported in high-grade breast cancer biopsy samples (Forma et al., 2012; Going et al., 2007; Liu et al., 2009).

In our study, we observed increased protein expression of TopBP1 in the malignant cells compared to the non-tumorigenic breast epithelial cells. We demonstrate that TopBP1 overexpression can induce transformation of non-tumorigenic MCF10A 3D breast acinar cultures to acquire properties similar to that of the malignant MCF10CA1a cells by inducing genomic instability and mutation in the TP53 gene (Figure 10). Our findings also emphasize the functional role of the cellular microenvironment in cancer initiation where TopBP1 overexpressing cells grown as 3-dimensional cultures underwent cellular transformation, which is not feasible by the cells when grown as monolayer cultures.

bioRxiv preprint doi: https://doi.org/10.1101/2022.04.05.487132; this version posted April 6, 2022. The copyright holder for this preprint (which was not certified by peer review) is the author/funder, who has granted bioRxiv a license to display the preprint in perpetuity. It is made available under aCC-BY-NC-ND 4.0 International license.

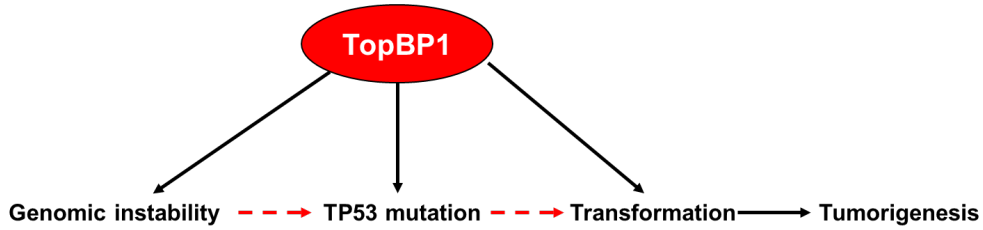


Figure 10: Schematic representation depicting the role of TopBP1 tumorigenesis.

Overexpression of TopBP1 led to TP53 mutation in MCF10A cells grown as breast acinar cultures. This suggests that TopBP1 has the potential to regulate genome stability. This genome stability regulatory function of TopBP1 is also context dependent as TP53 mutation was not observed in TopBP1 overexpressing cells grown as monolayer cultures. This also emphasizes the role of the 3D environment in the transformation process as a change in morphology was not observed in MCF10A cells overexpressing TopBP1 grown as monolayer cultures.

Analysis of the cellular and nuclear pleomorphism and extent of the architectural disorder are the preliminary diagnostic and prognosis determination method for breast carcinoma (Debnath and Brugge, 2005). 3D cultures of breast epithelial cells and cancer cells recapitulate most of the features of these cells *in vivo*. Detailed analysis of these characteristic features can aid in ascertaining the role of perturbed genes. The morphometric analysis of TopBP1 OE acini revealed that TopBP1 overexpression induced changes in the acinar morphology which resembled cancerous spheroids. TopBP1 overexpressing cells formed spheroids with a larger surface area and volume and with filled lumen. In support of this observation, TopBP1 is known to play a major role in maintaining genome stability, ensuring proper DNA replication and G1-S cell cycle transition (Kim et al., 2005); perturbation in its level can distort DNA synthesis and cell cycle which may in turn, alter the nuclear content. We also found that TopBP1 OE acini to have increased proliferation, with a greater percentage of cells in the S and G2-M phases of the cell cycle in comparison to the MCF10A control acini.

De-regulation of apicobasal polarity is one of the characteristics of epithelial cancers (Debnath and Brugge, 2005). In invasive cancers, cells lose contact with neighbouring cells and break down the basement membrane to invade other tissues (Moreno-Bueno et al., 2008). In our study, we demonstrate TopBP1 overexpression leads to disruption of basal polarity. The loss of basal polarity markers α6-integrin and Laminin V indicated reduced interaction of the acinar cells with the ECM, which may indicate an invasive

bioRxiv preprint doi: https://doi.org/10.1101/2022.04.05.487132; this version posted April 6, 2022. The copyright holder for this preprint (which was not certified by peer review) is the author/funder, who has granted bioRxiv a license to display the preprint in perpetuity. It is made available under aCC-BY-NC-ND 4.0 International license.

phenotype. We also found that overexpression of TopBP1 leads to Golgi dispersal, a known apical marker in MCF10A 3D cultures. Golgi dispersal is observed in various cancer cell lines, which may be the reason for altered polarity as Golgi plays a major role in maintaining polarized trafficking of proteins (Griffiths and Simons, 1986; Keller et al., 2001).

EMT is a process through which epithelial cells de-differentiate and acquire mesenchymal phenotype that can increase their motility and invasiveness. However, recent studies suggest that partial EMT phenotypes help in migration and metastasis (Aiello et al., 2018). We observed a similar pattern of expression of various EMT markers between TopBP1 OE and MCF10CA1a cells. N-cadherin and vimentin (mesenchymal markers) were downregulated, while E-cadherin (an epithelial marker) was upregulated in TopBP1 OE dissociated cells which was similar to that observed in MCF10CA1a cells. A recent study also suggests the role of E-cadherin in promoting metastasis in invasive ductal carcinoma (Padmanaban et al., 2019),which changes our perspective on EMT in tumorigenesis. This may hold true in our scenario as overexpression of TopBP1 led to increased migration and invasion. MCF10A cells are non-tumorigenic breast epithelial cells that require cell-cell contact and anchorage for their growth and do not have tumor forming ability. We observed that TopBP1 OE cells induced colony formation, anchorage-independent growth and tumorigenesis, thus confirming the role of TopBP1 as a potent tumor initiator and progression factor.

ATR is a major sensor kinase that gets activated by single-strand breaks and leads to activation of Chk1 to induce cell cycle arrest and DNA repair. TopBP1 is an important mediator protein in this signaling pathway. Even though TopBP1 levels have been observed to be high in cancer cells, its role in inducing DNA damage was not proven. A recent study from Lin's group suggested an association between TopBP1 overexpression and genomic instability by TCGA analysis (Liu et al., 2021).We demonstrated that TopBP1 OE induced DNA damage and activation of DNA damage repair proteins in non-tumorigenic cells. We also observed that malignant cells have endogenous DNA damage compared to non-tumorigenic cells and altered activation of the proteins involved in the DNA damage response. Also, TopBP1 knockdown was able to partially revert these phenotypes thus confirming the role of TopBP1 in inducing genome instability.

bioRxiv preprint doi: https://doi.org/10.1101/2022.04.05.487132; this version posted April 6, 2022. The copyright holder for this preprint (which was not certified by peer review) is the author/funder, who has granted bioRxiv a license to display the preprint in perpetuity. It is made available under aCC-BY-NC-ND 4.0 International license.

p53 is a well-studied tumor suppressor gene that is generally mutated in cancers. TopBP1 is known to bind to the DNA binding domain of p53 and inhibit its transcription activity of inducing apoptosis and cell cycle arrest without affecting its activation at S15 and total protein levels (Liu et al., 2009). However, we observed total p53 and p53 S15 levels were significantly increased in TopBP1 OE 3D dissociated cells. Even though p53 levels were high, p21 levels were low, as well as the proportion of cells in S and G2-M phases were high in TopBP1 OE dissociated cells confirming the inability of p53 to induce cell cycle arrest. Lin's group have also demonstrated the role of TopBP1 in inducing mutant p53 gain of function to induce proliferation and reduce apoptosis (Liu et al., 2011). It was surprising that TopBP1 OE in a non-tumorigenic MCF10A cell line grown for 16 days in 3D culture had a similar TP53 mutation as was observed in the malignant cell line MCF10CA1a that was derived from MCF10A following H-Ras mutation and then passaging for 100 generations in mice. This TP53 mutation led to the formation of the mut p53 protein with an amino acid change from methionine to isoleucine at the 237th reside (M237I). This mutation is reported in various cancers, where the somatic mutation has been reported in 176 cancers, out of which 26 were breast cancers (Jordan et al., 2010). Interestingly, SUM149PT, which is a triple negative breast cancer (TNBC) cell line harbors a p53 mutation at M237I (Wasielewski et al., 2006). M237I-p53 forms amyloid oligomers in glioblastoma cells expressing a chemoresistant gain-of-function phenotype (Pedrote et al., 2020).

Thus taken together, overexpression of TopBP1 induces transformation of non-tumorigenic breast epithelial cells when grown on extracellular matrix as 3-dimensional cultures. These transformed cells have phenotypic and genotypic characteristics concurrent to malignant cells with a mutation in the TP53 gene. Our study also opens multiple avenues for investigating and tracking the initiation as well as early-stage changes in cancers. TopBP1 being a novel regulator in the process of tumorigenesis, also exposes itself as a potential target to combat cancer(s). Cancers resulting from higher TopBP1 protein expression can be targeted with therapeutic molecules that can either inhibit the function or reduce the half-life of TopBP1 inside cells, thus eventually regulating genomic instability and functions of p53.

bioRxiv preprint doi: https://doi.org/10.1101/2022.04.05.487132; this version posted April 6, 2022. The copyright holder for this preprint (which was not certified by peer review) is the author/funder, who has granted bioRxiv a license to display the preprint in perpetuity. It is made available under aCC-BY-NC-ND 4.0 International license.

Materials and Methods

Ethics statements

Institutional Biosafety Committee (IBSC) clearance was obtained from the institute for preparing TopBP1 OE MCF10A cells and TopBP1 KD MCF10CA1a cells. All mouse studies were approved by the Institutional Animal Ethics Committee (IAEC) (IAEC/2018_02/010 and IISER_Pune/IAEC/2021_01/06). We only used athymic mice (Foxnl ^{nu} / Foxnl ^{nu}, 6-8 weeks old) for the *in vivo* tumorigenicity studies

Chemicals and antibodies

Insulin (I1882), Hydrocortisone (H0888), Choleratoxin (C8052), Epidermal growth factor (EGF- E9644), Puromycine dihydrochloride from Streptomyces alboniger (P8833), Polybrene (H9268), dimethyl sulfoxide (DMSO, D8418), Triton X-100 (T8787), Mitomycin C (M4287), Tris base (B9754), EDTA (E6758), propidium iodide (PI- P4170) and Na_3VO (S6508) were purchased from Sigma-Aldrich, USA. Matrigel® and Dispase (354235) were purchased from Corning, Sigma-Aldrich, USA. DQ Collagen (D12060), Phalloidin 633 (A12380) and Lipofectamine-2000 (11668) were purchased from Invitrogen, Thermo Fisher Scientific, USA. Pre-stained protein ladder (MBT092), NaF (RM1081), Na_2HPO_4 (GRM1417), and KH_2PO_4 (MB050) were purchased from HiMedia. NaCl (15918), was purchased from Qualigens. 16% paraformaldehyde (AA433689M) was purchased from Alfa Aesar. Hoechst 33258 (H3569) and Hoechst 33342 (H3570) were purchased from Molecular Probes, Thermo Fisher Scientific, USA. Antibodies used were from Bethyl, Abcam, Millipore, cell signalling (CST), Santacruz or Sigma (Supplementary Table 1).

Cell lines

HEK293T and MCF10A were generous gifts from Dr Jomon Joseph (NCCS, Pune) and Prof. Raymond C. Stevens (The Scripps Research Institute, California) respectively. MCF10AT1 and MCF10CA1a cells were purchased from ATCC.

Plasmids

CSII-EF-MCS plasmid was a gift from Dr Sourav Banerjee, NBRC, Manesar India. pCAG-HIVgp and pCMV-VSV-G-RSV-Rev plasmids were purchased from RIKEN BioResource Centre, Japan. pLKO.1.TRC was a gift from Dr Sorab Dalal, ACTREC, India and psPAX2 and pMD2.G were generous gifts from Dr Manas K Santra, NCCS, India. The vector maps are provided in Supplementary Figures S3-S6.

Cloning

bioRxiv preprint doi: https://doi.org/10.1101/2022.04.05.487132; this version posted April 6, 2022. The copyright holder for this preprint (which was not certified by peer review) is the author/funder, who has granted bioRxiv a license to display the preprint in perpetuity. It is made available under aCC-BY-NC-ND 4.0 International license.

TopBP1 was amplified from mVenus TopBP1 vector using the following primers: Forward: AAGGAAAAAAGCGGCCGCATATGTCCAGAAATGACAAAGAACCG Reverse: ATGGTTAACTTAGTGTACTCTAGGTCGTTTGATT (PCR mixture and reaction in Supplementary Table 2A-B). The amplified plasmids and CSII-EF MCS-mCherry vector were digested using HpaI and NotI HF (NEB, USA) restriction enzymes (Supplementary Table 2C). TopBP1 was ligated into mCherry-CSII-EF-MCS vector using T4 DNA ligase (NEB, USA) following incubation at 16ºC overnight (Supplementary Table 2D). Ligation mixture was used to transform DH5α competent cells, and the colonies were screened by digesting with HpaI and NotI HF to check for insert release.

shTopBP1 lentiviral plasmids were generated as per Addgene protocol. Briefly, pLKO1. TRC vector was digested with EcoRI and AgeI restriction enzymes (NEB, USA) (Supplementary Table 3A), and the 7 kb fragment was excised and gel extracted using QIAquick Gel Extraction Kit (28706). The shTopBP1 oligos (forwad: CCGGAAGTGGTTGTAACAGCGCATCTTCTCGAGAAGATGCGCTGTTACAACCACTTTTTTTG and reverse: AATTCAAAAAAAGTGGTTGTAACAGCGCATCTTCTCGAGAAGATGCGCTGTTACAACCACTT) were annealed (Supplementary Tables 3B-C), and ligated into the digested vector (Supplementary Table 3D). The clones obtained were screened using XhoI (NEB, USA) digestion.

Cell culture

HEK293T cells were grown on 100mm tissue culture-treated dishes (Eppendorf or Corning) with high glucose-containing Dulbecco's Modified Eagle Medium (DMEM; Lonza) supplemented with 10% heat-inactivated fetal bovine serum (Invitrogen, Thermo Fisher Scientific, USA) and 100 units/ml of penicillin-streptomycin (Invitrogen, Thermo Fisher Scientific, USA). MCF10A, MCF10AT1 and MCF10CA1a cells were grown as monolayer cultures in growth medium and 3D in assay medium as previously mentioned (Anandi et al, 2017). Cells were incubated at 37ºC in humidified 5% CO_2 incubators (Eppendorf or Thermo Fisher Scientific, USA).

Lentiviral preparation and transduction using lipofectamine-mediated transfection

Lentiviral particles to generate TopBP1 overexpressing MCF10A cells were prepared as previously mentioned (Sharma and Lahiri, 2021). Briefly, HEK293T cells were transfected with 1 µg of mCherry-CSII-EF-MCS or mCherry-CSII-EF-MCS-TopBP1 plasmid along with

bioRxiv preprint doi: https://doi.org/10.1101/2022.04.05.487132; this version posted April 6, 2022. The copyright holder for this preprint (which was not certified by peer review) is the author/funder, who has granted bioRxiv a license to display the preprint in perpetuity. It is made available under aCC-BY-NC-ND 4.0 International license.

1 µg of pCAG-HIVgp and 0.5 µg pCMV-VSV-G-RSV-Rev packaging plasmids using Lipofectamine 2000. 1ml growth media containing 15% horse serum was added to the cells 24 hours post-transfection. The viral supernatant collected 48 hours post-transfection was used to transduce MCF10A cells. Transduced MCF10A cells were sorted using the BD Aria Fusion sorter (BD Biosciences, USA).

For the generation of MCF10CA1a cells with TopBP1 knockdown, HEK293T cells were transfected with 1 µg of pLKO1.TRC or shTopBP1-TRC plasmid along with 1 µg of psPAX2 and 0.5 µg pMD2 packaging plasmids using Lipofectamine 2000 to generate lentiviral particles. These lentiviral particles were used to transduce MCF10CA1a cells, and cells with TopBP1 knockdown were selected using 1 µg/ml puromycin.

3D dissociation

For dissociating cells from 3D acini, the 16-day 3D cultures were treated with 250 µl of Dispase and incubated at 37ºC for 30 minutes. The dissociated cells along with Matrigel® were transferred to a 15 ml falcon and incubated at 37ºC for 10 minutes. The dislodged acini were centrifuged at 900 rpm for 10 minutes and plated in 12-well culture plates after washing twice with 1X PBS. The attached cells were passaged and expanded once 70% confluency was reached.

Immunofluorescence

Immunofluorescence of 2D and 3D cultures were performed as mentioned previously (Anandi et al., 2017). For IF of 3D cultures, 0.5 % Triton X was added to the wash buffers for better penetration of antibodies. Cells / acini were imaged on the SP8 confocal microscope (Leica, Germany) under 63X/40X oil immersion objective. A minimum of 200 cells or 50 acini were analyzed for the phenotypic characterization.

Immunoblotting

Immunoblotting analysis using specific antibodies were performed as mentioned previously (Bodakuntla et al., 2014). Images were acquired on ImageQuant LAS4000 gel documentation system (GE Healthcare, now Cytiva Life Sciences).

Cell proliferation assay

For cell proliferation assay, 2.5 X 10^5 mCherry or TopBP1 OE MCF10A 3D dissociated cells were seeded on a 35mm dish. 72 hrs post seeding, the cell count was measured

bioRxiv preprint doi: https://doi.org/10.1101/2022.04.05.487132; this version posted April 6, 2022. The copyright holder for this preprint (which was not certified by peer review) is the author/funder, who has granted bioRxiv a license to display the preprint in perpetuity. It is made available under aCC-BY-NC-ND 4.0 International license.

using Sceptar™ hand-held automated cell counter (Millipore, Sigma-Aldrich, USA) as previously mentioned (Sharma and Lahiri, 2021).

Flow cytometry

The cell cycle profile was analyzed as mentioned previously (Sharma and Lahiri, 2021). Cell cycle profile was analyzed on a BD Accuri™ C6 flow cytometer (BD Biosciences, USA).

Wound healing Assay

Wound healing analysis was performed as mentioned previously (Anandi et al., 2016). Images were taken at 0 and 12 hrs of the assay at 10X objective on the ECLIPSE TS100 (Nikon, Japan) microscope and wound area was manually measured using ImageJ software (NIH, USA)

Single-cell migration assay

Cells were seeded in 24-well cell culture plates at a density of 2 X 10^5 cells per well and incubated at 37˚C for 10 hrs. Cells were stained with Hoechst 33342 for 15 minutes and replenished with fresh L15 media (12-700Q, Lonza). Cells were tracked for 3 hrs at 37°C, and images were taken at every 2 mins time interval on the EVOS FL Auto microscope (Life Technologies) at 20X magnification. The cells were tracked using Fast track software (DuChez, 2017), and the distance, displacement and velocity obtained were plotted in Graphpad prism (Graph Pad Software, La Jolla, CA, USA).

Gelatin Zymography

Assay medium of 3D cultures were collected 10 days post seeding and mixed with gelatin zymography sample buffer (25mM Tris-HCl, pH 7.6, 1mM NaCl, 1% NP-40). It was then resolved on a 8% SDS-PAGE containing 0.06% gelatin [w/v] as substrate. The gel was renatured with 1X renaturing buffer (2.5 % v/v of Triton X-100 in water) at room temperature (RT) for 30 minutes with constant shaking. After washing with distilled water, the gel was incubated in 1X Developing buffer (0.5 M Tris-HCL pH-7.8, 2M NaCl, 0.05M CaCl2 and 0.2% Brij35) for 48 hours. Meanwhile the same media mixed with 6X sample buffer was resolved on a 8% SDS-PAGE to find the total protein content in the media. Later, the gels were stained overnight in staining solution (0.1% w/v Coomassie Brilliant Blue (Sigma-Aldrich), 50% v/v methanol (Thermo Fisher Scientific, USA) and 10% v/v

bioRxiv preprint doi: https://doi.org/10.1101/2022.04.05.487132; this version posted April 6, 2022. The copyright holder for this preprint (which was not certified by peer review) is the author/funder, who has granted bioRxiv a license to display the preprint in perpetuity. It is made available under aCC-BY-NC-ND 4.0 International license.

acetic acid (Thermo Fisher Scientific, USA) and destained with destaining solution (40% v/v methanol and 10% v/v acetic acid) for 1 hour. The gel images were acquired on ImageQuant LAS4000 gel documentation system (GE Healthcare now Cytiva Life Sciences).

Colony formation assay

Cells were seeded in 6-well culture plates at a density of 300 cells per well. Cells were replenished with fresh media after 4 days of seeding. After 7 days of seeding, cells were washed twice with 1X PBS and fixed with 100% chilled methanol at 4°C for 15 minutes. Cells were stained with 0.5% of crystal violet stain (Himedia, S012) for 15 minutes with shaking at RT. After removing the stain, cells were washed with distilled water and images were taken on a HP Scanner (HP DeskJet 2332) after drying the plates. The number of colonies were manually counted.

Soft agar assay

Soft agar assay was performed as mentioned previously (Anandi et al., 2017). Ten randomly selected fields were imaged under 10X objective of ECLIPSE TS100 (Nikon, Japan) microscope and number of colonies were counted manually.

Tumorigenesis in mice

For mice injections, 6 X 10^6 mCherry or TopBP1 MCF10A 3D dissociated cells were resuspended in 100 μl of 1:1 mixture of PBS: Matrigel and injected into the flanks of athymic nude mice (Foxnl ^{nu} / Foxnl ^{nu}, 6-8 weeks old) (IAEC/2018_02/010). The mice were examined every week. The mice were sacrificed on the 7^{th} week and the tumors were dissected. The tumor size and volume were calculated by measuring the tumor dimensions using a Vernier calliper.

Whole exome sequencing

Genomic DNA was extracted from mCherry-MCF10A, TopBP1 OE 3D dissociated and MCF10CA1a cells using the DNeasy blood and Tissue kit (Qiagen, 69506) as per manufactures protocol. All three cell lines were sent to Dhiti Omics Technologies, Bengaluru, India for whole exome sequencing (Makiniemi et al.) using Agilent V6r2 (Agilent Technologies, Santa Clara, CA 95051, USA) and this targeted library was sequenced using HiSeq. The resultant raw data were then mapped to the human genome

bioRxiv preprint doi: https://doi.org/10.1101/2022.04.05.487132; this version posted April 6, 2022. The copyright holder for this preprint (which was not certified by peer review) is the author/funder, who has granted bioRxiv a license to display the preprint in perpetuity. It is made available under aCC-BY-NC-ND 4.0 International license.

(Hg19/GRCh37) using BWA algorithm (Abuin et al., 2015; Li and Durbin, 2009, 2010) and duplicates were removed using Picard toolkit (Github, Board institute). For all 3 cell lines mapping were in the cut-off limit (i.e mapping= >95% and Read Duplicates <20%). Further target enrichment was done using samtools and subsequent variant calling was done on BAM file using GATK pipeline to produce VCF formatted output file (BSD, MIT). All variants in the VCF file were then annotated using in-house pipeline with all required databases including OMIM, ClinVar HGBS coordinates, different population databases, etc (Ulintz et al., 2019). Sequencing data was analyzed manually to identify TP53 gene mutations in the cell lines.

Statistical Analysis

At least 3 biological independent replicates were performed for all the experiments. Hygens software (SVI, Hilversum, Netherlands) was used to calculate the surface area, volume and sphericity of the 3D acini or spheroids. Results were analyzed and plotted using GraphPad Prism (GraphPad Software, La Jolla, CA, USA). Mann Whitney U test was used to test the significance of difference of various parameters in the morphometric analysis and immunofluorescence. Paired Student's t-test or One-way ANOVA was performed to analyze the significance of difference of protein expression in immunoblotting.

Conflict of Interest

The authors declare that they have no competing interests.

Author Contributions

R.M.U and M.L conceived and conceptualized the project. R.M.U designed, performed and analyzed the experiments. R.M.U and M.L wrote the paper.

Funding

This study is supported by a grant from Science and Engineering Research Board (SERB), Govt. of India (EMR/2016/001974) and partly by IISER, Pune Core funding. R.M.U was funded by CSIR, India.

Acknowledgements

bioRxiv preprint doi: https://doi.org/10.1101/2022.04.05.487132; this version posted April 6, 2022. The copyright holder for this preprint (which was not certified by peer review) is the author/funder, who has granted bioRxiv a license to display the preprint in perpetuity. It is made available under aCC-BY-NC-ND 4.0 International license.

We thank Drs Richa Rikhy (IISER, Pune, India), and Sorab Dalal (ACTREC, Navi Mumbai, India) for their valuable suggestions. The authors acknowledge the IISER Pune Microscopy Facility and IISER-BD FACS facility for access to equipments and infrastructure. We thank National Facility for Gene Function in Health and Disease (IISER, Pune, India) for providing the animals and facilities. We also thank Lahiri lab members for their helpful comments and discussions.

References

Abuin, J.M., Pichel, J.C., Pena, T.F., and Amigo, J. (2015). BigBWA: approaching the Burrows-Wheeler aligner to Big Data technologies. Bioinformatics *31*, 4003-4005.

Aiello, N.M., Maddipati, R., Norgard, R.J., Balli, D., Li, J., Yuan, S., Yamazoe, T., Black, T., Sahmoud, A., Furth, E.E.*, et al.* (2018). EMT Subtype Influences Epithelial Plasticity and Mode of Cell Migration. Dev Cell *45*, 681-695 e684.

Anandi, L., Chakravarty, V., Ashiq, K.A., Bodakuntla, S., and Lahiri, M. (2017). DNA-dependent protein kinase plays a central role in transformation of breast epithelial cells following alkylation damage. J Cell Sci *130*, 3749-3763.

Anandi, V.L., Ashiq, K.A., Nitheesh, K., and Lahiri, M. (2016). Platelet-activating factor promotes motility in breast cancer cells and disrupts non-transformed breast acinar structures. Oncol Rep *35*, 179-188.

Araki, H., Leem, S.H., Phongdara, A., and Sugino, A. (1995). Dpb11, which interacts with DNA polymerase II(epsilon) in Saccharomyces cerevisiae, has a dual role in S-phase progression and at a cell cycle checkpoint. Proc Natl Acad Sci U S A *92*, 11791-11795.

Bodakuntla, S., Libi, A.V., Sural, S., Trivedi, P., and Lahiri, M. (2014). N-nitroso-N-ethylurea activates DNA damage surveillance pathways and induces transformation in mammalian cells. BMC Cancer *14*, 287.

Cancer Genome Atlas, N. (2012). Comprehensive molecular portraits of human breast tumours. Nature *490*, 61-70.

Chowdhury, P., Lin, G.E., Liu, K., Song, Y., Lin, F.T., and Lin, W.C. (2014). Targeting TopBP1 at a convergent point of multiple oncogenic pathways for cancer therapy. Nat Commun *5*, 5476.

bioRxiv preprint doi: https://doi.org/10.1101/2022.04.05.487132; this version posted April 6, 2022. The copyright holder for this preprint (which was not certified by peer review) is the author/funder, who has granted bioRxiv a license to display the preprint in perpetuity. It is made available under aCC-BY-NC-ND 4.0 International license.

Debnath, J., and Brugge, J.S. (2005). Modelling glandular epithelial cancers in three-dimensional cultures. Nat Rev Cancer *5*, 675-688.

Debnath, J., Muthuswamy, S.K., and Brugge, J.S. (2003). Morphogenesis and oncogenesis of MCF-10A mammary epithelial acini grown in three-dimensional basement membrane cultures. Methods *30*, 256-268.

Deisboeck, T.S., and Couzin, I.D. (2009). Collective behavior in cancer cell populations. Bioessays *31*, 190-197.

DuChez, B.J. (2017). Automated Tracking of Cell Migration with Rapid Data Analysis. Curr Protoc Cell Biol *76*, 12 12 11-12 12 16.

Forma, E., Krzeslak, A., Bernaciak, M., Romanowicz-Makowska, H., and Brys, M. (2012). Expression of TopBP1 in hereditary breast cancer. Mol Biol Rep *39*, 7795-7804.

Going, J.J., Nixon, C., Dornan, E.S., Boner, W., Donaldson, M.M., and Morgan, I.M. (2007). Aberrant expression of TopBP1 in breast cancer. Histopathology *50*, 418-424.

Griffiths, G., and Simons, K. (1986). The trans Golgi network: sorting at the exit site of the Golgi complex. Science *234*, 438-443.

Hanahan, D., and Weinberg, R.A. (2011). Hallmarks of cancer: the next generation. Cell *144*, 646-674.

Hirano, T., Funahashi, S., Uemura, T., and Yanagida, M. (1986). Isolation and characterization of Schizosaccharomyces pombe cutmutants that block nuclear division but not cytokinesis. EMBO J *5*, 2973-2979.

Jordan, J.J., Inga, A., Conway, K., Edmiston, S., Carey, L.A., Wu, L., and Resnick, M.A. (2010). Altered-function p53 missense mutations identified in breast cancers can have subtle effects on transactivation. Mol Cancer Res *8*, 701-716.

Karppinen, S.M., Erkko, H., Reini, K., Pospiech, H., Heikkinen, K., Rapakko, K., Syvaoja, J.E., and Winqvist, R. (2006). Identification of a common polymorphism in the TopBP1 gene associated with hereditary susceptibility to breast and ovarian cancer. Eur J Cancer *42*, 2647-2652.

bioRxiv preprint doi: https://doi.org/10.1101/2022.04.05.487132; this version posted April 6, 2022. The copyright holder for this preprint (which was not certified by peer review) is the author/funder, who has granted bioRxiv a license to display the preprint in perpetuity. It is made available under aCC-BY-NC-ND 4.0 International license.

Kastan, M.B., and Bartek, J. (2004). Cell-cycle checkpoints and cancer. Nature *432*, 316-323.

Keller, P., Toomre, D., Diaz, E., White, J., and Simons, K. (2001). Multicolour imaging of post-Golgi sorting and trafficking in live cells. Nat Cell Biol *3*, 140-149.

Kim, J.E., McAvoy, S.A., Smith, D.I., and Chen, J. (2005). Human TopBP1 ensures genome integrity during normal S phase. Mol Cell Biol *25*, 10907-10915.

Kumagai, A., Lee, J., Yoo, H.Y., and Dunphy, W.G. (2006). TopBP1 activates the ATR-ATRIP complex. Cell *124*, 943-955.

Li, H., and Durbin, R. (2009). Fast and accurate short read alignment with Burrows-Wheeler transform. Bioinformatics *25*, 1754-1760.

Li, H., and Durbin, R. (2010). Fast and accurate long-read alignment with Burrows-Wheeler transform. Bioinformatics *26*, 589-595.

Liu, K., Bellam, N., Lin, H.Y., Wang, B., Stockard, C.R., Grizzle, W.E., and Lin, W.C. (2009). Regulation of p53 by TopBP1: a potential mechanism for p53 inactivation in cancer. Mol Cell Biol *29*, 2673-2693.

Liu, K., Graves, J.D., Lin, F.T., and Lin, W.C. (2021). Overexpression of TopBP1, a canonical ATR/Chk1 activator, paradoxically hinders ATR/Chk1 activation in cancer. J Biol Chem *296*, 100382.

Liu, K., Lin, F.T., Ruppert, J.M., and Lin, W.C. (2003). Regulation of E2F1 by BRCT domain-containing protein TopBP1. Mol Cell Biol *23*, 3287-3304.

Liu, K., Ling, S., and Lin, W.C. (2011). TopBP1 mediates mutant p53 gain of function through NF-Y and p63/p73. Mol Cell Biol *31*, 4464-4481.

Lv, Y., Huo, Y., Yu, X., Liu, R., Zhang, S., Zheng, X., and Zhang, X. (2016). TopBP1 contributes to the chemoresistance in non-small cell lung cancer through upregulation of p53. Drug Des Devel Ther *10*, 3053-3064.

Makiniemi, M., Hillukkala, T., Tuusa, J., Reini, K., Vaara, M., Huang, D., Pospiech, H., Majuri, I., Westerling, T., Makela, T.P.*, et al.* (2001). BRCT domain-containing protein

bioRxiv preprint doi: https://doi.org/10.1101/2022.04.05.487132; this version posted April 6, 2022. The copyright holder for this preprint (which was not certified by peer review) is the author/funder, who has granted bioRxiv a license to display the preprint in perpetuity. It is made available under aCC-BY-NC-ND 4.0 International license.

TopBP1 functions in DNA replication and damage response. J Biol Chem *276*, 30399-30406.

Moreno-Bueno, G., Portillo, F., and Cano, A. (2008). Transcriptional regulation of cell polarity in EMT and cancer. Oncogene *27*, 6958-6969.

Padmanaban, V., Krol, I., Suhail, Y., Szczerba, B.M., Aceto, N., Bader, J.S., and Ewald, A.J. (2019). E-cadherin is required for metastasis in multiple models of breast cancer. Nature *573*, 439-444.

Pedrote, M.M., Motta, M.F., Ferretti, G.D.S., Norberto, D.R., Spohr, T., Lima, F.R.S., Gratton, E., Silva, J.L., and de Oliveira, G.A.P. (2020). Oncogenic Gain of Function in Glioblastoma Is Linked to Mutant p53 Amyloid Oligomers. iScience *23*, 100820.

Santner, S.J., Dawson, P.J., Tait, L., Soule, H.D., Eliason, J., Mohamed, A.N., Wolman, S.R., Heppner, G.H., and Miller, F.R. (2001). Malignant MCF10CA1 cell lines derived from premalignant human breast epithelial MCF10AT cells. Breast Cancer Res Treat *65*, 101-110.

Schupbach, M. (1971). The isolation and genetic classification of UV-sensitive mutants of Schizosaccharomyces pombe. Mutat Res *11*, 361-371.

Sharma, V.K., and Lahiri, M. (2021). Interplay between p300 and HDAC1 regulate acetylation and stability of Api5 to regulate cell proliferation. Sci Rep *11*, 16427.

Soule, H.D., Maloney, T.M., Wolman, S.R., Peterson, W.D., Jr., Brenz, R., McGrath, C.M., Russo, J., Pauley, R.J., Jones, R.F., and Brooks, S.C. (1990). Isolation and characterization of a spontaneously immortalized human breast epithelial cell line, MCF-10. Cancer Res *50*, 6075-6086.

Theveneau, E., and Mayor, R. (2011). Can mesenchymal cells undergo collective cell migration? The case of the neural crest. Cell Adh Migr *5*, 490-498.

Ulintz, P.J., Wu, W., and Gates, C.M. (2019). Bioinformatics Analysis of Whole Exome Sequencing Data. Methods Mol Biol *1881*, 277-318.

Wang, H., and Elledge, S.J. (2002). Genetic and physical interactions between DPB11 and DDC1 in the yeast DNA damage response pathway. Genetics *160*, 1295-1304.

bioRxiv preprint doi: https://doi.org/10.1101/2022.04.05.487132; this version posted April 6, 2022. The copyright holder for this preprint (which was not certified by peer review) is the author/funder, who has granted bioRxiv a license to display the preprint in perpetuity. It is made available under aCC-BY-NC-ND 4.0 International license.

Wang, J., Chen, J., and Gong, Z. (2013). TopBP1 controls BLM protein level to maintain genome stability. Mol Cell *52*, 667-678.

Wardlaw, C.P., Carr, A.M., and Oliver, A.W. (2014). TopBP1: A BRCT-scaffold protein functioning in multiple cellular pathways. DNA Repair (Amst) *22*, 165-174.

Wasielewski, M., Elstrodt, F., Klijn, J.G., Berns, E.M., and Schutte, M. (2006). Thirteen new p53 gene mutants identified among 41 human breast cancer cell lines. Breast Cancer Res Treat *99*, 97-101.

Woessner, J.F., Jr. (1991). Matrix metalloproteinases and their inhibitors in connective tissue remodeling. FASEB J *5*, 2145-2154.

Xu, Y.J., and Leffak, M. (2010). ATRIP from TopBP1 to ATR--in vitro activation of a DNA damage checkpoint. Proc Natl Acad Sci U S A *107*, 13561-13562.

Yamamoto, R.R., Axton, J.M., Yamamoto, Y., Saunders, R.D., Glover, D.M., and Henderson, D.S. (2000). The Drosophila mus101 gene, which links DNA repair, replication and condensation of heterochromatin in mitosis, encodes a protein with seven BRCA1 C-terminus domains. Genetics *156*, 711-721.

Yu, X., Chini, C.C., He, M., Mer, G., and Chen, J. (2003). The BRCT domain is a phospho-protein binding domain. Science *302*, 639-642.

Zhang, Y., Yan, W., and Chen, X. (2011). Mutant p53 disrupts MCF-10A cell polarity in three-dimensional culture via epithelial-to-mesenchymal transitions. J Biol Chem *286*, 16218-16228.

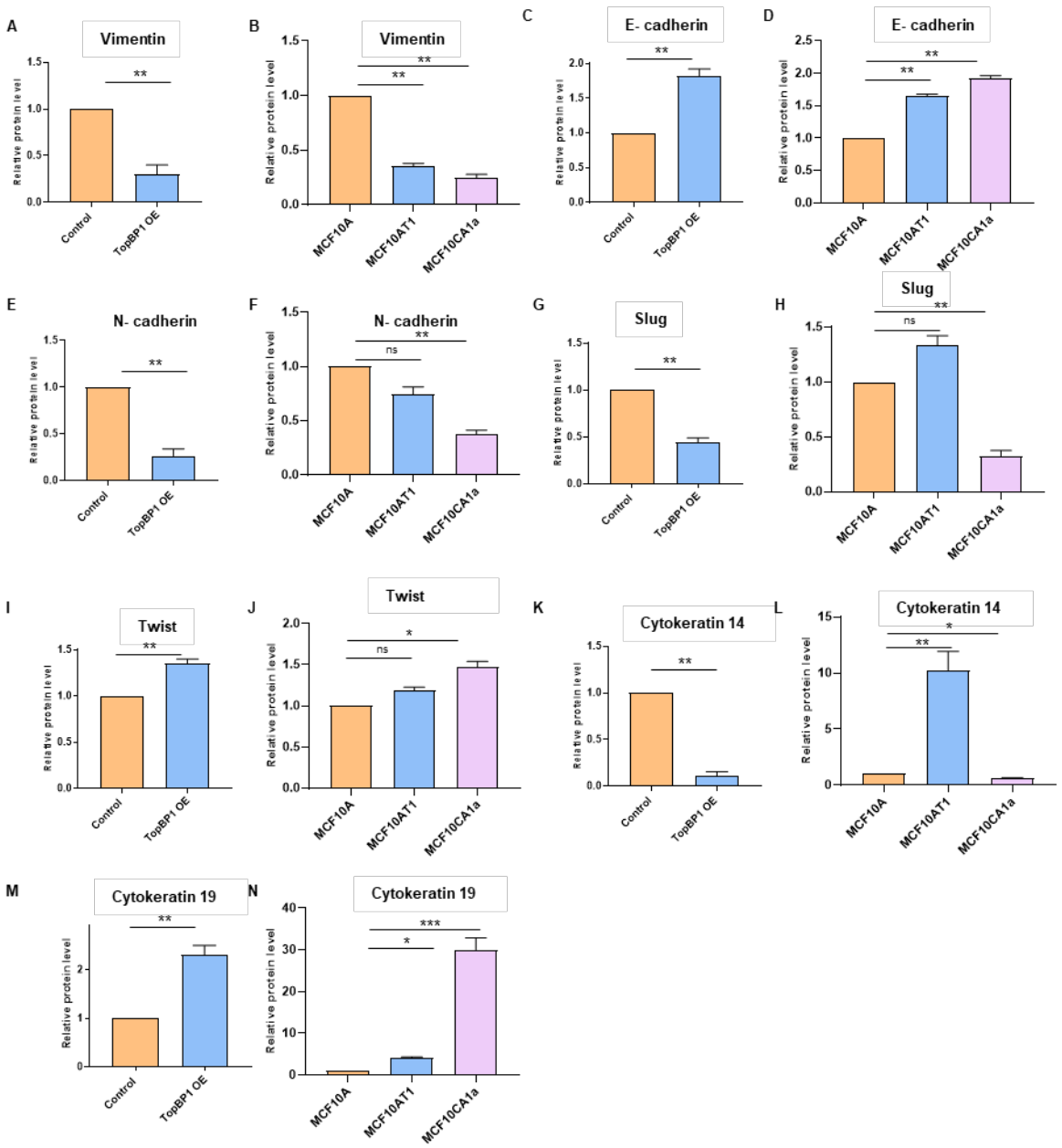
Supplementary information

Overexpression of TopBP1 leads to transformation with a TP53 mutation of non-tumorigenic breast epithelial cells

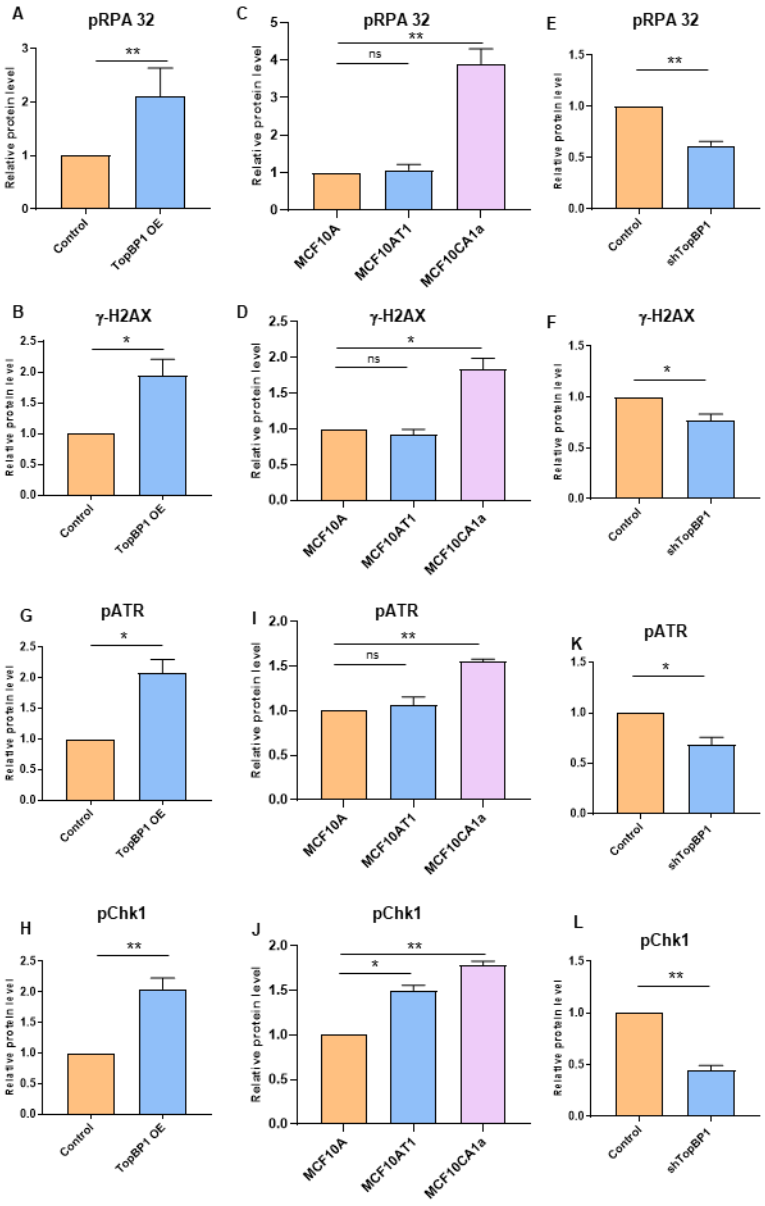
Rintu M Umesh and Mayurika Lahiri*

Department of Biology, Indian Institute of Science Education and Research, Dr. Homi Bhabha Road, Pune, Maharashtra 411008, India

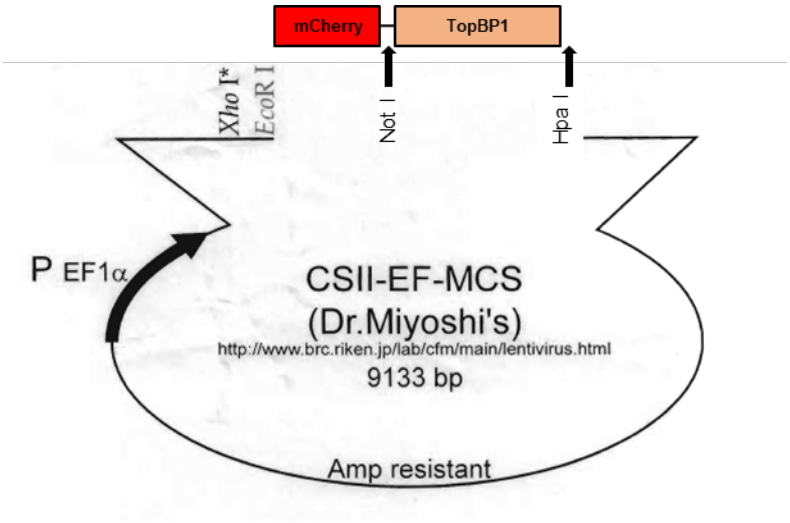
*Author for correspondence (mayurika.lahiri@iiserpune.ac.in)



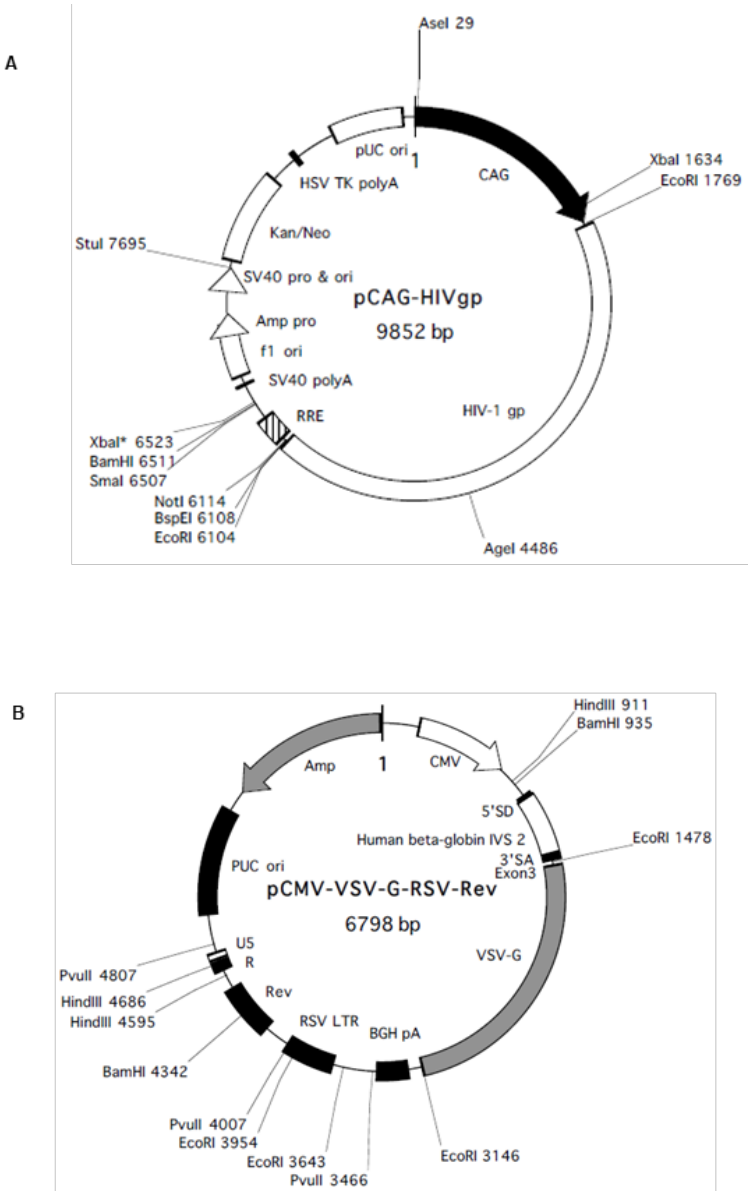
Supplementary Figure S1: To analyze the protein expression of various EMT markers, the cells were lyzed and immunoblotting was performed. A, C, E, G, I, K, M) mCherry MCF10A (control) and TopBP1 OE MCF10A 3D dissociated cells and B, D, F, H, J, L, N) MCF10A, MCF10AT1 and MCF10CA1a cells. Quantification was done to show the fold change of A-B) vimentin, C-D) E-cadherin, E-F) N-cadherin, G-H) Slug, I-J) Twist, K-L) Cytokeratin 14 and M-N) Cytokeratin 19 between mCherry MCF10A (control) and TopBP1 OE MCF10A 3D dissociated cells and MCF10A, MCF10AT1 and MCF10CA1a cell lysates after normalizing with the GAPDH. Statistical analysis was done using Paired Student's t-test for TopBP1 OE lysates and One-way ANOVA for MCF10A series (*** $p < 0.001$, ** $p < 0.01$, * $p < 0.05$, ns $p > 0.05$).



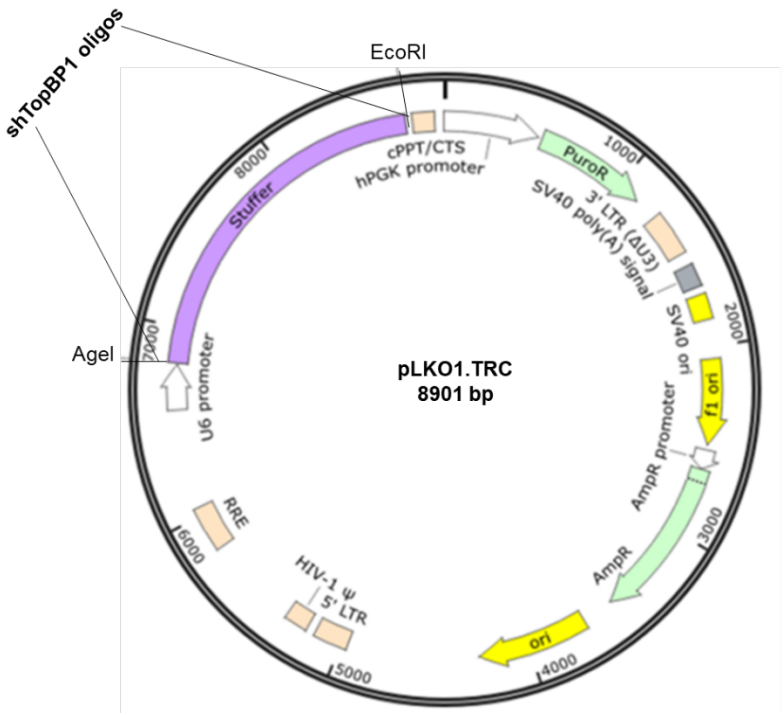
Supplementary Figure S2: To analyze the activation of various DNA damage repair proteins, the cells were lyzed and immunoblotting was performed A, B, G, H) mCherry MCF10A (control) and TopBP1 OE MCF10A 3D dissociated cells, C, D, I J) MCF10A, MCF10AT1, MCF10CA1a cells and pLKO.1 MCF10CA1a (control) and E, F, K, L) shTopBP1 MCF10CA1a cells. Quantification showing the fold change of A, C, E) pRPA 32, B, D, F) γH2AX, G, I, K) pATR, and H, J, L) pChk1. Phosphoproteins were quantified after normalizing to GAPDH. Statistical analysis was done using Paired Student's t-test for TopBP1 OE and shTopBP1 lysates and One-way ANOVA for MCF10A series (** $p < 0.01$, * $p < 0.05$, ns $p > 0.05$).



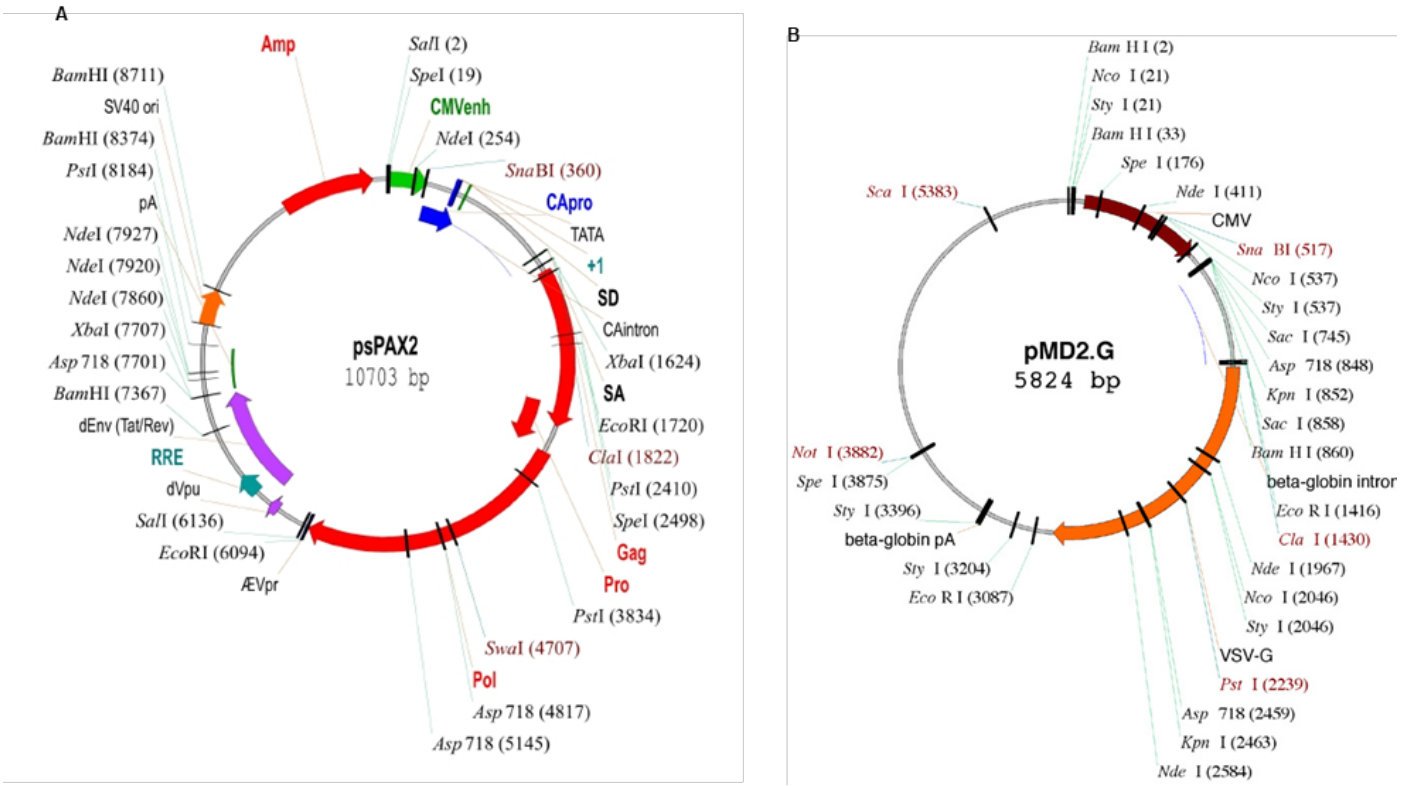
Supplementary Figure S3: TopBP1 was cloned into a CSII-EF-MCS vector with a mCherry tag between NotI and HpaI sites. The vector map of the CSII-EF-MCS plasmid was provided by Riken BioResource Centre, Japan**.**



Supplementary Figure S4: Vector map of A) HIV-1 gag and pol for lentivirus vector packaging and B) envelope VSVG protein and Rev packaging plasmid for the generation of TopBP1 overexpression lentiviral particles. The plasmids was purchased from RIKEN BioResource Centre, Japan and the vector map was provided by them.



Supplementary Figure S5: shTopBP1 oligos were annealed and cloned into pLKO.1.TRC vector with a puro selection marker between AgeI and EcoRI sites. The plasmid was a generous gift from Dr Sorab Dalal, ACTREC, India. The vector map was obtained from Addgene web site



Supplementary Figure S6: Vector map of A) psPAX2 gag and pol for lentivirus vector packaging and B) epMD2.G VSVG protein packaging plasmid for the generation of shTopBP1 lentiviral particles. The plasmids were a generous gift from Dr Manas K Santra, NCCS, India. The vector maps were obtained from the Addgene website.

Supplementary Table 1: Antibodies used for IF and Immunoblotting

Primary Antibody	Catalogue no	IF	Immunoblotting
RPA 32/2 Phospho T21 (Abcam)	AB 61065		1:1000
RPA (CST)	2208		1:1000
Laminin V, anti-Mouse (Millipore)	MAB19562		
TopBP1, anti-Rabbit (Bethyl)	A300-111A	1:200	1:1000
Rat X Hu CD49fα6 integrin, anti –Rat (Millipore)	MAB1378	1:100	-
GM130, anti-Mouse (Millipore)	610822	1:100	
E-cadherin, anti-Mouse (BD)	610182		1:7500
N-cadherin, anti-Rabbit (Abcam)	AB18203		1:1000
Vimentin, anti-Mouse (Abcam)	AB 8069	1:200	1:10000
β-catenin, anti- Rabbit (Abcam)	ab32572	1:100	
PCNA- PC10 (CST)	2586		1:2500
Cytokeratin 14, anti-Mouse (Abcam)	ab7800		1:1000
Cytokeratin 19, anti-Rabbit (Abcam)	ab52625		1:1000
GAPDH, anti-Rabbit (Sigma)	G9545		1:40000
Slug- C19G7 (CST)	9585		1:1000
Twist (Abcam)	ab50581		1:1000
γH2AX Ser 139 (Santacruz)	sc517348		1:1000
pATR Ser 428 (CST)	2853		1:1000
ATR (Abcam)	AB 2905-100		1:1000
pChk1 (CST)	2348L		1:1000
Chk1(Santacruz)	SC 8408		1:1000
p-p53 S15 (CST)	9284S		1:1000
p53 (Bethyl)	A300-247A		1:5000
p21 (Abcam)	ab109520		1:1000
Cyclin A (Santacruz)	sc-271682		1:1000

Supplementary Table 2: Cloning of TopBP1 into CSII-EF MCS vector

A. Amplification of TopBP1

Reagents	Amount
DNA Template	500 ng
Forward Primer	3 µl
Reverse Primer	3 µl
10 mM dNTPs	12.5 µl
10X Pfu buffer	10 µl
Pfu polymerase	2 µl
Nuclease free water	To make up the volume to 100 µl

B. PCR cycle for amplification of TopBP1

Temperature (ºC)	Time (mins)	
95	2	
95	1	25 cycles
50	1	
72	10	
72	10	

C. Digestion of PCR product and CSII-EF-MCS-mCherry

Digestion reagents	Amount
DNA Template	5 µg
10 X Cut smart buffer	5 µl
Not I HF	5 µl
Hpa I	5 µl
Nuclease free water	To make up the reaction to 50 µl

D. Ligation reaction of TopBP1 and CS-II-EF-MCS-mCherry digested vector

Ligation reagents	Amount
Insert	75 ng
Vector	25 ng
10X T4 Ligase buffer	1 µl
T4 DNA Ligase	1 µl
Nuclease free water	To make up the reaction to 10 µl

Supplementary Table 3: Cloning of shTopBP1 into pLKO1.TRC vector

A. Restriction digestion of pLKO1.TRC vector

Digestion Reagents	Amount
DNA	~3 µg
10x cut smart buffer (NEB)	5 µl
AgeI Hf (NEB)	3 µl
EcoRI Hf (NEB)	3 µl
Nuclease free water	Make upto 50 µl

B. Annealing reaction for shTopBP1 oligos

Anealing Reagents	Volume (µl)
TopBP1 shRNA forward oligo	1.0
TopBP1 shRNA reverse oligo	1.0
10 x T4 DNA Ligase buffer (Takara)	1.0
T4 PNK	0.5
Nuclease free water	6.5

C. PCR program for annealing of shTopBP1 oligos

Temperature	37 °C	95 °C	90 °C	85 °C	80 °C	75 °C	70 °C	65 °C	60 °C	55 °C	50 °C	45 °C	40 °C	35 °C	30 °C	25 °C	4°C
Time	30’	5’	1’	1’	1’	1’	1’	1’	1’	1’	1’	1’	1’	1’	1’	1’	hold

D. Ligation reaction for annealed shTopBP1 oligos and digested pLKO1.TRC

Reagents	Amount
Digested pLKO.1-TRC	25ng
shTopBP1	125ng
T4 DNA Ligase (Takara)	1 µl
10x T4DNA Ligase buffer(Takara)	1 µl
Nuclease free water	Upto 10 µl

frontiers in Genetics

BRIEF RESEARCH REPORT
published: 25 March 2021
doi: 10.3389/fgene.2021.634938

Prolonged Exposure to Platelet Activating Factor Transforms Breast Epithelial Cells

*Vaishali Chakravarty†‡, Libi Anandi†‡, K. A. Ashiq†‡, K. Abhijith, Rintu Umesh and Mayurika Lahiri**

Department of Biology, Indian Institute of Science Education and Research, Pune, India

OPEN ACCESS

Edited by:
Hari S. Misra, Bhabha Atomic Research Centre (BARC), India

Reviewed by:
Chandrima Das, Saha Institute of Nuclear Physics (SINP), India
Constantinos Demopoulos, National and Kapodistrian University of Athens, Greece

***Correspondence:**
Mayurika Lahiri
mayurika.lahiri@iiserpune.ac.in
orcid.org/0000-0001-9456-4920

†These authors have contributed equally to this work

‡Present address:
Vaishali Chakravarty, Enveda Therapeutics India Pvt. Ltd., VCR Park, Vishakhapatnam, India
Libi Anandi, Department of Biology, Center for Genomics and Systems Biology, New York University, New York, NY, United States
K. A. Ashiq, National Centre for Cell Science, Pune, India

Specialty section:
This article was submitted to Genetics of Common and Rare Diseases, a section of the journal Frontiers in Genetics

Received: *29 November 2020*
Accepted: *03 March 2021*
Published: *25 March 2021*

Citation:
Chakravarty V, Anandi L, Ashiq KA, Abhijith K, Umesh R and Lahiri M (2021) Prolonged Exposure to Platelet Activating Factor Transforms Breast Epithelial Cells. Front. Genet. 12:634938. doi: 10.3389/fgene.2021.634938

Lipid species are known to have various biological functions owing to their structural differences, and each of them possesses a specific role to play depending upon their location and distribution in the cell. Some of these lipids interact with proteins on the cell membrane and acts as second messengers. The level of lipid mediators is generally maintained in the cell by feedback mechanisms; however, their improper degradation or enhanced production leads to their accumulation in the tumor microenvironment and disturbs the homeostasis of the cell. Platelet activating factor (PAF) is a known phospholipid mediator secreted upon immunological challenges by platelets, neutrophils, basophils, and macrophages. PAF, as a potent inflammatory molecule, is well studied, and its role in various cancers and cardiovascular diseases has also been investigated. Interestingly, increased levels of PAF have been found in the blood plasma of smokers, and breast cancer cells have shown the accumulation of PAF in presence of cigarette smoke extract. This accumulation was found to increase tumor cell motility that in turn could promote metastasis. Beyond this, however, the effect of PAF on tumorigenesis has not yet been well explored. Here, we show that the continuous exposure of 3D breast acinar cultures to PAF resulted in the activation of various oncogenic signaling pathways leading to transformation. We also found that the presence of PAF in the micro-environment increased the expression of PAF receptor (PAF-R), which corroborated with the higher expression of PAF-R detected in some epithelial cancers, as per literature. Thus, this study impresses on the fact that the presence of PAF alters the cellular microenvironment and eventually triggers irreversible effects that can cumulatively lead to transformation.

Keywords: platelet activating factor, transformation, breast cancer, epithelial-mesenchymal transition, polarity

INTRODUCTION

Immune system holds a key position in maintaining cellular homeostasis, and an imbalance can lead to various abnormities including cancer. Hence, it is one of the primary targets while designing therapy for malignancies. Tumor infiltrating cells, such as leukocytes and macrophages, are common entities in cancers, and their interaction with the tumor micro-environment components is widely studied (Hanahan and Weinberg, 2011). Such entities are known to promote tumor progression and invasion, and thus hold a clinical relevance in

various cancers (Man et al., 2013). The interaction of the immune cells and the cancer cells could be through direct cell-cell contact or may also be mediated by secretory molecules. One such molecule is platelet activating factor (PAF). PAF is an autacoid phospholipid mediator, which is secreted in response to an agonist by various immune cells and elicits various immunoregulatory reactions such as platelet aggregation, allergy, anaphylaxis, and many more (Foa et al., 1985; Hanahan and Weinberg, 2011). Overall, it is known to induce various physiological and pathological processes that eventually affect the respiratory, vascular, and even reproductive system (Papakonstantinou et al., 2017). PAF production is tightly regulated by biosynthetic and degradative mechanisms since uncontrolled levels can cause various pathologies. PAF acetyl hydrolase (PAF-AH) controls the level of PAF in the system by degradative mechanisms (Chen et al., 2007).

In the early studies, after the role of PAF was established in various pleiotropic activities, its effects were observed in various diseases as well (Lordan et al., 2019). PAF-AH activity was seen to be inhibited when human plasma was treated with cigarette smoke extract (CSE). This was also strengthened by the results that showed increased plasma concentration of PAF in smokers, indicating the role of PAF in the development of cardiovascular diseases in smokers (Miyaura et al., 1992). Kispert et al. (2015) has shown that CSE inhibits PAF-AH activity, thus leading to the accumulation of PAF in the endothelial cells. In a recent study with a bladder cancer cell line, the same group has reported similar results, wherein grade III HT-1376 cells showed higher PAF accumulation followed by greater adherence in presence of CSE, exhibiting highly aggressive manifestations (Kispert et al., 2019). Investigations by Bussolati et al. showed the presence of high amounts of PAF in MCF-7, MDA-MB 231, and T47D cells. This synthesized PAF enhanced cell motility as well as increased proliferation in MDA-MB 231 cells (Bussolati et al., 2000). An early report from Bennett et al. demonstrates that PAF induces phenotypic transformation in rat embryonic cells. They have shown increased cell density, growth in low serum condition, and anchorage-independent growth, which are the indicators of transformation, in the presence of dose-dependent increase in PAF concentration (Bennett et al., 1993).

Although PAF is a lipid mediator, it is not known to freely diffuse through the cell membrane and studies clearly state that PAF activates a G-protein coupled receptor, PAF-R and mediates its activities through this axis. PAF-R is ubiquitously expressed across tissues, and its role in various cancers has been established (Ishii and Shimizu, 2000; Jancar and Chammas, 2014). The PAF-PAFR axis activation suggests a feedback control loop that maintains the PAFR levels in pathological conditions (Chen et al., 2015a; Lv et al., 2017). Two groups in 2015 have shown the role of PAFR in non small cell lung carcinoma (NSCLC) and esophageal squamous cell carcinoma (ESCC). In NSCLC, the activation of PAF-PAF-R axis induces epithelial-mesenchymal transition (EMT), leading to invasion and metastasis of NSCLC cells (Chen et al., 2015a). Role of PAF-R in ESCC malignancy has been stated *via* the activation of oncogenic signaling through FAK/PI3K/AKT/NF-kB axis (Chen et al., 2015b). Previous report from the lab has shown that breast cancer cells in the presence of PAF shows higher motility and when MCF10A, a non-tumorigenic breast epithelial cell line, was grown on an ECM, in presence of PAF, disrupts the luminal phenotype (Anandi et al., 2016). Results from the lab as well as mounting evidence from literature imposed heavily on the necessity to investigate the role of PAF in the transformation of three-dimensional (3D) cultures of MCF10A cells. In the current study, we have focused on elucidating the transformation phenotypes acquired by MCF10A breast acinar cultures in the presence of PAF and the activation of PI3-K/AKT signaling pathway to strengthen the oncogenic potential of PAF.

MATERIALS AND METHODS

Cell Lines and Culture Conditions

MCF10A cell line was a generous gift from Prof. Raymond C. Stevens (The Scripps Research Institute, California, United States) and 2D monolayer cultures and 3D cultures were grown according to the standard protocols (Debnath et al., 2003). 3D cultures were maintained for 20 days by supplementing fresh media every 4 days. Methylcarbamyl PAF C-16, procured as a 10 mg/ml solution in ethanol (Cayman chemicals, 60908), was diluted in sterile PBS to make a working stock of 100 μM. Required volume of the working stock was directly added to the desired volume of media, to achieve a final concentration of 200 nM. PAF treatment was given 3 h post seeding and along with every media change.

Immunoflourescence

Acini from the 3D cultures were extracted using PBS-EDTA treatment for apical proteins and other proteins using normal method of extraction. Immunostaining was done using a previously described protocol (Anandi et al., 2017). Samples were imaged using 40X oil immersion objective of SP8 confocal microscope (Leica, Germany).

Details of chemical, antibodies, and statistical analysis used and methods for 3D "on top" cultures, immunoblot analysis, RNA Extraction, cDNA preparation, semi-quantitative PCR, soft agar assay, DQ collagen invasion assay, and gelatin zymography can be found in **Supplementary Material**.

RESULTS

PAF Treatment on 3D Cultures of MCF10A Leads to Increased Proliferation

3D breast acinar cultures, grown on laminin rich matrix, attain a growth arrested state with a monolayer of cells around a hollow lumen, after 12 days of culturing. Cells in such stable structures are usually arrested in the G1 Phase (Fournier et al., 2006). Based on our previous data (Anandi et al., 2016), to ascertain if PAF treatment resulted in the presence of hyperproliferating and actively dividing cells, that resulted in large acini, we immunostained the PAF-treated 20-day cultures with Ki67, a proliferation marker. Acini with more than five

cells positive for Ki67 are considered to be hyperproliferating (Wu and Gallo, 2013). Eighty percent of the PAF treated acini were found to be hyperproliferating (**Figure 1A**). Further, immunoblotting revealed a 1.4-fold upregulation in Ki67 protein levels (**Figure 1B**). This shows that PAF leads to the formation of large multiple layered acini that have evaded the growth-arrested state and are hyperproliferating thus qualifying as a transformation phenotype.

Apico-Basal Polarity and Cell-Cell Junctions Gets Disrupted in the Presence of PAF Treatment

One of the important features of epithelial architecture is polarization. Epithelial cells attain apico-basal polarity when placed in a 3D environment unlike cells on a 2D plane, which only have front and rear polarities. Alongside, cell-cell junction is an important component in maintaining the epithelial tissue homeostasis. In this study, it is evident that PAF affects the orientation of epithelial polarity and leads to compromised cell-cell junctions. There are various proteins that are known to act as markers of polarity such as integrins, laminins, and also Golgi (Debnath et al., 2003; Debnath and Brugge, 2005). E-cadherin is an adherens junction protein, which is well-established in MCF10A unlike the tight junctions, which are poorly developed (Ivers et al., 2014). E-cadherin is a central component of the zona adherens junction complex, and the loss of E-cadherin is a key indicator of tumor aggressiveness (Kourtidis et al., 2017). The 3D cultures of MCF10A treated with PAF were extracted after 20 days and immunostained with apical and basal markers such as GM130, α6-integrin, and Laminin-V. α6-integrin, receptors for the ECM, marks the basal region of the acini and stains across the basolateral regions. In the presence of PAF, the staining pattern was altered dramatically by change in expression level as well as membrane distribution of the protein (**Figure 2A**). Seventy-three percent of acini treated with PAF exhibited marked loss of α6-integrin from the basal region and also enhanced cytoplasmic staining was observed, which we quantified as loss and mis-localized phenotype. Epithelial cells have a remarkable property of attachment to the ECM *via* the basement membrane (BM). This BM is disrupted in the cases of primary metastasis in breast carcinomas (Shaw et al., 2004). Laminins are a group of BM proteins and LamininV is one of the components of BM (Shaw et al., 2004). Acini grown in the presence of PAF showed gross disruption in LamininV staining, thus indicating loss of BM protein due to PAF treatment. Seventy-two percent of acini show disrupted as well as the loss of membrane localization of LamininV (**Figure 2B**). GM130, which is a cis-Golgi marker, was mislocalized to the basal and lateral regions in PAF-treated acini, whereas in the control acini Golgi localization remained apical. Upon quantifying, it was observed that 100% of Golgi was mislocalized in PAF-treated acini (**Figure 2C**). These results indicate a clear loss of apical as well as basal polarity in MCF10A 3D cultures grown in the presence of PAF. Immunostaining for β-catenin revealed a diffused localization of β-catenin at cell-cell junction as well as in intercellular granular pockets, which is also indicative of aberrant protein trafficking (**Figure 2D**). To further confirm the disruption of the cell-cell junctions, cells from day 20 spheroids were dissociated (referred to as dissociated cells hereafter) and immunostained for E-cadherin and β-catenin. Loss of E-cadherin by immunostaining was observed in the presence of PAF (**Figure 2E**) and analyzed using intensity plot profiling (**Figure 2G**). β-catenin also showed similar diffused patterns in the dissociated cells as was observed in the acinar cultures (**Figure 2F**). The diffused pattern was analyzed using a plot profiling of lines drawn across cell-cell junctions and then calculating Full Width Half Max (FWHM) as depicted in the schematic in **Figure 2H**. The FWHM values were significantly higher in PAF exposed cells as compared to

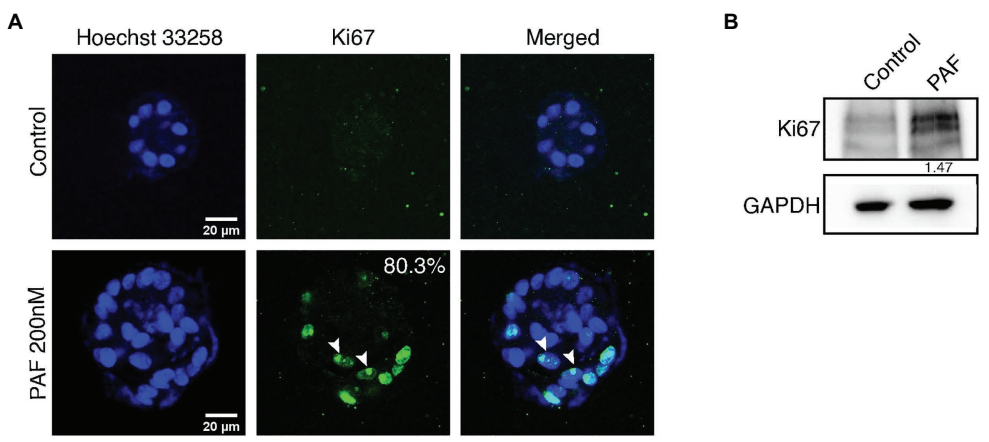


FIGURE 1 | PAF treatment on 3D cultures of MCF10A leads to increased proliferation. MCF10A cells grown as 3D cultures for 20 days treated with and without PAF (200 nM) were immunostained with the proliferation marker, Ki67. **(A)** Representative image showing hyperproliferation in PAF-treated acini. The data are from $N = 5$ set of experiments. **(B)** Protein lysates from 20-day cultures were immunoblotted for Ki67. The values represent the relative expression of Ki67 normalized to GAPDH.

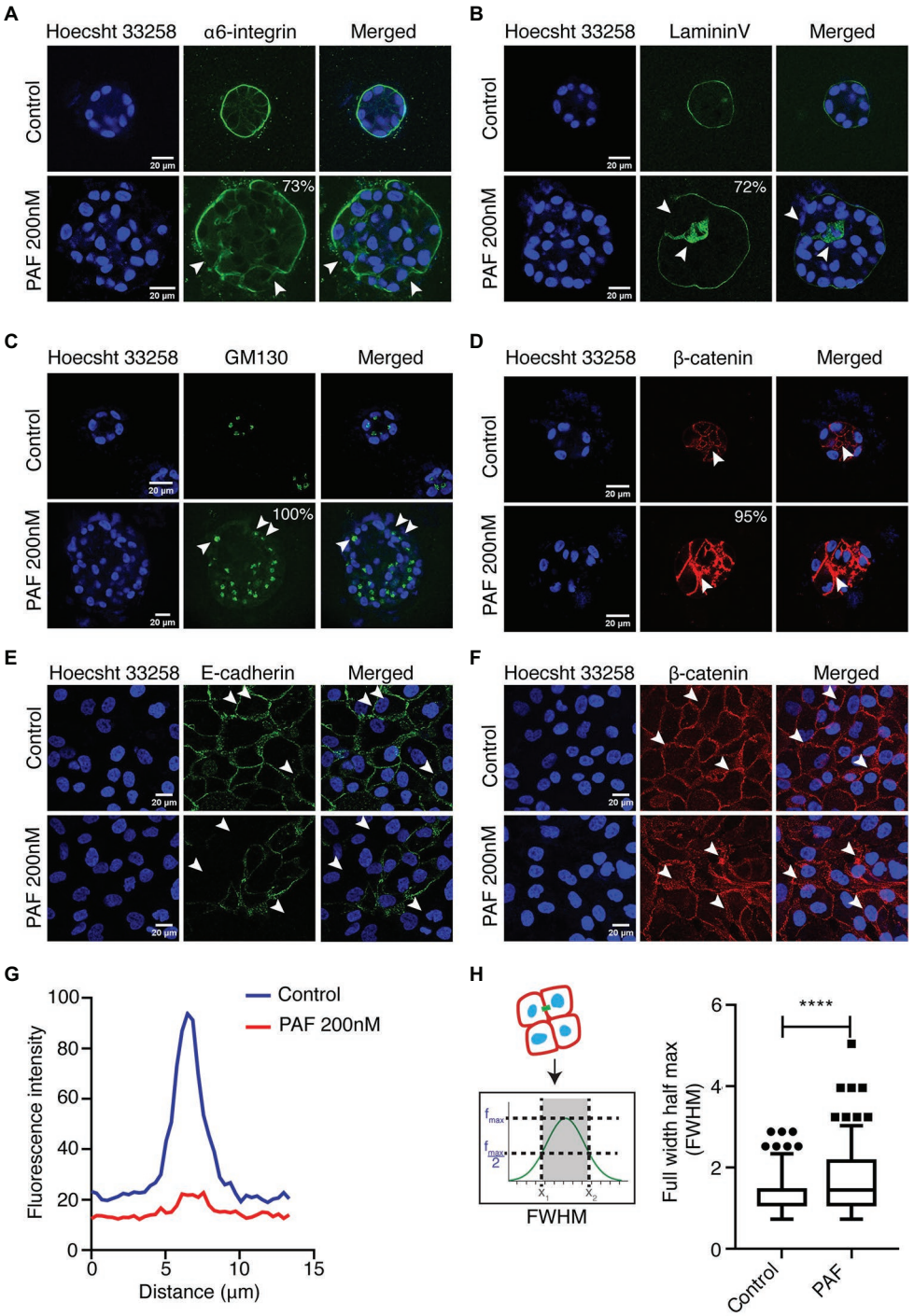


FIGURE 2 | PAF treatment alters acinar polarity and leads to the disruption of cell-cell junctions. PAF-treated 20 days 3D cultures of MCF10A were immunostained with polarity and cell-cell junction markers. Nucleus is stained with Hoecsht 33,258 (blue). **(A)** Immunostained images of α6-integrin (green) marks the basal polarity ($N = 4$). **(B)** Immunostained images of LamininV (green) marks the basement membrane of the acini ($N = 4$). **(C)** Immunostained images of GM130 (green) marks apical polarity ($N = 3$). **(D)** Immunostained images of β-catenin (red) marks the cell-cell junctions. **(E)** Dissociated cells of control and PAF-treated acini immunostained with E-cadherin (green), a cell-cell junction marker and the image is a representative of the phenotype ($N = 3$). **(F)** Dissociated cells of control and PAF treated acini immunostained with β-catenin (red), a cell-cell junction marker and the image is a representative of the diffused phenotype ($N = 3$). **(G)** Median fluorescent intensity of E-cadherin line profile showing loss phenotype. **(H)** FWHM profile of β-catenin line profile showing diffused phenotype. The phenotypes are quantified from $N > 3$ set independent experiments. Statistical analysis was performed for **(H)** using Mann Whitney U test; *****$p < 0.0001$.

untreated dissociated cells (**Figure 2H**). This clearly indicated that PAF treatment altered epithelial polarity and also led to a loss and/or disruption of cell-cell junctions.

PAF Treatment Induces Partial EMT-Like Phenotype

EMT is a process of transition of epithelial cells into mesenchymal cells. This program has been distinctively viewed as a two-stage program with two discrete cell populations of epithelial and mesenchymal cells expressing the cell-type specific proteins (Pastushenko and Blanpain, 2019). However, recent studies indicate that EMT is a gradual process that takes place through stages that are known as intermediate states. This state circumscribes the co-expression of epithelial and mesenchymal markers. It has also been shown in similar studies that this hybrid/incomplete state of EMT is more culpable to poor survival and higher chances of resistance to therapy (Lambert et al., 2017; Pastushenko and Blanpain, 2019).

Vimentin, a known mesenchymal marker, showed an upregulated phenotype in the acini grown in the presence of PAF (**Figures 3A,B**). The protein expression of the different EMT markers was also investigated as shown in (**Figure 3C**). Vimentin and N-cadherin protein levels showed an upregulation in the presence of PAF, and densitometric analysis showed a 2-fold and 1.76-fold increase in the respective protein levels. Fibronectin, which is also a mesenchymal marker, is also upregulated in the presence of PAF. E-cadherin, an epithelial and a cell-cell junction marker showed a 0.5-fold reduction in protein level, which further corroborated the loss that was observed earlier (**Figure 2E**). β-catenin protein levels did not show a significant change probably because there has not been a major loss of the protein but more of cellular redistribution from the junctions to the cytoplasm as granules. Hence, a clear difference in protein level was not observed. Slug, a transcription factor, showed a 1.47-fold increase at protein level.

Transcript levels of the various EMT markers were also investigated in the 20-day PAF-treated 3D cultures. Fibronectin, slug, and twist transcript levels were measured using semi-quantitative PCR. Fibronectin transcript level was more than 2-fold higher in the RNA lysates collected post 20 days of PAF treatment. The transcript levels of slug and twist also showed a 2-fold upregulation in the presence of PAF (**Figure 3D**). The quantifications of the transcript level were performed using densitometric analysis using ImageJ software. The role of tumor micro-environment (TM) is well-established in various cancers including breast cancer (Yu and Elble, 2016). TM is composed of different inflammatory and immune cells, apart from other components, which have been known to induce EMT-like phenotype (Yu and Elble, 2016). As mentioned before, PAF is a phospholipid mediator that is widely known to play a role in the activation of various immune cells. Hence, the above results are indicative of the formation of a link between hybrid state of EMT, TM and PAF; all leading to transformation.

Figure 3E shows the phase contrast images of control and PAF-treated dissociated cells grown as monolayer cultures. Control cells appear like MCF10A cells, epithelial-like, and cuboidal, while PAF-treated cells appear spindle-like, large, and elongated. This appearance is retained when cells are both sparsely or densely seeded. This morphology strengthens the fact that PAF has the ability to transform MCF10A breast epithelial cells.

Since the data indicate induction of EMT, this was further supported by performing DQ collagen™ assay. PAF dissociated cells showed increased fluorescence when observed under SP8 confocal microscope (Leica, Germany; **Figure 3F**), which was quantified (**Figure 3G**). To strengthen the hypothesis that PAF induces invasion, gelatin zymography was performed using the conditioned media (CM) from the 3D breast acinar cultures. Increased activation of MMP-2 (1.42-fold) and MMP-9 (2.23-fold) were observed in the conditioned media collected from the PAF-treated samples (**Figure 3H**), thus indicating the ability of PAF stimulation to induce invasion, which is a known marker for transformation. Taken together, our data clearly indicate the induction of partial EMT and invasion in PAF-treated cells thereby leading to a transformation phenotype.

Effect of PAF on Anchorage Independent Growth of MCF10A Cells and Activation of the PI3K/AKT Pathway

Anchorage independent growth is a key characteristic feature that cells attain when they have undergone transformation, and this ability is considered as a fundamental property of cancer cells. This capacity to grow on a semisolid substratum serves as a proxy for *in vivo* tumorigenicity (Horibata et al., 2015). In our study, soft agar assay was performed to investigate whether prolonged PAF-treatment could transform the cells, thus allowing them to grow in an anchorage-independent manner. Dissociated cells of both control and PAF-treated acini were grown on soft agar for 27 days and then stained with MTT, a tetrazolium dye, to visualize the colonies and to distinguish the dead cells from live ones. **Figures 4A,B** clearly show PAF dissociated cells to have gained the capability to form colonies in an anchorage-independent manner, which supports the hypothesis that PAF induces *in vitro* tumorigenesis.

Our data indicate PAF stimulation of non-tumorigenic breast epithelial cells to undergo transformation; however, the mechanism of this transformation process is not known. In the current study, PAF-R showed a 2-fold upregulation in transcript levels of the PAF-stimulated lysates (**Figure 4C**). Further, PAF-treated 3D culture lysates were immunoblotted and probed for pAKT and total AKT. pAKT showed close to 3-fold increase in activation with concomitant increase in AKT protein expression upon prolonged treatment with PAF (**Figure 4D**).

In support of the existing literature, our data also show MMP-2 and MMP-9 activation downstream of pAKT activation. Increased cellular proliferation observed in the presence of PAF is suggestive of the contribution of the AKT pathway in the PAF-mediated transformation of MCF10A cells grown as 3D cultures. Hence, we predict the following pathway (**Figure 4E**) using existing data and current literature; however, further research is required to delineate the mechanism of transformation through PAF. Since our data are preliminary,

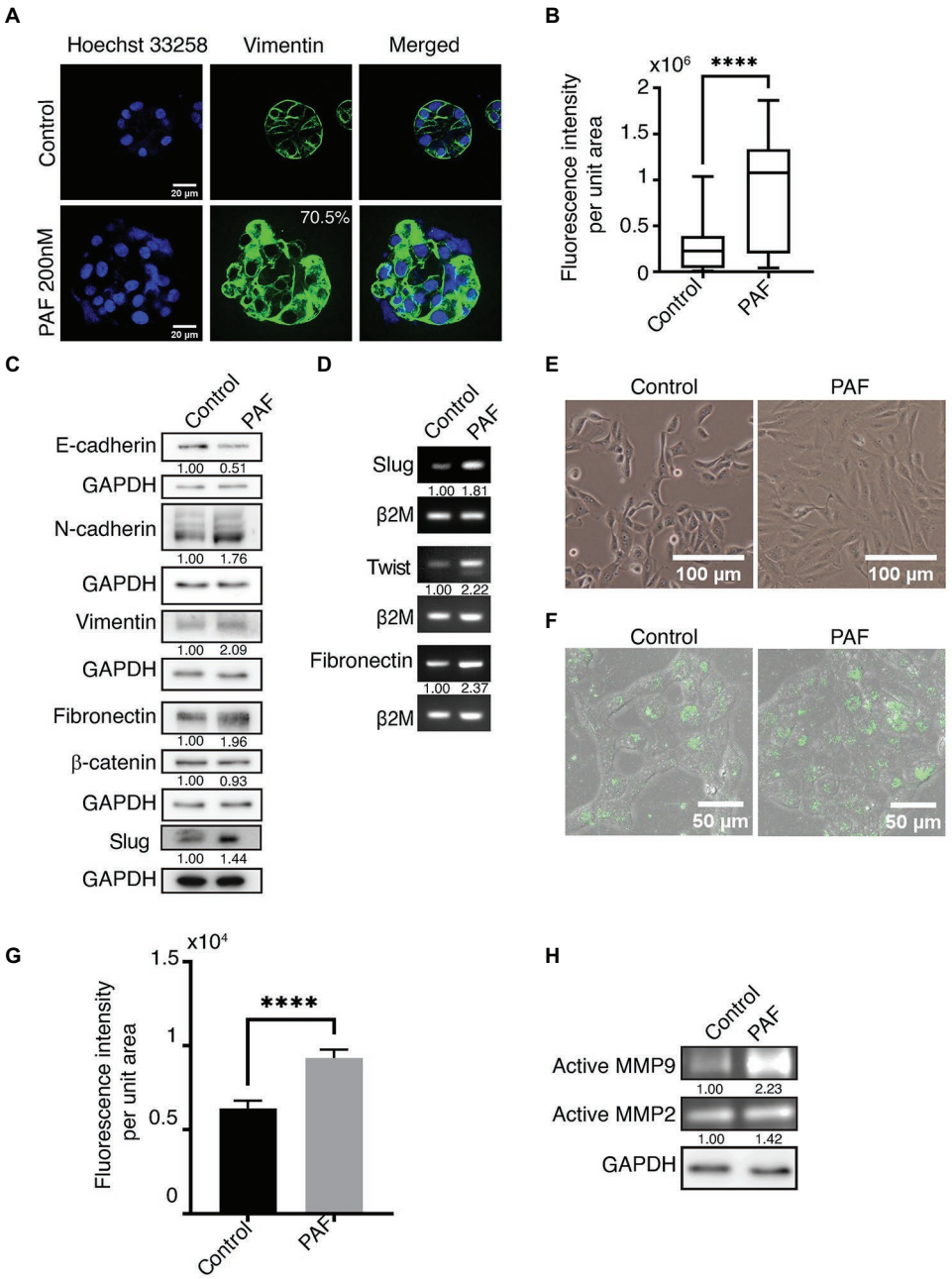


FIGURE 3 | PAF treatment induces partial epithelial-mesenchymal transition (EMT)-like phenotype. MCF10A cells grown for 20 days on Matrigel™ treated with and without 200 nM PAF immunostained and immunoblotted with EMT markers. **(A)** PAF-treated acini showed upregulated vimentin expression (green). **(B)** Box plot depicts the acinar fluorescence (CTCF) of vimentin ($N = 4$). **(C)** 20-day 3D culture lysates of control and PAF immunoblotted for various EMT markers. The values represent fold change with respect to control and normalized to GAPDH ($N = 3$). **(D)** mRNA expression analysis done for various EMT markers using RNA lysates. The values represent fold change with respect to control and normalized to β2M ($N = 3$). **(E)** Phase contrast images of dissociated cells of PAF treated acini grown as 2D cultures showed a mesenchymal phenotype. **(F)** Dissociated cells of control and PAF, seeded on rat tail collagen type1 containing DQ™ collagen type1 and fluorescence intensity captured on SP8 confocal microscope (Leica, Germany). **(G)** Quantification of the DQ fluorescence per cell ($n = 150$). **(H)** Coomassie-stained gel showing gelatinase activity using conditioned media from 3D cultures. The values represent fold change with respect control and normalized to GAPDH. Statistical analysis was performed for **(A)** and **(F)** using Mann Whitney U test; $^{****}p < 0.0001$.

further studies are called for using small molecule inhibitors to thoroughly dissect the signaling mechanism. Overall, PAF leads to phenotypic transformation of breast epithelial cells when grown on ECM for 20 days and the activation of the oncogenic molecular players warrants deeper investigations for the mechanism.

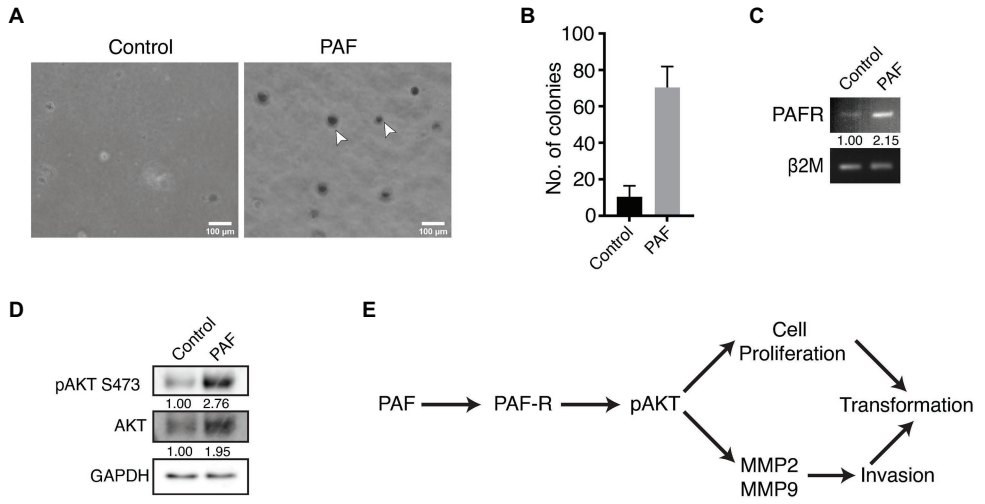


FIGURE 4 | Effect of PAF on anchorage independent growth of MCF10A cells and activation of the PI3K/AKT pathway. Dissociated cells were grown on soft agar and stained with MTT to visualize colonies formed and the pathway for PAF induced transformation. **(A)** Phase contrast images showing MTT stained colonies grown on soft agar. **(B)** Quantification of the number of colonies formed on soft agar ($N = 3$). **(C)** Transcript level of PAF-R. The values represent fold change with respect to control and normalized to β2M ($N = 3$). **(D)** Western blot indicating activation of AKT through PAF-R. The values represent fold change with respect to control and normalized to GAPDH ($N = 3$). **(E)** Pathway showing the activation of AKT downstream of PAF-R activation.

DISCUSSION

PAF is long known as a potent inflammatory bioactive molecule that is unequivocally proven to give rise to aberrant physiological effects (Lordan et al., 2019). Its role in various types of cancer is studied; however, the mechanism that leads to cancer is still understudied (Tsoupras et al., 2009). The current study will be instrumental in defining the mode of action of PAF in transforming non-tumorigenic breast epithelial cells. Health hazards of high levels of PAF in the system were studied earlier by Kispert et al., and although it is known to be naturally present in the living system, improper degradation leads to its accumulation and hence leads to cellular and molecular anomalies (Chen et al., 2007; Kispert et al., 2015, 2019). Bussolati et al. (2000) have shown that the stimulated secretion of PAF promotes migration, proliferation, and neo-angiogenesis in breast cancer cells, clearly indicating its role in carcinogenesis (Bussolati et al., 2000). Cell microenvironment perturbations by exogenous or endogenous sources lead to increased cellular proliferation that results in a loss of hollow lumen followed by the formation of multiple layers of cells in the lumen. Such a phenotype is predictive of transformation and can be a representative model for early stage mammary cancer *in vitro* (Vidi et al., 2013). Formation of a polarized, growth-arrested acinar structure with glandular epithelial cells surrounding a hollow lumen is archetypal of perfectly synchronized cellular and molecular events culminating into a normal breast acinus. When this tissue architecture is disturbed, cell survival, and differentiation processes get largely affected and eventually pave the way to tumor formation (Vidi et al., 2013). Transformation is the initial step to this process, wherein the normal cell signaling goes haywire, and there is an aberrant expression of genes leading to malignant phenotypes, and this phenomenon is nearly recapitulated using the 3D breast acinar model system. Formation of disorganized acinar structures is characteristic of transformation and various phenotypic changes are categorized under lack of growth arrest, loss of cell polarity, disruption of BM and cell-cell junctions, EMT, and ability to grow in anchorage-independent conditions (Debnath et al., 2003). Our study encompasses all the above phenotypes in the zest to investigate the role of PAF in transformation of breast epithelial cells using the 3D breast acinar model.

Investigations revealed that continuous PAF treatment for 20 days leads to the disruption of polarity manifested by loss of apico-basal polarity. Generally, for apical polarity, *in vitro* studies as well as pathologists utilize Golgi marker as a strong identifying marker to understand polarity alteration leading to transformation or cancer (Debnath et al., 2003). Golgi is the hub for signal transduction for various pathways and alteration in its localization affects the polarized secretion of proteins from the ER to the plasma membrane and other compartments that in turn affects the signal transduction pathways (Millarte and Farhan, 2012). Hence, although the global secretory pattern does not change, but the directed trafficking of cargo is impaired. Alongside, breakage of BM is the key to loss of basal polarity. This phenomenon is significant because it provides a hallway to invading cells into the surrounding ECM and further into tissue stroma. The entirety of the BM is necessary to limit tumor growth and invasion and for this reason many solid tumors show discontinuous or a loss of BM (Ioachim et al., 2002). These investigations and the supporting literature revealed a structural loss of tissue architecture and loss of epithelial polarity in the presence of

PAF, indicating that such phenotypes are important components toward the maintenance of polarity and disruption of these leads to transformation and gives direct evidence in cancer development and progression (Lee and Vasioukhin, 2008).

E-cadherin, a cell-cell junction protein is known to maintain epithelial polarity by being a center for the intercommunicating signals between catenins and the cytoskeletal network and disruptions in this contact lead to various morphogenetic and developmental defects apart from loss of epithelial polarity (Olson et al., 2019). E-cadherin complexes with cytoplasmic β-catenin at the junctions and aberrations in this interaction leads to an increased flux of cytoplasmic β-catenin resulting in transformation and such an observation is commonly noted in solid tumors and epithelial cancers (Kourtidis et al., 2017). In our study, the loss of E-cadherin and diffused β-catenin at the junctions was observed in cells treated with PAF. Dissociation of the E-cadherin and β-catenin proteins from the complex leads to aberrant expression at the cell membrane and attributes to malignant progression, as well as has importance as a prognostic marker (Kaur et al., 2013). β-catenin expression leads to the transcription of various EMT inducing genes, thus identifying the various proteins that are under its transcriptional activity that lead to EMT is important (Solanas et al., 2008). EMT is a biological process that is employed during developmental stages; however, carcinoma cells hijack this program and herein the cells tend to lose their epithelial-like characteristics, both morphologically and functionally, and become mesenchymal or express such characteristics. Induction of EMT leads to the activation of various oncogenic programs including enhanced migration, invasion, metastasis, and the evasion of apoptotic stimuli (Kalluri and Weinberg, 2009; Scheel and Weinberg, 2011). Such complex programs are orchestrated by various EMT regulating transcription factors such as Snail, Slug, Twist, Zeb1, to name a few, to culminate into EMT. Apart from transcription factors, loss of cell-cell contacts and aberrant polarity also triggers EMT initiation. As cells fall loose in the cell matrix, they degrade it and attain mobility and this process is an attribute to EMT, which leads to the expression of mesenchymal proteins (Lamouille et al., 2014; Puisieux et al., 2014). Considering SNAIL1 and TWIST, the master regulators of EMT, they are classically known to repress E-cadherin and this opens the gate for tumor cells to migrate, either by mesenchymal movement or by amoeboid movement (Padmanaban et al., 2019). Concurrently, as E-cadherin levels decrease, N-cadherin levels increase and literature suggests that N-cadherin expression is TWIST-dependent (Alexander et al., 2006). Apart from the typical EMT markers, there are other molecules as well that play important roles in pathological EMT pathways. Fibronectin is an extracellular matrix protein, which gets enriched when EMT is induced, as well as various MMP's are expressed, which aid in the degradation of the matrix and enable tumor cells to invade deeper into tissues. Studies show that MMP-2 and MMP-9 deficient mice show impaired tumor cell growth and poor metastasis (Itoh et al., 1998). So, the conjoint efforts of BM disruption, mesenchymal expression, and MMP activation hold key position in inducing EMT, and the study suggests the same. However, inherent heterogeneity that arises in carcinoma cells, the tissue-wise difference in signal that cells receive to drive the EMT program, the signaling pathways that get activated in response to the induction of EMT, and the original state of the normal differentiated cells are few of the factors that deter making a perfect molecular trait chart that describes EMT (Lambert et al., 2017).

Traditionally, anchorage independent growth is a key feature of a transformed cell, and this phenomenon is well studied in the limited scope of *in vitro* culture system through colony formation in low attachment conditions. In our study, we have shown that acinar cultures grown in the presence of PAF attain anchorage independent growth, when grown on soft agar. As a first attempt these investigations gave enough evidence to show that PAF leads to transformation and the molecular players involved in this process is probably pAKT (S473; Chen et al., 2015b). Further studies are necessary to delineate the pathways that are involved in transformation through PAF.

Until now several investigations have shown that PAF plays a leading role in inflammation, platelet aggregation, leukocyte migration, and many such inflammatory mechanisms (Chignard et al., 1979; Bussolati et al., 2000). Cigarette smoke exposure is shown to promote bladder cancer and motility leading to metastasis in breast cancer cells *via* PAF (Kispert et al., 2015, 2019). In our study, we show that continuous exposure of PAF to 3D breast acinar cultures for 20 days leads to the formation of aberrant acinar morphology as well as the functional disruption of acinar morphogenesis, which might be due to activation of the PI3K/AKT pathway.

DATA AVAILABILITY STATEMENT

The original contributions presented in the study are included in the article/**Supplementary Material**, further inquiries can be directed to the corresponding author.

AUTHOR CONTRIBUTIONS

LA, VC, and ML: study conceptualization, supervision, study design, and wrote the paper. LA, VC, KAA, KA, and RU: data collection. All authors contributed to the article and approved the submitted version.

FUNDING

This study was supported by a grant from the Science and Engineering Research Board (SERB), Government of India (EMR/2016/001974) and partly by the IISER, Pune core funding. LA was supported by the INSPIRE fellowship. KAA was supported by the INSPIRE scholarship, Government of India. KA and RU were supported by the CSIR fellowship, Government of India.

ACKNOWLEDGMENTS

We acknowledge the IISER Pune Microscopy Facility for access to equipment and infrastructure. We thank Lahiri lab members for their timely help with the experiments and comments.

SUPPLEMENTARY MATERIAL

The Supplementary Material for this article can be found online at: https://www.frontiersin.org/articles/10.3389/fgene.2021.634938/full#supplementary-material

REFERENCES

Alexander, N. R., Tran, N. L., Rekapally, H., Summers, C. E., Glackin, C., and Heimark, R. L. (2006). N-cadherin gene expression in prostate carcinoma is modulated by integrin-dependent nuclear translocation of Twist1. *Cancer Res.* 66, 3365–3369. doi: 10.1158/0008-5472.CAN-05-3401

Anandi, V. L., Ashiq, K. A., Nitheesh, K., and Lahiri, M. (2016). Platelet-activating factor promotes motility in breast cancer cells and disrupts non-transformed breast acinar structures. *Oncol. Rep.* 35, 179–188. doi: 10.3892/or.2015.4387

Anandi, L., Chakravarty, V., Ashiq, K. A., Bodakuntla, S., and Lahiri, M. (2017). DNA-dependent protein kinase plays a central role in transformation of breast epithelial cells following alkylation damage. *J. Cell Sci.* 130, 3749–3763. doi: 10.1242/jcs.203034

Bennett, S. A., Leite, L. C., and Birnboim, H. C. (1993). Platelet activating factor, an endogenous mediator of inflammation, induces phenotypic transformation of rat embryo cells. *Carcinogenesis* 14, 1289–1296. doi: 10.1093/carcin/14.7.1289

Bussolati, B., Biancone, L., Cassoni, P., Russo, S., Rola-Pleszczynski, M., Montrucchio, G., et al. (2000). PAF produced by human breast cancer cells promotes migration and proliferation of tumor cells and neo-angiogenesis. *Am. J. Pathol.* 157, 1713–1725. doi: 10.1016/S0002-9440(10)64808-0

Chen, J., Lan, T., Zhang, W., Dong, L., Kang, N., Zhang, S., et al. (2015a). Feed-forward reciprocal activation of PAFR and STAT3 regulates epithelial-mesenchymal transition in non-small cell lung cancer. *Cancer Res.* 75, 4198–4210. doi: 10.1158/0008-5472.can-15-1062

Chen, J., Lan, T., Zhang, W., Dong, L., Kang, N., Zhang, S., et al. (2015b). Platelet-activating factor receptor-mediated PI3K/AKT activation contributes to the malignant development of esophageal squamous cell carcinoma. *Oncogene* 34, 5114–5127. doi: 10.1038/onc.2014.434

Chen, J., Yang, L., Foulks, J. M., Weyrich, A. S., Marathe, G. K., and McIntyre, T. M. (2007). Intracellular PAF catabolism by PAF acetylhydrolase counteracts continual PAF synthesis. *J. Lipid Res.* 48, 2365–2376. doi: 10.1194/jlr.M700325-JLR200

Chignard, M., Le Couedic, J. P., Tence, M., Vargaftig, B. B., and Benveniste, J. (1979). The role of platelet-activating factor in platelet aggregation. *Nature* 279, 799–800. doi: 10.1038/279799a0

Debnath, J., and Brugge, J. S. (2005). Modelling glandular epithelial cancers in three-dimensional cultures. *Nat. Rev. Cancer* 5, 675–688. doi: 10.1038/nrc1695

Debnath, J., Muthuswamy, S. K., and Brugge, J. S. (2003). Morphogenesis and oncogenesis of MCF-10A mammary epithelial acini grown in three-dimensional basement membrane cultures. *Methods* 30, 256–268. doi: 10.1016/S1046-2023(03)00032-X

Foa, R., Bussolino, F., Ferrando, M. L., Guarini, A., Tetta, C., Mazzone, R., et al. (1985). Release of platelet-activating factor in human leukemia. *Cancer Res.* 45, 4483–4485.

Fournier, M. V., Martin, K. J., Kenny, P. A., Xhaja, K., Bosch, I., Yaswen, P., et al. (2006). Gene expression signature in organized and growth-arrested mammary acini predicts good outcome in breast cancer. *Cancer Res.* 66, 7095–7102. doi: 10.1158/0008-5472.CAN-06-0515

Hanahan, D., and Weinberg, R. A. (2011). Hallmarks of cancer: the next generation. *Cell* 144, 646–674. doi: 10.1016/j.cell.2011.02.013

Horibata, S., Vo, T. V., Subramanian, V., Thompson, P. R., and Coonrod, S. A. (2015). Utilization of the soft agar colony formation assay to identify inhibitors of tumorigenicity in breast cancer cells. *J. Vis. Exp.* e52727. doi: 10.3791/52727

Ioachim, E., Charchanti, A., Briasoulis, E., Karavasilis, V., Tsanou, H., Arvanitis, D. L., et al. (2002). Immunohistochemical expression of extracellular matrix components tenascin, fibronectin, collagen type IV and laminin in breast cancer: their prognostic value and role in tumour invasion and progression. *Eur. J. Cancer* 38, 2362–2370. doi: 10.1016/S0959-8049(02)00210-1

Ishii, S., and Shimizu, T. (2000). Platelet-activating factor (PAF) receptor and genetically engineered PAF receptor mutant mice. *Prog. Lipid Res.* 39, 41–82. doi: 10.1016/S0163-7827(99)00016-8

Itoh, T., Tanioka, M., Yoshida, H., Yoshioka, T., Nishimoto, H., and Itohara, S. (1998). Reduced angiogenesis and tumor progression in gelatinase A-deficient mice. *Cancer Res.* 58, 1048–1051.

Ivers, L.P., Cummings, B., Owolabi, F., Welzel, K., Klinger, R., and Saitoh, S., et al. (2014). Dynamic and influential interaction of cancer cells with normal epithelial cells in 3D culture. *Cancer Cell Int.* 14:108. doi: 10.1186/s12935-014-0108-6

Jancar, S., and Chammas, R. (2014). PAF receptor and tumor growth. *Curr. Drug Targets* 15, 982–987. doi: 10.2174/1389450115666140903111812

Kalluri, R., and Weinberg, R. A. (2009). The basics of epithelial-mesenchymal transition. *J. Clin. Invest.* 119, 1420–1428. doi: 10.1172/JCI39104

Kaur, J., Sawhney, M., DattaGupta, S., Shukla, N. K., Srivastava, A., Walfish, P. G., et al. (2013). Clinical significance of altered expression of β-catenin and E-cadherin in oral dysplasia and cancer: potential link with ALCAM expression. *PLoS One* 8:e67361. doi: 10.1371/journal.pone.0067361

Kispert, S., Marentette, J., and McHowat, J. (2015). Cigarette smoke induces cell motility via platelet-activating factor accumulation in breast cancer cells: a potential mechanism for metastatic disease. *Physiol. Rep.* 3:e12318. doi: 10.14814/phy2.12318

Kispert, S., Marentette, J., and McHowat, J. (2019). Cigarette smoking promotes bladder cancer via increased platelet-activating factor. *Physiol. Rep.* 7:e13981. doi: 10.14814/phy2.13981

Kourtidis, A., Lu, R., Pence, L. J., and Anastasiadis, P. Z. (2017). A central role for cadherin signaling in cancer. *Exp. Cell Res.* 358, 78–85. doi: 10.1016/j.yexcr.2017.04.006

Lambert, A. W., Pattabiraman, D. R., and Weinberg, R. A. (2017). Emerging biological principles of metastasis. *Cell* 168, 670–691. doi: 10.1016/j.cell.2016.11.037

Lamouille, S., Xu, J., and Derynck, R. (2014). Molecular mechanisms of epithelial-mesenchymal transition. *Nat. Rev. Mol. Cell Biol.* 15, 178–196. doi: 10.1038/nrm3758

Lee, M., and Vasioukhin, V. (2008). Cell polarity and cancer--cell and tissue polarity as a non-canonical tumor suppressor. *J. Cell Sci.* 121, 1141–1150. doi: 10.1242/jcs.016634

Lordan, R., Tsoupras, A., Zabetakis, I., and Demopoulos, C. A. (2019). Forty years since the structural elucidation of platelet-activating factor (PAF): historical, current, and future research perspectives. *Molecules* 24:4414. doi: 10.3390/molecules24234414

Lv, X. X., Liu, S. S., Li, K., Cui, B., Liu, C., and Hu, Z. W. (2017). Cigarette smoke promotes COPD by activating platelet-activating factor receptor and inducing neutrophil autophagic death in mice. *Oncotarget* 8, 74720–74735. doi: 10.18632/oncotarget.20353

Man, Y. G., Stojadinovic, A., Mason, J., Avital, I., Bilchik, A., Bruecher, B., et al. (2013). Tumor-infiltrating immune cells promoting tumor invasion and metastasis: existing theories. *J. Cancer* 4, 84–95. doi: 10.7150/jca.5482

Millarte, V., and Farhan, H. (2012). The Golgi in cell migration: regulation by signal transduction and its implications for cancer cell metastasis. *ScientificWorldJournal* 2012:498278. doi: 10.1100/2012/498278

Miyaura, S., Eguchi, H., and Johnston, J. M. (1992). Effect of a cigarette smoke extract on the metabolism of the proinflammatory autacoid, platelet-activating factor. *Circ. Res.* 70, 341–347. doi: 10.1161/01.RES.70.2.341

Olson, A., Le, V., Aldahl, J., Yu, E. J., Hooker, E., He, Y., et al. (2019). The comprehensive role of E-cadherin in maintaining prostatic epithelial integrity during oncogenic transformation and tumor progression. *PLoS Genet.* 15:e1008451. doi: 10.1371/journal.pgen.1008451

Padmanaban, V., Krol, I., Suhail, Y., Szczerba, B. M., Aceto, N., Bader, J. S., et al. (2019). E-cadherin is required for metastasis in multiple models of breast cancer. *Nature* 573, 439–444. doi: 10.1038/s41586-019-1526-3

Papakonstantinou, V. D., Lagopati, N., Tsilibary, E. C., Demopoulos, C. A., and Philippopoulos, A. I. (2017). A review on platelet activating factor inhibitors: could a new class of potent metal-based anti-inflammatory drugs induce anticancer properties? *Bioinorg. Chem. Appl.* 2017:6947034. doi: 10.1155/2017/6947034

Pastushenko, I., and Blanpain, C. (2019). EMT transition states during tumor progression and metastasis. *Trends Cell Biol.* 29, 212–226. doi: 10.1016/j.tcb.2018.12.001

Puisieux, A., Brabletz, T., and Caramel, J. (2014). Oncogenic roles of EMT-inducing transcription factors. *Nat. Cell Biol.* 16, 488–494. doi: 10.1038/ncb2976

Scheel, C., and Weinberg, R. A. (2011). Phenotypic plasticity and epithelial-mesenchymal transitions in cancer and normal stem cells? *Int. J. Cancer* 129, 2310–2314. doi: 10.1002/ijc.26311

Shaw, K. R., Wrobel, C. N., and Brugge, J. S. (2004). Use of three-dimensional basement membrane cultures to model oncogene-induced changes in mammary epithelial morphogenesis. *J. Mammary Gland Biol. Neoplasia* 9, 297–310. doi: 10.1007/s10911-004-1402-z

Solanas, G., Porta-de-la-Riva, M., Agustí, C., Casagolda, D., Sánchez-Aguilera, F., Larriba, M. J., et al. (2008). E-cadherin controls beta-catenin and NF-kappaB transcriptional activity in mesenchymal gene expression. *J. Cell Sci.* 121, 2224–2234. doi: 10.1242/jcs.021667

Tsoupras, A. B., Iatrou, C., Frangia, C., and Demopoulos, C. A. (2009). The implication of platelet activating factor in cancer growth and metastasis: potent beneficial role of PAF-inhibitors and antioxidants. *Infect. Disord. Drug Targets* 9, 390–399. doi: 10.2174/187152609788922555

Vidi, P. A., Bissell, M. J., and Lelièvre, S. A. (2013). Three-dimensional culture of human breast epithelial cells: the how and the why. *Methods Mol. Biol.* 945, 193–219. doi: 10.1007/978-1-62703-125-7_13

Wu, X., and Gallo, K. A. (2013). The 18-kDa translocator protein (TSPO) disrupts mammary epithelial morphogenesis and promotes breast cancer cell migration. *PLoS One* 8:e71258. doi: 10.1371/journal.pone.0085166

Yu, Y., and Elble, R. C. (2016). Homeostatic signaling by cell-cell junctions and its dysregulation during cancer progression. *J. Clin. Med.* 5:26. doi: 10.3390/jcm5020026

Conflict of Interest: The authors declare that the research was conducted in the absence of any commercial or financial relationships that could be construed as a potential conflict of interest.

Copyright © 2021 Chakravarty, Anandi, Ashiq, Abhijith, Umesh and Lahiri. This is an open-access article distributed under the terms of the Creative Commons Attribution License (CC BY). The use, distribution or reproduction in other forums is permitted, provided the original author(s) and the copyright owner(s) are credited and that the original publication in this journal is cited, in accordance with accepted academic practice. No use, distribution or reproduction is permitted which does not comply with these terms.

THE JOURNAL OF PHYSICAL CHEMISTRY B
A JOURNAL OF THE AMERICAN CHEMICAL SOCIETY

pubs.acs.org/JPCB

Article

Emergence of Aggregation Induced Emission (AIE), Room-Temperature Phosphorescence (RTP), and Multistimuli Response from a Single Organic Luminogen by Directed Structural Modification

Published as part of The Journal of Physical Chemistry virtual special issue "Kankan Bhattacharyya Festschrift".

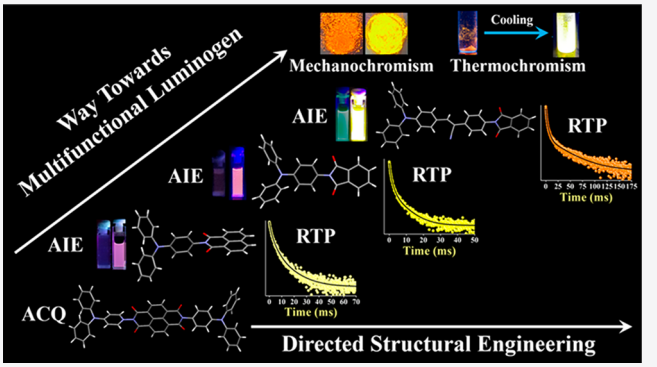
Abhijit Chatterjee, Joy Chatterjee, Subrahmanyam Sappati, Tariq Sheikh, Rintu M. Umesh, Madan D. Ambhore, Mayurika Lahiri, and Partha Hazra*

Cite This: https://doi.org/10.1021/acs.jpcb.1c08126

Read Online

ACCESS | Metrics & More | Article Recommendations | Supporting Information

ABSTRACT: Multifunctional organic luminogens exhibiting simultaneous aggregation induced emission (AIE), room-temperature phosphorescence (RTP), and mechanochromism have recently attracted considerable attention owing to their potential applications in optoelectronics and bioimaging. However, a comprehensive correlation among these three distinguished properties is yet to be unveiled, which will help to decipher defined methodologies to design future generation multifunctional organic materials. Herein, we have demonstrated a route to obtain a multifunctional organic luminogen, starting from an ACQphore (TPANDI) by simple structural engineering. We have shown that a slight reduction in length of the planar acceptor moieties can effectively inhibit the undesirable $\pi-\pi$ stacking interaction between molecules in the condensed state and thereby cause an ACQ to AIE type transformation from TPANDI to TPANMI and TPAPMI. Both TPANMI and TPAPMI exhibit RTP properties (even in ambient condition) because of the presence of a reasonably low singlet−triplet energy gap (ΔE_{ST}). In our study, these two luminogens were found to be mechano-inactive. Interestingly, an insertion of cyano-ethylene group and benzene linker in between the triphenylamine and phthalimide moieties introduced another luminogen TPACNPMI, which can simultaneously exhibit AIE, RTP, and mechanochromic properties.



Downloaded via IISER PUNE on November 19, 2021 at 11:08:21 (UTC).
See https://pubs.acs.org/sharingguidelines for options on how to legitimately share published articles.

INTRODUCTION

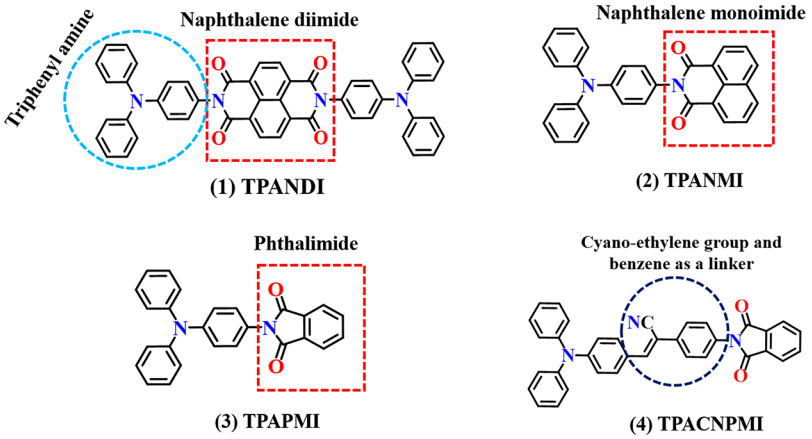
Solid-state luminescence is a burgeoning field of fundamental and applied research. Especially, organic emitters that exhibit reversibility between distinct luminescence colors or multi-stimuli-responsive behavior (e.g., mechanochromism, thermochromism, and vapochromism) have gathered considerable attention owing to their potential applications in optoelectronic devices, sensors, probes, security, and storage devices.[1−8] However, most of the organic emitters suffer a notorious aggregation caused quenching (ACQ) effect in the solid state, which truncates their scope of various applications as a proficient light emitting candidate.[9] In 2001, Tang and co-workers paved the way toward the avoidance of this undesirable event.[10] A new photophysical term was coined as aggregation induced emission (AIE) and aggregation induced emission enhancement (AIEE) in this context. These two intriguing phenomena can transform nonemissive or weakly emissive aggregates of organic luminogens into highly emissive ensembles in a higher content of antisolvent or in the solid state by inhibiting the $\pi-\pi$ cofacial stacking of adjacent aromatic ring.[9] Consequently, it led toward the revelation of a new horizon for organic luminogens to be utilized in real-world applications, such as organic light-emitting diodes (OLEDs), light-emitting liquid crystals, optical waveguide emitters, and in several biomedical as well as biosensing applications.[11−20]

Recently, amalgamation of several photophysical processes with the AIE and mechanochromism has augmented the field of solid-state luminescence and has emerged as a primary methodology to develop multifunctional "all in one" type future generation luminogens.[20,21] One of the most capable accelerators for the development of this particular field is the

Received: September 15, 2021
Revised: October 26, 2021

© XXXX American Chemical Society

Scheme 1. Structures of the Designed Organic Luminogens



triplet state engineering, which involves phenomena like thermally activated delayed fluorescence (TADF) and room-temperature phosphorescence (RTP). In particular, RTP has drawn considerable attention owing to its potential application in the development of highly efficient, environmentally friendly, heavy-metal free and cost-effective luminescent materials for optoelectronic devices as well as for biological applications.[22−24] Generally, phosphorescence occurs via a spin-forbidden process, which involves an intersystem crossing from the lowest singlet (S_1) to the lowest triplet state (T_1) followed by a radiative transition from the T_1 state to the ground S_0 state. The intersystem crossing is facilitated by spin−orbit coupling, which is more prevalent in the case of heavy-metal-containing moieties. Therefore, for metal-free organic luminogens, spin-forbidden transitions remain inadequate, and nonradiative decay through intermolecular collisions and molecular motion becomes predominant. Researchers came up with several notions to increase the rate of intersystem crossing by promoting spin−orbit coupling in organic emitters and a subsequent increment in the rate of radiative relaxation from T_1 to S_0. Bolton et al. reported a turn-on phosphorescence in the crystal state of 2,5-dihexyloxy-4-bromobenzaldehyde; where, the authors revealed a C−Br···O═C type halogen bonding to be responsible for this type of turn-on phosphorescence in crystals.[25] Later, Shi et al. also demonstrated a Br···Br type halogen bonding in crystal phase, which expedites RTP in a series of dibromo benzene derivatives with an alkyl group.[26] Several prodigious works on the development of multifunctional luminogens have also been reported, where RTP and mechanochromic properties coexist in a single organic molecule. For instance, Prof. Tang's group reported three-mono- or dibromo-substituted benzophenone derivatives, which exhibited simultaneous RTP and mechanochromic properties.[27] Crystallization of these luminogens induced the phosphorescence emission to occur through structural rigidification, and those crystals were found to exhibit a blue-shifted emission upon grinding. Xue et al. reported a carbazole-based luminogen exhibiting persistent RTP with a lifetime of ∼540 ms.[28] Moreover, a phosphorescence to fluorescence emission switching was observed upon mechanical stimulus, which was caused by molecular planarization and enhanced $\pi-\pi$ interaction under grinding. Prof. Chi and co-workers reported that the original microcrystals of both the SHB_2T and SDB_2T (constituted by sulfone as acceptor and dibenzo thiophene as donor) exhibit white light emission with blue-violet fluorescence and yellow phosphorescence along with mechanochromic properties. Here, the microcrystals of SDB_2T showed a red-shift of the fluorescence emission from 392 to 414 nm and an enfeebled yellow phosphorescence upon mechanical grinding, and thus manifesting a white to blue emission tuning.[29]

Despite conducting considerable research works in this field, several structure−property correlations are yet to be unraveled, which is consequential to develop facile and well-defined methodologies in the field of multifunctional organic luminogens. In this regard, the establishment of a comprehensive interrelation among AIE, mechanochromism, and RTP can provide adequate transparency to the structure−property relationships of these luminophores, which will also help to decipher several photophysical processes and eventually lead to the advancement of multifunctional organic materials. Here in this article, we have designed and synthesized four organic luminogens. Starting from a molecule with ACQ properties, we have demonstrated that a simple structural modification can effectively modulate the packing fashion in the condensed state and can bring about an ACQ to AIE type transformation. Moreover, the presence of closely spaced singlet and triplet energy states in all these AIE active luminogens can facilitate the intersystem crossing (ISC) process, and consequently, it leads toward room-temperature phosphorescence behavior. Finally, it was observed that an introduction of a cyano-ethylene group along with a benzene linker in between the donor and acceptor could bring about easy and distinct mechanochromic behavior in the final molecule. Thus, starting from a molecule with ACQ nature, upon minimal and systematic modification of molecular structure, a multifunctional luminogen with AIE, RTP along with easy and distinct mechanochromic properties was obtained.

DESIGN STRATEGY

In order to implement our desired target, we have considered the following points during the design of our organic luminogens: presence of (a) donor−acceptor (D−A) type framework in each luminogen; (b) a twisted and flexible donor moiety; (c) a planar acceptor core, the length of which can be reduced to decrease the extent of the $\pi\cdots\pi$ interaction in the subsequent molecules, thereby achieving ACQ to AIE type transformation; and (d) multiple sites to facilitate several noncovalent interactions, which can lead to the emergence of RTP as well as mechanochromic behavior. Most importantly,

https://doi.org/10.1021/acs.jpcb.1c08126
J. Phys. Chem. B XXXX, XXX, XXX−XXX

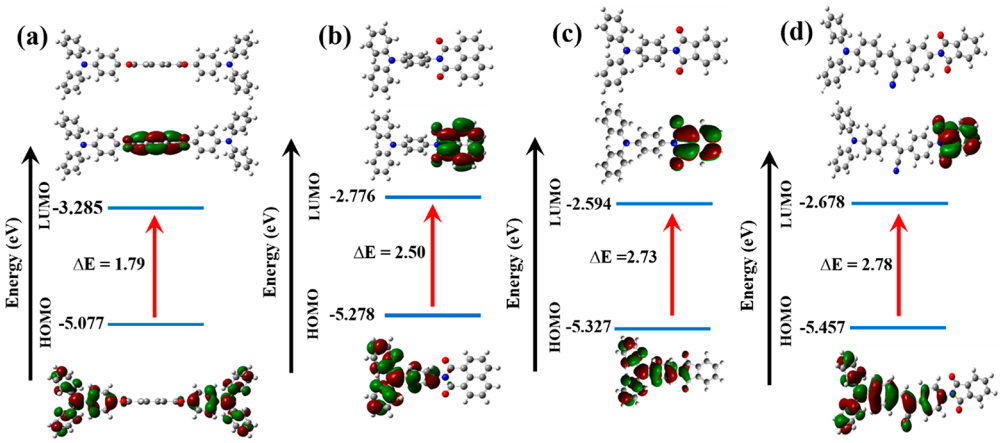


Figure 1. HOMO and LUMO molecular orbitals of (a) TPANDI, (b) TPANMI, (c) TPAPMI, and (d) TPACNPMI with their associated energy values.

(e) the donor and acceptor moieties have been chosen in such a way that, they contain atoms with nonbonding electrons, which can favor the (n, π^*) transition leading to an increased rate of intersystem crossing between several excited singlet and triplet states and thereby facilitating the RTP process.[30] Assessing the aforementioned aspects, initially, we have designed three luminogens, namely, TPANDI, TPANMI, TPAPMI with triphenylamine as donor and naphthalene diimide, naphthalene monoimide, and phthalimide as electron-deficient acceptors, respectively (Scheme 1). Triphenylamine (TPA), owing to its propeller shaped structure, can inhibit the undesirable $\pi-\pi$ stacking in the aggregated state, which can be useful as an efficient building block for the AIE luminogens. Also, the twisted skeleton and higher degree of flexibility of TPA moiety can expedite the multistimuli-responsive behavior in TPA-based luminogens.[31,32] On the contrary, all the acceptors are structurally planar and can behave as an excellent electron acceptor because of their electron-deficient nature. Moreover, the presence of carbonyl oxygen along with the nitrogen atoms present in the acceptor molecule can promote the production of triplet excitons through (n, π^*) transition. In the fourth luminogen, namely, TPACNPMI, we have inserted an additional cyano-ethylene group along with a benzene linker between the donor TPA and acceptor phthalimide moiety (Scheme 1). The presence of carbonyl oxygen and the incorporation of cyano-ethylene group can make several strong and short contacts with the neighboring aromatic hydrogen atoms, leading to the increase in its degree of responsiveness under mechanical stimulus.

MATERIALS AND METHODS

Synthesis and Characterization. Herein, we adopted two different synthetic schemes to synthesize our designed luminogens.

(a) The first synthetic route involves nitration of triphenylamine using $NaNO_3$ and glacial acetic acid in chloroform, followed by its reduction from nitro to amine using $NH_2NH_2.H_2O$ and Pd/C catalyst in ethanol at reflux condition. Lastly, the condensation reaction was done with 1,4,5,8-napthalenetetracarboxylic dianhydride, 1,8-napththalic anhydride, and phthalic anhydride to produce TPANDI, TPANMI, and TPAPMI, respectively (Scheme S1).

(b) TPACNPMI was synthesized using a different synthetic route (Scheme S2). Initially, monoformylation of triphenylamine was carried out using $POCl_3$ and DMF, followed by a condensation reaction with 4-nitrophenylacetonitrile in piperidine/ethanol solution, and then a reduction of the nitro functionality to amine was done using $SnCl_2$ in ethanol solvent. Finally, a condensation reaction was performed with phthalic anhydride in glacial acetic acid at reflux condition to synthesize the final compound, that is, TPACNPMI (details in ESI).

All the starting materials and final compounds were characterized using ^1H, ^{13}C NMR spectroscopy and HRMS studies (details in ESI). Single-crystal diffracted molecular structure has been provided as an additional characterization proof. Good quality single crystals of TPANDI were grown from a 1:1 mixture of DCM and methanol by slow evaporation method within 2−3 days; whereas for all other luminogens, crystals were obtained from the reaction mixture.

Instrumentation. Steady-state emission spectra (in the liquid state) were collected using the Fluoromax-4 spectrofluorometer (Horiba Jobin Yvon). Solid-state emission spectra, phosphorescence emission spectra were collected using Edinburgh FLS980 instruments. A microsecond flash lamp (of 1.5−2.5 μs bandwidth) was used during phosphorescence decay collection. Two-photon cell imaging was performed using a multiphoton microscope (Leica, Germany) at 63× oil immersion objective. All other instruments details are given in SI.

RESULTS AND DISCUSSION

Charge Transfer Analysis. To validate the viability of our molecular design, theoretical calculations were conducted using the DFT method at the B3LYP/6-311++G (d, p) level. The DFT-optimized molecular structures of the designed luminogens along with the highest occupied molecular orbitals (HOMOs) and lowest unoccupied molecular orbitals (LUMOs) with corresponding energy levels are shown in Figure 1. In all the cases, the HOMOs and LUMOs are spatially separated and reside exclusively on the donor and acceptor (NDI, NMI, PMI) moieties, respectively. Thus, there will be a substantial intramolecular charge transfer (ICT) from the electron-rich donor to the electron-deficient acceptor part upon photoexcitation. We also calculated the electron density

https://doi.org/10.1021/acs.jpcb.1c08126
J. Phys. Chem. B XXXX, XXX, XXX−XXX

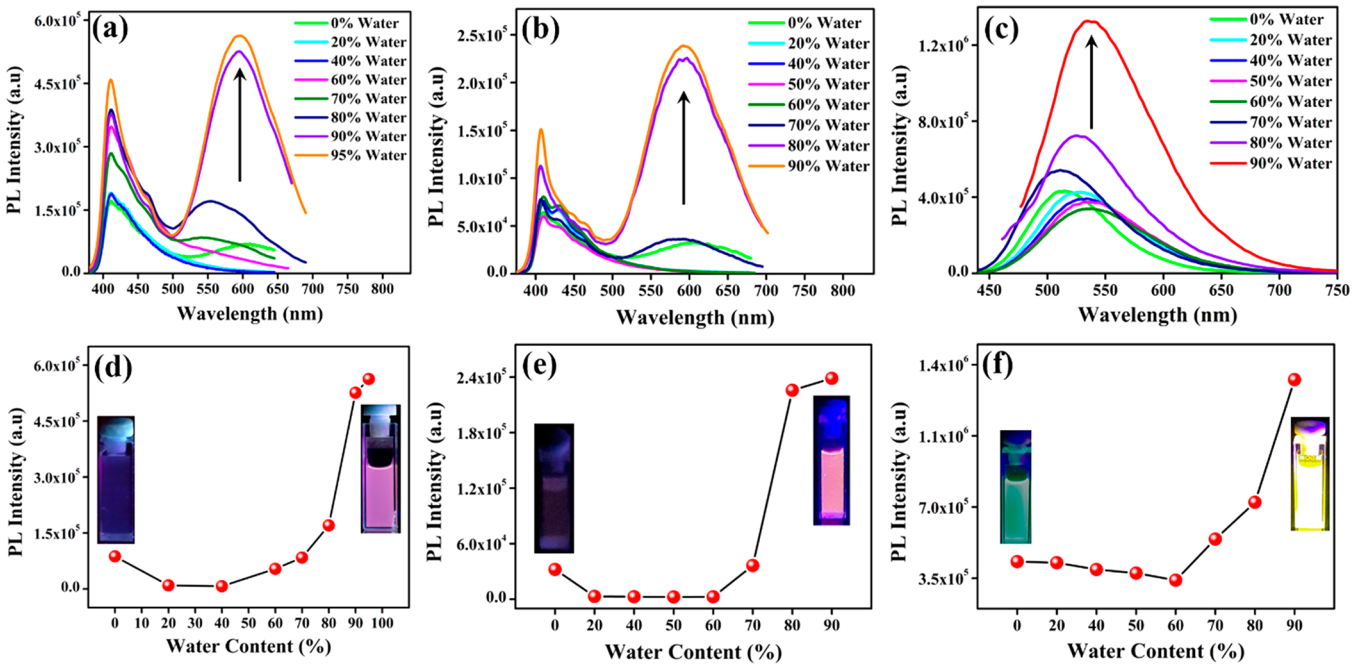


Figure 2. Emission spectra of (a) TPANMI and (b) TPAPMI in dioxane/water binary mixture. Emission spectra of (c) TPACNPMI in THF/water binary mixture. Emission intensity (of red-shifted emission peak) vs water content (%) plot for (d) TPANMI, (e) TPAPMI, (f) TPACNPMI along with cuvette images (ex 365 nm) at the lowest and highest water content. Emission spectra of TPANMI (a, d) and TPAPMI (b, e) were collected by exciting at 335 and 347 nm, respectively. Emission spectra of TPACNPMI (c, f) were collected by exciting at the respective absorption maximum (Figure S6).

difference map (EDDM) for the first bright transition (transition having considerable oscillator strength, obtained from time-dependent DFT calculation) to visualize the movement of charge during that particular transition. Notably, for charge transfer luminogens, these kinds of EDDM plots are usually accompanied by two different colors. Here, the cyan color signifies the region where the charge is being accumulated and the yellow color indicates the region from where the electronic charges are being depleted during an electronic transition (Figure S1). Interestingly, for the first bright transition, it was observed that the charges are getting depleted from the electron-rich TPA part (in TPACNPMI, it extends further until the cyano-ethylene and benzene linker part) and are getting accumulated in the electron-deficient NDI (for TPANDI), NMI (for TPANMI), and PMI (for TPAPMI and TPACNPMI) regions (Figure S1), which again validates the charge transfer nature of our luminogens.

Optical Properties and Aggregation Induced Emission (AIE) Study. In the solution phase, TPANDI, TPANMI, and TPAPMI show absorption band with vibrational structure in the range of 325−400 nm, 300−370 nm and 300−370 nm, respectively, which can be attributed to the $\pi-\pi^*$ electronic transitions (Figure S2). The emission spectra of TPANDI manifests two overlapped emission bands in THF, a band with vibrational feature peaked at ∼404 nm and another broad emission band with maxima at >460 nm, which are attributed to relaxation from the locally excited state (LE) and charge transfer (CT) states, respectively. The recognition of these emission bands have been further justified by collecting the emission spectra in the solvents of different polarities (Figure S3). In nonpolar solvent like toluene, the intensity of the red-shifted CT band is reasonably weak compared with the emission band generated due to decay from the LE state. Intensity of the red-shifted band increases with raising the solvent polarity, and gradually achieves the highest intensity in THF and acetonitrile. The relative difference between the intensities of LE and CT peaks gradually diminishes with increasing the solvent polarity. Interestingly, upon further increase in the solvent polarity (in DMSO), the intensity of the red-shifted emission band is significantly reduced (Figure S3) due to substantial stabilization of the CT state. TPANDI-like dual emissive features (from LE and CT state) were also observed in case of TPANMI and TPAPMI. For TPANMI, the LE and CT peaks were located at ∼390 nm and ∼600 nm, respectively, in 1,4-dioxane (Figure S3). Similarly, for TPAPMI, the emission maxima corresponding to LE and CT states were found to be centered at ∼ 380 nm and ∼ 600 nm, respectively, in the same solvent (Figure S3). For both these molecules, the CT band undergoes a gradual downturn in terms of emission intensity accompanied by a significant red-shift with increase in solvent polarity (from toluene to acetonitrile) (Figure S3). Unlike the previous luminogens, TPACNPMI exhibits two well-separated absorption bands, one in the UV region (centered at ∼ 295 nm) and another in the visible region (centered at ∼ 400 nm) in all organic solvents (Figure S2). The absorption band in the UV region can be attributed to the $\pi-\pi^*$ electronic transition, and the absorption band in the visible region can be accredited to the CT transition from the donor (TPA) to the acceptor (phthalimide) moiety. Interestingly, the emission spectra of TPACNPMI manifests a single emission peak, which is typically distinct from the emission features of the other three luminogens (Figure S3). In nonpolar solvent like *n*-hexane, the emission band is composed of vibrational structures, which gets broadened with a significant red shift when the polarity of the solvent is increased. Thus, the fwhm of the emission band also increases from 55 nm (in *n*-hexane) to 103 nm (in acetonitrile) (Figure S3). Although the relative

https://doi.org/10.1021/acs.jpcb.1c08126
J. Phys. Chem. B XXXX, XXX, XXX−XXX

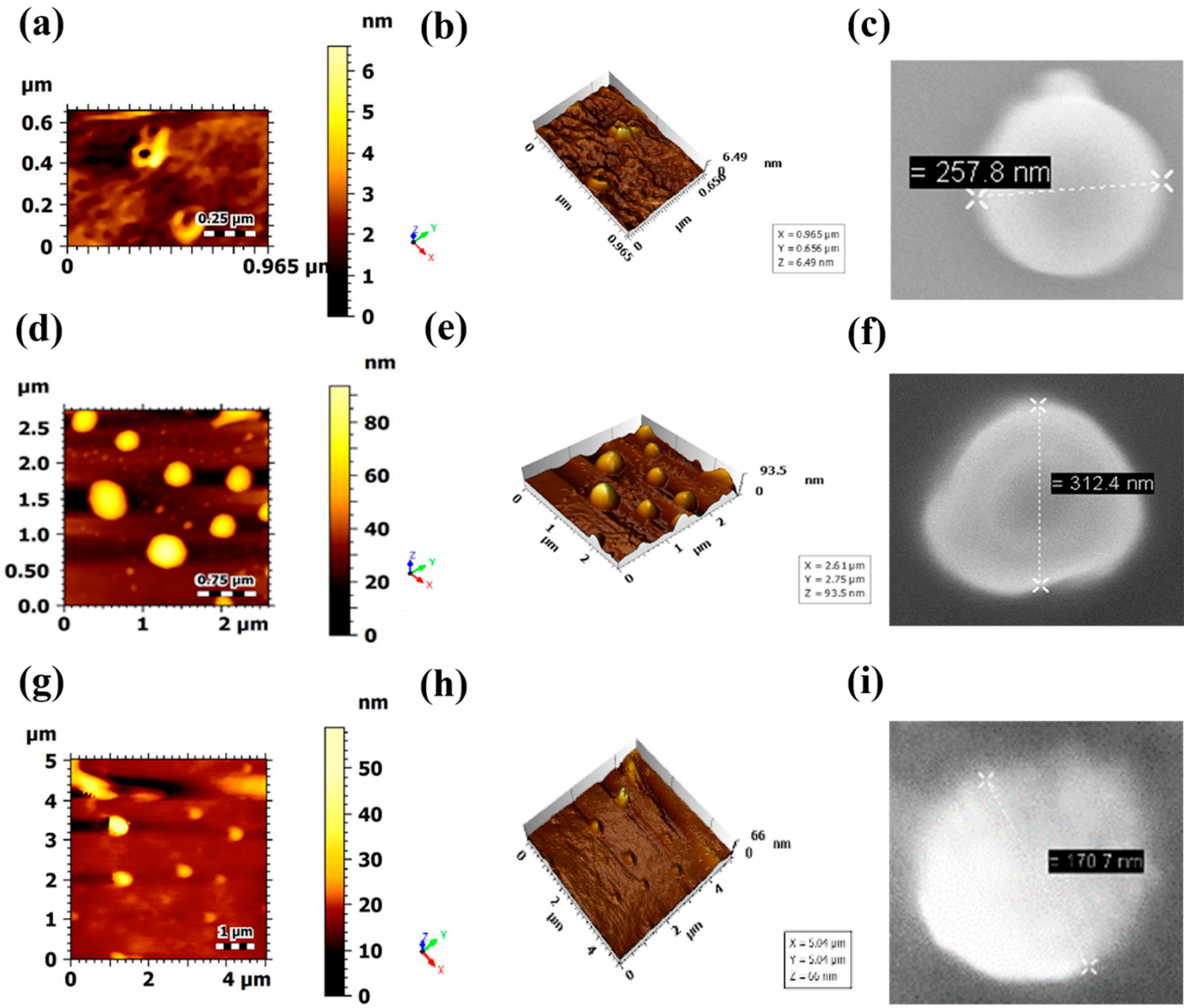


Figure 3. AFM images of aggregates formed by (a) TPANMI, (d) TPAPMI, and (g) TPACNPMI. AFM images (3D height) of aggregates formed by (b) TPANMI, (e) TPAPMI, and (h) TPACNPMI. FESEM images of aggregates formed by (c) TPANMI, (f) TPAPMI, and (i) TPACNPMI.

contributions of LE and CT states in the broad emission band are indeterminate from the solvent dependent studies, nevertheless the higher fwhm with dissipating vibrational features strongly suggest an increased CT character in the emissive excited state.

Solid state luminescence properties are mostly dictated by the emission behavior of luminogens in the aggregated state. Since the molecules are insoluble in water, increasing the aqueous proportion in a binary solvent system constituted of water/THF or 1,4-dioxane, would result in the formation of nanoaggregates. Hence, optical properties of all the molecules were studied in organic solvent (THF or 1,4-dioxane)/water binary mixtures (Figure 2). In case of TPANDI, the emission intensities of LE and CT bands get drastically reduced with an increasing aqueous proportion in a dilute solution (30 μM) of THF, and the luminogen becomes almost nonemissive at very high water content (Figure S5), which clearly depicts TPANDI to be an ACQphore. Surprisingly, the emissive behavior of nanoaggregates resulting from TPANMI, TPAPMI, and TPACNPMI is significantly different compared with that of TPANDI. For both TPANMI and TPAPMI (Figure 2), the CT band (at ∼ 602 nm for TPANMI and at ∼ 604 nm for TPAPMI) gets depleted at lower water contents (fraction of water, f_w = 20% and 40%) in dioxane/water system. However, as the water content is gradually increased further to 60% (for TPANMI) and 70% (for TPAPMI), the particular peak rises up with a moderate blue-shift of ∼50 nm. The initial depletion in the intensity at lower water content is due to adequate stabilization of the CT state owing to higher polarity of water and represents the solvatochromic behavior of the molecules. The uprise of the blue-shifted CT peak can be attributed to the formation of nanoaggregates induced by the immediate hydrophobic environment formed at relatively higher water content. Interestingly, as the water content was increased further up to ≥90%, the intensity of the CT peak was increased ∼6 fold compared to the intensity obtained in bulk 1,4-dioxane (Figure 2). This particular finding can be regarded as a consequence of the aggregation induced emission (AIE) effect. For TPACNPMI, upon increasing the water content initially up to 60%, the emission peak exhibits a continuous red shift

https://doi.org/10.1021/acs.jpcb.1c08126
J. Phys. Chem. B XXXX, XXX, XXX−XXX

from 515 to 538 nm, along with a declining intensity, which suggests that the solvatochromic nature of the molecule dominates in lower water contents (Figure 2). However, when the water fraction slightly increases to 70%, a sudden enhancement takes place with a blue-shift of ∼ 30 nm. Interestingly, beyond f_w = 70%, the emission is further enhanced with a red-shift up to 535 nm at 90% of water content (Figure 2). All these features suggest an aggregation induced emission (AIE) behavior of TPACNPMI. Furthermore, the formation of nanoaggregates at higher water content for all these AIEgens were confirmed by DLS, AFM, and SEM studies (Figure 3, Figure S7).

The disparity in the emissive behavior of TPANDI and the other three luminogens in the aggregated state may emerge from the diverse spatial arrangements of the respective molecules in the solid state. In order to visualize the relative orientation of the molecules in the condensed state, single-crystal X-ray diffraction (SCXRD) studies were carried out. Aggregation caused quenching (ACQ) usually occurs because of an effective $\pi\cdots\pi$ stacking interaction between adjacent organic monomers. SCXRD analysis of TPANDI crystal illustrates that two neighboring planar NDI core moieties lie above one another (cofacial type) at a very close distance of ∼3.3 Å (Figure 4a, Figure S8) with a subtle displacement,

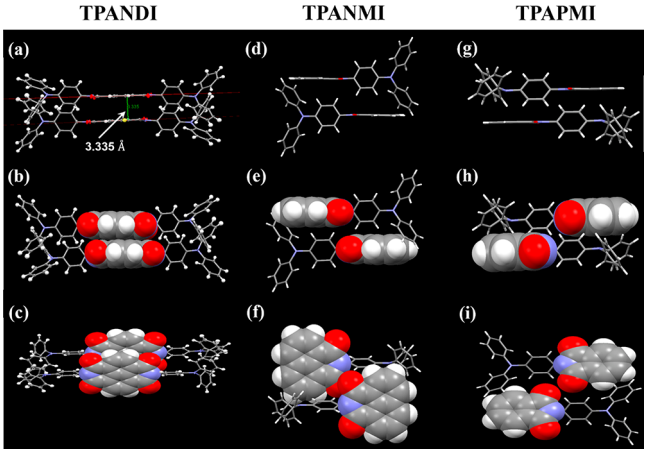


Figure 4. (a) $\pi-\pi$ stacking interaction between two acceptor cores in TPANDI. Space-filling model of TPANDI from (b) side-view and (c) top-view. Arrangement of two neighboring molecules of (d) TPANMI and (g) TPAPMI in the crystalline state. Space-filling model of TPANMI from (e) side view, (f) top view. Space filling model of TPAPMI from (h) side view, (i) top view.

which falls in the range of an effective $\pi\cdots\pi$ stacking interaction (from 3.3−3.8 Å).[33] The presence of two bulky triphenylamine moieties at two terminal ends often restricts the cofacial stacking of molecules.[34] Nevertheless, in the case of TPANDI, the TPA moiety fails to inhibit the $\pi\cdots\pi$ stacking between two NDI moieties because of the higher length of the planar core, which ultimately results in emission quenching in the aggregated state. On the other hand, TPANMI and TPAPMI display an entirely different packing arrangement in the crystalline state. SCXRD analysis shows that TPANMI molecules are arranged in a brick-layer stacking mode, and TPAPMI adopts a herringbone packing mode in the crystalline state (Figure S8). The dihedral angle between the phenyl ring of TPA group adjacent to the acceptor moiety appears as one of the crucial factors in this regard. In TPANMI, the phenyl ring is attached to the planar NMI acceptor core with a large dihedral angle of 71.85° (Figure S13a); whereas, in the case of TPAPMI, the dihedral angle between the phenyl ring and the PMI group is only 43.03° (Figure S13b). Such a prominent change in the dihedral angle may be attributed to differential sizes of the acceptor moieties. Interestingly, for both cases, the space-filling model illustrates that the planar acceptor moieties are displaced in such a way that the NMI and PMI acceptor cores are lying above the donor-TPA moiety (Figure 4), which significantly reduces the $\pi\cdots\pi$ overlap between neighboring molecules. Notably, a shortened length of the planar acceptor moieties in TPANMI and TPAPMI, strengthen the impact of bulky triphenylamine. As a result, the diagonal and the perpendicular distance of two planar acceptor moieties were found to be increased (Figure 5), which results in the less effective $\pi\cdots\pi$ stacking. We believe that the synergistic effects of such shortened planar acceptor moieties and an emergence of the profound impact of bulky triphenylamine moiety together dictate their AIE behavior. Moreover, in TPACNPMI, two neighboring luminogens orient themselves in a head-to-tail fashion (Figure S8). Here, the terminal phthalimide moiety lies closer to the triphenylamine moiety of the neighboring luminogen in a slipped orientation. In this case, the presence of multiple rotatable single bonds increases the possibilities of several nonradiative decay pathways, which may affect the emission efficiency in bulk solvent; however, in the aggregated state due to restricted intramolecular rotation (RIR) and restricted intramolecular vibration (RIV) such nonradiative decay pathways may be ceased, leading to the emergence of its AIE properties.

Room-Temperature Phosphorescence (RTP) Study. Energy gap between the lowest singlet and the lowest triplet state of a donor−acceptor based luminogen is largely dependent on the nature of donor and acceptor moieties forming the molecular framework. A strong electron-rich donor and a strong electron-deficient acceptor can lead to a well-separated highest occupied molecular orbital (HOMO) and lowest unoccupied molecular orbital (LUMO), which eventually can lead to a less ΔE_{ST}.[35] We have already shown that the HOMO resides on the donor moiety (triphenylamine, TPA) and the LUMO lies on the respective acceptor moiety in all the four luminogens, and at the same time they maintain a large twisting angle between donor−acceptor. Such systems often provide a much smaller singlet−triplet energy gap or ΔE_{ST}, which can increase the rate of intersystem crossing or ISC. Moreover, all these luminogens contain atoms with nonbonding electrons, which are very useful for populating triplet state through intersystem crossing (ISC).[36,37] TPANMI in its crystalline phase (at room temperature), exhibits a broad spectrum with the emission maxima located at ∼625 nm (Figure 6) and a triexponential decay feature comprising ∼2, ∼7, and ∼ 32 ns lifetime components (Figure S9), which clearly indicates the excited state decay to be a fluorescence emission. However, a red-shifted emission band having maxima at ∼750 nm was obtained upon collecting the emission profile at 100 μs lamp triggered delay (Figure 6). Interestingly, a triexponential emission transient having lifetime components of ∼1, ∼4, and ∼12 ms was obtained (Figure 6) upon collecting the emission decay at ∼750 nm, which suggests the RTP behavior of TPANMI. Similarly, in the case of TPAPMI (at room temperature), the fluorescence decay at ∼ 617 nm was found to be triexponential in nature, having components of ∼0.7, ∼3, and ∼13 ns (Figure S9). When the emission profile

https://doi.org/10.1021/acs.jpcb.1c08126
J. Phys. Chem. B XXXX, XXX, XXX−XXX

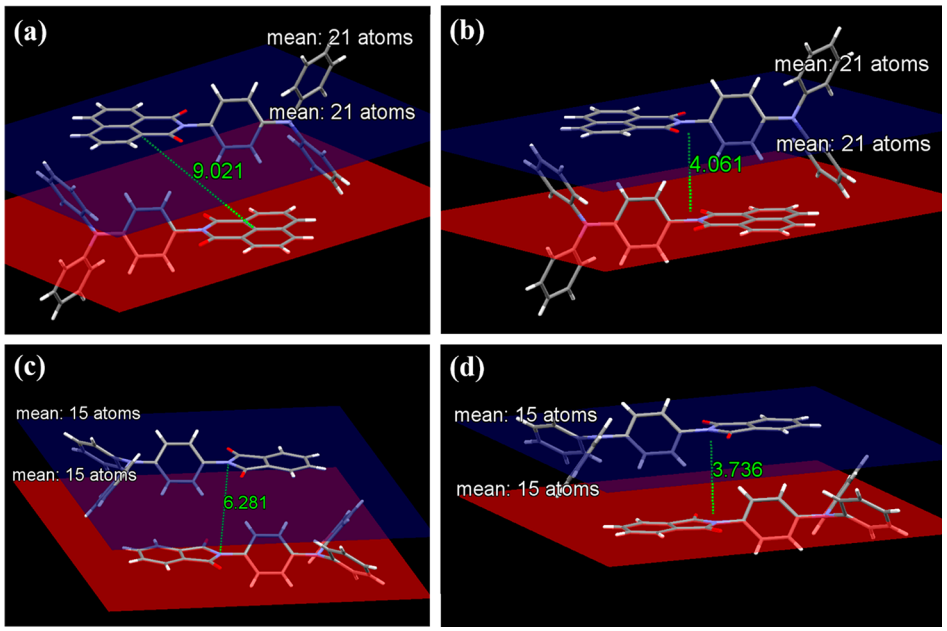


Figure 5. Diagonal distance (in Å) of two planar acceptor moieties in (a) TPANMI and (c) TPAPMI. Perpendicular distance (in Å) of the planes passing through the acceptor moieties of (b) TPANMI and (d) TPAPMI. Images have been processed by Mercury 3.7 software.

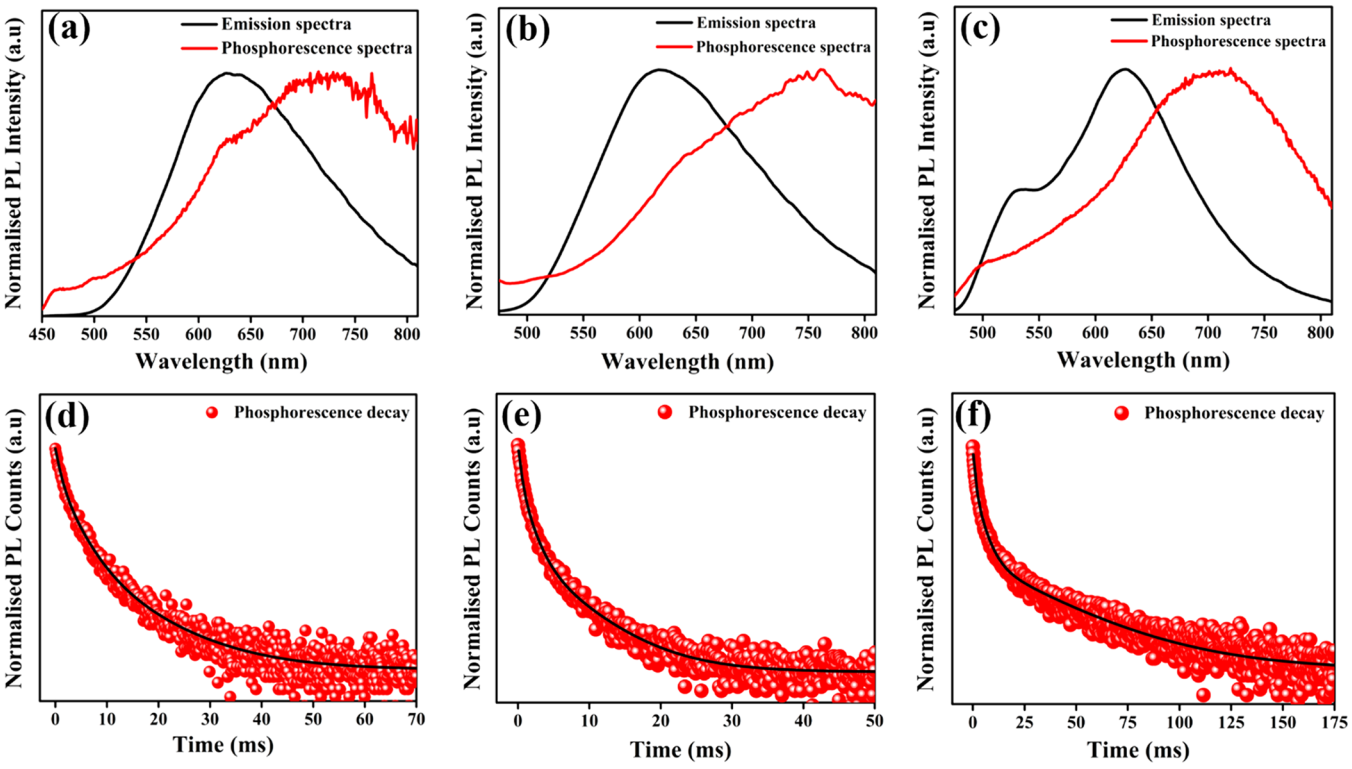


Figure 6. Emission spectra and phosphorescence spectra of (a) TPANMI, (b) TPAPMI, and (c) TPACNPMI. Phosphorescence decay profile for (d) TPANMI (collected at 750 nm), (e) TPAPMI (collected at 750 nm), and (f) TPACNPMI (collected at 715 nm) collected using 100 μs lamp triggered delay.

was collected at 100 μs lamp triggered delay, the phosphorescence spectrum was generated with an emission maximum centered at ~750 nm. The emission decay profile (collected at 750 nm) manifested triexponential behavior with components of ~433 μs, ~1.5 ms, and ~ 7 ms (Figure 6). Unlike the previous cases (TPANMI and TPAPMI), the crystals of TPACNPMI exhibit two different emission peaks at ~535 and ~ 635 nm, respectively (Figure 6). The emission transient at ~635 nm shows a triexponential behavior with components of ~1, ~5, and ~ 12 ns (Figure S9). Whereas, the decay profile corresponding to the emission peak at ~535 nm was found to be relatively shorter in terms of lifetime, having a biexponential nature with components of ~0.6 and ~ 3.3 ns (Figure S9). In this case also, upon collecting the emission at 100 μs lamp

https://doi.org/10.1021/acs.jpcb.1c08126
J. Phys. Chem. B XXXX, XXX, XXX−XXX

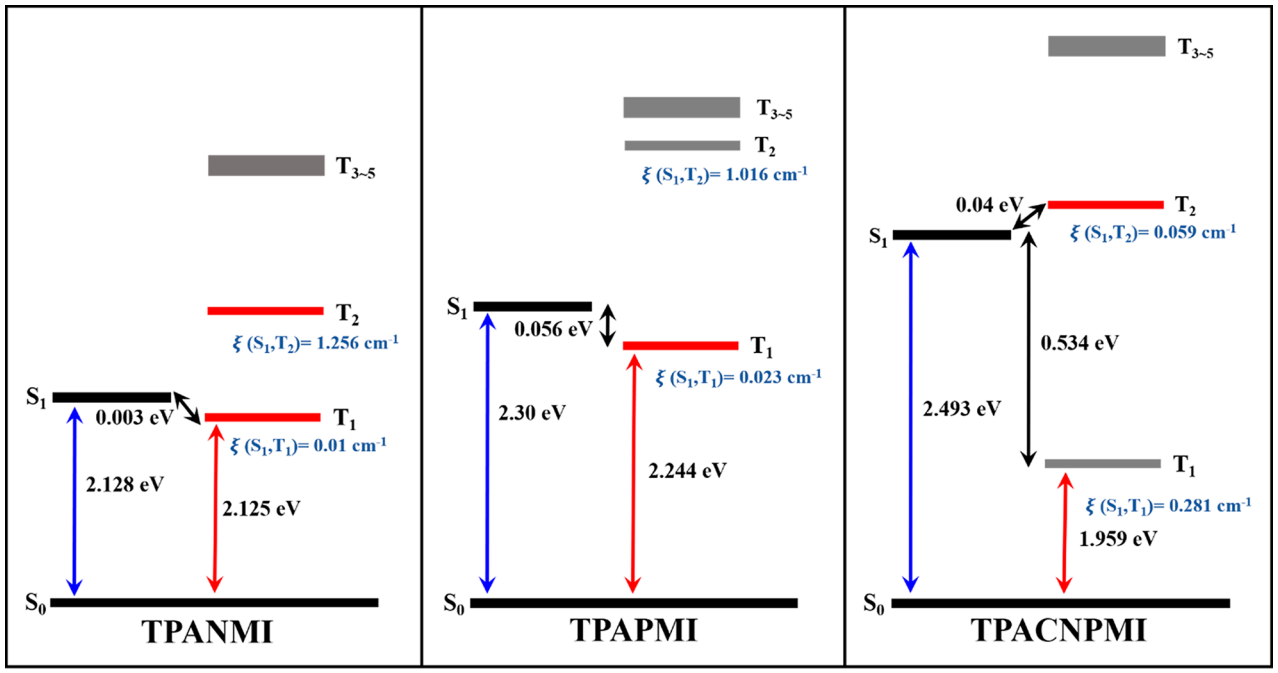


Figure 7. Energy level diagrams of TPANMI, TPAPMI, and TPACNPMI for both singlet and triplet states (ξ indicates spin−orbit coupling matrix element).

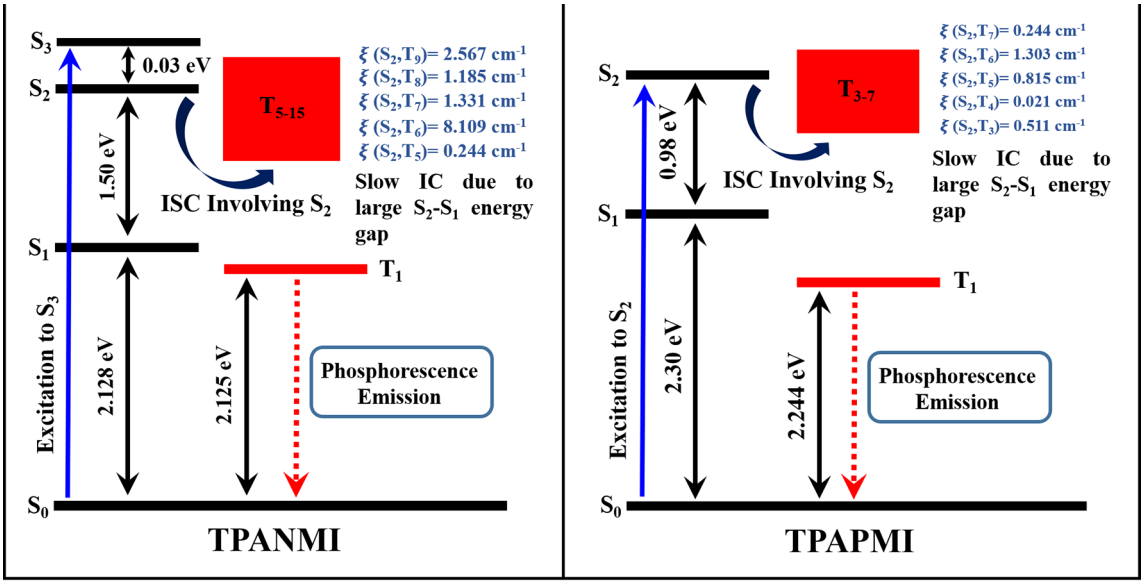


Figure 8. Energy level diagrams of TPANMI and TPAPMI for both the singlet and triplet states in case of a slow internal conversion (IC) rate (ξ indicates spin−orbit coupling matrix element).

triggered delay, a red-shifted phosphorescence spectrum was obtained with an emission maximum situated at ∼715 nm (Figure 6). Upon collecting the phosphorescence decay at ∼715 nm, a triexponential decay profile was found with components of ∼1, ∼4.5, and ∼39 ms (Figure 6).

To investigate the mechanism of the observed room-temperature phosphorescence from the AIE active luminogens, time-dependent density functional theory (TD-DFT) calculations were performed for both the singlet and triplet states. Here, it is pertinent to mention that an effective intersystem crossing is required for the phosphorescence emission channels to be activated, and the energy gap between the lowest singlet and lowest triplet states (ΔE_{ST}) can play a critical role in this regard, as the extent of an efficacious ISC process is inversely proportional to the ΔE_{ST} value. Interestingly, both the TPANMI and TPAPMI possess a reasonably small ΔE_{ST} value of 0.003 and 0.056 eV (Figure 7), respectively. In TPACNPMI, ΔE_{ST} is higher (0.534 eV) compared with the other two luminogens; however, because of the presence of another triplet state T_2 having considerably lower energy gap (0.04 eV) with the S_1 state (Figure 7), the intersystem crossing process is also facilitated here. Notably, all the above discussions are based on the assumption that the ISC process is occurring through the lowest singlet, that is, the S_1 state, even though it can be excited to higher singlet states. In another possible scenario, the ISC process also can take place

https://doi.org/10.1021/acs.jpcb.1c08126
J. Phys. Chem. B XXXX, XXX, XXX−XXX

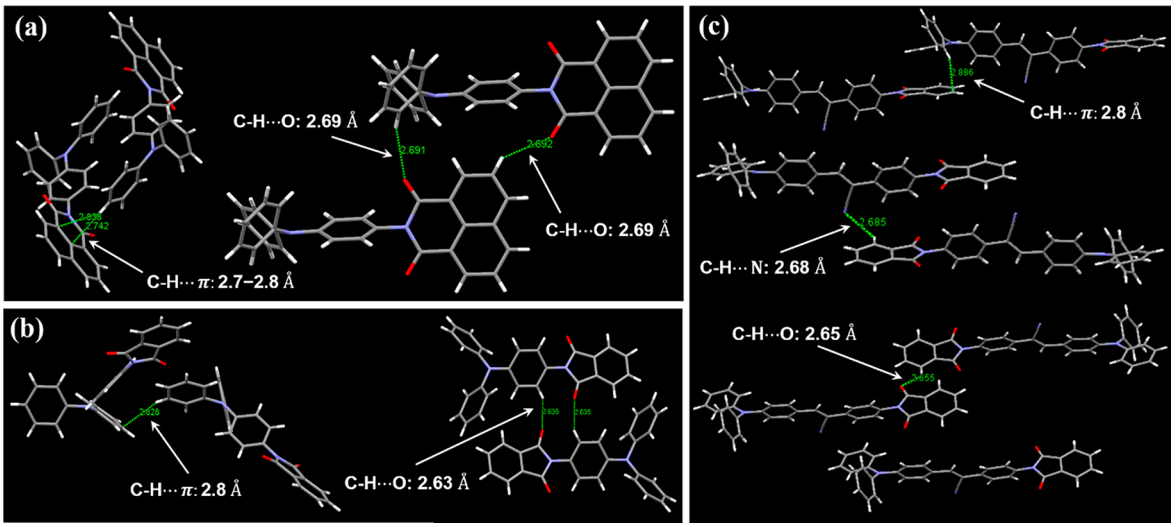


Figure 9. Presence of several short contact noncovalent interactions in the crystals of (a) TPANMI, (b) TPAPMI and (c) TPACNPMI. Images have been processed by Mercury 3.7 software.

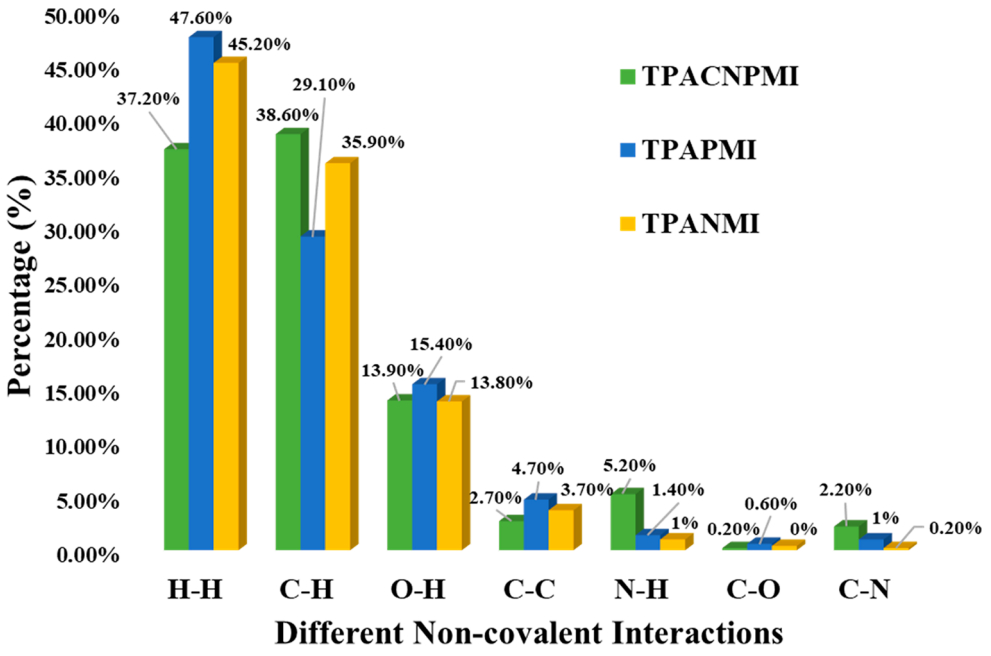


Figure 10. Histogram summarizing the contribution of different noncovalent interactions obtained from 2-D fingerprint plots in Hirshfeld surface analysis.

via excited singlet states other than S_1. For example, in TPANMI, the S_2-S_1 gap is calculated to be 1.50 eV, and such a high energy gap can lead to a slow IC process, thus, increasing the probability of ISC involving higher excited singlet state, S_2.[38] Although, in this case, the first bright excited singlet state is S_3 (oscillator strength, f = 0.3205), but it possesses a reasonably lower energy gap of 0.03 eV with the S_2 state; therefore, the excitons can quickly relax to the S_2 state through IC. As the S_2-S_1 energy gap is high, the ISC process can even take place via S_2 state (Figure 8). Notably, here the S_2 state is energetically very close (within ±0.3 eV) to numerous triplet states (T_5-T_{15}), and some of those states are having a high spin−orbit coupling matrix element (ξ) values (as high as 8.109) with the S_2 state (Figure 8), which facilitates the ISC process from the S_2 state. In TPAPMI, the energy gap between S_1 and S_2 is 0.98 eV, and the first bright state is S_2 (oscillator strength, f = 0.2155). S_2 and S_1 share a large energy gap; thus, the ISC process can even occur from S_2 state to several triplet states (T_3-T_7) having considerable ξ values (Figure 8). On the contrary, in TPACNPMI, the S_2-S_1 energy gap is comparatively lower (0.34 eV), which eventually leads to a faster IC, and the ISC process is more likely to take place via the S_1 state.[38] All these theoretical studies suggest favorable and efficient ISC processes for all the three luminogens and thereby lead to the emergence of efficient phosphorescence emission.

Short intermolecular contacts provide a constrained environment, which restricts the motion of several bond vibrations with higher energy (C−H stretching may possess energy of ∼0.37 eV in aromatic molecules), thereby reducing the extent of nonradiative deactivation.[27,39] Thus, noncovalent interactions play an important role to dictate the RTP characteristics

https://doi.org/10.1021/acs.jpcb.1c08126
J. Phys. Chem. B XXXX, XXX, XXX−XXX

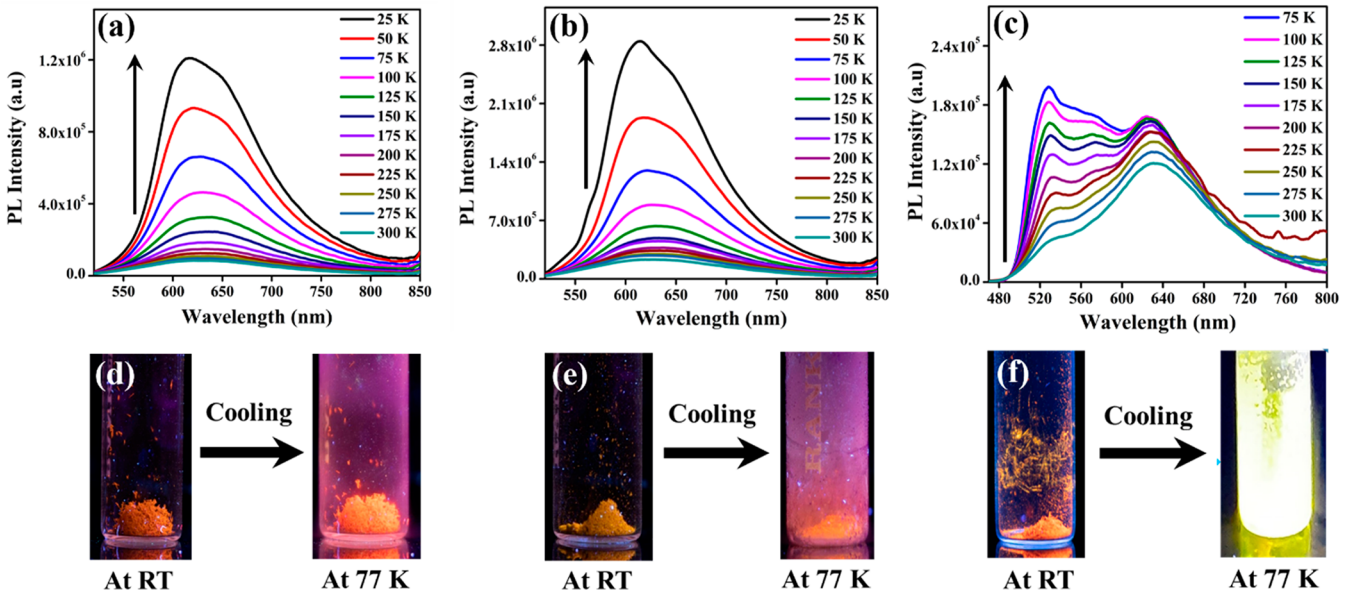


Figure 11. Temperature-dependent photoluminescence spectra of (a) TPANMI, (b) TPAPMI, and (c) TPACNPMI. Enhanced emission of (d) TPANMI, (e) TPAPMI in the crystalline phase under UV lamp (365 nm) at room temperature (RT, 295 K) and at 77 K. Emission switch of (f) TPACNPMI in the crystalline state under UV lamp (365 nm) at RT (295 K) and at 77 K.

of luminogens. To gain a better insight, crystal structures of TPANMI, TPAPMI and TPACNPMI were analyzed. All these AIE active luminogens have several noncovalent interactions with reasonably short distances in their crystalline phase, such as, C−H···π (2.7−2.8 Å), C−H···O (2.69 Å) in the case of TPANMI, and similarly, C−H···π (2.8 Å), C−H···O (2.63 Å) in case of TPAPMI (Figure 9). Interestingly, due to the incorporation of an additional cyano-ethylene group in TPACNPMI, additional C−H···N (2.68 Å) interactions were observed along with C−H···π (2.8 Å) and C−H···O (2.65 Å) interactions (Figure 9). In order to quantitatively evaluate each type of noncovalent interactions, Hirshfeld surface analysis was performed (Section S1). The specific contributions of several noncovalent interactions were calculated and summarized in Figure 10. It was observed that, van der Waals (H···H) interactions occupy a significant portion (Figure 10, Figure S10); even though the enthalpy of stabilization of such interactions are reasonably poor (~0.4−4 kJ/mol). Significant contributions of C−H···π (~10.3 kJ/mol)[40] and C−H···O interactions (usually ~41−104 kJ/mol)[41] account for higher enthalpy of stabilization leading to the formation of firmly packed molecular networks. Additionally, the percentage of C−H···N interactions (5.2%) were found to be increased in TPACNPMI due to the presence of additional cyano-ethylene moiety (Figure 10, Figure S10). Notably, the contribution of the π···π (C···C) interactions are relatively smaller compared to other interactions in all these three AIE luminogens. However, maximum contributions of π···π interactions (5.6%) were found in the case of TPANDI (Figure S11), which is accountable for its ACQ properties, as we discussed in the earlier section.

Temperature-Dependent Emission Properties. AIE luminogens exhibiting emission-switch upon decreasing the temperature have potential scope of applications in the fabrication of low-temperature thermal sensors.[42] Most of the common organic luminogens exhibit enhanced emission at cryogenic temperatures because of suppression in nonradiative decay pathways at lower temperatures; however, only a few of them can switch their emission color and can exhibit low-temperature thermochromic properties. In order to investigate the cryogenic emissive behavior, low-temperature photoluminescence studies were carried out for all the AIE active luminogens. It was observed that TPANMI and TPAPMI exhibited a gradually enhanced emission in the crystalline phase, upon lowering the temperature from room temperature (295 K) to 25 K, without any considerable emission switch (Figure 11). Surprisingly, a totally opposite scenario appears in the case of TPACNPMI. As already mentioned earlier, at room temperature (295 K), the orange-emissive crystals of TPACNPMI have two emission peaks at ~535 nm and ~635 nm. Upon decreasing the temperature, both the peaks became gradually enhanced because of the sequential decrease in the number of nonradiative decay channels. However, the extent of increment for the ~535 nm peak was higher compared with that of the ~635 nm peak upon decreasing the temperature (Figure 11). As a result, a distinct emission color switching from orange to greenish-yellow was observed at cryogenic temperatures, suggesting the presence of low-temperature thermochromic property in TPACNPMI.

Mechanochromic Study. Solid-state emissive properties of TPANMI, TPAPMI, and TPACNPMI should largely depend upon their molecular arrangements in crystalline phase owing to flexible nature of the molecules and the presence of several noncovalent interactions. Perturbing a particular arrangement by applying external mechanical stimuli and heat may lead to distinct alteration in photoluminescence properties and excited state processes in the bulk crystal. TPANMI crystals exhibit a broad emission spectrum with an emission maxima lying at ~625 nm. Even after vigorous grinding with a mortar and pestle (by maximum manual force), only a slight blue shift along with a ~15 nm reduction of fwhm was observed (Figure S12). In the case of TPAPMI also, no apparent luminescence color change was observed upon grinding the orange emitting crystals (Figure 12), with the emission maxima situated at ~612 nm (Figure S12). However, the emissive behavior of TPACNPMI was found to be quite

https://doi.org/10.1021/acs.jpcb.1c08126
J. Phys. Chem. B XXXX, XXX, XXX−XXX

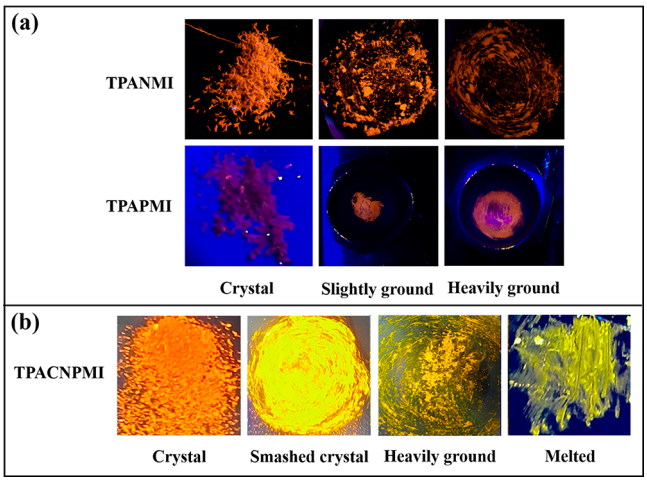


Figure 12. (a) Crystals of TPANMI and TPAPMI under different extents of mechanical stimuli. (b) Crystals of TPACNPMI upon different extents of mechanical stimuli and in the melted condition. All the images have been collected by exciting with a 365 nm UV lamp.

different. The microcrystals of TPACNPMI exhibits orange emission with an emission maximum locating at ∼615 nm. Interestingly, upon smashing the crystals by applying a moderate manual force with mortar and pestle, a ∼45 nm blue shift (Figure S12) in the emission maxima was observed with a luminescence color switching from orange to yellowish orange (emission maxima at ∼570 nm). It further experienced a blue shift of ∼30 nm upon heavy grinding (Figure S12) and exhibited a greenish-yellow emission (maximum at ∼540 nm) (Figure 12). Interestingly, upon melting the compound (TPACNPMI), a green emissive melt was obtained with the emission maxima situated at ∼527 nm (Figure S12), suggesting a meltochromic behavior of the luminogen. As TPACNPMI is responsive toward both pressure and temperature, it can be designated as a representative "stimuli-responsive" luminogen; whereas, such distinct luminescence color change was absent in other two luminogens, and therefore, they (TPANMI and TPAPMI) can be treated as "stimuli-inactive" luminogens. Such easy and prompt tricolor emission tuning properties of TPACNPMI with occurrence of orange, yellowish orange, and greenish yellow emission are still rare in the family of stimuli-responsive luminogens.

Majorly, three factors are responsible for a luminogen to exhibit mechanochromic activity, that is, flexibility, a twisted donor−acceptor based structure and presence of multiple noncovalent interactions.[8] For CT type luminogens in crystalline phase, mechanical grinding may lead to alteration in dihedral angle between the donor and the acceptor moieties due to the presence of sufficient flexibility and twisting characteristics in their molecular skeleton. This alteration in the dihedral angle can eventually lead to a modulation in the extent of orbital overlap between the donor and the acceptor moieties, and may give rise to a considerable shift in emission band. Notably, in all our designed luminogens, the presence of the propeller-shaped triphenylamine provides enough flexibility and twisting. In TPANMI, the three phenyl groups of donor TPA make dihedral angles of 71.85° (θ_1), 68.98° (θ_2), and 58° (θ_3), respectively, with the planar acceptor NMI which shows a twisted nature of the donor moiety (Figure S13a). In TPAPMI, similar twisted behavior is observed with relatively smaller dihedral angles (θ_1 = 43°, θ_2 = 54.13°, and θ_3 = 43°) due to a smaller size of phthalimide acceptor core (Figure S13b). In TPACNPMI also, the junctional phenyl group of TPA (adjacent to the cyano-ethylene moiety) makes large dihedral angles with the other two terminal phenyl groups (θ_2 = 86.77° and θ_3 = 57°) (Figure S14). Moreover, the junctional phenyl group of TPA moiety lies almost planar with the plane containing cyano-ethylene group and benzene linker with a quite small angle of 1.9° (Figure S15). Notably, this type of planar conformation might lead to an electronic structure having larger overlap between donor and acceptor orbitals generating a more stabilized CT state with red-shifted emission. However, upon mechanical grinding, a blue-shifted emission of TPACNPMI is observed, suggesting formation of a more twisted configuration where the extent of overlap between donor−acceptor orbitals is relatively smaller.[43] Moreover, the benzene linker in TPACNPMI provides an additional dihedral angle (69.59°) with the terminal planar phthalimide moiety (Figure S16); the presence of such additional dihedral angles is responsible for gaining extra flexibility and can be beneficial for deriving mechanochromic properties. Therefore, the incorporation of cyano-ethylene group along with the benzene linker can contribute additional flexibility in the molecular skeleton, and further, the presence of a planar central part opens up the possibilities of forming a twisted conformation under mechanical grinding, which together lead to the observed mechanochromism in TPACNPMI. Another factor that can bring about mechanochromic activity in a luminogen is the presence of several noncovalent interactions. Generally, a greater contribution of C−H···π interaction along with a meager π···π interaction (a higher ratio of C−H···π to π···π interaction) are highly desirable due to a higher enthalpy of stabilization of C−H···π interaction (∼10.3 kJ/mol).[8] A higher extent of π···π interaction can lead to a higher chance of planarity and exciton−phonon coupling in the bulk crystal,[44] which often give rise to a quenched emission with less emission contrast, and these are detrimental for observing mechanochromism. Notably, among all these luminogens, the TPACNPMI crystal has a maximum contribution of C−H···π interaction (38.60%) and a minimum contribution of π···π interaction (only 2.70%) (Figure 10), giving rise to a maximum ratio of C−H···π interaction to π···π interaction, that is, 14.29, which in the case of TPANMI and TPAPMI are 9.70 and 6.19, respectively. Furthermore, in TPACNPMI, an additional C−N···H interaction contribution of 5.20% is obtained due to the presence of cyano-ethylene moiety (Figure 10). All these factors are combinedly believed to be responsible for the observed mechano-active behavior of TPACNPMI.

The foremost importance of any mechanochromic luminogen is its ability of reversing back to the original pristine state. Intriguingly, under the naked eye, it was observed that the heavily ground powder of TPACNPMI (with greenish yellow emission emerging at ∼540 nm) transformed to the initial pristine state (with yellowish orange emission located at ∼570 nm) under thermal annealing with a diminished emission intensity (Figure S12). After recovery, the measured emission spectra exactly match with the emission profile of the pristine powder, which further validates our claim.

A PXRD experiment was also carried out to get insight into the details of the observed mechanochromic behavior. Crystals of TPACNPMI exhibit sharp and intense reflection peaks suggesting a well-ordered microcrystalline structure (Figure

https://doi.org/10.1021/acs.jpcb.1c08126
J. Phys. Chem. B XXXX, XXX, XXX−XXX

S17). With slight grinding of those crystals, a decrease in intensity of those peaks along with disappearance of some reflection peaks were observed (Figure S17). Notably, a further heavy grinding leads to an emergence of diffused or broad halo band (with the reduced intensity of reflection peaks) (Figure S17), which suggests a modulation of crystallinity in TPACNPMI and its transformation to an amorphous state. Similarly, in TPANMI and TPAPMI, the crystals exhibited sharp and intense reflection peaks indicative of crystallinity of those compounds; upon mechanical grinding, the diffraction peaks attenuate or even disappear with appearance of a broad halo (Figure S17), indicating an amorphous nature of the ground powder. However, TPANMI and TPAPMI did not exhibit a distinct emission shift upon mechanical grinding, which indicates such phase transition leads to formation of a state that is energetically very similar to that of the crystalline state and is responsible for its mechano-inactive behavior.

APPLICATIONS

Photoluminescence Thermometer. Conventional thermometers cannot be used in marine research, underground research, tunnels, automobile, and aircraft industries.[45,46] Thus, photoluminescence-based thermometers have recently drawn considerable attention because of their prompt response and good spatial resolution.[45,47] Among all of our designed luminogens, TPACNPMI seems to be a promising candidate for a luminescence-based thermometer, as it exhibits a well-distinct emission switching from greenish yellow to cyan-green emission upon cooling the solution containing TPACNPMI in a glass forming an alcoholic mixture (methanol and ethanol are taken in 4:1 ratio) from 295 to 77 K (Figure 13). However, the

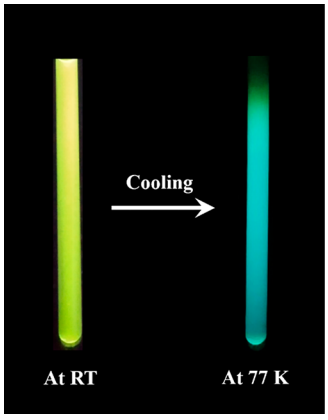


Figure 13. Distinct emission switch of TPACNPMI in a glass-freezing mixture (methanol:ethanol = 4:1) upon cooling from room temperature (295 K) to cryogenic temperature (77 K).

other two luminogens (TPANMI and TPAPMI) are not useful in this regard, as they are nonemissive both in RT (295 K) and at 77 K because of higher stabilization of the CT state in such polar medium.

Two-Photon Cell Imaging. Two-photon cell imaging has emerged as a powerful tool and has unmatched advantages over the conventional one-photon imaging because of minimal photodamaging, capability of deep tissue penetration, and excellent resolution.[48−50] In this context, aggregation-induced emissive organic luminogens (AIEgens) have emerged as an excellent class of compounds for two-photon bioimaging owing to their high emissivity in the aggregated state and minimum photobleaching effect.[51] Among all of our AIE active luminogens, intriguingly, TPACNPMI exhibits two-photon absorption properties (Figure 14). Moreover, the 1two-photon

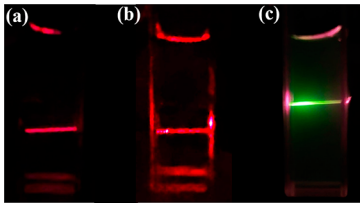


Figure 14. (a) A laser beam of 800 nm focused on a solution of TPANMI in 5% DMSO/water (10 μM) and no fluorescence was observed. (b) A laser beam of 800 nm focused on a solution of TPAPMI in 5% DMSO/water (10 μM) and no fluorescence was observed. (c) A laser beam of 800 nm focused on a solution of TPACNNMI in 5% DMSO/water (10 μM) and a clear green fluorescence was observed.

absorption cross-section of TPACNPMI measured at 845 nm excitation wavelength was found to be ∼510 GM (see section S3 in SI). Thus, we have performed two-photon imaging experiments using TPACNPMI. From the two-photon image, it is evident that our luminogen is well capable of lighting up cells, largely the cytoplasm part (Figure 15). In order to look

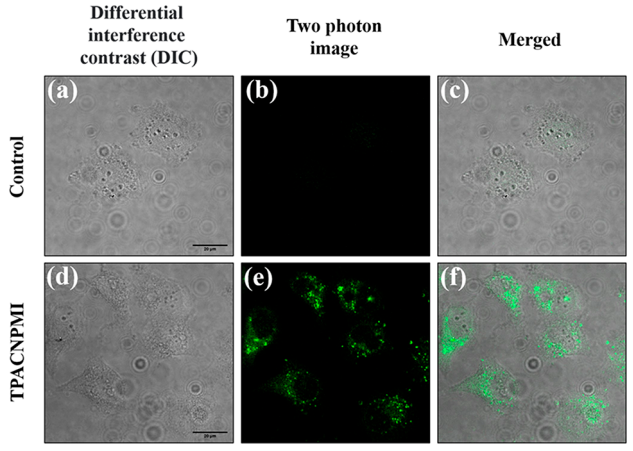


Figure 15. Two-photon microscopy image (excitation wavelength = 800 nm, collection window is from 550 to 620 nm) of MCF-7 cells: top row- without the treatment of dye and bottom row -with treatment of 10 μM TPACNPMI. (a and d) differential interference contrast (DIC) images, (b) cells without dye treatment, (e) cells treated with dye (TPACNPMI), and (c and f) DIC image merged with dye image.

into the cytotoxic behavior of our luminogen, the MTT viability assay of MCF7 cells was carried out. No significant decrease in viability was observed in samples incubated with up to 15 μM TPACNPMI (Figure S18), which indicates that TPACNPMI does not exhibit a toxic effect toward the cell up to that concentration.

CONCLUSION

In summary, this research article focuses on designing novel multifunctional luminogens exhibiting simultaneous AIE, RTP, and mechanochromic behavior by systematic molecular engineering. This journey starts from an ACQ phore, TPANDI. The longer and larger acceptor core in TPANDI

https://doi.org/10.1021/acs.jpcb.1c08126
J. Phys. Chem. B XXXX, XXX, XXX−XXX

makes it nonemissive in the aggregated state because of an effective $\pi-\pi$ stacking interaction in between planar naphthalene diimide moieties. Interestingly, a simple structural change in acceptor core from naphthalene diimide to naphthalene monoimide and phthalimide can effectively inhibit the $\pi-\pi$ stacking interaction in the condensed state and can bring about ACQ to AIE type transformation in TPANMI and TPAPMI. Moreover, the presence of closely spaced singlet and triplet states in all these AIE active luminogens can facilitate the intersystem crossing (ISC) process and consequently bring about room-temperature phosphorescence phenomenon. Although these two luminogens exhibit simultaneous AIE and RTP properties, they are mechanically inactive; therefore, further structural engineering is required to obtain simultaneous AIE, RTP, and mechanochromism. Finally, it has been demonstrated that an introduction of a cyano-ethylene group along with a benzene linker in between the donor triphenylamine and acceptor phthalimide moieties can bring about easy and distinct mechanochromic behavior (along with AIE and RTP properties) in the final molecule, that is, TPACNPMI. Thus, starting from a molecule with ACQ nature, upon minimal and systematic modification of molecular structure, a multifunctional luminogen with AIE, RTP, and easy and distinct mechanochromic properties was obtained.

■ ASSOCIATED CONTENT

Supporting Information

The Supporting Information is available free of charge at https://pubs.acs.org/doi/10.1021/acs.jpcb.1c08126.

Instrumentation, materials and methods, synthesis, characterization, crystallographic data, solution state photophysics, details of AIE studies, Hirshfeld surface analysis, mechanochromic studies, MTT assay, emission in aerated and degassed toluene, two-photon excited fluorescence spectra and two-photon absorption cross-sectional calculation, and other data (PDF)

■ AUTHOR INFORMATION

Corresponding Author

Partha Hazra − *Department of Chemistry and Centre for Energy Science, Indian Institute of Science Education and Research (IISER), Pune, India 411008;* orcid.org/0000-0003-0422-1399; Phone: +912025908077; Email: p.hazra@iiserpune.ac.in

Authors

Abhijit Chatterjee − *Department of Chemistry, Indian Institute of Science Education and Research (IISER), Pune, India 411008*

Joy Chatterjee − *Department of Chemistry, Indian Institute of Science Education and Research (IISER), Pune, India 411008*

Subrahmanyam Sappati − *Soft Condensed Matter, Raman Research Institute, Bengaluru, Karnataka, India 560080*

Tariq Sheikh − *Department of Chemistry, Indian Institute of Science Education and Research (IISER), Pune, India 411008;* orcid.org/0000-0002-4863-9642

Rintu M. Umesh − *Department of Biology, Indian Institute of Science Education and Research (IISER), Pune, India 411008*

Madan D. Ambhore − *Department of Chemistry, Indian Institute of Science Education and Research (IISER), Pune, India 411008*

Mayurika Lahiri − *Department of Biology, Indian Institute of Science Education and Research (IISER), Pune, India 411008;* orcid.org/0000-0001-9456-4920

Complete contact information is available at: https://pubs.acs.org/10.1021/acs.jpcb.1c08126

Author Contributions

A.C. and P.H. came up with the idea of the project. A.C. is the primary contributor in terms of design and development, execution, and compilation of the project. The electronic structure calculations have been performed by A.C. and S.S. The interpretation of the theoretical results is a combined effort of A.C. and S.S. J.C. provided useful insights during the implementation of this project. J.C. contributed in manuscript writing, improvement and figure preparation. T.S. contributed in the measurement of phosphorescence spectra, low-temperature PL studies and phosphorescence decay profiles. R.M.U. performed the two photon cell imaging experiment, and M.L. supervised the two photon cell imaging experiment. M.D.A. helped in solving the crystal structures. P.H. supervised the whole project and provided valuable insights throughout the progression of the project.

Notes

The authors declare no competing financial interest.

■ ACKNOWLEDGMENTS

P.H. acknowledges the Science and Engineering Research Board (DST-SERB), Government of India (CRG/2020/000567), for financial support. The support and the resources provided by "PARAM Brahma Facility" under the National Supercomputing Mission, Government of India at IISER Pune are gratefully acknowledged. A.C. and J.C. are thankful to IISER Pune for providing excellent facilities and fellowships. The authors acknowledge IISER Pune microscopy facility for access to equipment, infrastructure and Mr. Vijay Vittal for help in two-photon imaging experiment. T.S. acknowledges University Grants Commission (UGC), India for fellowship. Ms. Anindita Bhowmick from Prof. RGB group, IISER Pune is acknowledged for her valuable suggestions during the synthesis of the designed luminogens. We acknowledge reviewers for their valuable comments and suggestions.

■ REFERENCES

(1) Balch, A. L. Dynamic Crystals: Visually Detected Mechanochemical Changes in the Luminescence of Gold and Other Transition-Metal Complexes. *Angew. Chem., Int. Ed.* **2009**, *48* (15), 2641−2644.

(2) Yoon, S.-J.; Chung, J. W.; Gierschner, J.; Kim, K. S.; Choi, M.-G.; Kim, D.; Park, S. Y. Multistimuli Two-Color Luminescence Switching via Different Slip-Stacking of Highly Fluorescent Molecular Sheets. *J. Am. Chem. Soc.* **2010**, *132* (39), 13675−13683.

(3) Zhang, G.; Lu, J.; Sabat, M.; Fraser, C. L. Polymorphism and Reversible Mechanochromic Luminescence for Solid-State Difluoroboron Avobenzone. *J. Am. Chem. Soc.* **2010**, *132* (7), 2160−2162.

(4) Yagai, S.; Okamura, S.; Nakano, Y.; Yamauchi, M.; Kishikawa, K.; Karatsu, T.; Kitamura, A.; Ueno, A.; Kuzuhara, D.; Yamada, H.; et al. Design Amphiphilic Dipolar π-Systems for Stimuli-Responsive Luminescent Materials Using Metastable States. *Nat. Commun.* **2014**, *5* (1), 4013.

(5) Sun, H.; Liu, S.; Lin, W.; Zhang, K. Y.; Lv, W.; Huang, X.; Huo, F.; Yang, H.; Jenkins, G.; Zhao, Q.; et al. Smart Responsive

Phosphorescent Materials for Data Recording and Security Protection. *Nat. Commun.* **2014**, *5* (1), 3601.
(6) Li, Z.; Toivola, R.; Ding, F.; Yang, J.; Lai, P.-N.; Howie, T.; Georgeson, G.; Jang, S.-H.; Li, X.; Flinn, B. D.; et al. Highly Sensitive Built-In Strain Sensors for Polymer Composites: Fluorescence Turn-On Response through Mechanochemical Activation. *Adv. Mater.* **2016**, *28* (31), 6592−6597.
(7) Lavrenova, A.; Balkenende, D. W. R.; Sagara, Y.; Schrettl, S.; Simon, Y. C.; Weder, C. Mechano- and Thermoresponsive Photoluminescent Supramolecular Polymer. *J. Am. Chem. Soc.* **2017**, *139* (12), 4302−4305.
(8) Roy, B.; Reddy, M. C.; Hazra, P. Developing the Structure−Property Relationship to Design Solid State Multi-Stimuli Responsive Materials and Their Potential Applications in Different Fields. *Chem. Sci.* **2018**, *9* (14), 3592−3606.
(9) Mei, J.; Leung, N. L. C.; Kwok, R. T. K.; Lam, J. W. Y.; Tang, B. Z. Aggregation-Induced Emission: Together We Shine, United We Soar! *Chem. Rev.* **2015**, *115* (21), 11718−11940.
(10) Luo, J.; Xie, Z.; Lam, J. W. Y.; Cheng, L.; Chen, H.; Qiu, C.; Kwok, H. S.; Zhan, X.; Liu, Y.; Zhu, D.; et al. Aggregation-Induced Emission of 1-Methyl-1,2,3,4,5-Pentaphenylsilole. *Chem. Commun.* **2001**, *18*, 1740−1741.
(11) Li, D.; Yu, J.; Xu, R. Mesoporous Silica Functionalized with an AIE Luminogen for Drug Delivery. *Chem. Commun.* **2011**, *47* (39), 11077−11079.
(12) Qin, W.; Ding, D.; Liu, J.; Yuan, W. Z.; Hu, Y.; Liu, B.; Tang, B. Z. Biocompatible Nanoparticles with Aggregation-Induced Emission Characteristics as Far-Red/Near-Infrared Fluorescent Bioprobes for In Vitro and In Vivo Imaging Applications. *Adv. Funct. Mater.* **2012**, *22* (4), 771−779.
(13) Zhao, N.; Li, M.; Yan, Y.; Lam, J. W. Y.; Zhang, Y. L.; Zhao, Y. S.; Wong, K. S.; Tang, B. Z. A Tetraphenylethene-Substituted Pyridinium Salt with Multiple Functionalities: Synthesis, Stimuli-Responsive Emission, Optical Waveguide and Specific Mitochondrion Imaging. *J. Mater. Chem. C* **2013**, *1* (31), 4640−4646.
(14) Hu, R.; Leung, N. L. C.; Tang, B. Z. AIE Macromolecules: Syntheses, Structures and Functionalities. *Chem. Soc. Rev.* **2014**, *43* (13), 4494−4562.
(15) Wang, Z.; Yan, L.; Zhang, L.; Chen, Y.; Li, H.; Zhang, J.; Zhang, Y.; Li, X.; Xu, B.; Fu, X.; et al. Ultra Bright Red AIE Dots for Cytoplasm and Nuclear Imaging. *Polym. Chem.* **2014**, *5* (24), 7013−7020.
(16) Wang, H.; Liu, G. Advances in Luminescent Materials with Aggregation-Induced Emission (AIE) Properties for Biomedical Applications. *J. Mater. Chem. B* **2018**, *6* (24), 4029−4042.
(17) Feng, G.; Liu, B. Aggregation-Induced Emission (AIE) Dots: Emerging Theranostic Nanolights. *Acc. Chem. Res.* **2018**, *51* (6), 1404−1414.
(18) Guo, L.-X.; Xing, Y.-B.; Wang, M.; Sun, Y.; Zhang, X.-Q.; Lin, B.-P.; Yang, H. Luminescent Liquid Crystals Bearing an Aggregation-Induced Emission Active Tetraphenylthiophene Fluorophore. *J. Mater. Chem. C* **2019**, *7* (16), 4828−4837.
(19) Roy, R.; Sajeev, N. R.; Sharma, V.; Koner, A. L. Aggregation Induced Emission Switching Based Ultrasensitive Ratiometric Detection of Biogenic Diamines Using a Perylenediimide-Based Smart Fluoroprobe. *ACS Appl. Mater. Interfaces* **2019**, *11* (50), 47207−47217.
(20) De, J.; M. M, A. H.; Yadav, R. A. K.; Gupta, S. P.; Bala, I.; Chawla, P.; Kesavan, K. K.; Jou, J.-H.; Pal, S. K. AIE-Active Mechanoluminescent Discotic Liquid Crystals for Applications in OLEDs and Bio-Imaging. *Chem. Commun.* **2020**, *56* (91), 14279−14282.
(21) Han, T.; Gu, X.; Lam, J. W. Y.; Leung, A. C. S.; Kwok, R. T. K.; Han, T.; Tong, B.; Shi, J.; Dong, Y.; Tang, B. Z. Diaminomaleonitrile-Based Schiff Bases: Aggregation-Enhanced Emission, Red Fluorescence, Mechanochromism and Bioimaging Applications. *J. Mater. Chem. C* **2016**, *4* (44), 10430−10434.
(22) Kabe, R.; Notsuka, N.; Yoshida, K.; Adachi, C. Afterglow Organic Light-Emitting Diode. *Adv. Mater.* **2016**, *28* (4), 655−660.
(23) Zhen, X.; Tao, Y.; An, Z.; Chen, P.; Xu, C.; Chen, R.; Huang, W.; Pu, K. Ultralong Phosphorescence of Water-Soluble Organic Nanoparticles for In Vivo Afterglow Imaging. *Adv. Mater.* **2017**, *29* (33), 1606665.
(24) Hayduk, M.; Riebe, S.; Voskuhl, J. Phosphorescence Through Hindered Motion of Pure Organic Emitters. *Chem. - Eur. J.* **2018**, *24* (47), 12221−12230.
(25) Bolton, O.; Lee, K.; Kim, H.-J.; Lin, K. Y.; Kim, J. Activating Efficient Phosphorescence from Purely Organic Materials by Crystal Design. *Nat. Chem.* **2011**, *3* (3), 205−210.
(26) Shi, H.; An, Z.; Li, P.-Z.; Yin, J.; Xing, G.; He, T.; Chen, H.; Wang, J.; Sun, H.; Huang, W.; et al. Enhancing Organic Phosphorescence by Manipulating Heavy-Atom Interaction. *Cryst. Growth Des.* **2016**, *16* (2), 808−813.
(27) Gong, Y.; Chen, G.; Peng, Q.; Yuan, W. Z.; Xie, Y.; Li, S.; Zhang, Y.; Tang, B. Z. Achieving Persistent Room Temperature Phosphorescence and Remarkable Mechanochromism from Pure Organic Luminogens. *Adv. Mater.* **2015**, *27* (40), 6195−6201.
(28) Xue, P.; Sun, J.; Chen, P.; Wang, P.; Yao, B.; Gong, P.; Zhang, Z.; Lu, R. Luminescence Switching of a Persistent Room-Temperature Phosphorescent Pure Organic Molecule in Response to External Stimuli. *Chem. Commun.* **2015**, *51* (52), 10381−10384.
(29) Xu, B.; Wu, H.; Chen, J.; Yang, Z.; Yang, Z.; Wu, Y.-C.; Zhang, Y.; Jin, C.; Lu, P.-Y.; Chi, Z.; et al. White-Light Emission from a Single Heavy Atom-Free Molecule with Room Temperature Phosphorescence, Mechanochromism and Thermochromism. *Chem. Sci.* **2017**, *8* (3), 1909−1914.
(30) Zhao, J.; Wu, W.; Sun, J.; Guo, S. Triplet Photosensitizers: From Molecular Design to Applications. *Chem. Soc. Rev.* **2013**, *42* (12), 5323−5351.
(31) Chang, Z.-F.; Jing, L.-M.; Liu, Y.-Y.; Liu, J.-J.; Ye, Y.-C.; Zhao, Y. S.; Yuan, S.-C.; Wang, J.-L. Constructing Small Molecular AIE Luminophores through a 2,2-(2,2-Diphenylethene-1,1-Diyl)-Dithiophene Core and Peripheral Triphenylamine with Applications in Piezofluorochromism, Optical Waveguides, and Explosive Detection. *J. Mater. Chem. C* **2016**, *4* (36), 8407−8415.
(32) Zhan, Y.; Yang, P.; Li, G.; Zhang, Y.; Bao, Y. Reversible Piezofluorochromism of a Triphenylamine-Based Benzothiazole Derivative with a Strong Fluorescence Response to Volatile Acid Vapors. *New J. Chem.* **2017**, *41* (1), 263−270.
(33) Janiak, C. A Critical Account on $\pi-\pi$ Stacking in Metal Complexes with Aromatic Nitrogen-Containing Ligands. *J. Chem. Soc. Dalt. Trans.* **2000**, *21*, 3885−3896.
(34) Li, C.; Yang, W.; Zhou, W.; Zhang, M.; Xue, R.; Li, M.; Cheng, Z. Branching Effect for Aggregation-Induced Emission in Fluorophores Containing Imine and Triphenylamine Structures. *New J. Chem.* **2016**, *40* (10), 8837−8845.
(35) Samanta, P. K.; Kim, D.; Coropceanu, V.; Brédas, J.-L. Up-Conversion Intersystem Crossing Rates in Organic Emitters for Thermally Activated Delayed Fluorescence: Impact of the Nature of Singlet vs Triplet Excited States. *J. Am. Chem. Soc.* **2017**, *139* (11), 4042−4051.
(36) Sasikumar, D.; John, A. T.; Sunny, J.; Hariharan, M. Access to the Triplet Excited States of Organic Chromophores. *Chem. Soc. Rev.* **2020**, *49* (17), 6122−6140.
(37) Koninti, R. K.; Miyata, K.; Saigo, M.; Onda, K. Achieving Thermally Activated Delayed Fluorescence from Benzophenone by Host−Guest Complexation. *J. Phys. Chem. C* **2021**, *125* (31), 17392−17399.
(38) Isukapalli, S. V. K.; Lekshmi, R. S.; Samanta, P. K.; Vennapusa, S. R. Formation of Excited Triplet States in Naphthalene Diimide and Perylene Diimide Derivatives: A Detailed Theoretical Study. *J. Chem. Phys.* **2020**, *153* (12), 124301.
(39) Zhang, L.; Li, M.; Hu, T.-P.; Wang, Y.-F.; Shen, Y.-F.; Yi, Y.-P.; Lu, H.-Y.; Gao, Q.-Y.; Chen, C.-F. Phthalimide-Based "D−N−A" Emitters with Thermally Activated Delayed Fluorescence and Isomer-Dependent Room-Temperature Phosphorescence Properties. *Chem. Commun.* **2019**, *55* (81), 12172−12175.

https://doi.org/10.1021/acs.jpcb.1c08126
J. Phys. Chem. B XXXX, XXX, XXX−XXX

(40) Xie, Z.; Yang, B.; Li, F.; Cheng, G.; Liu, L.; Yang, G.; Xu, H.; Ye, L.; Hanif, M.; Liu, S.; et al. Cross Dipole Stacking in the Crystal of Distyrylbenzene Derivative: The Approach toward High Solid-State Luminescence Efficiency. *J. Am. Chem. Soc.* **2005**, *127* (41), 14152−14153.
(41) Itoh, Y.; Nakashima, Y.; Tsukamoto, S.; Kurohara, T.; Suzuki, M.; Sakae, Y.; Oda, M.; Okamoto, Y.; Suzuki, T. N+-C-H···O Hydrogen Bonds in Protein-Ligand Complexes. *Sci. Rep.* **2019**, *9* (1), 767.
(42) Wang, T.; Hu, Z.; Nie, X.; Huang, L.; Hui, M.; Sun, X.; Zhang, G. Thermochromic Aggregation-Induced Dual Phosphorescence via Temperature-Dependent Sp3-Linked Donor-Acceptor Electronic Coupling. *Nat. Commun.* **2021**, *12* (1), 1364.
(43) Imoto, H.; Fujii, R.; Naka, K. 3,4-Diaminomaleimide Dyes − Simple Luminophores with Efficient Orange-Red Emission in the Solid State. *Eur. J. Org. Chem.* **2018**, *2018* (6), 837−843.
(44) Dreuw, A.; Plötner, J.; Lorenz, L.; Wachtveitl, J.; Djanhan, J. E.; Brüning, J.; Metz, T.; Bolte, M.; Schmidt, M. U. Molecular Mechanism of the Solid-State Fluorescence Behavior of the Organic Pigment Yellow 101 and Its Derivatives. *Angew. Chem., Int. Ed.* **2005**, *44* (47), 7783−7786.
(45) Tang, S.-X.; Wang, N.; Xu, X.-D.; Feng, S. A Ratiometric Fluorescent Thermometer Based on Amphiphilic Alkynylpyrene Derivatives. *New J. Chem.* **2019**, *43* (17), 6461−6464.
(46) Feng, J.; Tian, K.; Hu, D.; Wang, S.; Li, S.; Zeng, Y.; Li, Y.; Yang, G. A Triarylboron-Based Fluorescent Thermometer: Sensitive Over a Wide Temperature Range. *Angew. Chem., Int. Ed.* **2011**, *50* (35), 8072−8076.
(47) Hariharan, P. S.; Venkataramanan, N. S.; Moon, D.; Anthony, S. P. Self-Reversible Mechanochromism and Thermochromism of a Triphenylamine-Based Molecule: Tunable Fluorescence and Nanofabrication Studies. *J. Phys. Chem. C* **2015**, *119* (17), 9460−9469.
(48) Lu, Q.; Wu, C.-J.; Liu, Z.; Niu, G.; Yu, X. Fluorescent AIE-Active Materials for Two-Photon Bioimaging Applications. *Front. Chem.* **2020**, *8*, 1205.
(49) Bednarska, J.; Zaleśny, R.; Arul Murugan, N.; Bartkowiak, W.; Ågren, H.; Odelius, M. Elucidating the Mechanism of Zn2+ Sensing by a Bipyridine Probe Based on Two-Photon Absorption. *J. Phys. Chem. B* **2016**, *120* (34), 9067−9075.
(50) Şimşek, Y.; Brown, A. Two-Photon Absorption Properties of Gold Fluorescent Protein: A Combined Molecular Dynamics and Quantum Chemistry Study. *J. Phys. Chem. B* **2018**, *122* (22), 5738−5748.
(51) Zheng, Z.; Zhang, T.; Liu, H.; Chen, Y.; Kwok, R. T. K.; Ma, C.; Zhang, P.; Sung, H. H. Y.; Williams, I. D.; Lam, J. W. Y.; et al. Bright Near-Infrared Aggregation-Induced Emission Luminogens with Strong Two-Photon Absorption, Excellent Organelle Specificity, and Efficient Photodynamic Therapy Potential. *ACS Nano* **2018**, *12* (8), 8145−8159.

https://doi.org/10.1021/acs.jpcb.1c08126
J. Phys. Chem. B XXXX, XXX, XXX−XXX

A Journal of the Gesellschaft Deutscher Chemiker

Angewandte International Edition GDCh Chemie

www.angewandte.org

Accepted Article

Title: A Glutathione Activatable Ion Channel Induces Apoptosis in Cancer Cells by Depleting Intracellular Glutathione Levels

Authors: Javid Ahmad Malla, Rintu M. Umesh, Saleem Yousf, Shrunal Mane, Shilpy Sharma, Mayurika Lahiri, and Pinaki Talukdar

This manuscript has been accepted after peer review and appears as an Accepted Article online prior to editing, proofing, and formal publication of the final Version of Record (VoR). This work is currently citable by using the Digital Object Identifier (DOI) given below. The VoR will be published online in Early View as soon as possible and may be different to this Accepted Article as a result of editing. Readers should obtain the VoR from the journal website shown below when it is published to ensure accuracy of information. The authors are responsible for the content of this Accepted Article.

To be cited as: *Angew. Chem. Int. Ed.* 10.1002/anie.202000961
Angew. Chem. 10.1002/ange.202000961

Link to VoR: http://dx.doi.org/10.1002/anie.202000961
http://dx.doi.org/10.1002/ange.202000961

WILEY-VCH

10.1002/anie.202000961

A Glutathione Activatable Ion Channel Induces Apoptosis in Cancer Cells by Depleting Intracellular Glutathione Levels

Javid Ahmad Malla,[a] Rintu M. Umesh,[b] Saleem Yousf,[a] Shrunal Mane,[b] Shilpy Sharma,[c] Mayurika Lahiri,[b] and Pinaki Talukdar*[a]

Abstract: Cancer cells use elevated glutathione (GSH) levels as an inner line of defense to evade apoptosis and develop drug resistance. In this study, we describe a novel 2,4-nitrobenzenesulfonyl (DNS) protected 2-hydroxyisophthalamide system that exploits GSH for its activation into free 2-hydroxyisophthalamide forming supramolecular M^+/Cl^- channels. Better permeation of the DNS protected compound into MCF-7 cells compared to the free 2-hydroxyisophthalamide and GSH-activatable ion transport resulted in higher cytotoxicity, which was associated with increased oxidative stress that further reduced the intracellular GSH levels and altered mitochondrial membrane permeability leading to the induction of the intrinsic apoptosis pathway. The GSH-activatable transport-mediated cell death was further validated in rat insulinoma cells (*INS-1E*); wherein the intracellular GSH levels showed a direct correlation to the resulting cytotoxicity. Lastly, the active compound was found to restrict the growth and proliferation of 3D spheroids of MCF-7 cells with efficiency similar to that of the anticancer drug doxorubicin.

1. Introduction

Apoptosis is a suicide mechanism that is an entirely normal function of eukaryotic cells to eliminate unhealthy cells. In our body, almost one million cells are eliminated (by apoptosis) every second and replaced with new cells (by proliferation) to maintain the cellular homeostasis. While on one hand, an increased rate of apoptosis has been related to neurodegenerative disorders, insulin-dependent diabetes, and hepatitis C infection, etc.; a decreased rate of apoptosis has been known to put one into the risk of developing autoimmune diseases and cancer. Although, cancer cells are under constant genomic instability, oncogenic stress, cellular hypoxia, and oxidative stress – conditions that favor apoptosis,[1] yet cancer cells often avoid these cellular responses by disabling the apoptotic pathways. As an example, oxidative stress has been characterised by the increased production reactive oxygen species (ROS; H_2O_2, O_2^-, OH^-, etc.), which can in turn affect metabolism and induce mitochondrial dysfunction in cells.[2] However, cancer cells possess the ability to combat oxidative stress via enzymatic[3] and nonenzymatic[4] antioxidant mechanisms. Indeed, elevated levels of ROS-scavenging molecules have been reported in these cells. Amongst the different cellular antioxidants, the tripeptide – glutathione (L-γ-glutamyl-L-cysteinyl-glycine, GSH) – is the most abundant intracellular thiol that nonenzymatically detoxifies ROS and helps prevent oxidative stress induced apoptosis in cancer cells.[5] Moreover, elevated levels of GSH in cancer cells (e.g. in breast, colon, lung, etc.) is also linked to development of resistance to several chemotherapeutic drugs.[6] Such a dual model of defense by GSH has caused serious limitations to the use of several anticancer drugs. Therefore, the development of new treatment modalities are warranted that target this GSH mediated internal defence mechanism to induce cytotoxicity in cancer cells.

It is a well-known fact that the cancer cells in tumor tissues have slightly decreased extracellular pH compared to the healthy cells due to the anaerobic glucose metabolism. Therefore, to overcome the limitation of the innocent death of healthy cells and to specifically target cancer cells, recent studies have been done by exploiting the acidic microenvironment of solid tumor tissues.[7] For example, prodigiosin – a secondary metabolite from *Serratia marcescens* – and its analogs work both as a Cl^-/anion antiporter and H^+/Cl^- symporter, and induce cytotoxicity in cancer cells majorly by altering the pH of cellular organelles.[8] This acidic microenvironment also acts as an external defense system for cancer cells wherein acidification of basic anticancer drugs occurs which inhibits their permeation into the cells.[9]

Our group has recently developed a photodynamic therapeutic approach to induce apoptosis in cancer cells by introducing photocleavable-procarrier that can be activated in cancer cells using a specific wavelength of light.[10] However, both these strategies are far from the real demands since light can be used for only surface phenomenon and pH gradient may not be sufficient enough for obtaining remarkable results *in vivo*. Therefore, there exists a great demand to develop new ion transport systems, which can be activated within the cells without the aid of external factors. Considering the higher intracellular GSH levels in cancer cells when compared to the healthy cells, we envisioned that ion transport systems that can be activated by the higher GSH concentrations could take advantage of the internal GSH defense of cancer cells to release ion transporting molecules, which then would induce apoptosis

[a] J A Malla, S. Yousf, Dr. P Talukdar
Department of Chemistry
Indian Institute of Science Education and Research Pune
Dr. Homi Bhabha Road, Pashan, Pune 411008, Maharashtra (India)
E-mail: ptalukdar@iiserpune.ac.in
[b] R. Umesh, S Mane, Dr. M. Lahiri
Department of Biology
Indian Institute of Science Education and Research Pune
Dr. Homi Bhabha Road, Pashan, Pune 411008, Maharashtra (India)
[c] Department of Biotechnology, Savitribai Phule Pune University
(Formerly University of Pune), Pune, Maharashtra 411007, India

Supporting information for this article is given via a link at the end of the document.

Accepted Manuscript

This article is protected by copyright. All rights reserved.

10.1002/anie.202000961

in these cells selectively by perturbing the ion homeostasis. Along these lines, Liu and coworkers have reported selenium containing organic nanoparticles as thiol sensitive ion carriers; however, these studies were confined only to artificial membranes.[11] Manna and coworkers recently reported the GSH mediated chloride transport by small ionophores; however, their system did not show significant cytotoxicity in Hela cells.[12]

In 2007, Li and coworkers reported a chloride channel based on the isophthalamide core by connecting it to two α-aminoxy acid units.[13] We hypothesized that the introduction of a bulky group at the C-2 position of the isophthalamide would not allow efficient self-assembly of the monomers thereby restricting the ion channel formation; and the selection of a thiol cleavable bulky group would allow its removal at high GSH concentrations. Thus, we introduced a hydroxyl group at the C-2 position of isophthalamide moiety, as the group is amenable to its linking to thiol cleavable groups (Figure 1A). The 2,4-dinitrobenzene sulfonyl (DNS) group was selected as thiol cleavable group,[14] as its cleavage is known to generate GS-2,4-dinitrobenzene conjugate (SG-DNB) and SO_2 as by products. Although, low levels of SO_2 may be harmless or even beneficial to cells; exposure to high doses of SO_2 has been known to generate high levels of ROS and thereby induce apoptosis.[15] Moreover, ROS production and apoptosis inducing activity of synthetic ion

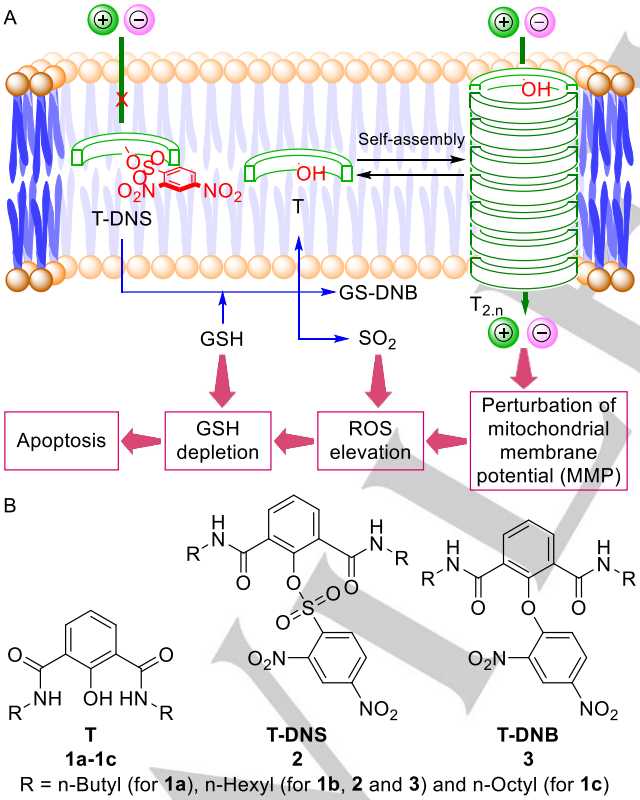


Figure 1. Schematic representation of channel activation inside cell by intracellular GSH, and supramolecular $\mathbf{T_{2.n}}$ channel formation from monomer **T** in cell membrane (A). Different processes involved in the depletion of intracellular GSH and induction of apoptosis have been depicted. The structures of the active transporters **1a–1c**, 2,4-dinitrosulfonyl protected protransporter **2**, and 2,4-dinitrophenyl protected protransporter **3** have been shown (B). The description of R groups in **1**, **2** and **3** is also provided.

channels is already discussed above. Therefore, the levels of GSH would be affected not only during the release of the ion channel-forming molecule, but would also be reduced significantly due to the ROS generated. Alkyl groups such as n-butyl, n-hexyl, and n-octyl were attached at each end of the 2-hydroxyisophthalamide moiety to design **1a-1c** so that the ion transport efficiency can be optimized, and a DNS-protected compound **2** was designed as the protransporter (Figure 1B). A 2,4-dinitrobenzene (DNB) protected compound **3** was also designed as the DNB group is known to be inert to GSH and only gets activated by the higher content of hydrogen sulfide (Figure 1B).[16] Thus, compound **3** is expected to act as a negative control for all our studies. Our results show that the compound **2** gets activated by intracellular GSH to form self-assembled ion channels in the lipid membranes, destroys the mitochondrial membrane potential (MMP), elevates the ROS levels in cells that further depletes the intracellular GSH levels, and finally induces apoptosis.

2. Results and Discussion

2.1. Synthesis:

The compounds **1a–1c** were synthesized from 2-methoxybenzene-1,3-dicarboxylic acid **6** by converting it to the acid chloride using oxalyl chloride,[17] which was then coupled with the respective amines to get the di-carboxyamides **7a−7c** (Scheme 1).[18] These products were subjected to O-deprotection using 1 M BBr_3 in dichloromethane to get the final compounds **1a−1c**, each containing a free hydroxyl group.[19] The DNS-protected compound **2** and DNB-protected compound **3** were synthesized by reacting compound **1b** with 2,4-dinitrobenzenesulfonyl chloride[14] and 2,4-dinitrochlorobenzene,[16] respectively. All compounds were purified by column chromatography, and the structures were confirmed by ^{1}H NMR, ^{13}C NMR, and HRMS data (see ESI).

1.1. Ion transport studies:

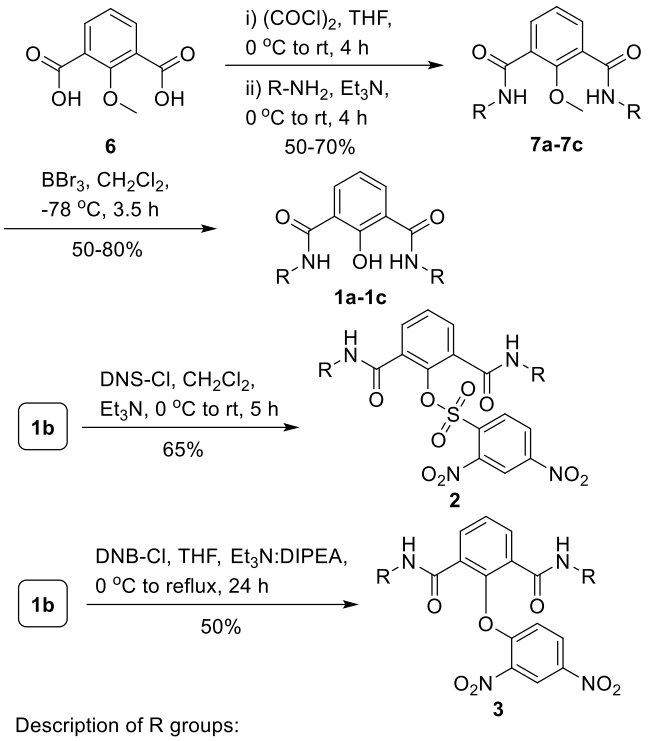
Ion transport activity:

Ion transport activities of compounds **1a−1c**, **2**, and **3** were evaluated across large unilamellar vesicles consisting of egg yolk phosphatidylcholine (EYPC−LUVs⊃HPTS) by 8-hydroxypyrene-1,3,6-trisulfonate (HPTS) based fluorometric methods.[20] The EYPC vesicles, entrapping the pH-sensitive HPTS dye (pK_a = 7.2), were prepared with internal and external pH = 7.0, and a pH gradient was then applied by addition of NaOH (i.e., ΔpH = 0.8) in the extravesicular buffer.[21] The collapse of the pH gradient upon the addition of **1a−1c**, **2** and **3** was monitored by the change in the dye fluorescence intensity at λ_{em} = 510 nm (λ_{ex} = 450 nm) (see ESI for details). The comparison of activities provided the activity sequence: **1a** < **1c** < **1b**, inferring that the compound **1b** works as the most efficient ion transporter (Figure 2A). This result corroborates to the calculated logP = 5.54 (Table S1, ESI) of the compound, which has been reported to be optimum for efficient permeation of the molecules across biological membranes.[22] The DNS-protected compound **2** and DNB-protected compound **3** were almost inactive at identical concentrations (Figure 2A). The addition of GSH to **2** was associated with an efficient transmembrane ion transport, similar to that observed for **1b**, thereby confirming the

Accepted Manuscript

This article is protected by copyright. All rights reserved.

10.1002/anie.202000961



Scheme 1. General scheme for the synthesis of **1a**–**1c**, **2**, and **3**.

thiol-mediated activation of ion transport process (Figure 2A).[23] The addition of GSH to **3**, on the other hand, did not show any significant increase in the ion transport rate (Figure 2A). These results confirmed the importance of SO_2 group in thiol-mediated cleavage of the DNS protecting group (Figure 2B). The dose-dependent activity data of compound **1b** (Figure 2C), upon Hill analysis, provided the effective concentration at 50% activity, EC_{50} = 6.54 μM and Hill coefficient, n = 2.2 (Figure S12). The determined Hill coefficient (EC_{50}) value corroborates to the supramolecular dimer **T_2** formed by monomers of **1b** as the active rosette structure for the for the supramolecular nanochannel assembly.

Ion selectivity studies:

The appreciable ion transport activity observed for compound **1b** led us to investigate the ion selectivity of the compound. Initially, the ion transport activity across EYPC-LUVs⊃HPTS was measured with intravesicular NaCl and an isoosmolar extravesicular M^+/Cl^- salt (where, M^+ = Li^+, Na^+, K^+, Rb^+, and Cs^+) were used to investigate the possible selectivity among the different cations.[24] The data provided the selectivity sequence as $K^+ > Rb^+ > Cs^+ > Na^+ \approx Li^+$ when the collapse of the applied pH gradient was monitored (Figure 2D). These results indicated the participation of these metal cations in the ion transport process.

To determine the role of anions in the transport process, the anion selectivity study was performed by varying the intravesicular as well as the extravesicular anions of NaX salt (X^- = Cl^-, Br^-, I^-, NO_3^-, and ClO_4^-),[25] and the collapse of rates of the applied pH gradient was compared in the presence of **1b**. The results from this experiment provided the selectivity sequence as $Cl^- > ClO_4^- > Br^- > I^- > NO_3^-$ that confirmed the highest selectivity was present for Cl^- (Figure 2E). Overall, these studies suggested the major involvement of alkali metal cations and inorganic anions in the transport process

Chloride leakage studies: To further confirm the Cl^- ion transport activity of **1b**, the EYPC-LUVs were prepared by entrapping lucigenin dye (i.e. EYPC-LUVs⊃lucigenin) and $NaNO_3$ salt, and a Cl^-/NO_3^- gradient was applied by adding NaCl (2 M) in the extravesicular buffer. The influx of the Cl^- was measured by monitoring the fluorescence intensity of intravesicular dye at λ_{em} = 535 nm (λ_{ex} = 450 nm).[26] A dose-dependent quenching of lucigenin fluorescence was observed upon addition of the compound **1b** (Figure S17A). These data indicated that the supramolecular channel formed by the compound **1b** can allow the influx of Cl^- across liposomes.

To get further support for the cotransport mechanism, valinomycin (a known K^+ transporter)[27] was coupled with **1b** and the ion transport rate was monitored. KCl was added to the extravesicular buffer to create the Cl^-/NO_3^- gradient. Then valinomycin was added along with **1b** to monitor their cooperative effect.[10] The ion transport rate in the absence and presence were comparable (Figure 2F) that suggests the lack of cooperative transport by valinomycin and **1b**. In addition to this, the effect of different cations on the chloride efflux was also checked by varying the external cations,[28] which also supported KCl cotransport mechanism (Figure S17C). To reassure that the M^+/Cl^- symport mechanism is operating in the transport process, the EYPC liposomes, entrapping NaCl (200 mM) and 1.0 mM of lucigenin dye, were prepared. Then, the isoosmolar Na_2SO_4 was added to the extravesicular solution and Cl^- efflux was monitored with time. A similar experiment was also performed with extravesicular isoosmolar $NaNO_3$. The results indicate that there is no difference in the transport rate of two ions by **1b** (Figure 2G), suggesting that the symport mechanism of ion transport is operative.

1.2. Evidence of channel mechanism:

The formation of the transmembrane ion channels by the compound **1b** was proved by planar bilayer conductance measurements, where the ionic conductance across the planar lipid bilayer membrane was measured.[29] In this typical experiment, planar lipid bilayer membrane composed of diphytanoyl phosphatidylcholine (diPhyPC) lipid was used to insulate the two chambers (*cis* and *trans* chambers) containing KCl solution (1.0 M). The addition of **1b** (10.0 μM) to the system showed up distinct channel openings and closing at different holding potentials, confirming the formation of ion channels (Figure 3A, B). The single-channel conductance was found to be 160 ± 2 pS, and channel diameter was calculated to be 6.6 ± 0.16 Å. The variation of current with voltage (*I-V* plot) in the presence of the symmetric solution of KCl (1.0 M each) showed a linear variation, i.e., ohmic behavior (Figure 3C), which is expected for the non-dipolar nature of the channel. When the ion selectivity of the channel was checked using unsymmetric

Accepted Manuscript

This article is protected by copyright. All rights reserved.

10.1002/anie.202000961

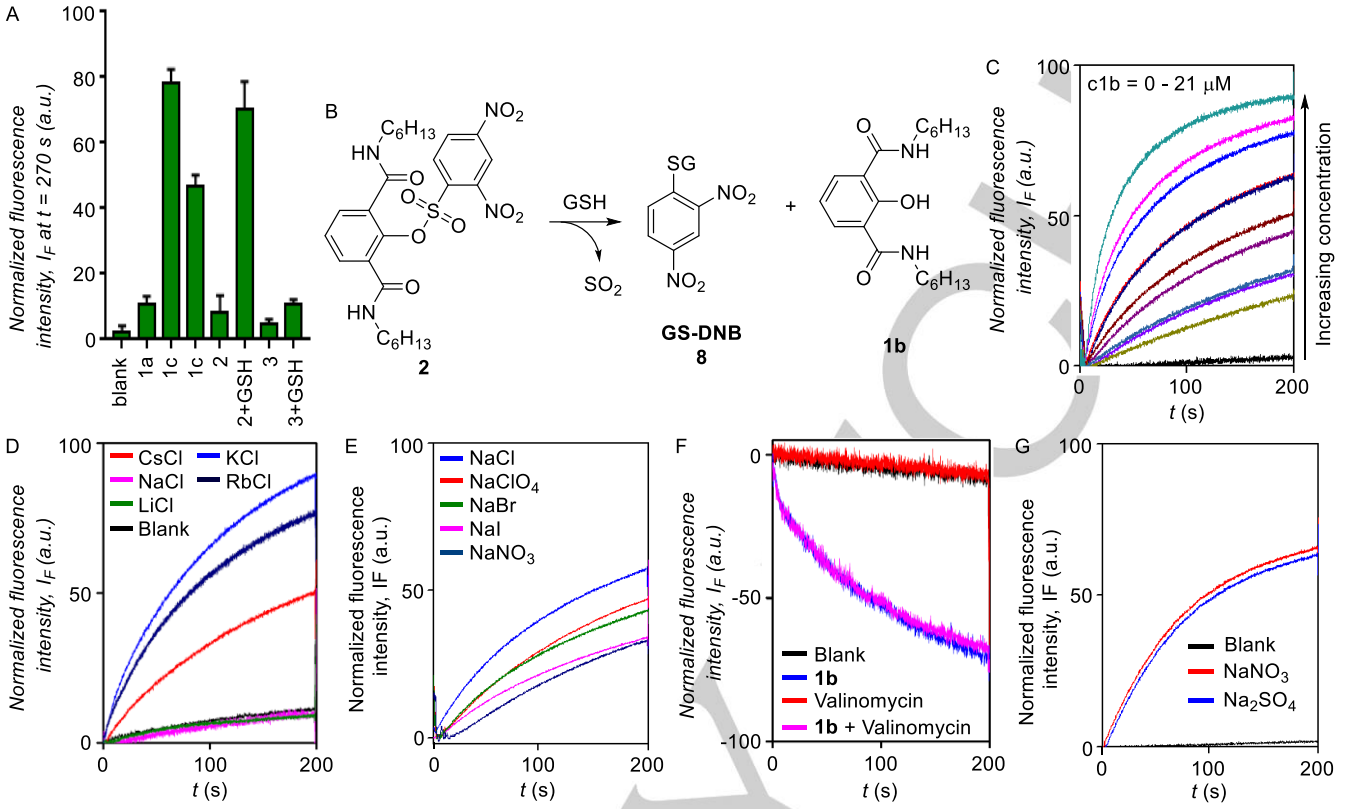


Figure 2. Comparative ion transport activities of **1a–1c**, **2** and **3** and GSH activation of **2** and **3** (A) (normalized fluorescence at 170 s after the sample addition); GSH mediated cleavage of the DNS group from **2** to release **1b**, SO_2 and **8** (B); dose-dependent transport activity of **1b** (C); cation selectivity of **1b** (0.3 μM) (D) and anion selectivity of **1b** (7.0 μM) (E); comparison of Cl^- influx across EYPC-LUVs⊃lucigenin for **1b** (10 μM) in presence and absence of valinomycin (0.125 μM) (F) and Cl^- efflux across EYPC-LUVs⊃lucigenin by **1b** (12 μM) in the presence of intravesicular Cl^- and either SO_4^{2-} or NO_3^- as isoosmolar extravesicular anion (G).

solutions of KCl in two compartments (i.e., 0.5 M in *trans* and 1.0 M KCl in *cis*), it was observed that the rate of Cl^- transport is higher than the rate of K^+ transport with a permeability ratio P_{Cl}–/P_{K}+ = 50 ± 1 (Figure 3C).

1.3. Molecular modeling of the ion channel:

From the literature reports it is evidenced that in 2-hydroxy-N^1,N^3-dialkylylisophthalamide the phenolic oxygen forms hydrogen bond with one of the amide hydrogens (C–O···H–N) and phenolic hydrogen forms hydrogen bond with one of the amide oxygens (C=O···H–O) thereby prefer the **Conf-1** (Figure S19A).[30] Hence, this conformation of **1b** was considered for generating the ion channel model. At first, two molecules of **1b** in the **Conf-1** were placed face-to-face to form a dimeric rosette and then seven units of such rosettes were placed in a coaxial manner to generate the channel. Subsequently, the channel was optimized using MOPAC2012[31] software with the PM6-DH+[32] method. In the optimized supramolecular nanotubular assembly, intramolecular C–O···H–N and C=O···H–O interactions were still evident (Figure S19B, C). Moreover, the intermolecular C–O···H–N interactions and π-π stacking interactions among aromatic rings were observed, giving stability to the assembly. In the geometry-optimized channel, eleven water molecules were placed in the lumen, along with one K^+ ion above and one Cl^- ion below sixth water molecule. The whole system was then optimized using the method stated above. In the optimized structure (Figure 3D, Figure S19D), the water molecules formed a continuous array through intermolecular H–O···H–O interactions. In the channel lumen, the K^+ ion showed electrostatic interaction with the Cl^- ion and dipole-cation interaction with the carbonyl oxygen (Figure S19E). The anion was further involved in O–H···Cl^- interactions two neighboring water molecules.

1.4. UV-visible and fluorescence spectral studies:

The UV-visible spectrum of **1b** (10.0 μM) was recorded in Dulbecco's Phosphate-Buffered Saline (DPBS) buffer (pH 7.2), which showed an absorption band at 300 − 375 nm with the λ_{max} at 335 nm (Figure S20A). When the compounds **1b**, **2** and **3** (10.0 μM each) were excited with 335 nm light, an intense fluorescence emission band centered at 410 nm was observed for **1b**, whereas **2** and **3** were nonfluorescent due to quenching of fluorescence by DNS[33] and DNB groups[16] (Figure S20B). Further, the release of compound **1b** from **2** (10.0 μM) was monitored in the presence of GSH (5 molar equivalents) by measuring the fluorescence intensity at λ = 410 nm (λ_{ex} = 330 nm) with time (80 s). The increase in fluorescence in the presence upon addition of the thiol undoubtedly demonstrated

Accepted Manuscript

This article is protected by copyright. All rights reserved.

10.1002/anie.202000961

the release of **1b** (Figure S20C). Similar study with **3** did not show any time-dependent increase of fluorescence.[34]

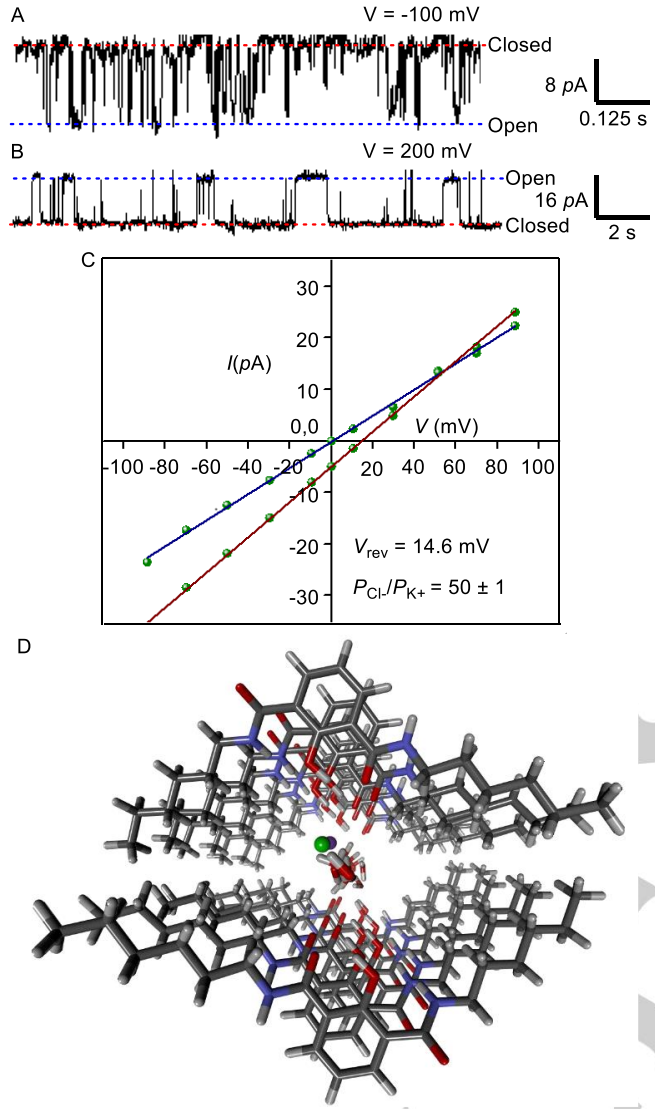


Figure 3. Single-channel conductance of **1b** (10.0 μM) recorded at -100 mV (A) and at 100 mV (B) under symmetrical KCl solutions; *I-V* plots of **1b** under symmetrical and unsymmetrical concentrations of KCl (C); top view of the geometry optimized structure of formed by the barrel-rosette assembly of **1b** with eleven H_2O, one K^+ and one Cl^- (D).

1.1. Cellular viability studies:

The viability of MCF-7 cells was monitored using the MTT assay after incubating these cells with **1b**, **2** and **3** (0 – 100 μM each) for 24 hours. The addition of compound 2 was associated with highest cytotoxicity with IC_{50} value around 0.5 – 1.0 μM (Figure 4A; blue) when compared to those treated with **3** (red). On the other hand, the IC_{50} obtained for compound **1b** was ~ 50 μM and was found to be relatively less toxic when compared to compound **2** (Figure 4A, green). Indeed, a much higher permeation of propidium iodide, a dye known to easily cross the compromised cell membranes to bind with nuclear constituents,[35] was observed in MCF-7 cells treated with compound **2** (1.0 μM) for 24 h (Figure 4B, C, and Figure S21).

Next, to understand the reason for the differences in the cytotoxicity, live cell imaging of MCF-7 cells was performed to study the membrane permeability and cytoplasmic abundance of the compounds under study. Briefly, MCF-7 cells were incubated with the compounds for 30 minutes and observed under a confocal microscope (Leica Sp8). Interestingly, a marked enhancement in blue fluorescence was observed in MCF-7 cells treated cells treated with **2** (Figure 4F) when compared to **1b** (Figure 4E) or the untreated/control cells (Figure 4D). Based on these observations, we propose that the proactive channel molecule **2** is more permeable compared to active channel **1b**.[10] These results are supported by the fact that compound **2** contains a sulfonyl group – known to have a better membrane permeability. These results can be rationalized based on the reactivity of **2** with GSH. Since MCF-7 cells have elevated GSH content,[36] the DNS group upon entering the cells reacts with GSH; hence, compound **2** gets cleaved to subsequently release **1b** (measured by blue fluorescence intensity quantitation as depicted in Figure 4G), thereby leading to increased cytotoxicity. On the other hand, the DNB group responds poorly to GSH;[16] hence, its cleavage is poor and it is associated with less cell death.

As can be seen from Figure 2B, the observed cytotoxicity for compound **2** can also be due to the by-products SO_2 and **8**. In order to exclude this, the cytotoxicity of MCF-7 cells was evaluated in the presence of compounds **9** (Figure S23), which upon reaction with thiol, releases benzylamine, **8** and SO_2 within 30 minutes;[37] and compound **10** (Figure S23), which in the presence of intracellular esterases, is known to release SO_2 and other non-toxic bi-products.[38] Both compounds **9** (green) and **10** (blue) showed significantly lesser cytotoxicity when compared to **2** (purple) at identical concentrations, thereby, indicating that the observed cytotoxicity is mainly associated with compound **1b** formed from **2** (Figure 4H).

To further investigate the importance of intracellular GSH in activating compound **1b**, viability assays were performed in the rat insulinoma cells – *INS-1E*.[39] A recent report has shown that the GSH-content in these cells can be modulated by varying the glucose concentration in the media without significantly affecting the cellular viability.[40] The cytotoxicity mediated by compound **2** (0 – 20.0 μM) was significantly higher in *INS-1E* cells cultured in low glucose media (i.e., high GSH levels) when compared to those in high glucose media (i.e., low GSH levels) (Figure 4I, J). As we had hypothesized, compound **3** (0 – 20.0 μM) did not induce considerable cytotoxicity in both low and high GSH containing cells, thereby proving that the release of **1b** does not take place from **3**.

1.2. Cytotoxicity is enhanced by ion transport:

Reports from our lab[41] and others[42] have shown that the perturbation of Cl^- ion homeostasis by means of synthetic channels and carriers mediate apoptosis in cells. Therefore, to gain insight about Cl^- mediated cytotoxicity, viability in MCF-7 cells was performed with compound **2** (0 – 20.0 μM) in the

Accepted Manuscript

This article is protected by copyright. All rights reserved.

10.1002/anie.202000961

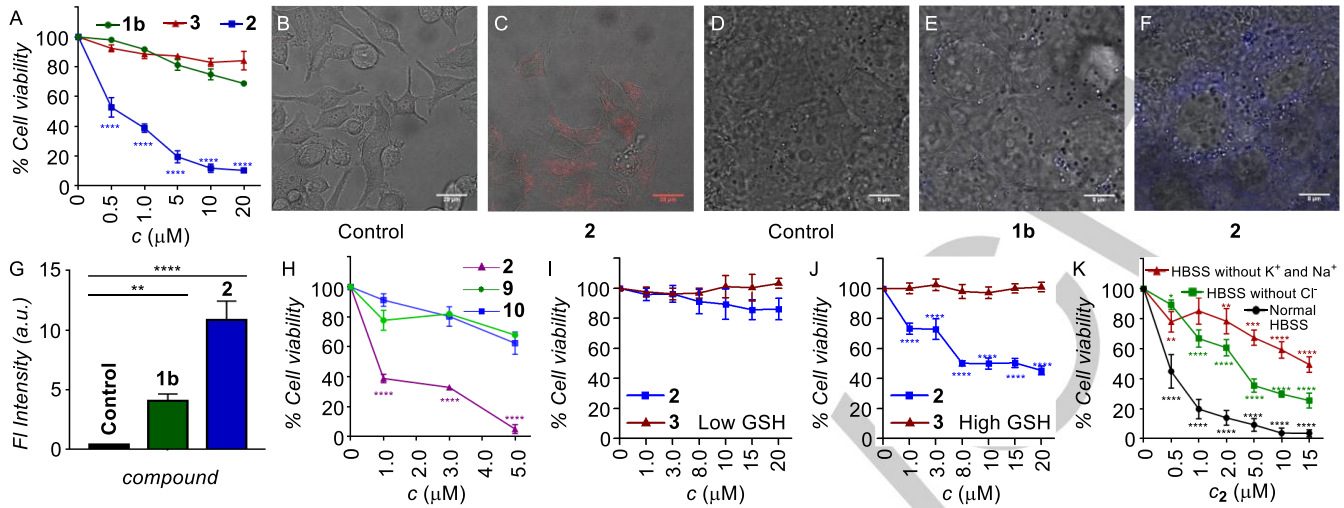


Figure 4. Dose-dependent cell viability of MCF-7 cells incubated with **1b**, **2** and **3** (0 – 20 μM each) for 24 hours (A). Live cell images of MCF-7 cells upon treating with 0 μM (B) and 1.0 μM of compound **2** (C) for 15 minutes followed by staining with propidium iodide. Live cell imaging of control (D), **1b** (5 μM, E) and **2** (5 μM, F) in MCF-7 cell line after 30 minutes of incubation; quantification of fluorescence inside the cells (G). Dose-dependent cell viability of MCF-7 cells incubated with **2**, **9** and **10** (0 – 5.0 μM each) for 24 hours (H). Dose-dependent cell viability of *INS-1E* cells in incubated with **2** and **3** (0 – 20.0 μM each) for 24 hours under low (I) and high GSH (J) concentrations. Cell viability of MCF-7 cells in presence and absence of Na^+ and K^+ and Cl^- ions incubated with **2** at different concentrations (K). * represents $p < 0.05$, **, $p < 0.01$ and *** for $p < 0.001$ using Tukey HSD tests.

presence of HBSS (Hanks balanced salt solution) buffer with and without Cl^- ions.[43] Interestingly, cells cultured in HBSS with Cl^- showed enhanced cytotoxicity (Figure 4K; Black) compared to HBSS without Cl^- (Figure 4K; Green) thereby demonstrating that cell death is mediated via Cl^- transport. In addition to Cl^- the import of cations such as K^+ and Na^+ also triggers the apoptosis process. We have already shown above that compound **1b** is a symporter of M^+/Cl^- across the lipid bilayer (Figure 2D, E). Therefore, the effect of M^+ ions (K^+ and Na^+) on cellular viability was assessed. Briefly, MCF-7 cells were incubated with compound **2** (0 – 20.0 μM) in HBSS buffer with and without M^+ ions. A higher cytotoxicity was observed with compound **2** in presence of K^+ and Na^+ ions (Figure 4K, brown), thereby confirming the K^+ and Na^+ ions also play a role in mediating cytotoxicity.

1.3. Chloride channel formation and GSH depletion triggers apoptosis in cancer cells:

Apoptosis involves the disruption of mitochondrial membrane potential (MMP),[44] which subsequently results in the release of cytochrome c from the mitochondrial membrane into the cytoplasm – one of the switches that trigger apoptosis.[45] The change in MMP was investigated using MMP sensitive JC-1 dye,[46] which shows red fluorescence emission due to the formation of J-aggregates in the healthy mitochondrial membranes. However, the depolarization of MMP leads to dispersion of the formed aggregates, resulting in green fluorescence emission.[47] Interestingly, MCF-7 cells treated with compound **2** (1.0 μM) for 24 hours showed a significant decrease in the red fluorescence and a simultaneous enhancement in the green emission (Figure 5B) when compared to the control cells (Figure 5A). The quantification of the red/green ratio (Figure 5C) in treated cells compared to the control confirmed the enhancement in the MMP depolarization.[41a, 44b] This was associated with increased generation of both mitochondrial (Figure 5D, green) and cellular ROS (Figure 5D, brown, S25,) as detected by the Mitosox[40] and 2',7'dichlorodihydrofluorescein diacetate (H_2DCFDA)[44b, 48] dyes, respectively.

It is well-documented in the literature that abnormally high ROS levels lead to the increased apoptosis in cancer cells by reducing the GSH levels.[49] We had hypothesized that compound **2** works as a double-edged sword to reduce the intracellular GSH levels by (i) getting activated into **1b** by reacting with GSH (Figure 2B), and (ii) increasing the ROS levels as a consequence of perturbation in ion homeostasis.[41, 43, 50] Indeed, the GSH levels (as measured by ^{1}H NMR) in MCF-7 cells treated with compound **2** (green) were significantly reduced when compared with the control cells (Figure 5E; red), thereby proving our hypothesis.

The enhancement in levels of ROS is well known to open up the mitochondrial permeability transition pores (PTP),[51] which releases the cytochrome c from the mitochondrial membrane into the cytosol.[52] Indeed, MCF-7 cells incubated with 1.0 μM (Figure 5G) of compound **2** showed significantly enhanced fluorescence intensity depicting the release of cytochrome c release into the cytoplasm when compared to the control cells (Figure 5F). Since, the released cytochrome c binds to the Apaf-1 to form the cytochrome c/Apaf-1 apoptosome complex and switches on the apoptotic pathway by caspase 9 activation. Indeed, immunoblot analysis performed to evaluate the expression of caspase 9 in MCF-7 cells incubated with compound **2** (1.0 μM) showed a statistically significant increase

Accepted Manuscript

This article is protected by copyright. All rights reserved.

10.1002/anie.202000961

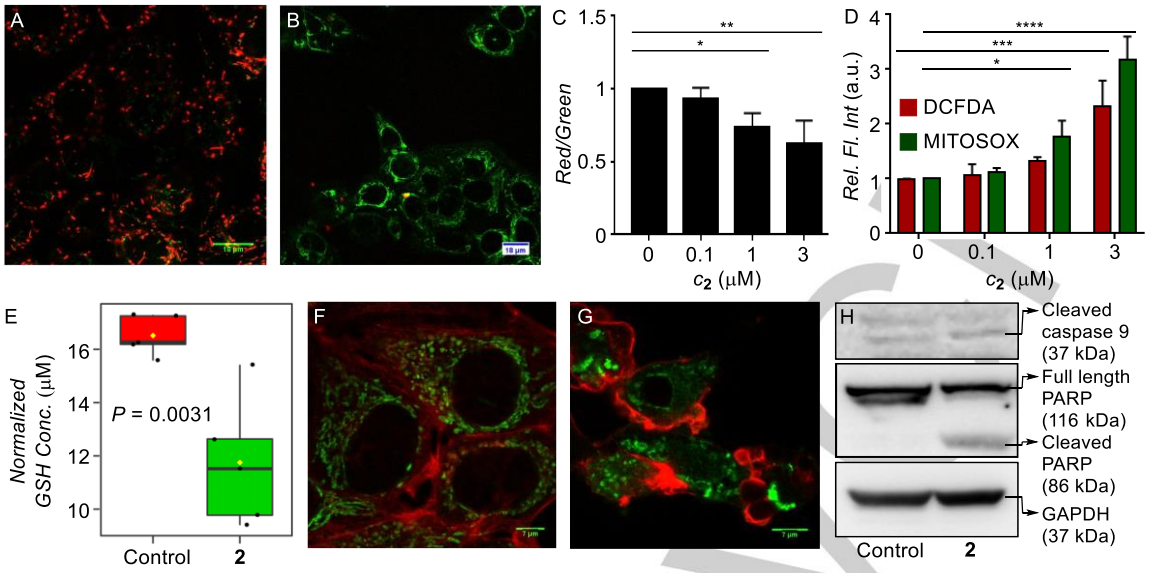


Figure 5. Live cell images of MCF-7 cells upon treating with 0 μM (A) and 1.0 μM (B) of compound **2** for 24 h followed by staining with JC-1 dye, red and green channel images were merged to generate the given image (Scale bar = 18 μm). Quantification of change in the red/green ratio with concentration of **2** in MCF-7 cells incubated with **2** (C); quantification of dose-dependent mitochondrial and cellular ROS generation in MCF-7 cells incubated with **2** by Mitosox dye and H_2DCFDA dye (D). Quantification of glutathione levels in untreated MCF cells and those treated with compound **2** (1 μM) by ^{1}H NMR (E). Release of cytochrome c from MCF-7 cells upon treating with 0 μM (F) and 1.0 μM (G) of compound **2**. Immunostaining was performed with cytochrome c specific primary antibody (green). Phalloidin (red) co-staining was used to mark the boundaries; expression of cleaved caspase 9, full length and cleaved PARP-1 in MCF-7 cells, after 24 h incubation with **2** (0 and 1.0 μM) determined by immunoblot analysis (H). * represents $p < 0.05$, **, $p < 0.01$ and *** for $p < 0.001$ using Tukey HSD tests.

in the expression of cleaved caspase 9 when compared to the control cells (Figure 5H and Figure S28).

As a prominent evidence of the apoptotic pathway, the expression level of cleaved poly (ADP-ribose) polymerase facilitate apoptosis. Cleavage of full-length PARP-1 (116 kDa) to generate cleaved PARP-1 (86 kDa) was observed upon incubation of MCF-7 cells with **2** (1.0 μM) (Figure 5H). These data clearly indicate that the mitochondrial/intrinsic apoptosis pathway is being activated in MCF-7 cells upon treated with compound **2**.

1.4. Compound 2 inhibits the growth and proliferation of 3D spheroids:

Previous literature shows that Doxorubicin (DOX) works as a potent inhibitor of MCF-7 cells when grown in 2D and 3D culture models.[53] It has been demonstrated that DOX at concentrations between 0.8-1.0 μM significantly affects the proliferation of the cells. After gaining insights into the mechanism of action of compound **2** in 2D cultures, we further tested if it could inhibit 3D cultures of MCF-7 cells. A seven-day protocol was developed wherein the drugs (DOX or compound **2**) were administered to the developing 3D cultures on days 4, 5 and 6 (Figure 6A). Immunofluorescence staining done using Phalloidin and Hoechst 33258 clearly indicates that the compound **2** (Figure 6B) significantly reduces the surface area (Figure 6C), surface volume (Figure 6E) and the number of cells per spheroid (Figure 6D) when compared to the control. Interestingly the results were similar to those obtained using DOX, thereby, indicating the potential of compound **2** to inhibit tumor growth *in vivo.*

2. Conclusion

We have developed a novel glutathione-activatable synthetic ion channel system that plays a role in mediating caspase-dependent apoptosis in MCF-7 cells. The intracellular glutathione releases the channel-forming N^1,N^3-dihexyl-2-hydroxyisophthalamide system **1b** from its 2,4-nitrobenzenesulfonyl (DNS) protected protransporter **2**, which forms transmembrane ion channels capable of conducting M^+/Cl^- symport across biological membranes. This symport is associated with increased ROS levels which in turn reduced intracellular GSH levels; altered mitochondrial membrane permeability (MMP); mediated cytochrome c release associated with activation of caspase 9 and PARP cleavage – the major inducers of apoptosis. These results were further confirmed using a 3D model of MCF-7 cells wherein the addition of compound **2** was able to restrict growth and proliferation of the spheroids, similar to those reported for DOX – a standard drug used for breast cancer treatment. These studies will provide attractive approaches to explore the application of synthetic ion transport systems for therapeutic approaches.

Accepted Manuscript

This article is protected by copyright. All rights reserved.

10.1002/anie.202000961

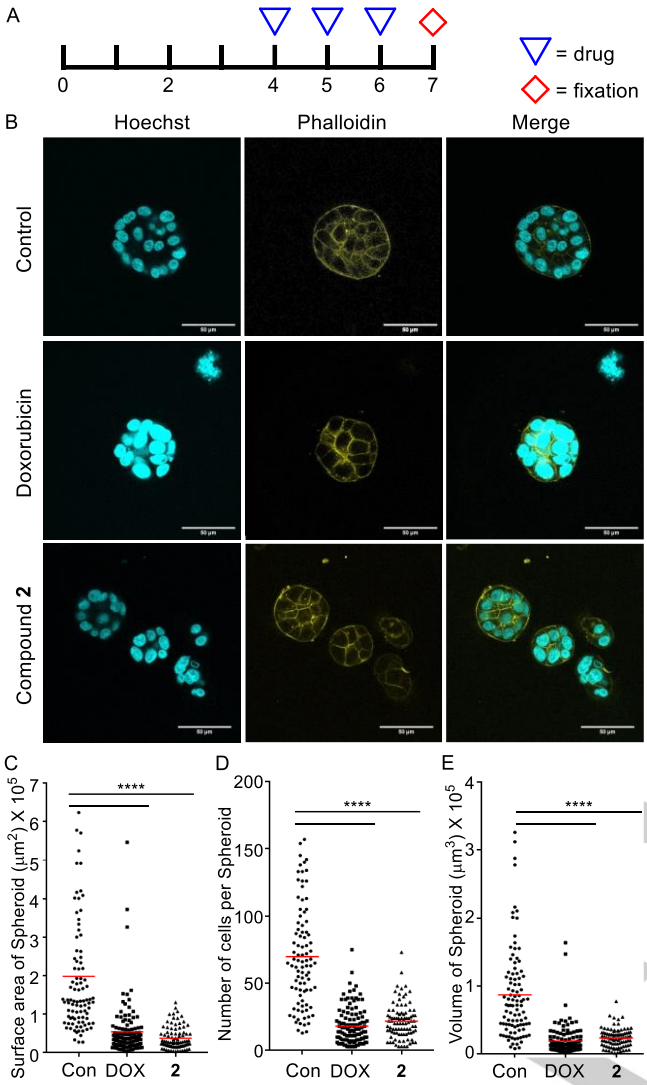


Figure 6. Representation of the protocol for induction of 3D cultures in MCF-7 cells. The drug intervention was done on days 4, 5, and 6, using compound **2** (2 μM) and doxorubicin (positive control, 0.8 μM). DMSO was used in control wells (A). Immunofluorescence for 3D cultures using Phalloidin (stains actin filaments) and Hoechst 33258 (B). Quantitation of surface area (μm^2) (C); number of cells per spheroid (D); and spheroid volume (μm^3) (E) under different experimental conditions were performed using Image J software. Con = control and DOX = doxorubicin. * Represents $p < 0.05$, **, $p < 0.01$ and **** for $p < 0.001$ using Tukey HSD tests.

Experimental Section

Experimental details are available in the electronic supporting information.

Acknowledgements

This work was supported by SERB, Govt. of India (EMR/2016/001897 to P.T.; EMR/2016/001974 to M.L.), Department of Biotechnology (DBT), Govt. of India (BT/HRD/NBA/36/06/2018 to P.T.) and University Grants Commission (UGC-FRP), Govt. of India (F.4-5(18-FRP)(IV-Cycle)/2017(BSR) to S.S.). We thank Prof. Claes Wollheim and Prof. Pierre Maechler, University Medical Centre, Geneva, Switzerland for providing *INS-1E* cells. This research used resources of IISER Pune NMR, microscopy and Perkin Elmer (Ensight multimode plate reader) facilities. We thank Dr. H. Chakrapani from IISER Pune for the kind gift of compounds **9** and **10**.

Keywords: Ion channel • Co-transport • Glutathione Depletion • Reactive oxygen species • Apoptosis

REFERENCES

[1] K. Fernald, M. Kurokawa, *Trends Cell Biol.* **2013**, *23*, 620 – 633.

[2] a) R. Olinski, T. Zastawny, J. Budzbon, J. Skokowski, W. Zegarski, M. Dizdaroglu, *FEBS Lett.* **1992**, *309*, 193 – 198; b) B. N. Ames, M. K. Shigenaga, T. M. Hagen, *Proc. Natl. Acad. Sci. U.S.A.* **1993**, *90*, 7915 – 7922.

[3] a) H. Sies, *Eur. J. Biochem.* **1993**, *215*, 213 – 219; b) O. M. Ighodaro, O. A. Akinloye, *Alexandria Med. J.* **2018**, *54*, 287 – 293.

[4] S. Toyokuni, K. Okamoto, J. Yodoi, H. Hiai, *FEBS Lett.* **1995**, *358*, 1 – 3.

[5] R. Quintana-Cabrera, S. Fernandez-Fernandez, V. Bobo-Jimenez, J. Escobar, J. Sastre, A. Almeida, J. P. Bolaños, *Nat. Commun.* **2012**, *3*, 718.

[6] a) G. Wu, Y. Z. Fang, S. Yang, J. R. Lupton, N. D. Turner, *J. Nutr.* **2004**, *134*, 489 – 492; b) N. Traverso, R. Ricciarelli, M. Nitti, B. Marengo, A. L. Furfaro, M. A. Pronzato, U. M. Marinari, C. Domenicotti, *Oxid. Med. Cell Longev.* **2013**, *2013*, 10.

[7] I. F. Tannock, D. Rotin, *Cancer Res.* **1989**, *49*, 4373 – 4384.

[8] a) W. Van Rossom, D. J. Asby, A. Tavassoli, P. A. Gale, *Org. Biomol. Chem.* **2016**, *14*, 2645 – 2650; b) S. Ohkuma, T. Sato, M. Okamoto, H. Matsukya, K. Arai, T. Kataoka, K. Nagai, H. H. Wasserman, *Biochem. J.* **1998**, *334*, 731 – 741; c) J. T. Davis, in *Anion Recognition in Supramolecular Chemistry* (Eds.: P. A. Gale, W. Dehaen), Springer Berlin Heidelberg, Berlin, Heidelberg, **2010**, pp. 145 – 176.

[9] J. W. Wojtkowiak, D. Verduzco, K. J. Schramm, R. J. Gillies, *Mol. Pharm.* **2011**, *8*, 2032 – 2038.

[10] S. B. Salunke, J. A. Malla, P. Talukdar, *Angew. Chem. Int. Ed.* **2019**, *58*, 5354 – 5358, *Angew. Chem.* **2019**, *131*, 5408 – 5412.

[11] C. Lang, X. Zhang, Z. Dong, Q. Luo, S. Qiao, Z. Huang, X. Fan, J. Xu, J. Liu, *Nanoscale* **2016**, *8*, 2960 – 2966.

[12] N. Akhtar, N. Pradhan, A. Saha, V. Kumar, O. Biswas, S. Dey, M. Shah, S. Kumar, D. Manna, *Chem. Commun.* **2019**, *55*, 8482 – 8485.

[13] X. Li, B. Shen, X.-Q. Yao, D. Yang, *J. Am. Chem. Soc.* **2007**, *129*, 7264 – 7265.

[14] D. Kand, T. Saha, M. Lahiri, P. Talukdar, *Org. Biomol. Chem.* **2015**, *13*, 8163 – 8168.

[15] a) J. Bai, Z. Meng, *Environ. Mol. Mutagen.* **2010**, *51*, 112 – 122; b) J. Liu, Y. Huang, S. Chen, C. Tang, H. Jin, J. Du, *Oxid. Med. Cell Longev.* **2016**, *2016*, 8; c) J. Xie, R. Li, R. Fan, Z. Meng, *Inhal. Toxicol.* **2009**, *21*, 952 – 957.

[16] S. Peng, T. Zhong, T. Guo, D. Shu, D. Meng, H. Liu, D. Guo, *New J. Chem.* **2018**, *42*, 5185 – 5192.

[17] A. L. Trifonov, V. V. Levin, M. I. Struchkova, A. D. Dilman, *Org. Lett.* **2017**, *19*, 5304 – 5307.

[18] S. K. Kim, J. M. Lim, T. Pradhan, H. S. Jung, V. M. Lynch, J. S. Kim, D. Kim, J. L. Sessler, *J. Am. Chem. Soc.* **2014**, *136*, 495 – 505.

[19] T. Routasalo, J. Helaja, J. Kavakka, A. M. P. Koskinen, *Eur. J. Org. Chem.* **2008**, *2008*, 3190 – 3199.

[20] A. Roy, D. Saha, A. Mukherjee, P. Talukdar, *Org. Lett.* **2016**, *18*, 5864 – 5867.

[21] A. Roy, A. Gautam, J. A. Malla, S. Sarkar, A. Mukherjee, P. Talukdar, *Chem. Commun.* **2018**, *54*, 2024 – 2027.

Accepted Manuscript

This article is protected by copyright. All rights reserved.

[22] T. Saha, S. Dasari, D. Tewari, A. Prathap, K. M. Sureshan, A. K. Bera, A. Mukherjee, P. Talukdar, *J. Am. Chem. Soc.* **2014**, *136*, 14128 – 14135.

[23] S. R. Malwal, D. Sriram, P. Yogeeswari, V. B. Konkimalla, H. Chakrapani, *J. Med. Chem.* **2012**, *55*, 553 – 557.

[24] A. Gilles, M. Barboiu, *J. Am. Chem. Soc.* **2016**, *138*, 426 – 432.

[25] J. A. Malla, A. Roy, P. Talukdar, *Org. Lett.* **2018**, *20*, 5991 – 5994.

[26] C. M. Dias, H. Li, H. Valkenier, L. E. Karagiannidis, P. A. Gale, D. N. Sheppard, A. P. Davis, *Org. Biomol. Chem.* **2018**, *16*, 1083 – 1087.

[27] S.-H. Park, S.-H. Park, E. N. W. Howe, J. Y. Hyun, L.-J. Chen, I. Hwang, G. Vargas-Zuñiga, N. Busschaert, P. A. Gale, J. L. Sessler, I. Shin, *Chem.* **2019**, *5*, 2079 – 2098.

[28] D. Mondal, A. Sathyan, S. V. Shinde, K. K. Mishra, P. Talukdar, *Org. Biomol. Chem.* **2018**, *16*, 8690 – 8694.

[29] A. V. Jentzsch, D. Emery, J. Mareda, S. K. Nayak, P. Metrangolo, G. Resnati, N. Sakai, S. Matile, *Nat. Commun.* **2012**, *3*, 905.

[30] a) P. Ghosh, G. Federwisch, M. Kogej, C. A. Schalley, D. Haase, W. Saak, A. Lützen, R. M. Gschwind, *Org. Biomol. Chem.* **2005**, *3*, 2691 – 2700; b) M. Eckshtain-Levi, R. Lavi, D. S. Yufit, B. Daniel, O. Green, O. Fleker, M. Richman, S. Rahimipour, A. Gruzman, L. Benisvy, *Chem. Commun.* **2016**, *52*, 2350 – 2353.

[31] J. J. P. Stewart, MOPAC2012; (2012) Stewart Computational Chemistry: Colorado Springs, CO, USA.

[32] P. Májek, R. Elber, *J. Chem. Theory Comput.* **2010**, *6*, 1805 – 1817.

[33] H. Zhang, C. Zhang, R. Liu, L. Yi, H. Sun, *Chem. Commun.* **2015**, *51*, 2029 – 2032.

[34] L. Yuan, Q.-P. Zuo, *Sens. Actuators. B Chem.* **2014**, *196*, 151 – 155.

[35] T. Suzuki, K. Fujikura, T. Higashiyama, K. Takata, *J. Histochem. Cytochem.* **1997**, *45*, 49 – 53.

[36] a) Z. Benderra, A. Trussardi, H. Morjani, A. M. Villa, S. M. Doglia, M. Manfait, *Eur. J. Cancer* **2000**, *36*, 428 – 434; b) M. P. Gamcsik, K. K. Millis, O. M. Colvin, *Cancer Res.* **1995**, *55*, 2012 – 2016.

[37] K. A. Pardeshi, S. R. Malwal, A. Banerjee, S. Lahiri, R. Rangarajan, H. Chakrapani, *Bioorg. Med. Chem. Lett.* **2015**, *25*, 2694 – 2697.

[38] K. A. Pardeshi, G. Ravikumar, H. Chakrapani, *Org. Lett.* **2018**, *20*, 4 – 7.

[39] A. Merglen, S. Theander, B. Rubi, G. Chaffard, C. B. Wollheim, P. Maechler, *Endocrinology* **2004**, *145*, 667 – 678.

[40] S. Yousf, D. M. Sardesai, A. B. Mathew, R. Khandelwal, J. D. Acharya, S. Sharma, J. Chugh, *Metabolomics* **2019**, *15*, 55.

[41] a) T. Saha, A. Gautam, A. Mukherjee, M. Lahiri, P. Talukdar, *J. Am. Chem. Soc.* **2016**, *138*, 16443-16451; bT. Saha, M. S. Hossain, D. Saha, M. Lahiri, P. Talukdar, *J. Am. Chem. Soc.* **2016**, *138*, 7558 – 7567.

[42] a) P. A. Gale, J. T. Davis, R. Quesada, *Chem. Soc. Rev.* **2017**, *46*, 2497 – 2519; b) N. Busschaert, S.-H. Park, K.-H. Baek, Y. P. Choi, J. Park, E. N. W. Howe, J. R. Hiscock, L. E. Karagiannidis, I. Marques, V. Félix, W. Namkung, J. L. Sessler, P. A. Gale, I. Shin, *Nat. Chem.* **2017**, *9*, 667 – 675.

[43] S.-K. Ko, S. K. Kim, A. Share, V. M. Lynch, J. Park, W. Namkung, W. Van Rossom, N. Busschaert, P. A. Gale, J. L. Sessler, I. Shin, *Nat. Chem.* **2014**, *6*, 885 – 892.

[44] a) S. Sakamuru, M. S. Attene-Ramos, M. Xia, *Methods Mol. Biol.* **2016**, *1473*, 17 – 22; b) S. Patil, M. M. Kuman, S. Palvai, P. Sengupta, S. Basu, *ACS Omega* **2018**, *3*, 1470 – 1481.

[45] a) A. Ashkenazi, *Nat. Rev. Drug Discov*. **2008**, *7*, 1001 – 1012; b) C. D. Bortner, J. A. Cidlowski, *Cell Death Differ.* **2002**, *9*, 1307 – 1310.

[46] S. T. Smiley, M. Reers, C. Mottola-Hartshorn, M. Lin, A. Chen, T. W. Smith, G. D. Steele, L. B. Chen, *Proc. Natl. Acad. Sci. U.S.A.* **1991**, *88*, 3671 – 3675.

[47] A. Cossarizza, M. Baccarani-Contri, G. Kalashnikova, C. Franceschi, *Biochem. Biophys. Res. Commun.* **1993**, *197*, 40 – 45.

[48] D. Wu, P. Yotnda, *J. Vis. Exp.* **2011**, 3357.

[49] J. S. Armstrong, K. K. Steinauer, B. Hornung, J. M. Irish, P. Lecane, G. W. Birrell, D. M. Peehl, S. J. Knox, *Cell Death Differ.* **2002**, *9*, 252 – 263.

[50] J. A. Malla, R. M. Umesh, A. Vijay, A. Mukherjee, M. Lahiri, P. Talukdar, *Chem. Sci.* **2020** (https://doi.org/10.1039/C9SC06520B).

[51]a) A. P. Halestrap, *J. Mol. Cell. Cardiol.* **2009**, *46*, 821 – 831; b) M. Crompton, *Biochem. J.* **1999**, *341*, 233 – 249.

[52] a) M. Madesh, G. Hajnóczky, *J. Cell Biol.* **2001**, *155*, 1003 – 1015; b) S.-H. Park, Y. P. Choi, J. Park, A. Share, O. Francesconi, C. Nativi, W. Namkung, J. L. Sessler, S. Roelens, I. Shin, *Chem. Sci.* **2015**, *6*, 7284 – 7292.

[53] C. J. Lovitt, T. B. Shelper, V. M. Avery, *BMC Cancer* **2018**, *18*, 41.

Accepted Manuscript

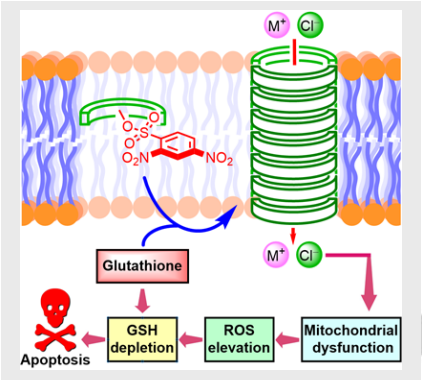
This article is protected by copyright. All rights reserved.

10.1002/anie.202000961

Entry for the Table of Contents

Research Article

Compromised Intracellular glutathione defense by activation of ion channel leading to ROS production and apoptosis



*Javid Ahmad Malla,[a] Rintu Umesh,[b] Saleem Yousf, [a] Shrunal Mane, [b] Shilpy Sharma, [c] Mayurika Lahiri, [b]and Pinaki Talukdar**

Page No. – Page No.
A Glutathione Activatable Ion Channel Induces Apoptosis in Cancer Cells by Depleting Intracellular Glutathione Levels

WILEY-VCH
Accepted Manuscript

This article is protected by copyright. All rights reserved.

Chemical Science

ROYAL SOCIETY OF CHEMISTRY

EDGE ARTICLE

View Article Online
View Journal | View Issue

Check for updates

Cite this: *Chem. Sci.*, 2020, **11**, 2420

All publication charges for this article have been paid for by the Royal Society of Chemistry

Apoptosis-inducing activity of a fluorescent barrel-rosette M^+/Cl^- channel†

Javid Ahmad Malla, [a] Rintu M. Umesh,[b] Amal Vijay,[a] Arnab Mukherjee, [a] Mayurika Lahiri [b] and Pinaki Talukdar [a]*

Synthetic transmembrane ion transport systems are emerging as new tools for anticancer therapy. Here, a series of 2-hydroxy-N^1,N^3-diarylisophthalamide-based fluorescent ion channel-forming compounds are reported. Ion transport studies across large unilamellar vesicles confirmed that the compound with two 3,5-bis(trifluoromethyl)phenyl arms is the most efficient transporter among the series and it facilitates M^+/Cl^- symport. The compound formed supramolecular ion channels with a single-channel conductance of 100 ± 2 pS, a diameter of 5.06 ± 0.16 Å and a permeability ratio, P_{Cl^-}/P_{K^+} of 8.29 ± 1. The molecular dynamics simulations of the proposed $\mathbf{M}_{2.11}$ channel (*i.e.* 11 coaxial layers of a dimeric rosette) with K^+ and Cl^- in the preequilibrated POPC lipid bilayer with water molecules illustrated various aspects of channel formation and ion permeation. Cell viability assay with the designed compounds indicated that cell death is being induced by the individual compounds which follow the order of their ion transport activity and chloride and cations play roles in cell death. The inherent fluorescence of the most active transporter was helpful to monitor its permeation in cells by confocal microscopy. The apoptosis-inducing activity upon perturbation of intracellular ionic homeostasis was established by monitoring mitochondrial membrane depolarization, generation of reactive oxygen species, cytochrome c release, activation of the caspase 9 pathway, and finally the uptake of the propidium iodide dye in the treated MCF7 cells.

Received 24th December 2019
Accepted 16th January 2020

DOI: 10.1039/c9sc06520b

rsc.li/chemical-science

Open Access Article. Published on 29 January 2020. Downloaded on 6/30/2020 3:14:16 PM.
This article is licensed under a Creative Commons Attribution-NonCommercial 3.0 Unported Licence.

Introduction

Ion transport across the cell membrane is a very crucial physiological process that ensures the healthy functions of cells.[1–8] The cell membrane creates a thermodynamic barrier for polar molecules and ions to pass through its hydrophobic middle core. To ensure the regulated membrane transport of these species, nature has endowed the cells with very special molecular machineries in the form of ion transport systems and other pore forming protein molecules.[5,9,10] The ion transport systems involve ion channels which can span the membrane and provide a hydrophilic pathway for ions to pass through.[11–13] On the other hand, there are small molecular systems, called ion carriers, which can pick up ions from one side of the membrane and flip to the other side for releasing these ions.[14] Any defect or damage in these complex transport systems (channelopathies) can have drastic effects on the physiological functions of the cell.[15] The typical examples of channelopathies include cystic fibrosis which is caused by the mutation in the CFTR channel.[16] Similarly Barter's syndrome, Dent's disease, Long QT syndrome, osteoporosis, epilepsy, Parkinson's disease *etc.* are other disorders which are caused by channelopathies.[15,17,18] To treat these channelopathies, the identification of their causes becomes an important concern to the scientific community. In this regard, various studies have come out and the process continues. However, to solve these kinds of problems chemists have come up with an alternative approach to replace the defective channels with structurally simple organic motifs, which can restore the ion transport in defective cells by functioning as ion channels or ion carriers.[19–22] So synthetic ion transport systems may open new opportunities for the treatment of these channelopathies. Along with these findings, the renewed interest in the field of synthetic ion transport systems has emerged after anticancer activity was observed in prodigiosin,[23–25] a naturally occurring ionophore, which acts as a chloride and HCl carrier. Afterward, various synthetic chloride ion carriers[26–30] and chloride channels[9] were evaluated for anticancer activity and were found to induce apoptosis in cancer cells through the caspase-dependent intrinsic pathway. In the field of symporters, the first synthetic KCl symporter was reported by Smith and coworkers, using a ditopic receptor for NaCl and KCl transport.[31] This was followed by Kyu-Sung Jeong and coworkers, who used an

[a]*Department of Chemistry, Indian Institute of Science Education and Research Pune, Dr Homi Bhabha Road, Pashan, Pune 411008, Maharashtra, India. E-mail: ptalukdar@iiserpune.ac.in*

[b]*Department of Biology, Indian Institute of Science Education and Research Pune, Dr Homi Bhabha Road, Pashan, Pune 411008, Maharashtra, India*

† Electronic supplementary information (ESI) available. CCDC 1904396. For ESI and crystallographic data in CIF or other electronic format see DOI: 10.1039/c9sc06520b

This journal is © The Royal Society of Chemistry 2020

Open Access Article. Published on 29 January 2020. Downloaded on 6/30/2020 3:14:16 PM.
This article is licensed under a Creative Commons Attribution-NonCommercial 3.0 Unported Licence.

azacrown as a K^+ binding motif and urea as a chloride binding motif.[32] Gale and coworkers developed their calix[4]pyrrole as CsCl and RbCl transporters where Cl^- binding was through H-bonding and Cs^+ was tightly bound to pyrrole rings.[33] Matile and coworkers reported ditopic transport systems operating *via* halogen bonding.[34] These two types of transport systems work using cation activated anion transport.[34] The latest example of a metal halide symport was presented by Madhavan and coworkers, with a peptide connected to an aminopicolinic acid unit, having more preference for cations over anions.[35] However, none of these symporters have been evaluated for biological impacts.

Herein, we report a series of fluorescent molecules that form self-assembled barrel-rosette channels to facilitate the symport of M^+ and Cl^- across liposomes. These channels allow the transport of Cl^- and K^+ as well as Na^+ across the cell membrane to induce apoptotic cell death. The design included the central core of 2-hydroxy-N^1,N^3-diarylisophthalamide connected to two identical aromatic side arms such as phenyl, 4-methylphenyl, 4-trifluoromethylphenyl or 3,5-bis(trifluoromethyl)phenyl to get molecules **1a–1d** (Fig. 1A). It was envisaged that the intramolecular C=O···H–O and C–O···H–N interactions would provide a preorganized geometry of individual monomers. The intermolecular π–π stacking interactions among aromatic rings and hydrogen bonding interactions among amide moieties would lead to the aggregation of individual monomers in the membrane to form an active channel (Fig. 1B).[3] Theoretical estimations, based on the calculator plugins of the MarvinSketch program,[36] indicated that the variation of terminal aromatic groups from phenyl to 4-methylphenyl, 4-trifluoromethylphenyl and 3,5-bis(trifluoromethyl)phenyl would decrease the pK_a of both amide protons (Table S1†). Therefore, in the resulting supramolecular channel, the amide protons of **1d** would contribute to the maximum extent in forming intra- and intermolecular (with neighboring monomers and water molecules present in the cavity and anions) hydrogen bonds. Estimated pK_a = 6.42 for the 2-hydroxyl group of each compound indicated that in the supramolecular channel, one or more hydroxyl groups may get deprotonated at physiological pH providing cation binding sites. The recognition sites for cations can also be provided by either a C–F or a C=O moiety *via* cation–dipole interactions. We envisaged that the 2-hydroxyl group would also be useful in generating inherent fluorescence of these molecules due to the push–pull effect. The MarvinSketch program[36] also predicted that the lipophilicity (logP)[37,38] of the compounds would increase as **1a** < **1b** < **1c** < **1d** contributing to the better membrane permeability of the channel formed by **1d**.

Results and discussion

Compounds **1a–1d** were synthesized from protected acid **4** by converting it to the acid chloride using oxalyl chloride,[39] which was then coupled with the respective aromatic amine to get the corresponding amide **5a–5d** (Scheme 1). The product was subjected to *O*-methyl deprotection using 1 M BBr_3 in dichloromethane[40] to get the corresponding final compound **1a–1d** with a free hydroxyl group. All newly synthesized compounds were purified by column chromatography, and characterized by ^{1}H NMR, ^{13}C NMR, HRMS, IR, and melting point. The single-crystal X-ray diffraction study of **1c** provided the molecular geometry containing the intramolecular C=O···H–O and C–O···H–N hydrogen bonding interactions (Fig. S11†).

The ion transport activity of 2-hydroxy-N^1,N^3-diarylisophthalamide derivatives **1a–1d** was checked by different fluorometric methods across egg yolk phosphatidylcholine unilamellar vesicles (EYPC-LUVs).[41–45] At first, large EYPC-LUVs, entrapping the pH-sensitive dye 8-hydroxypyrene-1,3,6-trisulfonate (HPTS, pK_a = 7.2), were prepared, and NaOH was added in the extravesicular buffer to create a pH gradient (*i.e.*, ΔpH = 0.8). The rate of change in the fluorescence intensity was monitored after the addition of **1a–1d**, separately, and finally, Triton X-100 was added to lyse the vesicles for the complete leakage of the HPTS dye.[46] The comparison of activities showed the activity sequence **1a** < **1b** < **1c** ≪ **1d**, inferring **1d** as the most efficient transporter of ions (Fig. 2A). The activity sequence of **1a–1d** suggests that the pK_a values of the amide protons have major control over the transport rate as compared to logP values. The EC_{50} value, *i.e.*, the concentration required to reach half of the maximum activity, was calculated to be 0.48 μM (compound to lipid ratio = 0.58 mol%), and the Hill coefficient,

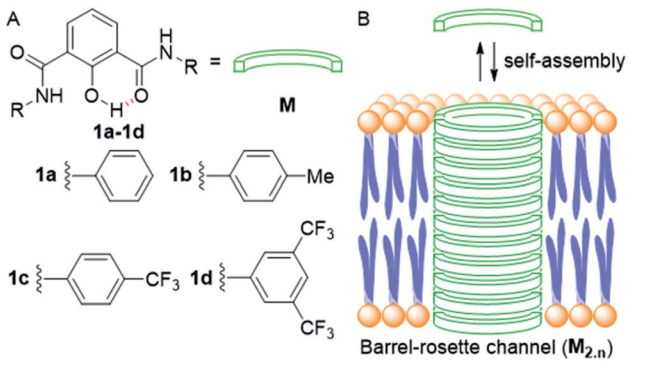
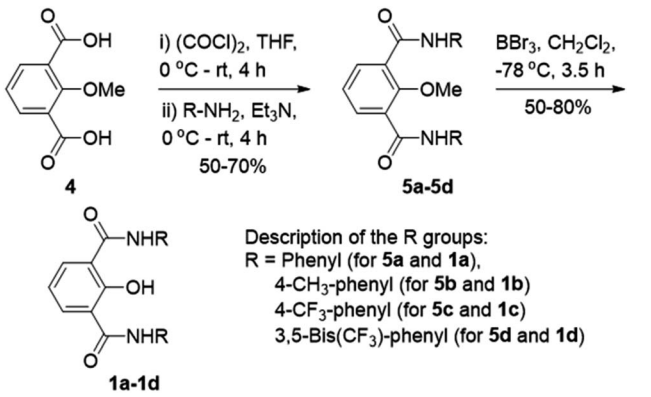
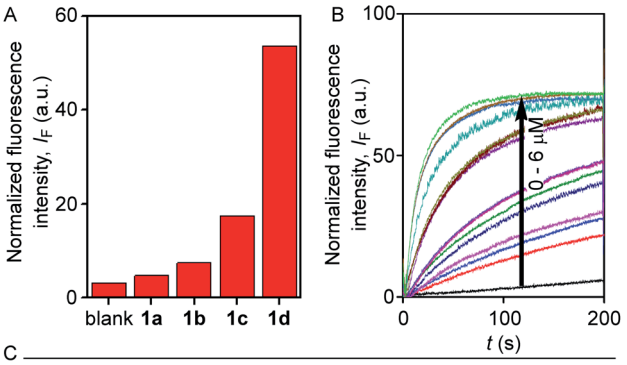


Fig. 1 Structure of designed channel-forming compounds **1a–1d** (A); self-assembly of individual monomers **M** into rosette channel $M_{2.n}$ in the lipid bilayer membrane (B).



Scheme 1 Synthesis of **1a–1d**.

Open Access Article. Published on 29 January 2020. Downloaded on 6/30/2020 3:14:16 PM.
This article is licensed under a Creative Commons Attribution-NonCommercial 3.0 Unported Licence.



C

Compound	logP	pK_{a1}	pK_{a2}	EC_{50} (μM)	n
1a	3.85	12.0	12.77	ND	ND
1b	4.88	12.17	12.95	3.78	2.6
1c	5.61	11.63	12.41	2.06	1.9
1d	7.30	10.5	11.27	0.47	1.79

Fig. 2 Comparison of ion transport activity of compounds **1a–1d** (0.5 μM) at 200 seconds across EYPC-LUVs⊃HPTS (A). Concentration profile of compound **1d** (B); and correlation table for the estimated logP and pK_a values with experimentally determined EC_{50} and Hill coefficient (n) values (C).

n, was calculated to be almost equal to 2 (Fig. 2C). These data suggest that a noncovalent dimer of the compound is the active structure for the supramolecular nanochannel assembly.[47] The Hill analysis could not be performed with the dose-dependent activity data of **1a** due to its precipitation at higher concentrations.

The excellent ion transport activity of **1d** inspired us to investigate the ion selectivity of this channel forming molecule. First, the ion transport activity across EYPC-LUVs⊃HPTS with intravesicular NaCl and an isoosmolar extravesicular MCl (where, $M^+ = Li^+$, Na^+, K^+, Rb^+, and Cs^+) was used to determine the selectivity among the different cations.[48–50] The data provided the selectivity sequence as $K^+ \approx Rb^+ > Cs^+ > Na^+ > Li^+$ (Fig. 3A). To see if there is any role of anions involved in the transport process, the anion selectivity study was performed by varying the intravesicular and extravesicular anions of NaX salts ($X^- = Cl^-$, Br^-, I^-, NO_3^-, and ClO_4^-), and changes in the ion transport rate were checked upon applying a pH gradient of 0.8 (pH_{in} = 7.0 and pH_{out} = 7.8).[48,51,52] Interestingly, the data confirmed a considerable selectivity of the channel towards Cl^- compared to the other anions (Fig. 3B). The selectivity studies suggested that both inorganic cations and anions are involved in the transport across the channel formed by **1d**.

To further confirm the Cl^- ion transport activity of **1d**, the EYPC-LUVs⊃lucigenin was prepared by entrapping the lucigenin dye and $NaNO_3$ salt and investigated in detail by monitoring the fluorescence intensity of the intravesicular lucigenin dye at λ_{em} = 535 nm (λ_{ex} = 450 nm).[53,54] Subsequently, a Cl^-/NO_3^- gradient was applied by the addition of a concentrated solution of 2 M NaCl in the extravesicular buffer. Concentration-dependent quenching of lucigenin fluorescence was observed upon addition of channel forming compound **1d** (Fig. 3C). These data show that the supramolecule formed by the compound can allow the influx of Cl^- across liposomes. The variation of extravesicular cations corroborated with cation selectivity obtained by the HPTS assay (Fig. 3D). So, to get further support for the symport mechanism of ion transport, the valinomycin coupled assay with **1d** was carried out.[29] KCl was added to the extravesicular buffer to create the Cl^-/NO_3^- gradient. Then valinomycin was added along with **1d** to monitor any cooperative effect. There was no enhancement of the transport rate, which suggests that there is no cooperative transport by valinomycin and **1d** (Fig. S5†). So the operating transport mechanism should be the symport mechanism. To further confirm the symport mechanism, the EYPC liposomes were prepared by entrapping NaCl (200 mM) and 1.0 mM of the lucigenin dye. Then, isoosmolar Na_2SO_4 was added to the extravesicular solution and Cl^- efflux was monitored. A similar experiment was also performed with extravesicular isoosmolar $NaNO_3$. The results indicate that there is no difference in the transport rate of two ions by **1d** (Fig. 3E), suggesting that the symport mechanism of ion transport is operative.[28]

To investigate the integrity of the membrane after addition of **1d** or the formation of supramolecular pores in the

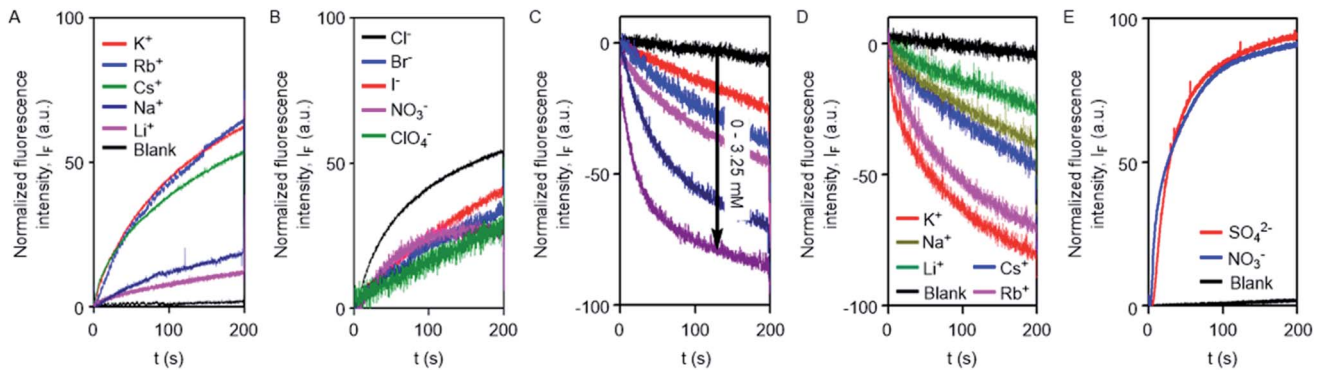


Fig. 3 Cation selectivity **1d** (0.1 μM) across EYPC-LUVs⊃HPTS (A). Anion selectivity of **1d** (0.5 μM) across EYPC-LUVs⊃HPTS (B). Cl^- ion influx across EYPC-LUVs⊃lucigenin upon addition of **1d** (0–3.25 μM) (C). Cation dependent Cl^- ion influx across EYPC-LUVs⊃lucigenin upon addition of **1d** (1.5 μM) (D). Cl^- efflux across EYPC-LUVs⊃lucigenin by **1d** (2.5 μM) in the presence of intravesicular Cl^- and either SO_4^{2-} or NO_3^- as an isoosmolar extravesicular anion (E).

 This journal is © The Royal Society of Chemistry 2020

Open Access Article. Published on 29 January 2020. Downloaded on 6/30/2020 3:14:16 PM.
This article is licensed under a Creative Commons Attribution-NonCommercial 3.0 Unported Licence.

membrane, the leakage of carboxyfluorescein (CF) was monitored across EYPC-LUVs⊃CF.[55] It is well known that a high concentration of CF molecules inside the liposomes leads to the fluorescence quenching of the dye due to collisions among the molecules. However, efflux of these molecules from the liposomes into the external buffer restores their fluorescence (λ_{em} = 517 nm, λ_{ex} = 492 nm). When compound **1d** was added to the liposomes, there was no significant enhancement in the fluorescence intensity of CF (Fig. S9†), indicating that neither the membrane is getting damaged, nor the larger pores are being formed by **1d**.

To confirm the formation of the transmembrane ion channel by compound **1d**, the ionic conductance across the planar lipid bilayer membrane was measured.[56] In this experiment, two compartments (cis and trans chambers) containing KCl solution (1.0 M) were separated by a planar lipid bilayer membrane composed of diphytanoyl phosphatidylcholine (diPhyPC) lipid.[57,58] The addition of **1d** (2.0 μM) to the system led to the distinct channel openings and closing at different holding potentials, confirming the formation of ion channels (Fig. 4A, B). The single-channel conductance was found to be 100 ± 2 pS, and the channel diameter = 5.06 ± 0.16 Å was calculated by the Hille equation (eqn (1))

$$1/g = (l + \pi d/4) \times (4\rho/\pi d2) \quad (1)$$

where g = the corrected conductance (obtained by multiplying the measured conductance with the Sansom's correction factor), l = the thickness of the membrane (34 Å), and ρ = the resistivity of the recording solution (ρ = 9.44 Ω cm).

The variation of current with voltage (I–V plot) in the presence of the symmetric solution of KCl (1.0 M each) showed a linear variation, *i.e.*, ohmic behavior, which confirms the non-dipole nature of the channel. When the ion selectivity of the channel was checked using unsymmetric solutions of KCl in two chambers (*i.e.*, 1.0 M in cis and 0.5 M KCl in trans), it was observed that the rate of Cl^- transport is higher than the rate of K^+ transport with a permeability ratio P_{Cl^-}/P_{K^+} = 8.29 ± 1 (Fig. 4C). These data suggest that the electrogenic transport of Cl^- gives the current signals during the recordings.

To get further support for channel formation, the temperature dependent ion transport in DPPC-LUVs⊃HPTS was studied. Compound **1d** showed some decrease in the activity at 30 °C compared to that at 45 °C (Fig. S10†). This behavior is normal for various biological and synthetic ion channels due to hindered partition at lower temperature.[41]

Based on the crystal structure of **1c** (Fig. S12†), it is evident that each 2-hydroxy-N^1,N^3-diarylisophthalamide molecule exists predominantly in an intramolecular C═O···H–O and C–O···H–N hydrogen bonded preorganized geometry. The conformational study of **1d** using the Conflex 8 program[59,60] also indicated similar hydrogen bonded conformations of the di-amide core (Fig. S12†). At first, eleven molecules of **1d** in the **Conf-1a** were placed on top of another to form one side of the channel. Subsequently, the other side of the channel was constructed in the same way and the two halves of the channel were arranged face-to-face to form the barrel-rosette channel. The constructed channel was further optimized using MOPAC2012 (ref. 61) software with the PM6-DH+ (ref. 62) method to get the final channel (Fig. S13A†). This optimized channel was then placed in the POPC lipid bilayer membrane, and molecular dynamics (MD) simulations were carried out (see ESI† for methods). The equilibrated channel is shown in Fig. 5A. Fig. S13B† shows the densities of various constituents of the channel indicating the proper formation of the channel. The top view of the channel with a pore diameter is shown in Fig. S13C.† Fig. S13D† shows that the variation in the pore diameter is minimal around an

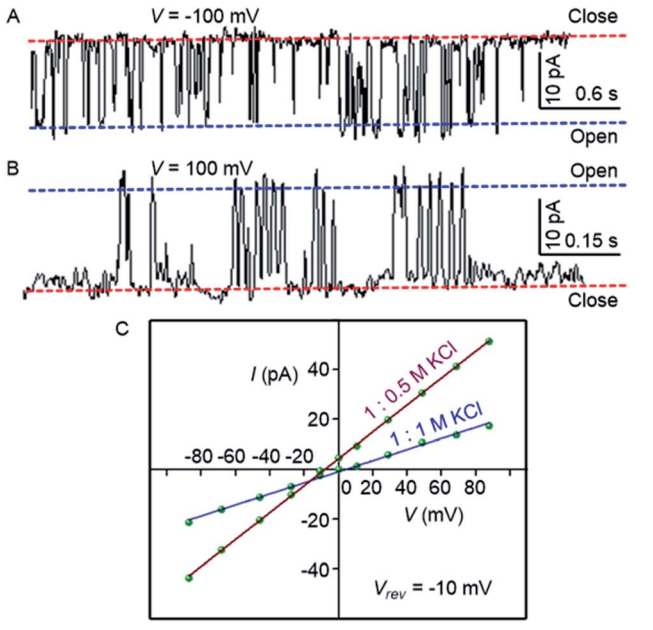


Fig. 4 Single-channel conductance of **1d** (2.0 μM) recorded at −100 mV (A) and at 100 mV (B) in symmetrical KCl solutions. I–V plots of **1d** in symmetrical and unsymmetrical concentrations of KCl (C).

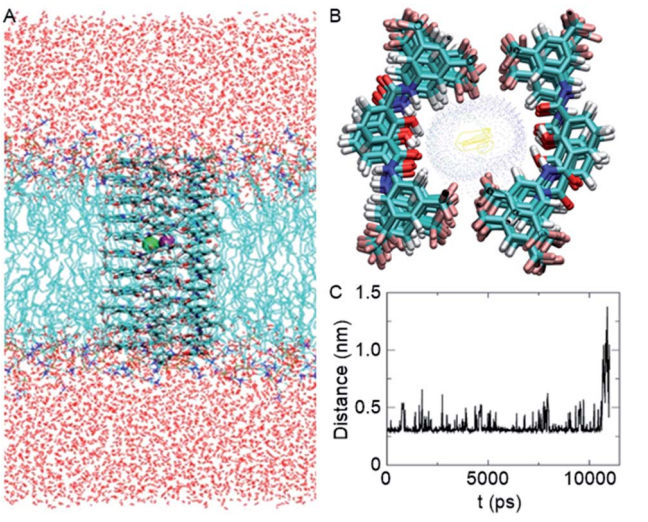


Fig. 5 Equilibrated channel-POPC/water system (A), top view of the zoomed channel without lipid membrane (B), and variation of the distance between K^+ and Cl^- ions during the production run (C).

Open Access Article. Published on 29 January 2020. Downloaded on 6/30/2020 3:14:16 PM.
This article is licensed under a Creative Commons Attribution-NonCommercial 3.0 Unported Licence.

average of 5.3 Å during the simulations, in excellent agreement with the experiment.

In the simulated channel, upon inspection at various time frames (Fig. S14A–D†), multiple noncovalent interactions were found to stabilize the channel structure and helps in ion recognition in the channel lumen. The stacking interactions among aromatic rings (among successive central phenyl rings and among successive aromatic arms) and the hydrophobic interactions among CF_3 groups were found to be present. Moreover, intermolecular C═O···H–$O_{(phenolic)}$ and C–O···H–N interactions were also evident in the channel. The water molecules inside the channel formed a continuous array with multiple intermolecular H–O···H–O interactions with neighbouring water molecules. The water molecules were also involved in hydrogen bonding with C–F and C═O groups of the channel forming molecules (Fig. S14E†). The K^+ ion was involved in cation–dipole interactions with neighbouring F-centres of the channel forming molecules and with O-centres of the neighbouring water molecules (Table S2†). The Cl^- ion was involved in C–O–H···Cl^- interactions with channel forming molecules and O–H···Cl^- interactions with neighbouring water molecules (Table S3†). Interestingly, the permeation of K^+ and Cl^- in the channel took place with an interionic distance within 5 Å, confirming the presence of electrostatic interactions (Fig. 5C, S16†). In the bulk water, the ions got separated due to hydration.

The inherent fluorescence of **1d** encouraged us to use it for confocal live cell imaging to check whether the molecules of the compound stay only in the membrane or can permeate inside the cell as well. The live cell imaging of **1d** in the human epithelial breast cancer cell line, MCF7, indicated that the compound does not remain confined to the cell membrane only, but permeates into the cytosolic part as well (Fig. 6).[20] Next, we monitored the time of insertion of the compound in the cell using real-time analysis. The results indicated that the compound enters the cells within a few seconds of incubation (see uploaded video†). Interestingly, the real-time analysis also indicated a change in the cell morphology within a few minutes and a decrease in the cell volume was observed. Such a decrease in the cell volume is indicative of the apoptotic volume decrease (AVD), which is a well-known initial event of apoptosis.[63–65]

Encouraged by this observation, we evaluated the viability of cells in the presence of compounds **1a–1d**. A single-point screening of the cell viability was done by the MTT assay after incubation of **1a–1d** in the MCF7 cell line for 24 hours.[9] As

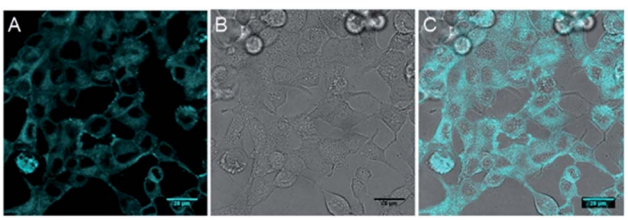


Fig. 6 Live cell imaging of **1d** at 10 μM in MCF7 cell line; fluorescence (A), DIC image (B) and overlay image (C). Cyan color was given for better contrast. Scale bar 80 μm.

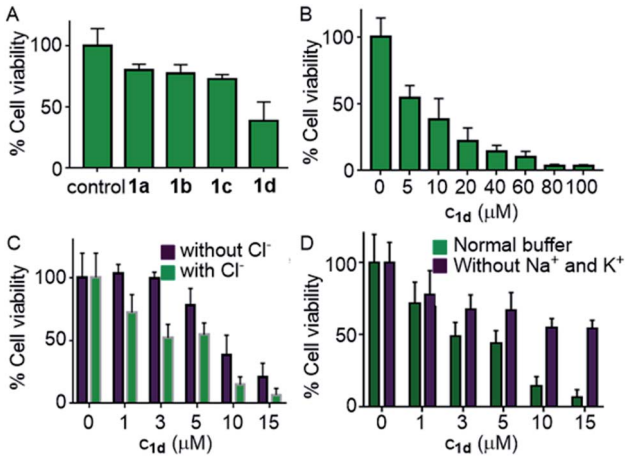


Fig. 7 Cell viability obtained from single-point screening of compounds **1a–1d** (10 μM each) by the MTT assay after 24 h incubation (A); dose-dependent cell viability in the presence of **1d** (B); cell viability of MCF7 cells in the presence and absence of Cl^- ions incubated with **1d** at different concentrations (C); and in the presence and absence of Na^+ and K^+ ions (D).

expected, compound **1d** displayed maximum cell killing activity (Fig. 7A). Next, the dose-dependent effects of **1d** on MCF7 cells were studied which showed a decrease in the cell viability upon increasing the concentration of the compound giving the IC_{50} value of approximately 5.0 μM (Fig. 7B).

Next, the chloride mediated cell death was studied by comparing the cell viability both in the presence and absence of chloride ions in the culture medium. The chloride mediated apoptosis is well studied in the literature.[9,26,66] So two different types of HBSS (Hanks balanced salt solution) were prepared, with and without Cl^- ions for using as the extracellular media. The MCF7 cells were suspended in both the media and incubated with compound **1d** at different concentrations around the IC_{50} value. As expected, with chloride ions in the extracellular buffer the compound showed more cell death compared to that without chloride ions (Fig. 7C). This experiment clearly demonstrates that the chloride-mediated cell death takes place. As the compound is a M^+/Cl^- symporter, we decided to evaluate the effect of K^+ ions and Na^+ ions on the cell death. Since the concentration of Na^+ ions is very high outside the cell compared to K^+ ions, we expected a better involvement of Na^+ ions, if the symport process is taking place. So to evaluate the effect of cations, we again prepared two different HBSS buffers, with and without K^+ and Na^+ ions and used as the extracellular media. Compound **1d** showed higher cell viability which was observed for **1d** without both K^+ and Na^+ ions in the extracellular media in comparison to that when studied in the presence of normal HBSS buffer (containing Na^+, K^+, and Cl^- ions) (Fig. 7D). These results confirm that the cell death is mediated by Cl^- and cations.

To evaluate whether cell death is being mediated by necrosis or apoptosis, the events involved in the apoptotic pathway were evaluated in detail. The observed AVD is already an indication of apoptosis. Apoptosis is also evidenced by the disruption of

 This journal is © The Royal Society of Chemistry 2020

Open Access Article. Published on 29 January 2020. Downloaded on 6/30/2020 3:14:16 PM.
This article is licensed under a Creative Commons Attribution-NonCommercial 3.0 Unported Licence.

mitochondrial membrane potential (MMP),[67,68] which subsequently results in cytochrome c release. The release of cytochrome c in the cytoplasm switches on the apoptotic signaling cascade.[69–71] Firstly, we monitored the change in mitochondrial membrane potential by using the MMP sensitive JC-1 dye. This dye exhibits red fluorescence emission due to the formation of J-aggregates in the healthy mitochondrial membrane, while depolarization of the mitochondrial membrane leads to dispersion of the dye in the cytosol, resulting in green fluorescence emission. The MCF7 cells were incubated with compound **1d** (10 μM), followed by the treatment with the JC-1 dye. The cells were analysed under a confocal microscope to monitor the changes in the red and green fluorescence in the treated cells. The study showed a prominent decrease in the red fluorescence and a concomitant increase in the green emission (Fig. 8).[70,72] The quantification of the pixel intensity ratio (green/red = 2.57)[9] in treated cells compared to the control (green/red = 0.263) confirmed the enhancement in the depolarization of MMP due to the change in ionic homeostasis of cells.

This change in ionic homeostasis of cells leads to a disturbance in the electron transport chain in the mitochondrial respiratory cycles, which results in reactive oxygen species (ROS) production.[73–76] Thus, 2′,7′-dichlorodihydrofluorescein diacetate (H_2DCFDA),[68,77] a ROS probe, was used to monitor ROS generation in cells. The probe remains in the non-fluorescent state in the diacetate protected form. However, upon cellular internalization, the hydrolysis of the ester groups by the esterases followed by the ROS-mediated oxidation generates a green fluorescent 2′,7′-dichlorofluorescein (DCF). The MCF7 cells were treated with **1d** in a time-dependent manner and then stained with H2DCFDA, and the cells were analysed under a confocal microscope. A significant enhancement in the green fluorescence was observed, which clearly demonstrates the generation of ROS as a result of ion transport by **1d** (Fig. S19†).

The elevated ROS levels are known to cause the opening of the mitochondrial permeability transition pores (PTPs),[78,79] which are formed by natural ion channels present in the mitochondrial membrane. This process results in the disruption of the mitochondrial outer membrane and a subsequent release of cytochrome c from the mitochondrial membrane into cytosol.[80,81] Therefore, to monitor the release of cytochrome c into the cytosol, immunostaining with a specific antibody was used. The MCF7 cells were treated with **1d** and then processed for immunofluorescence to see if any release of cytochrome c is taking place. A considerable enhancement in the fluorescence intensity and dispersion of the fluorescence signal over cytosol (Fig. 8) indicates the release of cytochrome c.

In the intrinsic apoptotic pathway, the released cytochrome c binds to the Apaf-1 to form an apoptosome. Then, the cytochrome c/Apaf-1 complex activates the caspase 9 pathway, which then activates the caspase 3 pathway.[69,82–84] Therefore, we analysed the caspase 9 pathway by immunoblot analysis of the cleaved caspase 9 level in MCF7 cells upon addition of **1d**. The incubation of the cells with **1d** led to a significant increase in the expression of cleaved caspase 9 (Fig. 9). The increase in the levels of caspase 9 was quantified with respect to the GAPDH (loading control). So, the expression of cleaved caspase 9 confirms the activation of the intrinsic pathway of apoptosis. To further confirm the apoptotic pathway, the expression of cleaved poly(ADP-ribose) polymerase (PARP) was checked. PARP cleavage by endogenous caspases is a very well-known phenomenon.[85–87] PARP-1 cleavage prevents DNA repair to facilitate apoptosis. A significant amount of degradation of full-length PARP-1 (116 kDa) with a concomitant increase of cleaved PARP-1 (86 kDa) was observed in the immunoblot analysis of MCF7 cells incubated with 10 μM concentration of **1d** (Fig. 9A).

For a final validation of the overall process, the propidium iodide (PI) assay was used. The dye binds to the nuclear

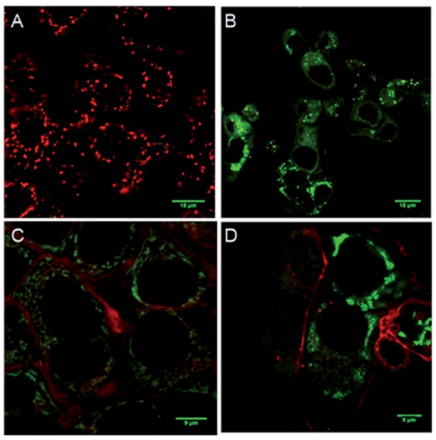


Fig. 8 Live cell imaging of MCF7 cells upon treatment with 0 μM (A) and 10 μM (B) of **1d** for 24 h followed by staining with the JC-1 dye. Red and green channel images were merged to generate the displayed image (A). MCF7 cells treated first with 0 μM (C) and 10 μM (D) of **1d** for 8 h and then fixed and analyzed for cytochrome c release by immunostaining with the cytochrome c specific primary antibody (green). Phalloidin (red) co-staining was used to mark the boundaries.

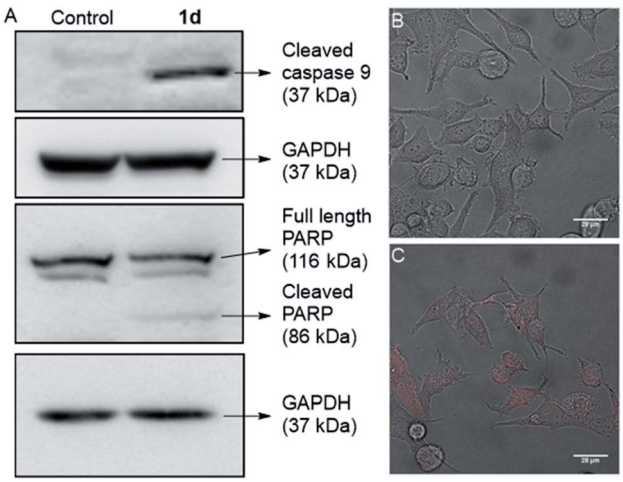


Fig. 9 Immunoblot assay for active caspase 9 in MCF7 cells, after 24 h incubation with 0 μM and 10 μM of **1d** (A). Data were quantified with respect to glyceraldehyde 3-phosphate dehydrogenase (GAPDH) levels. Live cell images of MCF-7 cells incubated with compound 0 μM (B) and 10 μM of **1d** (C), and the propidium iodide (PI; red) probe.

Open Access Article. Published on 29 January 2020. Downloaded on 6/30/2020 3:14:16 PM.
This article is licensed under a Creative Commons Attribution-NonCommercial 3.0 Unported Licence.

constituents of the cell, typically DNA and RNA, however, it is impermeable to the healthy cells.[88] The dye can easily cross the cell membrane of damaged cells and bind to the nuclear constituents. So the MCF7 cells were treated with **1d** for 24 h and then stained with PI. The live cell imaging of the cells clearly showed that the PI uptake is very prominent in the case of treated cells, compared to control cells (Fig. 9B, C, and S20†). So these data finally validate that the cells have been damaged by treatment with **1d**.

Conclusions

In summary, we have synthesized fluorescent 2-hydroxy-N^1,N^3-diarylisophthalamides which form efficient ion channels in the lipid bilayer membranes. The compound with two 3,5-bis(trifluoromethyl)phenyl arms was the most active among the entire series when ion transport activity was measured across large unilamellar vesicles. The study also confirmed the symport of M^+ and Cl^-. The channel formation was also validated by planar bilayer conductance measurement studies, which gave the channel diameter $= 5.06 \pm 0.16$ Å. The permeability ratio, $P_{Cl^-}/P_{K^+} = 8.29 \pm 1$, indicates higher selectivity for Cl^- compared to K^+. We have also constructed an atomistic model of the channel and performed MD simulations to show various interactions of the channel molecules with themselves and with the ions. The simulations show that the pore diameter is maintained at an average value of 5.3 Å. Also, both cations and ions permeate together through the channel, keeping a smaller distance till it reaches the bulk water. Inherent fluorescence of the compound was helpful in the live cell imaging of MCF7 cells, which indicated the presence of the compound in the cell membrane and in the cytoplasmic content. The channel facilitates the transport of chloride and cations across the cellular membrane, and the process resulted in the perturbation of the ionic homeostasis of cells leading to significant cell death. The mechanism of cell death was confirmed by the mitochondrial membrane depolarization and reactive oxygen species generation. These processes resulted in the cellular apoptosis, which was confirmed by cytochrome c release, activation of the caspase 9 pathway, PARP cleavage, and staining of nuclear contents by propidium iodide. To the best of our knowledge, the present study demonstrates the first example of an inherently fluorescent synthetic channel with an ambivalent chemical motif for complexation and transport of both cations and chloride ions simultaneously. Therefore, this system can be considered as a synthetic congener of naturally occurring sodium-potassium-chloride co-transporters (NKCCs). Such design will encourage the future development of synthetic channels for biomedical applications such as cancer treatment, channel replacement therapy *etc.*

Conflicts of interest

There are no conflicts to declare.

Acknowledgements

We thank Ms. Aishwarya Venkataravi of IISER Pune for the valuable discussions about microscopy. We also thank Ms. Shivani Sharma for her help in solving the single crystal XRD data. We would like to acknowledge IISER, Pune microscopy facility. This work was supported by SERB, Govt. of India (EMR/2016/001897) and Department of Biotechnology (DBT), Govt. of India (BT/HRD/NBA/36/06/2018).

Notes and references

1 W. D. Stein, *Channels, Carriers, and Pumps: An Introduction to Membrane Transport*, Academic Press, San Diego, CA, 1990.
2 P. Agre, *Angew. Chem., Int. Ed.*, 2004, **43**, 4278–4290.
3 T. J. Jentsch, C. A. Hubner and J. C. Fuhrmann, *Nat. Cell Biol.*, 2004, **6**, 1039–1047.
4 L. Song, M. R. Hobaugh, C. Shustak, S. Cheley, H. Bayley and J. E. Gouaux, *Science*, 1996, **274**, 1859–1866.
5 J. T. Davis, O. Okunola and R. Quesada, *Chem. Soc. Rev.*, 2010, **39**, 3843–3862.
6 S. B. Hladky, *J. Membr. Biol.*, 1979, **46**, 213–237.
7 S. Y. Chiu and G. F. Wilson, *J. Physiol.*, 1989, **408**, 199–222.
8 T. E. DeCoursey, K. G. Chandy, S. Gupta and M. D. Cahalan, *Nature*, 1984, **307**, 465–488.
9 T. Saha, A. Gautam, A. Mukherjee, M. Lahiri and P. Talukdar, *J. Am. Chem. Soc.*, 2016, **138**, 16443–16451.
10 T. W. Allen, O. S. Andersen and B. Roux, *Proc. Natl. Acad. Sci. U. S. A.*, 2004, **101**, 117–122.
11 M. Bayrhuber, T. Meins, M. Habeck, S. Becker, K. Giller, S. Villinger, C. Vonrhein, C. Griesinger, M. Zweckstetter and K. Zeth, *Proc. Natl. Acad. Sci. U. S. A.*, 2008, **105**, 15370–15375.
12 D. A. Doyle, J. M. Cabral, R. A. Pfuetzner, A. Kuo, J. M. Gulbis, S. L. Cohen, B. T. Chait and R. MacKinnon, *Science*, 1998, **280**, 69–77.
13 R. MacKinnon, *Angew. Chem., Int. Ed.*, 2004, **43**, 4265–4277.
14 X. Wu and P. A. Gale, *J. Am. Chem. Soc.*, 2016, **138**, 16508–16514.
15 B. Dworakowska and K. Dolowy, *Acta Biochim. Pol.*, 2000, **47**, 685–703.
16 P. A. Gale, J. T. Davis and R. Quesada, *Chem. Soc. Rev.*, 2017, **46**, 2497–2519.
17 O. K. Steinlein, *Chem. Rev.*, 2012, **112**, 6334–6352.
18 J. J. Kasianowicz, *Chem. Rev.*, 2012, **112**, 6215–6217.
19 H. Li, H. Valkenier, L. W. Judd, P. R. Brotherhood, S. Hussain, J. A. Cooper, O. Jurček, H. A. Sparkes, D. N. Sheppard and A. P. Davis, *Nat. Chem.*, 2015, **8**, 24.
20 S. N. Berry, V. Soto-Cerrato, E. N. W. Howe, H. J. Clarke, I. Mistry, A. Tavassoli, Y. T. Chang, R. Pérez-Tomás and P. A. Gale, *Chem. Sci.*, 2016, **7**, 5069–5077.
21 N. L. Mora, A. Bahreman, H. Valkenier, H. Li, T. H. Sharp, D. N. Sheppard, A. P. Davis and A. Kros, *Chem. Sci.*, 2016, **7**, 1768–1772.
22 B. Shen, X. Li, F. Wang, X. Yao and D. A. Yang, *PLoS One*, 2012, **7**, e34694.
23 P. A. Gale, R. Pérez-Tomás and R. Quesada, *Acc. Chem. Res.*, 2013, **46**, 2801–2813.
24 A. Furstner, *Angew. Chem., Int. Ed.*, 2003, **42**, 3582–3603.
25 R. Perez-Tomas and M. Vinas, *Curr. Med. Chem.*, 2010, **17**, 2222–2231.

 This journal is © The Royal Society of Chemistry 2020

Open Access Article. Published on 29 January 2020. Downloaded on 6/30/2020 3:14:16 PM.
This article is licensed under a Creative Commons Attribution-NonCommercial 3.0 Unported Licence.

26 S. K. Ko, S. K. Kim, A. Share, V. M. Lynch, J. Park, W. Namkung, W. Van Rossom, N. Busschaert, P. A. Gale, J. L. Sessler and I. Shin, *Nat. Chem.*, 2014, **6**, 885–892.
27 V. Soto-Cerrato, P. Manuel-Manresa, E. Hernando, S. Calabuig-Fariñas, A. Martínez-Romero, V. Fernández-Dueñas, T. Sahlholm, K. Knöpfel, M. García-Valverde, A. M. Rodilla, E. Jantus-Lewintre, R. Farràs, F. Ciruela, R. Pérez-Tomás and R. Quesada, *J. Am. Chem. Soc.*, 2015, **137**, 15892–15898.
28 N. Busschaert, M. Wenzel, M. E. Light, P. Iglesias-Hernández, R. Pérez-Tomás and P. A. Gale, *J. Am. Chem. Soc.*, 2011, **133**, 14136–14148.
29 T. Saha, M. S. Hossain, D. Saha, M. Lahiri and P. Talukdar, *J. Am. Chem. Soc.*, 2016, **138**, 7558–7567.
30 L. A. Jowett, E. N. W. Howe, V. Soto-Cerrato, W. Van Rossom, R. Pérez-Tomás and P. A. Gale, *Sci. Rep.*, 2017, **7**, 9397.
31 A. V. Koulov, J. M. Mahoney and B. D. Smith, *Org. Biomol. Chem.*, 2003, **1**, 27–29.
32 J. H. Lee, Y. R. Choi, P. Kang, M. G. Choi and K. S. Jeong, *J. Org. Chem.*, 2014, **79**, 6403–6409.
33 C. C. Tong, R. Quesada, J. L. Sessler and P. A. Gale, *Chem. Commun.*, 2008, **47**, 6321–6323.
34 A. Vargas Jentzsch, D. Emery, J. Mareda, P. Metrangolo, G. Resnati and S. Matile, *Angew. Chem., Int. Ed.*, 2011, **50**, 11675–11678.
35 D. Basak, S. Sridhar, A. K. Bera and N. Madhavan, *Org. Biomol. Chem.*, 2016, **14**, 4712–4717.
36 *Marvin 5.8.0*, ChemAxon, 2012, http://www.chemaxon.com.
37 V. Saggiomo, S. Otto, I. Marques, V. Félix, T. Torroba and R. Quesada, *Chem. Commun.*, 2012, **48**, 5274–5276.
38 C. A. Lipinski, F. Lombardo, B. W. Dominy and P. J. Feeney, *Adv. Drug Delivery Rev.*, 1997, **23**, 3–25.
39 A. L. Trifonov, V. V. Levin, M. I. Struchkova and A. D. Dilman, *Org. Lett.*, 2017, **19**, 5304–5307.
40 T. Routasalo, J. Helaja, J. Kavakka and A. M. P. Koskinen, *Eur. J. Org. Chem.*, 2008, **2008**, 3190–3199.
41 A. L. Sisson, M. R. Shah, S. Bhosale and S. Matile, *Chem. Soc. Rev.*, 2006, **35**, 1269–1286.
42 P. Talukdar, G. Bollot, J. Mareda, N. Sakai and S. Matile, *J. Am. Chem. Soc.*, 2005, **127**, 6528–6529.
43 S. V. Shinde and P. Talukdar, *Chem. Commun.*, 2018, **54**, 10351–10354.
44 A. Roy, A. Gautam, J. A. Malla, S. Sarkar, A. Mukherjee and P. Talukdar, *Chem. Commun.*, 2018, **54**, 2024–2027.
45 T. Saha, S. Dasari, D. Tewari, A. Prathap, K. M. Sureshan, A. K. Bera, A. Mukherjee and P. Talukdar, *J. Am. Chem. Soc.*, 2014, **136**, 14128–14135.
46 T. Saha, A. Roy, M. L. Gening, D. V. Titov, A. G. Gerbst, Y. E. Tsvetkov, N. E. Nifantiev and P. Talukdar, *Chem. Commun.*, 2014, **50**, 5514–5516.
47 S. Litvinchuk, G. Bollot, J. Mareda, A. Som, D. Ronan, M. R. Shah, P. Perrottet, N. Sakai and S. Matile, *J. Am. Chem. Soc.*, 2004, **126**, 10067–10075.
48 J. A. Malla, A. Roy and P. Talukdar, *Org. Lett.*, 2018, **20**, 5991–5994.
49 A. Gilles and M. Barboiu, *J. Am. Chem. Soc.*, 2016, **138**, 426–432.
50 C. Ren, J. Shen and H. Zeng, *J. Am. Chem. Soc.*, 2017, **139**, 12338–12341.
51 C. Ren, X. Ding, A. Roy, J. Shen, S. Zhou, F. Chen, S. F. Yau Li, H. Ren, Y. Y. Yang and H. Zeng, *Chem. Sci.*, 2018, **9**, 4044–4051.
52 C. Ren, F. Zeng, J. Shen, F. Chen, A. Roy, S. Zhou, H. Ren and H. Zeng, *J. Am. Chem. Soc.*, 2018, **140**, 8817–8826.
53 B. P. Benke, P. Aich, Y. Kim, K. L. Kim, M. R. Rohman, S. Hong, I. C. Hwang, E. H. Lee, J. H. Roh and K. Kim, *J. Am. Chem. Soc.*, 2017, **139**, 7432–7435.
54 C. R. Yamnitz, S. Negin, I. A. Carasel, R. K. Winter and G. W. Gokel, *Chem. Commun.*, 2010, **46**, 2838–2840.
55 M. J. Langton, L. M. Scriven, N. H. Williams and C. A. Hunter, *J. Am. Chem. Soc.*, 2017, **139**, 15768–15773.
56 M. Jung, H. Kim, K. Baek and K. Kim, *Angew. Chem., Int. Ed.*, 2008, **47**, 5755–5757.
57 N. Sakai and S. Matile, *Langmuir*, 2013, **29**, 9031–9040.
58 A. V. Jentzsch, D. Emery, J. Mareda, S. K. Nayak, P. Metrangolo, G. Resnati, N. Sakai and S. Matile, *Nat. Commun.*, 2012, **3**, 905.
59 H. Goto, S. Obata, N. Nakayama and K. Ohta, *CONFLEX 8*, CONFLEX Corporation, Tokyo, Japan, 2012.
60 H. Goto and E. Osawa, *J. Am. Chem. Soc.*, 1989, **111**, 8950–8951.
61 J. J. P. Stewart, *MOPAC2012*, Stewart Computational Chemistry: Colorado Springs, CO, USA, 2012.
62 P. Májek and R. Elber, *J. Chem. Theory Comput.*, 2010, **6**, 1805–1817.
63 C. D. Bortner and J. A. Cidlowski, *Cell Death Differ.*, 2002, **9**, 1307.
64 R. Núñez, S. M. Sancho-Martínez, J. M. L. Novoa and F. J. López-Hernández, *Cell Death Differ.*, 2010, **17**, 1665.
65 M. A. Model, *Am. J. Physiol.: Cell Physiol.*, 2014, **306**, C417–C424.
66 N. Busschaert, S. H. Park, K. H. Baek, Y. P. Choi, J. Park, E. N. W. Howe, J. R. Hiscock, L. E. Karagiannidis, I. Marques, V. Félix, W. Namkung, J. L. Sessler, P. A. Gale and I. Shin, *Nat. Chem.*, 2017, **9**, 667.
67 S. Sakamuru, M. S. Attene-Ramos and M. Xia, *Methods Mol. Biol.*, 2016, **1473**, 17–22.
68 S. Patil, M. M. Kuman, S. Palvai, P. Sengupta and S. Basu, *ACS Omega*, 2018, **3**, 1470–1481.
69 A. Ashkenazi, *Nat. Rev. Drug Discovery*, 2008, **7**, 1001–1012.
70 S. T. Smiley, M. Reers, C. Mottola-Hartshorn, M. Lin, A. Chen, T. W. Smith, G. D. Steele and L. B. Chen, *Proc. Natl. Acad. Sci. U. S. A.*, 1991, **88**, 3671–3675.
71 N. Zamzami and G. Kroemer, *Curr. Biol.*, 2003, **13**, R71–R73.
72 A. Cossarizza, M. Baccarani-Contri, G. Kalashnikova and C. A. Franceschi, *Biochem. Biophys. Res. Commun.*, 1993, **197**, 40–45.
73 S. S. Sabharwal and P. T. Schumacker, *Nat. Rev. Cancer*, 2014, **14**, 709–721.
74 G. Y. Liou and P. Storz, *Free Radical Res.*, 2010, **44**, 479–496.
75 L. A. Sena and N. S. Chandel, *Mol. Cell*, 2012, **48**, 158–167.
76 S. Galadari, A. Rahman, S. Pallichankandy and F. Thayyullathil, *Free Radicals Biol. Med.*, 2017, **104**, 144–164.
77 D. Wu and P. Yotnda, *J. Visualized Exp.*, 2011, **57**, 3357.

Open Access Article. Published on 29 January 2020. Downloaded on 6/30/2020 3:14:16 PM.
This article is licensed under a Creative Commons Attribution-NonCommercial 3.0 Unported Licence.



78 A. P. Halestrap, *J. Mol. Cell. Cardiol.*, 2009, **46**, 821–831.
79 M. Crompton, *Biochem. J.*, 1999, **341**, 233–249.
80 M. Madesh and G. Hajnoczky, *J. Cell Biol.*, 2001, **155**, 1003–1015.
81 V. P. Skulachev, *Apoptosis*, 2006, **11**, 473–485.
82 S. P. Cullen and S. J. Martin, *Cell Death Differ.*, 2009, **16**, 935–938.
83 J. Wu, T. Liu, J. Xie, F. Xin and L. Guo, *Cell. Mol. Life Sci.*, 2006, **63**, 949–957.
84 Y. Shi, *Mol. Cell*, 2002, **9**, 459–470.
85 S. H. Park, Y. P. Choi, J. Park, A. Share, O. Francesconi, C. Nativi, W. Namkung, J. L. Sessler, S. Roelens and I. Shin, *Chem. Sci.*, 2015, **6**, 7284–7292.
86 G. V. Chaitanya, A. J. Steven and P. P. Babu, *J. Cell Commun. Signal.*, 2010, **8**, 31.
87 A. H. Boulares, A. G. Yakovlev, V. Ivanova, B. A. Stoica, G. Wang, S. Iyer and M. Smulson, *J. Biol. Chem.*, 1999, **274**, 22932–22940.
88 T. Suzuki, K. Fujikura, T. Higashiyama and K. Takata, *J. Histochem. Cytochem.*, 1997, **45**, 49–53.

This journal is © The Royal Society of Chemistry 2020